

Ultra-High-Energy Cosmic Rays

Luis A. Anchordoqui

Department of Physics & Astronomy, Lehman College, City University of New York, NY 10468, USA

Department of Physics, Graduate Center, City University of New York, NY 10016, USA

Department of Astrophysics, American Museum of Natural History, NY 10024, USA

Abstract

In this report we review the important progress made in recent years towards understanding the experimental data on ultra-high-energy ($E \gtrsim 10^9$ GeV) cosmic rays. We begin with a general survey of the available data, including a description of the energy spectrum, the nuclear composition, and the distribution of arrival directions. At this point we also give a synopsis of experimental techniques. After that, we introduce the fundamentals of cosmic ray acceleration and energy loss during propagation, with a view of discussing the conjectured nearby sources. Next, we survey the state of the art regarding the high- and ultra-high-energy cosmic neutrinos which may be produced in association with the observed cosmic rays. These neutrinos could constitute key messengers identifying currently unknown cosmic accelerators, possibly in the distant universe, because their propagation is not influenced by background photon or magnetic fields. Subsequently, we summarize the phenomenology of cosmic ray air showers. We describe the hadronic interaction models used to extrapolate results from collider data to ultra-high energies and the main electromagnetic processes that govern the longitudinal shower evolution. Armed with these two principal shower ingredients and motivation from the underlying physics, we describe the different methods proposed to distinguish the primary particle species. In the end, we explore how ultra-high-energy cosmic rays can be used as probes of beyond standard model physics models.

Keywords: ultra-high-energy astrophysical phenomena – extensive air showers

arXiv:1807.09645v2 [astro-ph.HE] 31 Dec 2018

Contents

1	Introduction	3
2	Experimental observations and searches	5
2.1	Historical overview	5
2.2	Measurements of the cosmic ray intensity and its nuclear composition	8
2.3	Anisotropy searches	13
3	Quest for the origin(s) of UHECRs	29
3.1	Acceleration processes	29
3.1.1	Phenomenological considerations	29
3.1.2	Unipolar induction	30
3.1.3	Fermi acceleration at shock waves	35
3.2	Energy loss	45
3.2.1	Interaction rate of UHECRs on photon fields	45
3.2.2	Opacity of the CMB to UHECR protons	46
3.2.3	Photonuclear interactions	50
3.3	Plausible sources in our cosmic backyard	55
3.3.1	γ AGNs	55
3.3.2	SBGs	58
3.4	Fitting simultaneously the UHECR spectrum and its nuclear composition	62
3.5	Impact of ν and γ -ray observations on UHECR models	68
3.6	Grand unified spectrum of diffuse extragalactic background radiation	73
4	Phenomenology of UHECR air showers	77
4.1	Nature's calorimeter	77
4.2	Systematic uncertainties in air shower measurements from hadronic interaction models	78
4.3	Electromagnetic processes	85
4.4	Paper-and-pencil air shower modeling	89
5	UHECR as probes of particle physics beyond the electroweak scale	92
5.1	Testing models of the early universe via top-down production of cosmic rays and neutrinos	92
5.2	Search for Lorentz invariant breaking effects	96
5.3	Delve into the electroweak sector in search for new physics at subfermi distances	99

6 Looking ahead	102
Acknowledgments	103
Appendix A	104
Appendix B	105
Appendix C	110
Bibliography	111

1. Introduction

For biological reasons our perception of the Universe is based on the observation of photons, most trivially by staring at the night-sky with our bare eyes. Conventional astronomy covers many orders of magnitude in photon wavelengths, from 10^5 cm radio-waves to 10^{-16} cm gamma-rays of TeV energy. This 70 octave span in photon frequency allows for a dramatic expansion of our observational capacity beyond the approximately one octave perceivable by the human eye. Photons are not, however, the only messengers of astrophysical processes; we can also observe baryonic cosmic rays, neutrinos, and gravitons (glaring as gravitational waves). On 2017 August 17, the Advanced LIGO and Advanced Virgo gravitational-wave detectors made their first observation of a binary neutron star merger, with subsequent identification of transient counterparts across the entire electromagnetic spectrum [1]. On 2017 September 22, the blazar TXS 0506+056 was observed simultaneously in neutrinos and photons [2]. These unprecedented observations have been hailed as the dawn of a new multi-frequency and multi-messenger era in astronomy.

Baryon astronomy may be feasible for neutral particles or possibly charged particles with energies high enough to render their trajectories magnetically rigid. Indeed, on 2018 January 18, the Pierre Auger Collaboration reported an indication of a possible correlation between nearby starburst galaxies and cosmic rays of energy $> 10^{10.6}$ GeV, with an a posteriori chance probability in an isotropic cosmic ray sky of 4.2×10^{-5} , corresponding to a 1-sided Gaussian significance of 4σ [3]. Should Mother Nature be so cooperative, the emission of extremely high energetic particles by starburst galaxies (predicted in the late '90s [4]) would become the first statistically ironclad observation of point sources in cosmic rays.

The history of cosmic ray studies has witnessed many discoveries central to the progress of high-energy physics, from the watershed identification of new elementary particles in the early days, to the confirmation of long-suspected neutrino oscillations. A major recent achievement is establishing the suppression of the spectrum at the highest energies [5–7], which may be the long-sought Greisen, Zatzepin, and Kuzmin (GZK) cutoff [8, 9]. The GZK effect is a remarkable example of the profound links between different regimes of physics, connecting as it does the behavior of the rarest, highest-energy particles in the Cosmos to the existence of Nature’s most abundant particles – the low energy photons in the relic microwave radiation of the Big Bang – while simultaneously demanding the validity of Special Relativity over a mind-boggling range of scales. Ultra-high-energy ($E \gtrsim 10^9$ GeV) cosmic rays (UHECRs) are the only particles with energies exceeding those available at terrestrial accelerators. These UHECRs carry about seven orders

of magnitude more energy than the beam of the large hadron collider (LHC). Hence, with UHECRs one can conduct particle physics measurements in the center-of-mass (c.m.) frame up to about one order of magnitude higher than the LHC energy reach.

In this review we concentrate on the physics of UHECRs focusing tightly on the interface between experiment and phenomenology. The layout is as follows. We begin in Sec. 2 with a brief summary of the most recent observations; guidance is given in the appendices to statistical formulae and significance tests referred to in the main text. In Sec. 3 we discuss the physics and astrophysics associated with the search for the UHECR origin. We first summarize the main acceleration mechanisms and then discuss the energy loss during propagation in the intergalactic space and in the source environment. Subsequently, we evaluate the multi-messenger relations connecting neutrino, gamma ray, and UHECR observations. In Sec. 4 we focus attention on the general properties and techniques for modeling extensive air showers initiated when UHECRs interact in the atmosphere. In Sec. 5 we examine how UHECRs can be used as probes of new physics beyond the highly successful but conceptually incomplete standard model (SM) of weak, electromagnetic, and strong interactions. Finally, in Sec. 6 we provide evidence-based guidance to set strict criteria for research and development of future UHECR experiments.

Before proceeding, we pause to present our notation. Unless otherwise stated, we work with natural (particle physicist's) Heaviside-Lorentz (HL) units with

$$\hbar = c = k = \varepsilon_0 = \mu_0 = 1. \quad (1)$$

The fine structure constant is $\alpha = e^2/(4\pi\varepsilon_0\hbar c) \simeq 1/137$. All SI units can then be expressed in electron Volt (eV), namely

$$1 \text{ m} \simeq 5.1 \times 10^6 \text{ eV}^{-1}, \quad 1 \text{ s} \simeq 1.5 \times 10^{15} \text{ eV}^{-1}, \quad 1 \text{ kg} \simeq 5.6 \times 10^{35} \text{ eV}, \quad (2)$$

$$1 \text{ A} \simeq 1244 \text{ eV}, \quad 1 \text{ G} \simeq 1.95 \times 10^{-2} \text{ eV}^2, \quad 1 \text{ K} \simeq 8.62 \times 10^{-5} \text{ eV}. \quad (3)$$

Electromagnetic processes in astrophysical environments are often described in terms of Gauss (G) units. For a comparison of formulas used in the literature, we note some conversion factors: $(e^2)_{\text{HL}} = 4\pi(e^2)_{\text{G}}$, $(B^2)_{\text{HL}} = (B^2)_{\text{G}}/4\pi$, and $(E^2)_{\text{HL}} = (E^2)_{\text{G}}/4\pi$. To avoid confusion we will present most of the formulas in terms of *invariant quantities* i.e., eB , eE and the fine-structure constant α . Distances are generally measured in Mpc $\simeq 3.08 \times 10^{22}$ m. Extreme energies are sometimes expressed in EeV $\equiv 10^9$ GeV $\equiv 10^{18}$ eV. The following is a list of additional useful conversion factors: $1 \text{ GeV} = 1.602 \times 10^{-3}$ erg, $h = 6.626 \times 10^{-27}$ erg Hz $^{-1}$, $hc = 1.986 \times 10^{-16}$ erg cm $= 1.986 \times 10^{-8}$ erg Å, $\hbar c = 1.973 \times 10^{-14}$ GeV cm, $1 \text{ sr} = 3.283 \times 10^3$ sq deg $= 4.255 \times 10^{10}$ sq arcsec, $1 \text{ WB} = 10^{-8}$ GeV cm $^{-2}$ s $^{-1}$ sr $^{-1}$, and one Jansky or $1 \text{ Jy} = 10^{-23}$ erg cm $^{-2}$ s $^{-1}$ Hz $^{-1}$. The Planck units of mass, length, and time are $M_{\text{Pl}} = \ell_{\text{Pl}}^{-1} = t_{\text{Pl}}^{-1} \sim 1.2 \times 10^{19}$ GeV. We adopt the usual concordance cosmology of a flat universe dominated by a cosmological constant, with dark energy density parameter $\Omega_{\Lambda} \approx 0.69$ and a cold dark matter plus baryon component $\Omega_m \approx 0.31$ [10]. The Hubble parameter as a function of redshift z is given by $H^2(z) = H_0^2[\Omega_m(1+z)^3 + \Omega_{\Lambda}]$, normalized to its value today, $H_0 = 100 h$ km s $^{-1}$ Mpc $^{-1}$, with $h = 0.678(9)$ [11]. The dependence of the cosmological time with redshift is $dz = -dt(1+z)H(z)$. This report will build upon the content of the lecture notes from the 6th CERN-Latin-American School of High-Energy Physics [12], the whitepaper contribution to the US Snowmass planning process [13], and [14–16].

2. Experimental observations and searches

2.1. Historical overview

In 1912 Hess carried out a series of pioneering balloon flights during which he measured the levels of ionizing radiation as high as 5 km above the Earth's surface [17]. His discovery of increased radiation at high altitude revealed that we are bombarded by ionizing particles from above. These cosmic ray (CR) particles are now known to consist primarily of protons, helium, carbon, nitrogen and other heavy ions up to iron. Measurements of energy and isotropy showed conclusively that one obvious source, the Sun, is not the main source. Only for CRs with kinetic energy $E_{\text{kin}} \lesssim 100$ MeV, where the solar wind shields protons coming from outside the solar system, does the Sun dominate the observed proton flux.¹ Spacecraft missions far out into the solar system, well away from the confusing effects of the Earth's atmosphere and magnetosphere, confirm that the abundances around 1 GeV are strikingly similar to those found in the ordinary material of the solar system. Exceptions are the overabundance of elements like lithium, beryllium, and boron, originating from the spallation of heavier nuclei in the interstellar medium.

Above about 10^5 GeV, the rate of CR primaries is less than one particle per square meter per year and direct observation in the upper layers of the atmosphere (balloon or aircraft), or even above (spacecraft) is inefficient. Only experiments with large apertures and long exposure times can hope to acquire a significant number of events. Such experiments exploit the atmosphere as a giant calorimeter. The incident cosmic radiation interacts with the atomic nuclei of air molecules and produces air showers which spread out over large areas. Already in 1938, Auger concluded from the size of the air showers that the spectrum extends up to and perhaps beyond 10^6 GeV [18, 19]. Data collected during 1954 and 1957 at the Agassiz Station of the Harvard College Observatory provided evidence for primary particles with $E \sim 10^9$ GeV [20]. In 1962, the array of scintillation detectors at the MIT Volcano Ranch station detected the first UHECR event with an estimated energy of $\mathcal{O}(10^{11})$ GeV [21].

In 1964, the cosmic microwave background (CMB) was discovered [22], and shortly thereafter it became self-evident that the relic photons would make the universe opaque to the propagation UHECRs [8, 9]. The GZK interactions occur, for example, for protons with energies beyond the photopion production threshold,

$$E_{\text{th}} = \frac{m_\pi (2m_p + m_\pi)}{4\varepsilon} \approx 3.4 \times 10^{10} \left(\frac{\varepsilon}{10^{-3} \text{ eV}} \right)^{-1} \text{ GeV}, \quad (4)$$

where m_p (m_π) denotes the proton (pion) mass and $\varepsilon \sim 10^{-3}$ eV is a typical CMB photon energy. After pion production, the proton (or perhaps, instead, a neutron) emerges with at least 50% of the incoming energy. This implies that the nucleon energy changes by an e -folding after a propagation distance $d_{68}^{\text{GZK}} \lesssim (\sigma_{p\gamma} n_\gamma \langle y \rangle)^{-1} \sim 15$ Mpc, where $n_\gamma \approx 410 \text{ cm}^{-3}$ is the number density of the CMB photons, $\sigma_{p\gamma} > 0.1$ mb is the photopion production cross section, $\langle y \rangle$ is the average energy fraction (in the laboratory system) lost by a nucleon per interaction, and where the subscript of the GZK distance specifies

¹Cosmic rays entering the Solar System have to overcome the outward-flowing solar wind. The energy of incoming cosmic rays is reduced through interactions with this wind, preventing the lowest energy ones from reaching the Earth. This effect is known as solar modulation. The Sun has an 11 yr activity cycle, which is echoed in the strength of the solar wind to modulate cosmic rays. Because of this effect the flux of cosmic rays reaching Earth is anti-correlated with the level of solar activity: when the solar activity is high and there are lots of sunspots, the flux of cosmic rays at Earth is low, and vice versa. The solar modulation is visible below about 1 GeV.

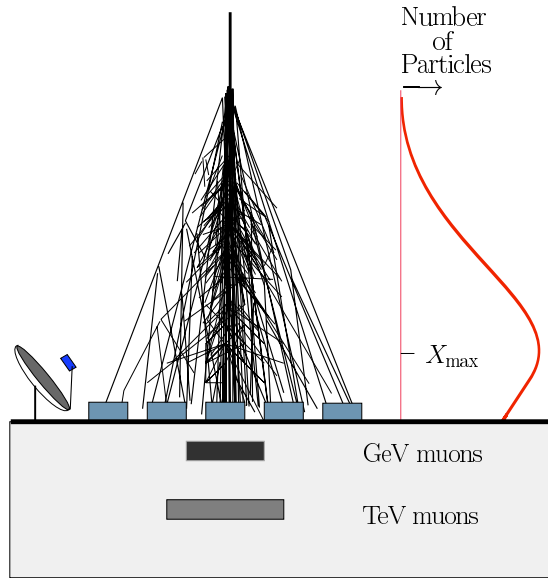


Figure 1: Particles interacting near the top of the atmosphere initiate an electromagnetic and hadronic cascade. Its profile is shown on the right. The different detection methods are illustrated. Mirrors collect the Cherenkov and nitrogen fluorescent light, arrays of detectors sample the shower reaching the ground, and underground detectors identify the muon component of the shower. The number of particles as a function of the amount of atmosphere penetrated by the cascade (X in g cm^{-2}) is known as the longitudinal profile. The integrated longitudinal profile provides a calorimetric measurement of the energy of the primary CR, with a relatively small uncertainty due to the correction for energy lost to neutrinos and particles hitting the ground. From Ref. [14].

the CR energy in EeV units. For heavy nuclei, the giant dipole resonance (GDR) can be excited at similar total energies and hence, for example, iron nuclei do not survive fragmentation over comparable GZK distances [23, 24]. Additionally, the survival probability for extremely high energy ($\approx 10^{11}$ GeV) γ -rays (propagating on magnetic fields $\gg 10^{-11}$ G) to a distance d , $p(> d) \approx \exp[-d/6.6 \text{ Mpc}]$, becomes less than 10^{-4} after traversing a distance of 50 Mpc [15]. All in all, as our horizon shrinks dramatically for $E \gtrsim 10^{11}$ GeV, one would expect a sudden suppression in the energy spectrum if the CR sources follow a cosmological distribution.

Throughout the past few decades, continuously running monitoring using sophisticated equipment on high altitude balloons and ingenious installations on the Earth's surface uncovered a plummeting flux that goes down from $10^4 \text{ m}^{-2} \text{ s}^{-1}$ at $E \sim 1 \text{ GeV}$ to $10^{-2} \text{ km}^{-2} \text{ yr}^{-1}$ at $E \sim 10^{11} \text{ GeV}$ [11]. In recent years, substantial progress has been made in measuring the extraordinarily low flux at the high energy end of the spectrum. There are two primary detection methods that have been successfully used in ground-based high exposure experiments. In the following paragraph we provide a terse overview of these approaches. For an authoritative review on experimental techniques and historical perspective see [25, 26].

When the incident cosmic radiation interacts with atomic nuclei of air molecules, it produces fluxes of secondary, tertiary, and subsequent generations of particles. All these particles together create a cascade, called air shower. As the cascade develops longitudinally the particles become less and less energetic since the energy of the incoming cosmic ray is redistributed among more and more participants. The transverse momenta acquired by the secondaries cause the particles to spread laterally as they propagate through the atmospheric target. Most of the air shower particles excite nitrogen molecules in the atmosphere, which fluoresce in the ultraviolet (UV). The size of an extensive air shower (EAS) at sea-level depends on the

primary energy and arrival direction. For showers of UHECRs, the cascade is typically several hundreds of meters in diameter and contains millions of secondary particles. Secondary electrons and muons produced in the decay of pions may be observed in scintillation counters or alternatively by the Cherenkov light emitted in water tanks. The separation of these detectors may range from 10 m to 1 km depending on the CR energy and the optimal cost-efficiency of the detection array. The shower core and hence arrival direction can be estimated by the relative arrival time and density of particles in the grid of detectors. The lateral particle density of the showers can be used to calibrate the primary energy. Another well-established method of detection (pioneered by the Fly’s Eye experiment [27] and its up-scaled version with high-resolution dubbed HiRes [28]) involves measurement of the shower longitudinal development (number of particles versus atmospheric depth, shown schematically in Fig. 1) by sensing the fluorescence light produced via interactions of the charged particles in the atmosphere. The emitted light is typically in the 300 – 400 nm UV range to which the atmosphere is quite transparent. Under favorable atmospheric conditions, EASs can be detected at distances as large as 20 km, about 2 attenuation lengths in a standard desert atmosphere at ground level. However, observations can only be done on clear moonless nights, resulting in an average 10% duty cycle.

In this review we concentrate on the latest results from the two UHECR experiments currently in operation: the Telescope Array and the Pierre Auger Observatory to which we will often refer as TA and Auger. TA has been collecting data since 2007 in Millard County, west central Utah. This facility is located at 39.3° N and 112.9° W, 1.4 km above sea level (equivalent to 880 g/cm² of atmospheric depth). The experiment consists of 507 scintillation surface detectors sensitive to muons and electrons [29], and 48 fluorescence telescopes located in three fluorescence detector stations overlooking the counters [30]. The spacing of the counters in the surface detector array is 1.2 km and they are placed over an area of approximately 700 km².

The Pierre Auger Observatory is located on the vast plain of *Pampa Amarilla*, near the town of Malargüe in Mendoza Province, Argentina (35.1° – 35.5° S, 69.6° W, and atmospheric depth of 875 g/cm²) [31]. The experiment began collecting data in 2004, with construction of the baseline design completed by 2008. From January 2004 until December 2016, Auger had collected in excess of 6.7×10^4 km² sr yr in exposure, significantly more exposure than other cosmic ray observatories combined [32]. Two types of instruments are employed. Particle detectors on the ground sample air shower fronts as they arrive at the Earth’s surface, while fluorescence telescopes measure the light produced as air shower particles excite atmospheric nitrogen.

The surface array [33] comprises 1.6×10^3 surface detector (SD) stations, each consisting of a tank filled with 12 tons of water and instrumented with 3 photomultiplier tubes which detect the Cherenkov light produced as particles traverse the water. The signals from the photomultipliers are read out with flash analog to digital converters at 40 MHz and timestamped by a GPS unit, allowing for detailed study of the arrival time profile of shower particles. The tanks are arranged on a triangular grid with a 1.5 km spacing, covering about 3×10^3 km². The surface array operates with close to a 100% duty cycle, and the acceptance for events above 10^{9.5} GeV is nearly 100%.

The fluorescence detector (FD) system [34] consists of 4 buildings, each housing 6 telescopes which overlook the surface array. Each telescope employs an 11 m² segmented mirror to focus the fluorescence light entering through a 2.2 m diaphragm onto a camera which pixelizes the image using 440 photomultiplier tubes. The photomultiplier signals are digitized at 10 MHz, providing a time profile of the shower as it develops in the atmosphere. The FD can be operated only when the sky is dark and clear, and has a duty cycle of 10-15%. In contrast to the SD acceptance, the acceptance of FD events depends strongly on energy [35], extending down to about 10⁹ GeV.

The two detector systems of Auger and TA provide complementary information, as the SD measures the lateral distribution and time structure of shower particles arriving at the ground, and the FD measures the longitudinal development of the shower in the atmosphere. A subset of showers is observed simultaneously by the SD and FD. These “hybrid” events are very precisely measured and provide an invaluable calibration tool. In particular, the FD allows for a roughly calorimetric measurement of the shower energy since the amount of fluorescence light generated is proportional to the energy deposited along the shower path; in contrast, extracting the shower energy via analysis of particle densities at the ground relies on predictions from hadronic interaction models describing physics at energies beyond those accessible to existing collider experiments. Hybrid events can therefore be exploited to set a model-independent energy scale for the SD array, which in turn has access to a greater data sample than the FD due to the greater live time.

In the remainder of the section, we describe recent results from Auger and TA, including measurements of energy spectrum and UHECR nuclear composition, as well as searches for anisotropy in the CR arrival directions.

2.2. Measurements of the cosmic ray intensity and its nuclear composition

The (differential) intensity of CRs is defined as the number of particles crossing a unit area dA per unit time dt and unit solid angle $d\Omega$, with energy within E and $E + dE$ [36],

$$J(E) = \frac{dN}{dA dt d\Omega dE} . \quad (5)$$

Throughout $J(> E) = \int_E^\infty dE' J(E')$ symbolizes the number of particles with energy $> E$ crossing an unit area per unit time and unit solid angle. For an isotropic intensity, the flux of particles from one hemisphere traversing a planar detector is found to be

$$\mathcal{F}(E) = \int d\Omega J(E) \cos \theta = J(E) \int_0^{2\pi} d\phi \int_0^{\pi/2} d\theta \sin \theta \cos \theta = \pi J(E) , \quad (6)$$

where θ and ϕ are the zenith and azimuthal angles, respectively. The (differential) number density of cosmic rays with velocity v is given by

$$n(E) = \frac{4\pi}{v} J(E) . \quad (7)$$

On the whole, the intensity could depend both on the position \mathbf{x} of the detector and on its orientation (θ, ϕ) . The intensity can be related to the CR phase space distribution, $f(\mathbf{x}, \mathbf{p})$, by substituting

$$dN = f(\mathbf{x}, \mathbf{p}) d^3x d^3p \quad (8)$$

into (5), with $d^3x = dA v dt$ and $d^3p = p^2 dp d\Omega$. This leads to

$$J(\mathbf{x}, p, \theta, \phi) = vp^2 \frac{dp}{dE} f(\mathbf{x}, \mathbf{p}) = p^2 f(\mathbf{x}, \mathbf{p}) . \quad (9)$$

The kinetic energy density of CRs can be expressed as

$$\epsilon_{\text{CR}} = \int dE E_{\text{kin}} n(E) = 4\pi \int dE \frac{E_{\text{kin}}}{v} J(E) . \quad (10)$$

The energy density of CRs in the local interstellar medium (LIS), i.e. with the intensity in (10) extrapolated outside the reach of the solar wind, is found to be $\epsilon_{\text{CR}} \approx 0.8 \text{ eV/cm}^3$ [37]. It is of interest to compare this value with the average energy density: (i) of baryons in the Universe $\epsilon_b \approx 100 \text{ eV/cm}^3$, (ii) of starlight in the Galactic disc $\epsilon_{\text{light}} \approx 5 \text{ eV/cm}^3$, (iii) of the Galactic magnetic field $\epsilon_B = B^2/2 \approx 0.6 \text{ eV/cm}^3$ (assuming $B \approx 5 \mu\text{G}$). Note that if the LIS energy density of cosmic rays would be taken as a fiducial value for the entire Universe, then roughly 1% of the energy of all baryons would be in the form of relativistic particles. This is highly unlikely. Therefore, the preceding estimates seem to indicate that most CRs are accumulated inside the Milky Way.

Above about 1 GeV, the energy spectrum is observed to fall roughly as a power law; namely, the CR intensity decreases nearly three orders of magnitude per energy decade, until eventually suffering a strong suppression around $E_{\text{supp}} \sim 10^{10.6} \text{ GeV}$ [11]. Individual experiments cover only a part of these 11 decades in energy, which means that a common picture needs to be pieced together from many data sets. The database of charged cosmic rays (CRDB) is a meritorious endeavor which maintains central machine-readable access to CR data collected by satellite and balloon experiments [38]. Because of their direct detection method, these experiments provide characterization of the separate elements in terms of their charge Ze , and hence they report the CR intensity per element. Above about 10^6 GeV direct detection methods become inefficient and ground-based experiment take over. Unfortunately, because of the highly indirect method of measurement, extracting precise information from EASs has proved to be exceedingly difficult, and hence the ability to discriminate the charge Ze of each CR is lost. The most fundamental problem is that the first generations of particles in the cascade are subject to large inherent fluctuations and consequently this limits the event-by-event energy resolution of the experiments. In addition, the c.m. energy of the first few cascade steps is well beyond any reached in collider experiments. Therefore, one needs to rely on models that attempt to extrapolate, using different mixtures of theory and phenomenology, our understanding of particle physics.

If the primary cosmic ray is a baryon, the air-shower development is driven by soft QCD interactions, which are computed from phenomenological models tuned to collider data. Hundreds to thousands of secondary particles are usually produced at the interaction vertex, many of which also have energies above the highest accelerator energies [39]. These secondary products are of course intrinsically hadrons. Generally speaking, by extrapolating final states observed at collider experiments, we can infer that, for pp collisions at c.m. energy $\sqrt{s} \gtrsim 100 \text{ TeV}$, the jet of hadrons contains about 75% pions (including 25% π^0 's, in accord with isospin invariance), 15% kaons, and 10% nucleons [40]. During the shower evolution, the hadrons propagate through a medium with an increasing density as the altitude decreases and the hadron-air cross section rises slowly with energy. Therefore, the probability for interacting with air before decay increases with rising energy. Moreover, the relativistic time dilation increases the decay length by a factor E_h/m_h , where E_h and m_h are the energy and mass of the produced hadron. When the π^0 's (with a lifetime of $\simeq 8.4 \times 10^{-17} \text{ s}$) do decay promptly to two photons, they feed the electromagnetic component of the shower. For other longer-lived mesons, it is instructive to estimate the critical energy at which the chances for interaction and decay are equal. For a vertical transversal of the atmosphere, such a critical energy is found to be: $\xi_c^{\pi^\pm} \sim 115 \text{ GeV}$, $\xi_c^{K^\pm} \sim 850 \text{ GeV}$, $\xi_c^{K_L^0} \sim 210 \text{ GeV}$, $\xi_c^{K_S^0} \sim 30 \text{ TeV}$ [41]. The dominant K^+ branching ratios are to $\mu^+\nu_\mu$ (64%), to $\pi^+\pi^0$ (21%), to $\pi^+\pi^+\pi^-$ (6%), and to $\pi^+\pi^0\pi^0$ (2%), whereas those of the K_S^0 are to $\pi^+\pi^-$ (60%), to $\pi^0\pi^0$ (30%), and for K_L^0 we have $\pi^\pm e^\mp \nu_e$ (40%), $\pi^\pm \mu^\mp \nu_\mu$ (27%), $\pi^0\pi^0\pi^0$ (19%), $\pi^+\pi^-\pi^0$ (12%) [11]. With these figures in mind, to a first approximation it seems reasonable to assume that in each generation of particles about 25% of the energy is transferred to the electromagnetic shower, and all

Table 1: Upper limits on the integral photon intensity with a spectrum $\propto E_\gamma^{-2}$ and no background subtraction [46].

$\log_{10}(E_0/\text{GeV})$	$\log_{10}[\Phi_\gamma(> E_0)/(\text{km}^{-2} \text{sr}^{-1} \text{yr}^{-1})]$
9.0	-1.60
9.3	-2.05
9.5	-2.10
9.7	-2.10
10.0	-2.65
10.3	-3.00
10.7	-3.40

hadrons with energy $\gtrsim \xi_c^{\pi^\pm}$ interact rather than decay, continuing to produce the hadronic shower.² Eventually, the electromagnetic cascade dissipates around 90% of the primary particle's energy and the remaining 10% is carried by muons and neutrinos.

As the cascade process develops in the atmosphere, the number of particles in the shower increases until the energy of the secondary particles is degraded to the level where ionization losses dominate. At this point the density of particles starts to decline. A well-defined peak in the longitudinal development, X_{max} , occurs where the number of e^\pm in the electromagnetic shower is at its maximum; see Fig. 1. X_{max} increases with primary energy, as more cascade generations are required to degrade the secondary particle energies. Evaluating X_{max} is a fundamental part of many of the composition analyses done when studying air showers. For showers of a given total energy E , heavier nuclei have smaller X_{max} because the shower is already subdivided into A nucleons when it enters the atmosphere. The average depth of maximum $\langle X_{\text{max}} \rangle$ scales approximately as $\ln(E/A)$ [43]. Therefore, since $\langle X_{\text{max}} \rangle$ can be determined directly from the longitudinal shower profiles measured with a fluorescence detector, the composition can be extracted after estimating E from the total fluorescence yield. Indeed, the parameter often measured is D_{10} , the rate of change of $\langle X_{\text{max}} \rangle$ per *decade* of energy.

Photons penetrate quite deeply into the atmosphere due to decreased secondary multiplicities and suppression of cross sections by the Landau-Pomeranchuk-Migdal (LPM) effect [44, 45]. Indeed, it is rather easier to distinguish photons from protons and iron than protons and iron are to distinguish from one another. For example, at 10^{10} GeV, the $\langle X_{\text{max}} \rangle$ for a photon is about 1,000 g/cm², while for protons and iron the numbers are 800 g/cm² and 700 g/cm², respectively. Searches for photon primaries have been conducted using both the surface and fluorescence instruments of Auger. While analysis of the fluorescence data exploits the direct view of shower development, analysis of data from the surface detector relies on measurement of quantities which are indirectly related to the X_{max} , such as the signal risetime at 1000 m from the shower core and the curvature of the shower front. Presently, the 95% CL upper limits on the integrated photon intensity, $\Phi_\gamma(> E_0)$, are given in Table 1. Further details on the analysis procedures can be found in [47–49].

²The electromagnetic shower fraction from pions only is less than 25%, but simulations show that inclusion of other hadronic resonances brings the electromagnetic shower fraction up to about 25% [42]. Thus, 25% is a reasonable estimate of the energy transfer to the electromagnetic shower in each generation of particles.

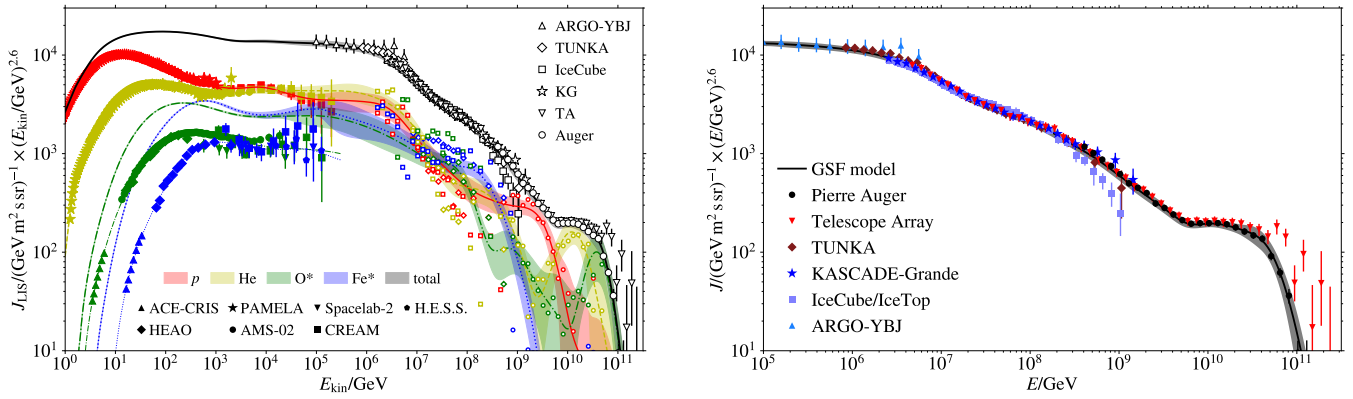


Figure 2: All-particle flux (black thick solid line), the flux contributed by protons (red line solid line), helium (yellow dashed line), the oxygen group (green dash-dotted line), and the iron group (blue dotted line). Bands around the model lines show a variation of one standard deviation. Data points show measurements which were energy-scale adjusted as described in [82]. Error bars represent combined statistical and systematic uncertainties. Data points of composition measurements from air-showers are not shown without error bars for clarity. In case of oxygen and iron, both the elemental flux and the group flux are shown; the smaller intensity without error band is the elemental intensity in each case. The intensity has been corrected for solar modulation as a function of kinetic energy of the nucleus using the force-field approximation [83] and modulation parameters from the CRDB [38, 84]. The distinction of kinetic energy and total energy makes no difference for high-energy cosmic rays, but the low energy results are easier to interpret when kinetic energy is used instead of total energy. Updated from Ref. [82]; courtesy of Hans Dembinski, Ralph Engel, Anatoli Fedynitch, Tom Gaisser, Felix Riehn, and Todor Stanev.

The Auger Collaboration reported a measurement of the average shower maximum as a function of energy using FD data [32]. The study is based on 42,466 events with $E > 10^{8.2}$ GeV, out of which 62 have been detected at $E > 10^{10.5}$ GeV. The $\langle X_{\max} \rangle$ evolves with energy at a rate of $D_{10} = 79$ g/cm² for $E < 10^{9.33 \pm 0.02}$ GeV, and $D_{10} = 26$ g/cm² for $E > 10^{9.33 \pm 0.02}$ GeV, in agreement with previous studies [50, 51]. Predictions of the energy evolution of $\langle X_{\max} \rangle$ from air shower simulations are around $D_{10} = 60$ g/cm², irrespective of the baryon number A of the primary and the model used to simulate hadronic interactions [52]. This implies that Auger high-quality, high-statistics data, when interpreted with existing hadronic event generators, exhibit a strong likelihood for a composition that becomes gradually lighter in the range $10^{8.2} \lesssim E/\text{GeV} \lesssim 10^{9.33}$, qualitatively consistent with a transition from a heavy Galactic composition, to a light extragalactic composition. For $E > 10^{9.33 \pm 0.02}$ GeV, the trend is reversed and the average baryon number increases with energy. Within uncertainties, the data from TA are consistent with these findings [53–56]. Studies aim to identify the primary particle species using Auger SD data yield results in agreement with FD observations [57, 58]. An interpretation of the full X_{\max} distribution in each energy bin is achieved by fitting a superposition of X_{\max} -templates obtained from simulations of p -, He-, N- and Fe-induced air showers to the data.

Combining TA [59] and Auger [87, 88] data with direct measurements from the HEAO satellite [60], HEN [61], PAMELA [62, 63], AMS-02 [64–66], CREAM-I, II and III [67–70], ACE-CRIS [71, 72], SpaceLab2 [73, 74], as well as air-shower measurements of high-energy CRs from H.E.S.S. [75], ARGO-YBJ [76], TUNKA [77], IceCube [79], and KASCADE-Grande (KG) [80, 81] a global spline fit (GSF) to the CR spectrum was implemented in [82]. The fitted GSF model is shown in Fig. 2; details are given in Appendix A. The global fit together with the adjusted energy-scales reveals detailed structure in the all-particle flux. The most salient features are: (i) a steepening of the spectrum, which is known in the cosmic vernacular as the “knee”, occurring at $E_{\text{knee}} \sim 10^{6.6}$ GeV; (ii) a less prominent “second knee”, corresponding to a further

softening, appears at $E_{2\text{knee}} \sim 10^{8.0}$ GeV; (iii) a pronounced hardening of the spectrum, generating the so-called ‘‘ankle’’ feature, becomes evident at $E_{\text{ankle}} \sim 10^{9.7}$ GeV. The results of the GSF are consistent with those obtained by the Auger Collaboration through a 5 parameter fit of the UHECR spectrum,

$$J(E) = \begin{cases} J_0 \left(\frac{E}{E_{\text{ankle}}} \right)^{-\gamma_1} & ; E \leq E_{\text{ankle}} \\ J_0 \left(\frac{E}{E_{\text{ankle}}} \right)^{-\gamma_2} \left[1 + \left(\frac{E_{\text{ankle}}}{E_{\text{supp}}} \right)^{\Delta\gamma} \right] \left[1 + \left(\frac{E}{E_{\text{supp}}} \right)^{\Delta\gamma} \right]^{-1} & ; E > E_{\text{ankle}} \end{cases}, \quad (11)$$

with $E_{\text{ankle}} = [5.08 \pm 0.06(\text{stat.}) \pm 0.8(\text{syst.})] \times 10^9$ GeV, $E_{\text{supp}} = [3.9 \pm 0.2(\text{stat.}) \pm 0.8(\text{syst.})] \times 10^{10}$ GeV, $\gamma_1 = 3.293 \pm 0.002(\text{stat.}) \pm 0.05(\text{syst.})$, $\gamma_2 = 2.53 \pm 0.02(\text{stat.}) \pm 0.1(\text{syst.})$, and $\Delta\gamma = 2.5 \pm 0.1(\text{stat}) \pm 0.4(\text{syst.})$ [32]. Note that E_{ankle} is about a factor 2.5 higher in energy than the observed break in D_{10} . The energy $E_{1/2}$ at which the integral spectrum drops by a factor of two below what would be the expected with no steepening is $E_{1/2} = [2.26 \pm 0.08(\text{stat.}) \pm 0.4(\text{syst.})] \times 10^{10}$ GeV. TA and Auger observations show remarkable agreement, except for a notable discrepancy at $E \gtrsim E_{\text{supp}}$. On January 2018, the TA Collaboration reported evidence for a declination dependence on the high energy end of the spectrum [85], suggesting that the shape of the spectrum for $E \gtrsim E_{\text{supp}}$ could carry an imprint of the source density distribution along the line of sight (which would be different in different directions of the sky) [86]. The GSF model, however, is built on the assumption that the CR intensity is isotropic and therefore pulled towards the Auger data points, which have much smaller uncertainties.

The variations of the spectral index γ in the energy spectrum reflect various aspects of cosmic ray production, source distribution, and propagation. The first and second knee seem to reflect the maximum energy of Galactic magnetic confinement, which grows linearly in the charge Ze of the nucleus. A comparison of E_{knee} and $E_{2\text{knee}}$ shows that the spectral structures are separated in energy by a factor of $(E_{2\text{knee}} - E_{\text{knee}})/E_{\text{knee}} \sim 25$. Then, if E_{knee} is interpreted as the energy at which protons escape the Galaxy (or ‘‘proton knee’’), the higher energy break $E_{2\text{knee}}$ occurs where we would expect the ‘‘iron knee’’ according to the idea of rigidity dependent cutoffs in the spectra of individual nuclei [89]. This would imply that the second knee indicates where the highest- Z CRs escape the Galaxy. It is worthwhile to stress again, that this picture is in qualitative agreement with Auger measurements of D_{10} , and it is also supported by measurements of the Telescope Array low-energy extension (TALE) [90].

There are three different models that can explain the ankle in terms of source characteristics and propagation effects. It has been advocated that the ankle feature could be well reproduced by a proton-dominated power-law spectrum, where the ankle is formed as a *dip* in the spectrum from the energy loss of protons via Bethe-Heitler pair production [91, 92]. However, the apparent dominance of heavy nuclei in the vicinity of 10^{10} GeV is in contradiction with this interpretation of the ankle. A second model explains the ankle as the superposition of an extragalactic population of UHECR nuclei with hard source spectra $\propto E^{-1.6}$ and maximum energy $E \sim Z \times 10^{9.7}$ GeV, and an *ad hoc* light ($p + \text{He}$) extragalactic component with steep emission spectra $\propto E^{-2.7}$ [93]. A more *natural* explanation of the entire spectrum and nuclear composition emerges while accounting for the ‘‘post-processing’’ of UHECRs through photodisintegration in the environment surrounding the source [94–96]. In this model relativistic nuclei accelerated by a central engine to extremely high energies remain trapped in the turbulent magnetic field of the source environment. Their escape time decreases faster than the interaction time with increasing energy, so that only the highest energy nuclei can escape the source unscathed. In effect, the source environment acts as a *high-pass filter* on the spectrum of

CRs. All nuclei below the energy filter interact, scattering off the far-infrared photons in the source environment. These photonuclear interactions produce a steep spectrum of secondary nucleons, which is overtaken by the harder spectrum of the surviving nucleus fragments above about $10^{9.6}$ GeV. These overlapping spectra could then carve an ankle-like feature into the source emission spectrum. The spectrum above the ankle exhibits a progressive transition to heavy nuclei, as the escape of non-interacting nuclei becomes efficient. Reproducing the data with such a model requires hard spectra $\propto E^{-1}$ at the sources. In fact, as shown by the Auger Collaboration, simultaneously reproducing just the component of the spectrum above the ankle together with the observed nuclear composition also requires hard spectra at the sources [97].

2.3. Anisotropy searches

There exists “lore” that convinces us that the highest energy CRs observed should exhibit trajectories which are *relatively* unperturbed by Galactic and intergalactic magnetic fields. Hence, it is natural to wonder whether anisotropy begins to emerge at these high energies. Furthermore, if the observed flux suppression is the GZK effect, there is necessarily some distance, $\mathcal{O}(100 \text{ Mpc})$, beyond which cosmic rays with energies near 10^{11} GeV will not be seen. Since the matter density within about 100 Mpc is not isotropic, this compounds the potential for anisotropy to emerge in the UHECR sample. On the one hand, if the distribution of arrival directions exhibits a large-scale anisotropy, this could indicate whether or not certain classes of sources are associated with large-scale structures (such as the Galactic plane, the Galactic halo, or the super-Galactic plane). On the other hand, if cosmic rays cluster within a small angular region or show directional alignment with powerful objects, one might be able to associate them with isolated sources in the sky.

The directional exposure $\omega(\hat{\mathbf{n}})$ provides the effective time-integrated collecting area for a flux from each direction of the sky $\hat{\mathbf{n}}(\alpha, \delta)$, characterized by the right ascension α and the declination δ . For an experiment at latitude λ , which is fully efficient for particles arriving with zenith angle $< \theta_{\text{max}}$ and that experiences stable operation, $\omega(\hat{\mathbf{n}})$ actually becomes independent of α when integrating the local-angle-detection efficiency over full periods of sidereal revolution of the Earth. Full efficiency means that the acceptance depends on θ only through the reduction in the perpendicular area given by $\cos \theta$. The ω dependence on δ relies on geometrical acceptance terms and is given by

$$\omega(\delta) = \frac{S \Delta t}{2\pi} (\cos \lambda \cos \delta \sin \zeta + \zeta \sin \lambda \sin \delta), \quad (12)$$

where S is the surface of the detector array, Δt is the time of data collection, and

$$\zeta = \begin{cases} 0 & ; \xi > 1, \\ \pi & ; \xi < -1, \\ \arccos \xi & ; \text{otherwise,} \end{cases} \quad (13)$$

with $\xi \equiv (\cos \theta_{\text{max}} - \sin \lambda \sin \delta) / (\cos \lambda \cos \delta)$ [98].

Before proceeding, we pause to note that there are differences as to how the primary energies are derived at Auger and TA, with systematic uncertainties in the energy scale of the experiments amounting to about 14% and 21% respectively, corresponding to about 70% uncertainty in the flux above a fixed energy threshold [99]. Therefore, when combining Auger and TA data to obtain full sky coverage it is necessary to cross-calibrate the energy scales of the two datasets to avoid introducing a spurious North/South asymmetry due to an energy scale mismatch. This is accomplished by exploiting the wide declination band

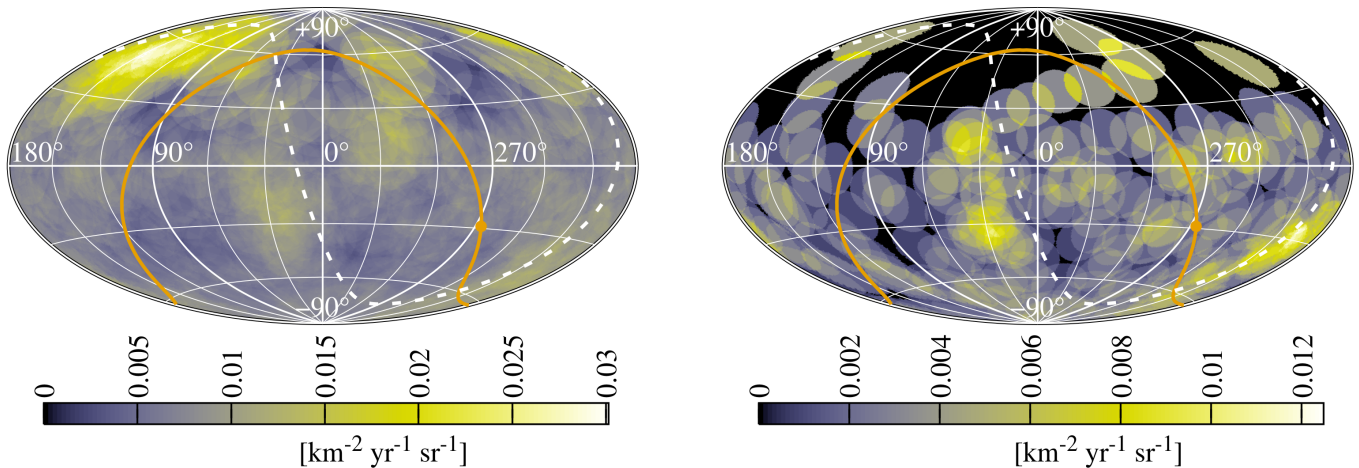


Figure 3: Estimated intensity of UHECRs above the indicated energy thresholds, averaged over circular moving windows, in equatorial coordinates. The galactic plane (orange solid), galactic center (orange dot) and super-galactic plane (white dashed) are also shown. From Ref. [99].

($-16^\circ \lesssim \delta \lesssim +45^\circ$) where the two datasets overlap. Regardless of the true arrival direction distribution, within a region of the sky $\Delta\Omega$ fully contained in the field of view (FoV) of both observatories, the sum over observed events $\sum_i 1/\omega(\hat{\mathbf{n}}_i)$ (with ω in km yr units) is an unbiased estimator of $\int_{\Delta\Omega} J(> E_{\text{th}}, \hat{\mathbf{n}}) d\hat{\mathbf{n}}$ and should be the same for both experiments except for statistical fluctuations. Here, $J(> E_{\text{th}}, \hat{\mathbf{n}})$ is the directional UHECR integrated intensity in $\text{km}^{-2} \text{yr}^{-1} \text{sr}^{-1}$ units. This yardstick is generally adopted to cross-calibrate the energy scales and to determine $E_{\text{th,Auger}}$ and $E_{\text{th,TA}}$ such that the Auger flux above $E_{\text{th,Auger}}$ matches the TA flux above $E_{\text{th,TA}}$ [99].³

The observed arrival direction distribution is obtained by convoluting the flux per steradian with the detector exposure, giving

$$\frac{dN}{d\Omega}(\hat{\mathbf{n}}) = J(> E_{\text{th}}, \hat{\mathbf{n}}) \omega(\hat{\mathbf{n}}). \quad (14)$$

The distribution of arrival directions can be exposed through the average directional (integral) intensity smoothed out at an angular scale Θ ,

$$\langle J(> E_{\text{th}}, \hat{\mathbf{n}}) \rangle_{\Theta} = \frac{1}{\int_{\Theta} d\hat{\mathbf{n}}} \int_{\Theta} d\hat{\mathbf{n}}' f(\hat{\mathbf{n}}, \hat{\mathbf{n}}') \frac{1}{\omega(\hat{\mathbf{n}}')} \frac{dN}{d\hat{\mathbf{n}}'}, \quad (15)$$

where $f(\hat{\mathbf{n}}, \hat{\mathbf{n}}')$ is the top-hat filter function of radius Θ and E_{th} the threshold energy. For an illustration of this technique, we consider 602 events collected by Auger from January 2004 to March 2014, with a total exposure of approximately $6.6 \times 10^4 \text{ km}^2 \text{sr yr}$, $\theta \leq 80^\circ$, and $E \geq 40 \text{ EeV}$, as well as 83 events collected by TA from May 2008 to May 2015 with a total exposure of about $8.7 \times 10^3 \text{ km}^2 \text{sr yr}$, $\theta \leq 55^\circ$, and $E \geq 57 \text{ EeV}$. The left panel of Fig. 3 shows the directional intensity of UHECRs recorded by TA and Auger, with energy above $E_{\text{th,TA}} = 57 \text{ EeV}$ and $E_{\text{th,Auger}} = 42 \text{ EeV}$ averaged out at $\Theta = 20^\circ$. The

³Actually, the region of the sky which is mostly used spans the declination band $-12^\circ \lesssim \delta \lesssim +42^\circ$. This is because including directions too close to the edge of the FoV of one of the observatories would result in larger statistical fluctuations due to very large values of $1/\omega(\hat{\mathbf{n}}_i)$ near the edge.

fiducial values for the energy threshold and the smoothing angle were extracted from searches of over-densities anywhere in the sky by the TA Collaboration [100]. Actually, the selected energy threshold of 57 EeV follows from a prior analysis by the Auger Collaboration [101], which had initially led to capture an anisotropy with 99% confidence level that was not confirmed by subsequent data [102]. A hot spot is visible in the direction $(\alpha, \delta) = (147^\circ, 43^\circ)$ [100], which is found to be the region with the largest intensity. The right panel of Fig. 3 displays the intensity sky map for higher energy thresholds $E_{\text{th,TA}} = 89$ EeV and $E_{\text{th,Auger}} = 54$ EeV averaged out at $\Theta = 12^\circ$. This energy threshold and smoothing angle correspond to the search for local over-densities in Auger data [102]. A clustering of events is visible in the direction $(\alpha, \delta) = (198^\circ, -25^\circ)$ [102], which is found to be the region with the largest intensity.

The existence of a signal in a region *on-source* is judged by the event count number N_{on} originating from that region. The counts in it are due to the potential source and the background. To estimate the statistical significance of a measured signal one can compare the number of events N_{on} that are detected in the *on-source* region to the number of background events $N_{\text{bg}} = \eta N_{\text{off}}$ that are expected in the *on-source* region. The number of *off-source* events, N_{off} , is estimated through numerical simulations of virtual events sampled randomly and uniformly in $(\alpha, \sin \delta)$, with $0 \leq \alpha \leq 2\pi$ and $-\pi/2 \leq \delta \leq \pi/2$. The normalization factor is given by $\eta = N/N_{\text{sim}}$, where N is the total number of observed events in the data-sample and N_{sim} is the number of virtual events. A widely accepted method for statistically inferring the existence of a source is the *hypothesis test* based on maximum likelihood principles. This test statistic (TS) requires the use of two hypotheses and a statistical description of each of them. The usual approach is to confront the null hypothesis (events coming only from background; no source present), with its negation (events coming from background and a source). This method provides the *statistical Li-Ma significance* for the rejection of the null (background only) hypothesis,

$$S_1^{\text{LM}} = \sqrt{2} \left\{ N_{\text{on}} \ln \left[\frac{(1 + \eta)N_{\text{on}}}{\eta(N_{\text{on}} + N_{\text{off}})} \right] + N_{\text{off}} \ln \left[\frac{(1 + \eta)N_{\text{off}}}{N_{\text{on}} + N_{\text{off}}} \right] \right\}^{1/2}, \quad (16)$$

which is valid only in the limit of large statistics [103]; see Appendix B for details.

The largest evidence for intermediate-scale ($\Theta = 20^\circ$) clustering above the statistical expectation was actually unmasked with $N_{\text{ob}} = 72$ events above $E_{\text{th,TA}} = 57$ EeV recorded between 2008 May 11 and 2013 May 4 [100]. The Li-Ma significance map of this data-sample is shown in the left panel of Fig. 4. The maximum excess, characterized by $N_{\text{on}} = 19$, $N_{\text{sim}} = 10^5$, $N_{\text{bg}} = 4.49$, is centered at $(\alpha, \delta) = (147^\circ, 43^\circ)$ and has a Li-Ma significance $S_{1,\text{max}}^{\text{LM}} = 5.1\sigma$. Note that this is not the hot-spot chance probability as the Li-Ma significance does not take into account random clustering, i.e. the probability of such a hotspot appearing by chance anywhere in an isotropic sky. To estimate the correction (a.k.a. penalty) factor, the TA Collaboration generated 10^6 Monte Carlo data sets each having 72 spatially random events within the experiment field of view (i.e., reproducing the statistics of the experimental data-sample), assuming a uniform distribution over the TA surface detector exposure. The maximum $S_{1,\text{max}}^{\text{LM}}$ significances were calculated for each Monte Carlo dataset following the same prescription adopted for the observed data. For 10^6 simulations, in 365 instances $S_{1,\text{max}}^{\text{LM}} > 5.1\sigma$, yielding a chance probability to observe the hotspot in an isotropic cosmic-ray sky of $p_{\text{TA}} \simeq 365/10^6 \simeq 3.7 \times 10^{-4}$, equivalent to a one-sided Gaussian significance of 3.4σ .

On 2017, the significance and shape of the hot-spot were updated using $N_{\text{ob}} = 143$ events above $E_{\text{th,TA}} = 57$ EeV collected through Spring 2017 [104]. Initially the excess search was performed following the original $\Theta = 20^\circ$ oversampling, but it was apparent from the sky map that the hot-spot became bigger in radius. The TA Collaboration then made a scan over Θ , limited to $15^\circ, 20^\circ, 25^\circ, 30^\circ$, and 35° , to

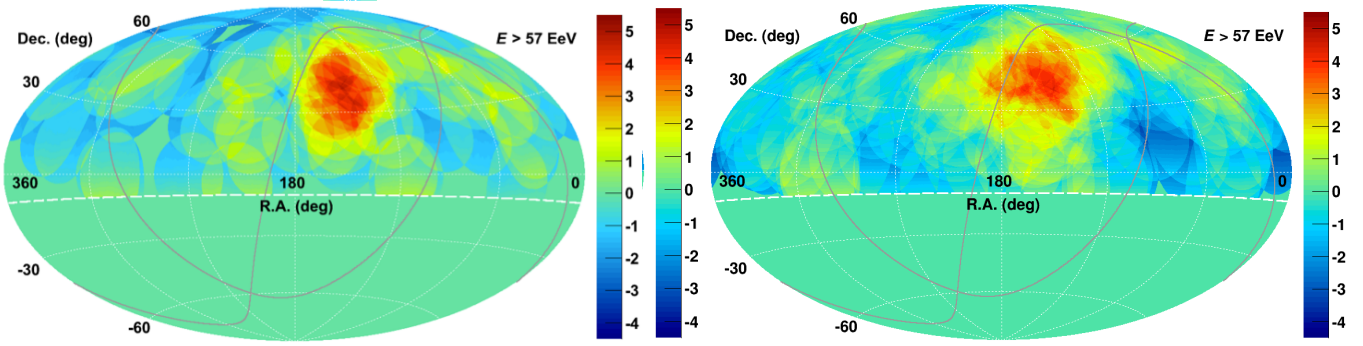


Figure 4: The Li-Ma significance skymap representing direction-dependent excesses and deficit with respect to the isotropic background in equatorial coordinates. The left panel corresponds to 5 yr of TA data with $E > 57$ EeV and with the original 20° oversampling (from Ref. [100]). The right panel corresponds to 9 yr of TA data with 25° oversampling (from Ref. [104]).

determine the best fit to the data. The maximum significance shows up at $\Theta = 25^\circ$, with $N_{\text{on}} = 34$ and $N_{\text{bg}} = 13.5$. The Li-Ma significance map of this new data-sample is shown in the right panel of Fig. 4. The hot-spot is now re-centered at $(\alpha, \delta) = (148^\circ, 45^\circ)$, about 1.5° away from the center position found in the original search. The local (pre-trial) Li-Ma significance is 5.1σ and the global (post-trial) significance is 3.0σ . A Kolmogorov-Smirnov test shows that the rate of arrival of events to the hot-spot is consistent with the fluctuations expected from a Poisson distribution with a mean of 2.8 events per year. However, the rate of event arrivals is also inconsistent with chance excess from an isotropic distribution, a Poisson average of 0.9 events per year, at about 2.6σ .

A new interesting development in this direction is that the TA Collaboration has also reported evidence of an energy dependent intermediate scale anisotropy appearing as a deficit of low energy ($10^{10.20} \leq E/\text{GeV} \leq 10^{10.75}$) events followed by an excess of high energy ($E \geq 10^{10.75}$ GeV) events in the same region of the sky, with a maximum local pre-trial significance of 6.2σ [105]. The anisotropy is contained inside a spherical bin of radius 28° centered at $(\alpha, \delta) = (139^\circ, 45^\circ)$, which is roughly 7° away from the center of the hot-spot. The post-trial probability of this coincidence appearing by chance anywhere on an isotropic sky is found to be 9×10^{-5} , equivalent to a 3.7σ global significance. This new feature is very suggestive of energy dependent magnetic deflection of UHECRs.

Spherical harmonic moments are well-suited for capturing anisotropies at any angular scale in the intensity of UHECRs [98]. However, an unambiguous measurement of the full set of spherical harmonic coefficients requires a full-sky coverage [106–109]. Because of the partial-sky coverage of ground-based experiments, extraction of the multipolar moments turns out to be nearly impossible without explicit assumptions on the shape of the underlying angular distribution. Under the circumstances, the search for anisotropies in the distribution of arrival directions is customarily performed through harmonic analyses in right ascension of the event counting rate, within the declination band defined by the field of view of the experiment [110]. Note that ground-based facilities which experience stable operation over a period of a year or more can have a relatively uniform exposure in α . The relevant declination-integrated directional intensity, which embraces genuine anisotropies $\delta J(\alpha)$, can be written as

$$J(> E_{\text{th}}, \alpha) = \frac{\mathcal{F}_0}{2\pi} [1 + \delta J(\alpha)], \quad (17)$$

where $\mathcal{F}_0/(2\pi)$ is the isotropic component. Of course, because of changes in the experimental conditions

small variations of the exposure in sidereal time would be expected. These variations translate into small variations of the directional exposure in right ascension $\delta\omega(\alpha)$, and therefore

$$\omega(\alpha) = \int d\delta \cos \delta \omega(\alpha, \delta) = \omega_0[1 + \delta\omega(\alpha)], \quad (18)$$

where ω_0 indicates the uniform exposure. The 1-dimensional distribution of arrival directions which is driven by the right ascension of events, $dN/d\alpha$, also embraces authentic anisotropies $\delta J(\alpha)$, but coupled to the directional exposure variations, i.e.,

$$\begin{aligned} \frac{dN}{d\alpha} &= \frac{\mathcal{F}_0 \omega_0}{2\pi} [1 + \delta\omega(\alpha)][1 + \delta J(\alpha)] \\ &= \frac{\mathcal{F}_0 \omega_0}{2\pi} [1 + \delta\omega(\alpha)] \left[1 + \sum_{m=1}^{\infty} a_m \cos(m\alpha) + \sum_{m=1}^{\infty} b_m \sin(m\alpha) \right], \end{aligned} \quad (19)$$

where $\delta J(\alpha)$ has been expanded in a Fourier series with coefficients a_m and b_m . Note that the Fourier coefficients defined by the harmonic decomposition in (19) give a direct measure of the anisotropy in right ascension relative to the monopole, isotropic flux. Using the basic orthogonality relation of trigonometric functions it follows that

$$a_m = \frac{1}{\pi a_0} \int \frac{d\alpha}{1 + \delta\omega(\alpha)} \frac{dN}{d\alpha} \cos(m\alpha), \quad (20a)$$

$$b_m = \frac{1}{\pi a_0} \int \frac{d\alpha}{1 + \delta\omega(\alpha)} \frac{dN}{d\alpha} \sin(m\alpha), \quad (20b)$$

with

$$a_0 = \frac{1}{2\pi} \int \frac{d\alpha}{1 + \delta\omega(\alpha)} \frac{dN}{d\alpha}. \quad (20c)$$

The event counting rate $dN/d\alpha$ is the intrinsic estimator of the distribution of arrival directions. The coefficients of the Fourier expansion can be estimated through a representation of the counting rate by a sum of Dirac functions over the circle, i.e., $dN/d\alpha = \delta(\alpha, \alpha_i)$. Namely, the estimators \hat{a}_m and \hat{b}_m can be calculated using discrete sums running over the N observed events:

$$\hat{a}_m = \frac{2}{\mathcal{N}_\alpha} \sum_{i=1}^N \frac{\cos(m\alpha_i)}{1 + \delta\omega(\alpha_i)} \quad \text{and} \quad \hat{b}_m = \frac{2}{\mathcal{N}_\alpha} \sum_{i=1}^N \frac{\sin(m\alpha_i)}{1 + \delta\omega(\alpha_i)}, \quad (21a)$$

where the coefficient a_0 has been estimated as $\hat{a}_0 = \mathcal{N}_\alpha/(2\pi)$, and

$$\mathcal{N}_\alpha = \sum_{i=1}^N \frac{1}{1 + \delta\omega(\alpha_i)} \quad (21b)$$

indicates the numbers of events that would have been detected should the directional exposure been completely uniform in α .

The results of the harmonic analysis are generally given using more intuitive geometrical parameters, such as the amplitude of the harmonic modulation

$$\hat{r}_m = \sqrt{\hat{a}_m^2 + \hat{b}_m^2}, \quad (22)$$

and the phase associated to the right ascension of the maximum flux

$$\hat{\varphi}_m = \arctan(\hat{b}_m/\hat{a}_m), \quad (23)$$

defined modulo $2\pi/m$. The probability that an amplitude equal to or larger than \hat{r}_m arises from an isotropic distribution can be safely approximated by the cumulative distribution function of the Rayleigh distribution

$$p(\geq \hat{r}_m) = \exp\left(-\frac{\mathcal{N}_\alpha \hat{r}_m^2}{4}\right); \quad (24)$$

see Appendix C for details. To give a specific example, a vector of length $\mathcal{N}_\alpha \hat{r}_m^2/4 \geq 15$ would be required to claim an observation whose probability of arising from random fluctuation was 3×10^{-7} , equivalent to a two-sided Gaussian significance 5σ .

Results of numerical simulations, which take into account all three spatial degrees of freedom and the cosmological time-evolution of the universe (assuming the spatial distribution of sources follows the local mass distribution) suggest that the arrival directions of UHECRs are expected to have a pronounced dipolar anisotropy and rather weak higher-order contributions [111]. With this in mind, it is reasonable to assume that the UHECR flux per steradian is of the form:

$$J(> E_{\text{th}}, \alpha, \delta) = \frac{\mathcal{F}_0}{4\pi} (1 + \mathbb{k} \hat{\mathbf{k}} \cdot \hat{\mathbf{n}}), \quad (25)$$

where $\hat{\mathbf{n}}$ and $\hat{\mathbf{k}}$ respectively denote the unit vector in the direction of an arrival direction and in the direction of the dipole. In other words, the (differential) intensity in the direction $\hat{\mathbf{n}}$ consists of an isotropic part, $J_0 = \mathcal{F}_0/(4\pi)$, modulated by a dipolar component in $\cos(\hat{\mathbf{k}}, \hat{\mathbf{n}})$, and higher order terms are negligible. Here, $\mathbb{k} \in [0, 1]$ is the amplitude of the dipole, relative to the monopole. This means one has to derive from the data three parameters: one amplitude, \mathbb{k} , and two angles, $\hat{\mathbf{k}}$.

The first harmonic amplitude of the UHECR right ascension distribution can be directly related to \mathbb{k} . Namely, setting $m = 1$, we can rewrite \hat{a}_1 , \hat{b}_1 and \mathcal{N}_α as:

$$\hat{a}_1 = \frac{2}{\mathcal{N}_\alpha} \int_{\delta_{\min}}^{\delta_{\max}} d\delta \int_0^{2\pi} d\alpha \cos \delta J(> E_{\text{th}}, \alpha, \delta) \omega(\delta) \cos \alpha, \quad (26a)$$

$$\hat{b}_1 = \frac{2}{\mathcal{N}_\alpha} \int_{\delta_{\min}}^{\delta_{\max}} d\delta \int_0^{2\pi} d\alpha \cos \delta J(> E_{\text{th}}, \alpha, \delta) \omega(\delta) \sin \alpha, \quad (26b)$$

$$\mathcal{N}_\alpha = \int_{\delta_{\min}}^{\delta_{\max}} d\delta \int_0^{2\pi} d\alpha \cos \delta J(> E_{\text{th}}, \alpha, \delta) \omega(\delta), \quad (26c)$$

because the effects of the small modulation in α are already accounted for in the Rayleigh analysis [112]. Next, we write the angular dependence in $J(> E_{\text{th}}, \alpha, \delta)$ as $\hat{\mathbf{k}} \cdot \hat{\mathbf{n}} = \cos \delta \cos \delta_{\mathbb{k}} \cos(\alpha - \alpha_{\mathbb{k}}) + \sin \delta \sin \delta_{\mathbb{k}}$, where $\alpha_{\mathbb{k}}$ and $\delta_{\mathbb{k}}$ are the right ascension and declination of the apparent origin of the dipole, respectively. Performing the α integration in (26) it follows that

$$\hat{r}_1 = \left| \frac{A\mathbb{k}_\perp}{1 + B\mathbb{k}_\parallel} \right| \quad (27a)$$

where

$$A = \frac{\int d\delta \omega(\delta) \cos^2 \delta}{\int d\delta \omega(\delta) \cos \delta}, \quad B = \frac{\int d\delta \omega(\delta) \cos \delta \sin \delta}{\int d\delta \omega(\delta) \cos \delta}, \quad (27b)$$

$\mathbb{k}_{\parallel} = \mathbb{k} \sin \delta_{\mathbb{k}}$ is the component of the dipole along the Earth rotation axis, and $\mathbb{k}_{\perp} = \mathbb{k} \cos \delta_{\mathbb{k}}$ is the component in the equatorial plane. The coefficients A and B can be estimated from the data as the mean values of the cosine and the sine of the event declinations: $\langle \sin \delta \rangle$ and $\langle \cos \delta \rangle$. For a dipole amplitude \mathbb{k} , the measured amplitude of the first harmonic in right ascension \hat{r}_1 thus depends on the region of the sky observed, which is essentially a function of the latitude of the observatory λ , and the range of zenith angles considered. In the case of a small $B\mathbb{k}_{\parallel}$ factor, the dipole component in the equatorial plane can be obtained to linear order and is given by $\mathbb{k}_{\perp} \simeq \hat{r}_1 / \langle \cos \delta \rangle$, whereas the phase corresponds to the right ascension of the dipole direction $\hat{\phi}_1 = \alpha_{\mathbb{k}}$ [113].

Note that the Rayleigh analysis in right ascension is sensitive only to \mathbb{k}_{\perp} . A dipole component in the direction of the rotation axis of Earth induces no modulation of the flux in right ascension, but does so in the azimuthal distribution of arrival directions. A non-vanishing value of \mathbb{k}_{\parallel} leads to a sinusoidal modulation in azimuth with a maximum toward the northern or the southern direction. Thus, to reconstruct both dipole components, it is plausible to combine the first-harmonic analysis in α with a similar one in the azimuthal angle ϕ (say, measured counterclockwise from the east). The relevant estimators \hat{c}_1 and \hat{d}_1 are given by an expression analogous to (21), but in terms of the azimuth of the arrival direction of the shower rather than in terms of the right ascension,

$$\hat{c}_1 = \frac{2}{\mathcal{N}_{\phi}} \sum_{i=1}^N \frac{\cos \phi_i}{1 + \delta\omega(\alpha_i^0, \phi_i)} \quad \text{and} \quad \hat{d}_1 = \frac{2}{\mathcal{N}_{\phi}} \sum_{i=1}^N \frac{\sin \phi_i}{1 + \delta\omega(\alpha_i^0, \phi_i)}, \quad (28)$$

where α_i^0 is the local sidereal time (for practical reasons chosen so that it is always equal to the right ascension of the zenith at the center of the experiment), and $\mathcal{N}_{\phi} = \sum_{i=1}^N [1 + \delta\omega(\alpha_i^0, \phi_i)]^{-1}$. Writing $\hat{\mathbf{k}} \cdot \hat{\mathbf{n}}$ as a function of the local coordinates (θ, ϕ, α^0) ,

$$\begin{aligned} \hat{\mathbf{k}} \cdot \hat{\mathbf{n}} &= \sin \delta_{\mathbb{k}} (\cos \theta \sin \lambda + \sin \theta \cos \lambda \sin \phi) + \cos \delta_{\mathbb{k}} \cos \alpha_{\mathbb{k}} (-\sin \theta \cos \phi \sin \alpha^0 + \cos \theta \\ &\times \cos \lambda \cos \alpha^0 - \sin \theta \sin \lambda \sin \phi \cos \alpha^0) + \cos \delta_{\mathbb{k}} \sin \alpha_{\mathbb{k}} (\sin \theta \cos \phi \cos \alpha_0 + \cos \theta \\ &\times \cos \lambda \sin \alpha^0 - \sin \theta \sin \lambda \sin \phi \sin \alpha^0), \end{aligned} \quad (29)$$

the angular dependence of the intensity in the first harmonic amplitudes in ϕ can be expressed as

$$\hat{c}_1 = \frac{2}{\mathcal{N}_{\phi}} \int_0^{2\pi} d\alpha^0 \int_0^{2\pi} d\phi \int_{\theta_{\min}}^{\theta_{\max}} d\theta \sin \theta \cos \phi J(> E_{\text{th}}, \theta, \phi, \alpha^0) = 0, \quad (30)$$

$$\hat{d}_1 = \frac{2}{\mathcal{N}_{\phi}} \int_0^{2\pi} d\alpha^0 \int_0^{2\pi} d\phi \int_{\theta_{\min}}^{\theta_{\max}} d\theta \sin \theta \sin \phi J(> E_{\text{th}}, \theta, \phi, \alpha_0) = \frac{\pi}{\mathcal{N}_{\phi}} \mathcal{F}_0 \mathbb{k}_{\parallel} \cos \lambda \overline{\sin \theta}, \quad (31)$$

$$\mathcal{N}_{\phi} = \int_0^{2\pi} d\alpha^0 \int_0^{2\pi} d\phi \int_{\theta_{\min}}^{\theta_{\max}} d\theta \sin \theta J(> E_{\text{th}}, \theta, \phi, \alpha_0) = \pi \mathcal{F}_0 (\bar{1} + \mathbb{k}_{\parallel} \sin \lambda \overline{\cos \theta}), \quad (32)$$

where $\overline{f(\theta)} \equiv \int_{\theta_{\min}}^{\theta_{\max}} d\theta f(\theta) \sin \theta$ [114]. The coefficient \hat{c}_1 vanishes as anticipated, while \hat{d}_1 is related to \mathbb{k}_{\parallel} by

$$\hat{d}_1 = \frac{\mathbb{k}_{\parallel} \cos \lambda \langle \sin \theta \rangle}{1 + \mathbb{k}_{\parallel} \sin \lambda \langle \cos \theta \rangle}, \quad (33)$$

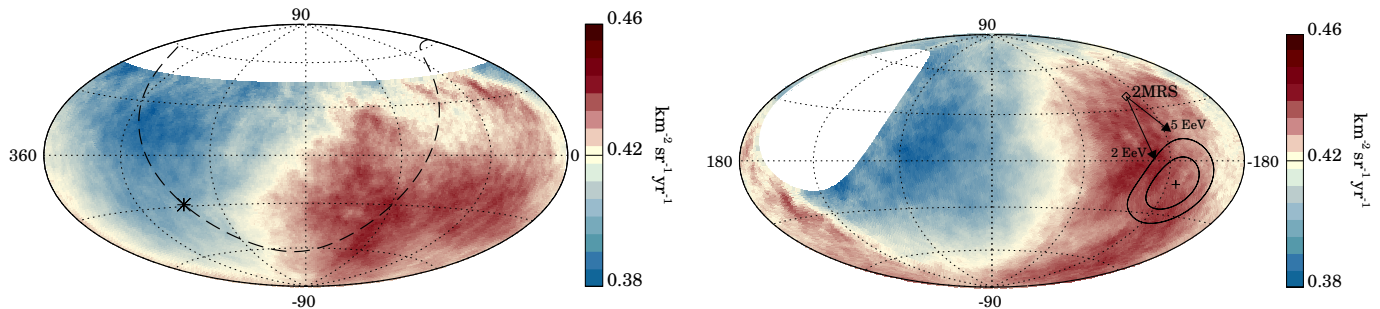


Figure 5: Sky map in equatorial coordinates using a Hammer projection (left) and Galactic coordinates (right) showing the CR intensity above 8 EeV smoothed with a 45° top-hat function. On the left panel, the Galactic center is marked with an asterisk and the Galactic plane is shown by a dashed line. On the right panel, the Galactic center is at the origin. The cross indicates the measured dipole direction; the contours denote the 68% and 95% confidence-level regions. The dipole in the 2MRS galaxy distribution is indicated. Arrows show the deflections expected for a particular model of the Galactic magnetic field [116–118] on particles with $E/Z = 5$ EeV and 2 EeV. From Ref. [115]

where $\overline{\sin \theta / \bar{1}}$ has been estimated as the mean value of $\sin \theta$ of the events themselves and likewise $\overline{\cos \theta / \bar{1}} \simeq \langle \cos \theta \rangle$. Note that for $\mathbb{k}_{\parallel} \sin \lambda \langle \cos \theta \rangle \ll 1$, the dipole component along the Earth’s rotation axis can be obtained to linear order as

$$\mathbb{k}_{\parallel} = \frac{\hat{d}_1}{\cos \lambda \langle \sin \theta \rangle}, \quad (34)$$

with $\tan \delta_{\mathbb{k}} = \mathbb{k}_{\parallel} / \mathbb{k}_{\perp}$. It is noteworthy that a pure dipole distribution is not possible, because the CR intensity cannot be negative in half of the sky. A *pure dipole deviation from isotropy* means a superposition of monopole and dipole, with the intensity everywhere ≥ 0 , as expressed by the Fourier expansion (19).

On November 2017, the Pierre Auger Collaboration reported a significant ($> 5\sigma$) large scale hemispherical asymmetry in the arrival directions of UHECR recorded between 1 January 2004 and 31 August 2016, from a total exposure of about $7.68 \times 10^4 \text{ km}^2 \text{ sr yr}$ [115]. The mean cosine of the declinations of the events in the sample is found to be $\langle \cos \delta \rangle = 0.78$, whereas the mean sine of the zenith angles of the events is $\langle \sin \theta \rangle = 0.65$. The Rayleigh analysis of the first harmonic in right ascension of 32,187 events with $E \geq 8$ EeV yields $\hat{r}_1 = 0.047_{-0.007}^{+0.008}$ and $\hat{\varphi}_1 = (100 \pm 10)^\circ$, with a random chance probability $p(\geq \hat{r}_1) = 2.6 \times 10^{-8}$. However, for the 81,701 events recorded with $4 < E/\text{EeV} < 8$, the amplitude of the first harmonic is significantly smaller: $\hat{r}_1 = 0.005_{-0.002}^{+0.006}$. In this energy bin $\hat{\varphi}_1 = (80 \pm 60)^\circ$ and the probability by chance is $p(\geq \hat{r}_1) = 0.6$. The data analysis in azimuthal angle leads to $\hat{d}_1 = -0.013 \pm 0.005$ in the $4 < E/\text{EeV} < 8$ energy bin and $\hat{d}_1 = -0.014 \pm 0.008$ in the $E \geq 8$ EeV bin. The probabilities that larger or equal absolute values for \hat{d}_1 arise from an isotropic distribution are 0.8% and 8%, respectively. The $E \geq 8$ EeV data are well-represented by a dipole with amplitude $\mathbb{k} = 0.065_{-0.009}^{+0.013}$ pointing in the direction $(\alpha_{\mathbb{k}}, \delta_{\mathbb{k}}) = (100_{-10}^{+10}, -24_{-13}^{+12})$. In a second study, the Auger Collaboration further scrutinized the highest-energy bin by splitting it into three energy ranges [119]. They found that the amplitude of the dipole increases with energy above 4 EeV. The growth can be fitted to a power law with index $= 0.79 \pm 0.19$. The Auger Collaboration also estimated the quadrupolar components of the anisotropy, which are shown to be not statistically significant. The dipolar pattern is clearly seen in the flux map in Fig. 5. In Galactic coordinates, the direction of this dipole is $(l_{\mathbb{k}}, b_{\mathbb{k}}) = (233^\circ, -13^\circ)$. This direction is about 125° from the Galactic center, suggesting that the UHECRs creating the anisotropy have an extragalactic origin.

Because of Liouville’s theorem, the distribution of cosmic rays must be anisotropic outside of the Galaxy

for an anisotropy to be observed at Earth [120, 121]. An anisotropy cannot arise through deflections of an originally isotropic flux by a magnetic field. This is because the intensity is constant along any possible CR trajectory. To get the picture, consider the time evolution of the phase space distribution within t and $t + dt$. The number of particles in an open ball around $(\mathbf{x}', \mathbf{p}')$ at $t' = t + dt$ is given by $dN = f(\mathbf{x}', \mathbf{p}') d^3x' d^3p'$. Now, $f(\mathbf{x}, \mathbf{p})$ would remain constant if the Jacobian of the $(\mathbf{x}, \mathbf{p}) \rightarrow (\mathbf{x}', \mathbf{p}')$ transformation satisfies

$$\mathcal{J} = \frac{\partial(\mathbf{x}', \mathbf{p}')}{\partial(\mathbf{x}, \mathbf{p})} = 1. \quad (35)$$

For (35) to stay staunch, it is sufficient to prove that the time-derivative $d\mathcal{J}/dt = 0$. In other words, the expansion of \mathcal{J} to first-order terms in dt must vanish. The evolution from t to $t + dt$ entails $\mathbf{x}' = \mathbf{x} + \mathbf{v} dt$ and $\mathbf{p}' = \mathbf{p} + \mathbf{F} dt$, and so

$$\text{diag } \mathcal{J} = \left(1, 1, 1, 1 + \frac{\partial F_x}{\partial p_x} dt, 1 + \frac{\partial F_y}{\partial p_y} dt, 1 + \frac{\partial F_z}{\partial p_z} dt \right), \quad (36)$$

whereas the off-diagonal elements are $\mathcal{O}(dt)$. All in all, the expansion of the Jacobian to first order in dt is given by

$$\mathcal{J} = 1 + \left(\frac{\partial F_x}{\partial p_x} + \frac{\partial F_y}{\partial p_y} + \frac{\partial F_z}{\partial p_z} \right) dt + \dots, \quad (37)$$

and therefore since the electromagnetic force satisfies $\nabla_p \cdot \mathbf{F} = 0$ the phase space distribution is constant along the CR trajectory [37]. In addition, the magnetic field does not change the magnitude of the cosmic ray momentum p , and so $p^2 f(\mathbf{x}, \mathbf{p})$ is preserved too. Now, it is straightforward to see from (9) that the intensity is constant along any possible CR trajectory.

A dipole anisotropy is expected due to the net motion of Earth with respect to the rest frame of UHECR sources, the so-called Compton-Getting effect [122]. Note that any observer moving relative to the coordinate system in which the distribution of UHECRs is isotropic will observe an anisotropic flux. Let $f(\mathbf{x}, \mathbf{p})$ be the distribution function of UHECRs in the frame S for which the intensity is isotropic, and $f(\mathbf{x}', \mathbf{p}')$ the one in S' associated to the observer frame S' moving with velocity \mathbf{u} with respect to S . The differentials d^3x and d^3p transform opposite under Lorentz transformations and the particle number dN is (of course) a scalar. Thus, Lorentz invariance implies $f(\mathbf{x}, \mathbf{p}) = f(\mathbf{x}', \mathbf{p}')$. The particle momentum in the frame S' is related to that in S by a Lorentz transformation

$$\mathbf{p}' = \gamma_u \left(\mathbf{p} - \frac{p}{v} \mathbf{u} \right), \quad (38)$$

where $v \sim 1$ is the UHECR velocity in S . For a non-relativistic motion of the observer, $\mathbf{u} \ll 1$ and so the anisotropy induced by the Compton-Getting effect is dominated by the lowest moment: its dipole moment. In addition, $\gamma_u \sim 1$, and so an expansion in the small parameter $\mathbf{p} - \mathbf{p}' = -p\mathbf{u}$, leads to

$$f'(\mathbf{p}') = f(\mathbf{p}') - p\mathbf{u} \cdot \frac{\partial f}{\partial \mathbf{p}} \Big|_{\mathbf{p}=\mathbf{p}'} + \mathcal{O}(u^2) = f(\mathbf{p}') \left(1 - \frac{\mathbf{u} \cdot \mathbf{p}}{p} \frac{\partial \ln f}{\partial \ln p} \right) \dots \quad (39)$$

From (9) it follows that $\ln J = 2 \ln p + \ln f$ and so

$$\frac{\partial \ln f}{\partial \ln p} = \frac{\partial \ln J}{\partial \ln p} - 2 = \frac{\partial \ln J}{\partial \ln E} \frac{\partial \ln E}{\partial \ln p} - 2. \quad (40)$$

Substituting (40) into (39) and multiplying by p^2 one arrives at

$$J'(E') \simeq J(E) \left[1 + \left(2 - \frac{\partial \ln J}{\partial \ln E} \right) \frac{\mathbf{u} \cdot \mathbf{p}}{p} \right]. \quad (41)$$

For particles with spectrum $J(E) \propto E^{-\gamma}$, the intensity observed in S' is given by

$$J'(E') \simeq J(E) [1 + (2 + \gamma) u \cos(\hat{\mathbf{u}}, \hat{\mathbf{p}})]. \quad (42)$$

Assuming that the sources of UHECRs are on average at rest with respect to the cosmological frame, the magnitude and direction of the velocity of the solar system \mathbf{u} can be inferred from the detection of the dipole anisotropy in the CMB. This gives $u = 369.0 \pm 0.9$ km/s in the direction $(l_{\text{CMB}}, b_{\text{CMB}}) = (264.00^\circ \pm 0.03^\circ, 48.24^\circ \pm 0.02^\circ)$ [123–125]. For $\gamma \simeq 2.53$, the predicted amplitude of the Compton-Getting effect, $\mathbb{k} = (2 + \gamma)u$, is only 0.56% [126]. This is about an order of magnitude smaller than the amplitude unmasked by the Pierre Auger Collaboration [115].

We have seen that at energies beyond a certain threshold, the GZK interactions between UHECRs and the universal photon backgrounds limits the distances that the particles would travel. For He, $d_{10}^{\text{GZK}} \sim 10^3$ Mpc, whereas for p and CNO $d_{10}^{\text{GZK}} \sim 10^{3.3}$ Mpc [127]. At lower energies the GZK distance increases, e.g., for p , $d_4^{\text{GZK}} \sim 10^{3.3}$ Mpc and for He and CNO is of the order of the Hubble distance. Note that if the intervening magnetic fields are negligible, then the UHECR horizon would be characterized by the GZK distance. Hence, since the GZK distance for CR energies at which the dipole has been observed is almost the Hubble distance, the UHECR dipole axis must be aligned with the CMB dipole (that follows the large-scale structure dipole matter distribution). Note, however, that both \mathbb{k} and $(l_{\mathbb{k}}, b_{\mathbb{k}})$ are not compatible with the CMB dipole [127].

The lifetime of a CR with velocity $v \sim 1$ is limited to $\tau_{E_{\text{EeV}}}^{\text{GZK}} \sim d_{E_{\text{EeV}}}^{\text{GZK}}/v$, where $E_{\text{EeV}} \equiv E/\text{EeV}$. The diffusion of this CR in the extragalactic magnetic field could limit its magnetic horizon to much less than $d_{E_{\text{EeV}}}^{\text{GZK}}$. For a diffusive propagation in a magnetic field \mathbf{B} , the horizon scale is the diffusion distance

$$d_{E_{\text{EeV}}}^{\mathbf{B}} \sim \sqrt{6 D \min \{ \tau_{E_{\text{EeV}}}^{\text{GZK}}, t_{\text{age}} \}}, \quad (43)$$

where D is the diffusion coefficient and t_{age} is the age of the source ($t_{\text{age}} \sim$ Hubble time if the source has always been active) [127]. The diffusion coefficient depends on the rigidity of the particles and on the strength and coherence length of the magnetic field. For a Kolmogorov turbulence, the diffusion coefficient can be approximated via a fitting function that accounts for both the resonant and non-resonant diffusion regimes

$$D \approx \left[0.03 \left(\frac{\lambda_{\text{Mpc}}^2 E_{\text{EeV}}}{Z B_{\text{nG}}} \right)^{1/3} + 0.5 \left(\frac{E_{\text{EeV}}}{Z B_{\text{nG}} \lambda_{\text{Mpc}}^{0.5}} \right)^2 \right] \text{Mpc}^2 \text{Myr}^{-1}, \quad (44)$$

where Ze is the CR charge, B_{nG} is the extragalactic magnetic field strength in nG and λ_{Mpc} its coherence length in Mpc [128].⁴ The diffusive approximation is valid for $6D < v d_{E_{\text{EeV}}}^{\text{GZK}}$, or equivalently when $d_{E_{\text{EeV}}}^{\mathbf{B}} <$

⁴Measurements of the Faraday rotation in the linearly polarized radio emission from distant quasars yield upper limits on the extragalactic magnetic field strength as a function of the reversal scale [129]. If electron densities follow that of the Lyman- α forest [130], the average magnitude of the magnetic field receives an upper limit of $B \sim 0.65$ nG for reversals on the scale of the horizon, and $B \sim 1.7$ nG for reversal scales on the order of 1 Mpc at the 2σ level [131].

$d_{E_{\text{EeV}}}^{\text{GZK}}$. If it takes more than the age of the Universe to enter the diffusion regime, then the propagation of UHECR becomes quasi-rectilinear. Altogether, the size of the region contributing to the observed CR intensity (and consequently to the observed anisotropy) is set by the CR horizon [132]

$$H_{E_{\text{EeV}}} = \min \left\{ \sqrt{6D\tau_{E_{\text{EeV}}}^{\text{GZK}}}, d_{E_{\text{EeV}}}^{\text{GZK}} \right\}. \quad (45)$$

For a homogeneous extragalactic magnetic field, characterized by $B_{\text{nG}} \approx 10$ and $\lambda_{\text{Mpc}} \approx 0.2$, the CR horizon shrinks dramatically; e.g. $H_{10} \sim 100$ Mpc for He and $H_{10} \sim 200$ Mpc for CNO and p [127].

Of particular interest here, the distribution of nearby – distance $\mathcal{O}(100 \text{ Mpc})$ – galaxies, as mapped by the 2 Micron All-Sky Redshift Survey (2MRS) [133], exhibits a dipolar structure in the direction $(l_{2\text{MRS}}, b_{2\text{MRS}}) = (251^\circ \pm 12^\circ, 37^\circ \pm 10^\circ)$ [134]. If the sources of UHECRs are a subset of these galaxies, then the arrival direction of CRs at Earth would follow the same structure. Numerical simulations indicate that a mixed-composition of CRs with $E \sim 10 \text{ EeV}$, propagating in a $B_{\text{nG}} \sim 1$ field, would create a dipole anisotropy with an amplitude of about 10% if the source distribution follows that of the 2MRS catalog up to about 100 Mpc [135].⁵ The dipole of the flux-weighted distribution of infrared-detected galaxies in the 2MRS catalogue is shown as an open diamond in Fig. 5. The direction of the 2MRS dipole is 55° away from the central direction of the dipole discovered by the Auger Collaboration. To illustrate how the Galactic magnetic field could influence the observed direction of the 2MRS dipole, the deflected positions of this dipole as predicted by the Jansson-Farrar (JF) model of the Galactic magnetic field [116–118] are indicated by arrows in Fig. 5, for two different CR rigidities that are compatible with the composition fractions shown in Fig. 2. The agreement between the directions of the UHECR and 2MRS dipoles is improved by adopting these assumptions about the nuclear composition and the deflections in the Galactic magnetic field. Note that if the UHECR sources are within 100 Mpc and the UHECR dipole is He-dominated, this would imply an extragalactic magnetic field strength of $\mathcal{O}(10 \text{ nG})$ [127].

One way to increase the chance of success in finding out the sources of UHECRs is to check for correlations between CR arrival directions and known candidate astrophysical objects. This is because even if the distribution of UHECRs is quasi-isotropic, the arrival directions could get stacked around some pre-defined directions. To calculate a meaningful statistical significance in such an analysis, it is important to define the search procedure *a priori* in order to ensure it is not inadvertently devised especially to suit the particular data set after having studied it. With the aim of avoiding accidental bias on the number of trials performed in selecting the cuts, the anisotropy analysis scheme must follow a pre-defined process. First an exploratory data sample should be employed for comparison with various source catalogs and for tests of various cut choices. The results of this exploratory period should then be used to design prescriptions to be applied to subsequently gathered data. The Auger Collaboration began the anisotropy searches with a prescription protocol [136]. However, collecting the rare ultra-high energy events is very expensive in terms of time. Given that the nominal lifetime of the experiment extends to 2025, the formality of a prescription at this stage becomes unpractical.

Following the latest report of the Auger Collaboration [3], the ensuing discussion is focussed on the search for intermediate-scale anisotropies in UHECR arrival directions associated with two prominent groups of extragalactic sources detected by the Large Area Telescope on board the Fermi Gamma Ray Space Telescope spacecraft (*Fermi-LAT*): (*i*) active galactic nuclei (AGNs) that emit γ -rays, so-called “ γ AGNs” and

⁵Note, however, that for $B_{\text{nG}} \sim 1$, the horizon is larger than the extend of the 2MRS catalog. Sources at larger distances would somewhat lower the anisotropy.

(ii) starburst galaxies (SBGs). The γ AGN source population is constructed using the 2FHL catalog, which includes 360 sources detected by *Fermi*-LAT above 50 GeV [137]. A selection of radio-loud objects within a 250 Mpc radius reduces the sample to 17 blazars and radio galaxies. Their $0.05 \leq E/\text{TeV} \leq 2$ integral flux \mathcal{F}_γ is used as a proxy for the UHECR flux. Given the distance of these objects, the γ -ray absorption by the infrared background light can be safely neglected; see Sec. 3.6. The detections of seven SBGs have been reported using *Fermi*-LAT data: NGC 253, M82, NGC 4945, NGC 1068 [138], NGC 2146 [139], Arp 220 [140], and Circinus [141]. Their gamma-ray luminosity has been shown to scale almost linearly with their continuum radio flux \mathcal{F}_γ [138], and therefore the continuum emission of SBGs at 1.4 GHz (for which a larger census exists) is adopted as a proxy for the UHECR flux.⁶ Among the 63 objects within 250 Mpc searched for gamma-ray emission in [138], 23 SBGs with a flux larger than 0.3 Jy are selected to define the working sample.

The UHECR sky is modelled as the sum of an isotropic component plus the anisotropic contribution (with signal fraction f_{sig}) from the sources. For the anisotropic component, each source is modeled as a Fisher-Von Mises distribution $\mathfrak{F}(\hat{\mathbf{n}}, \hat{\mathbf{s}}_i; \Theta)$ centered on the coordinates of the source location $\hat{\mathbf{s}}_i$, with the angular width (or search radius Θ) being a free parameter common to all sources.⁷ Smoothed density maps are constructed from a superposition of catalog sources, weighted by the electromagnetic flux of the source \mathcal{F}_γ . The smoothed density maps are described by a function $F(\hat{\mathbf{n}})$, such that its value in a given direction $\hat{\mathbf{n}}$ is proportional to the probability of detecting a CR in that direction, according to the model. Collectively, the probability density map function is given by

$$F(\hat{\mathbf{n}}; f_{\text{sig}}, \Theta) = \frac{\omega(\hat{\mathbf{n}})}{\mathcal{C}} \left[(1 - f_{\text{sig}}) + f_{\text{sig}} \sum_{i=1}^{N_{\text{cat}}} \mathcal{F}_{\gamma,i} w(z_i) \mathfrak{F}(\hat{\mathbf{n}}, \hat{\mathbf{s}}_i; \Theta) \right], \quad (46)$$

where \mathcal{C} is an overall normalization constant that guarantees $\int F d\hat{\mathbf{n}} = 1$, $w(z_i)$ is the weight attributed to the i th source located at z_i to account for the attenuation factor because of GZK interactions, and the sum extends over all sources in the catalog N_{cat} [145]. Then, the model map depends on two free parameters aimed at maximizing the degree of correlation with UHECR events: the fraction of all events due to the sources (anisotropic fraction) and the root-mean-square angular separation between an event and its source (search radius) in the anisotropic fraction. The search signal fraction f_{sig} controls to what extent a contribution from the considered astrophysical sources is preferred to over a purely isotropic distribution. The search radius Θ provides an effective description of CR deflections in the intervening magnetic fields. The fraction $(1 - f_{\text{sig}})$ parametrizes the isotropic component. Note that this isotropic contribution could originate in faint unresolved objects absent from the considered catalog, or else account for highly deflected nuclei in the Galactic \mathbf{B} -field. The GZK-weights are evaluated as the fraction of the events produced above a given energy threshold, which are able to reach the Earth from a source at a redshift z with an energy still above that same threshold [146]. The weights depend on both the shape of the emission spectra and the nuclear

⁶TeV γ -ray emission has been observed from M82 [142] and NGC 253 [143].

⁷The Fisher-Von Mises distribution, $\mathfrak{F}(\hat{\mathbf{n}}, \hat{\mathbf{s}}; \kappa) = \kappa \exp(\kappa \hat{\mathbf{n}} \cdot \hat{\mathbf{s}}) / (4\pi \sinh \kappa)$, is the equivalent of a Gaussian on the sphere \mathbb{S}^2 , where $\hat{\mathbf{s}} \in \mathbb{S}^2$ is the mean direction, $\kappa \geq 0$ is the concentration parameter, $\hat{\mathbf{n}} \in \mathbb{S}^2$ is a random unit vector on the sphere, and the remaining terms serve to normalize the distribution [144]. The parameter κ controls the concentration of data points $\hat{\mathbf{n}}_j$ around the mean direction $\hat{\mathbf{s}}$, with $j = 1, \dots, N$. In particular, for $\kappa = 0$, $\mathfrak{F}(\hat{\mathbf{n}}, \hat{\mathbf{s}}; \kappa)$ reduces to the uniform density on \mathbb{S}^2 , whereas as $\kappa \rightarrow \infty$, $\mathfrak{F}(\hat{\mathbf{n}}, \hat{\mathbf{s}}; \kappa)$ tends to a point density. The parameters $\hat{\mathbf{s}}$ and κ^{-1} are analogous to the mean and variance in the Gaussian distribution. Thus, the search radius is defined as the inverse square root of Fisher's concentration parameter, *viz.* $\kappa = \Theta^{-2}$.

composition at the sources. They are determined through a fit that simultaneously reproduces Auger data on the spectrum and composition [97].

The most probable values of the free parameters (f_{sig} and Θ) are estimated using a maximum-likelihood ratio test, which also quantifies the strength of each model by contrast with isotropy. The likelihood is defined as the product over the UHECR events of the model density in every UHECR direction

$$\mathcal{L}(f_{\text{sig}}, \Theta; \hat{\mathbf{n}}_j) = \prod_{j=1}^N F(\hat{\mathbf{n}}_j; f_{\text{sig}}, \Theta), \quad (47)$$

where $\hat{\mathbf{n}}_j$ is the direction of the j th event and N the number of events in the UHECR data sample [145]. As aforesated, the TS for deviation from isotropy is the likelihood ratio test, $-2 \ln \lambda_0$, between two nested hypotheses: the UHECR sky model and an isotropic model (null hypothesis); see Appendix B for details. Note that the condition $f_{\text{sig}} = 0$ yields the density map of isotropy, and consequently defines the null hypothesis. The TS is maximized as a function of two parameters: the search radius and the anisotropic fraction. The analysis is repeated for a sequence of energy thresholds varying in the range $10^{10.3} \lesssim E_{\text{th}}/\text{GeV} \lesssim 10^{10.9}$.

For SBGs, the maximum TS $\equiv -2 \ln \lambda_0 = 24.9$ is obtained with 894 events of $E > 39$ EeV. This corresponds to a local p -value of 3×10^{-6} , see Fig. B.26. The smearing angle and the anisotropic fraction corresponding to the best-fit parameters are $13_{-3}^{+4^\circ}$ and $(10 \pm 4)\%$, respectively. Remarkably, the energy threshold of largest statistical significance coincides with the observed suppression in the spectrum [32], implying that when we properly account for the barriers to UHECR propagation in the form of energy loss mechanisms [8, 9] we obtain a self consistent picture for the observed UHECR horizon. The scan in energy thresholds comes out with a penalty factor, which was estimated through Monte-Carlo simulations. The post-trial chance probability in an isotropic cosmic ray sky is 4.2×10^{-5} , corresponding to a 1-sided Gaussian significance of 4σ [3]. For γ AGNs, the maximum TS $\equiv -2 \ln \lambda_0 = 15.2$ is obtained with 177 events of $E > 60$ EeV. The maximum deviation for γ AGNs is found at an intermediate angular scale of $\Theta = 7_{-2}^{+4^\circ}$ with an anisotropic fraction $f_{\text{sig}} = (7 \pm 4)\%$. Penalizing for the energy scan, the maximum TS obtained for γ AGNs corresponds to a 2.7σ deviation from isotropy.

Because of possible incompleteness of the source-list in [138] near the Galactic plane ($|b| < 10^\circ$) and in the southern sky ($\delta < 35^\circ$), relevant SBGs could be missing from the selected sample. However, the Auger Collaboration verified that the conclusions remain unchanged if: (i) one uses all 63 objects listed in [138]; (ii) one uses the catalog given in [147] with 32 SBGs above 0.3 Jy, (iii) one adds the Circinus SBG absent from (i) and (ii); (iv) one uses only the six SBGs (NGC 253, M82, NGC 4945, NGC 1068, Circinus, NGC 2146) reported in the third *Fermi*-LAT source catalog (3FGL) [148], and their 1 to 100 GeV integral flux as a UHECR proxy.

Starburst galaxies provide the most significant indication that UHECRs are not distributed isotropically on an intermediate angular scale, with an a posteriori chance probability $p_{\text{Auger}} \simeq 4.2 \times 10^{-5}$. As shown in Fig. 6 the Auger signal is dominated by three nearby starbursts NGC 4945, M83, and NGC 253. In the bottom panel of Fig. 6 it can be seen that M82 is expected to be one of the dominant starbursts in the full-sky. Its declination of $\delta \approx 70^\circ$ N is outside the exposure of the Auger Observatory, but is covered in the northern hemisphere by the TA. Thought-provoking, the starburst galaxy M82 is close to the best-fit source position of the TA hot spot [149–153]. The multiplicative p -value for the two non-correlated observations is

$$p = p_{\text{TA}} \otimes p_{\text{Auger}} = 1.5 \times 10^{-8}, \quad (48)$$

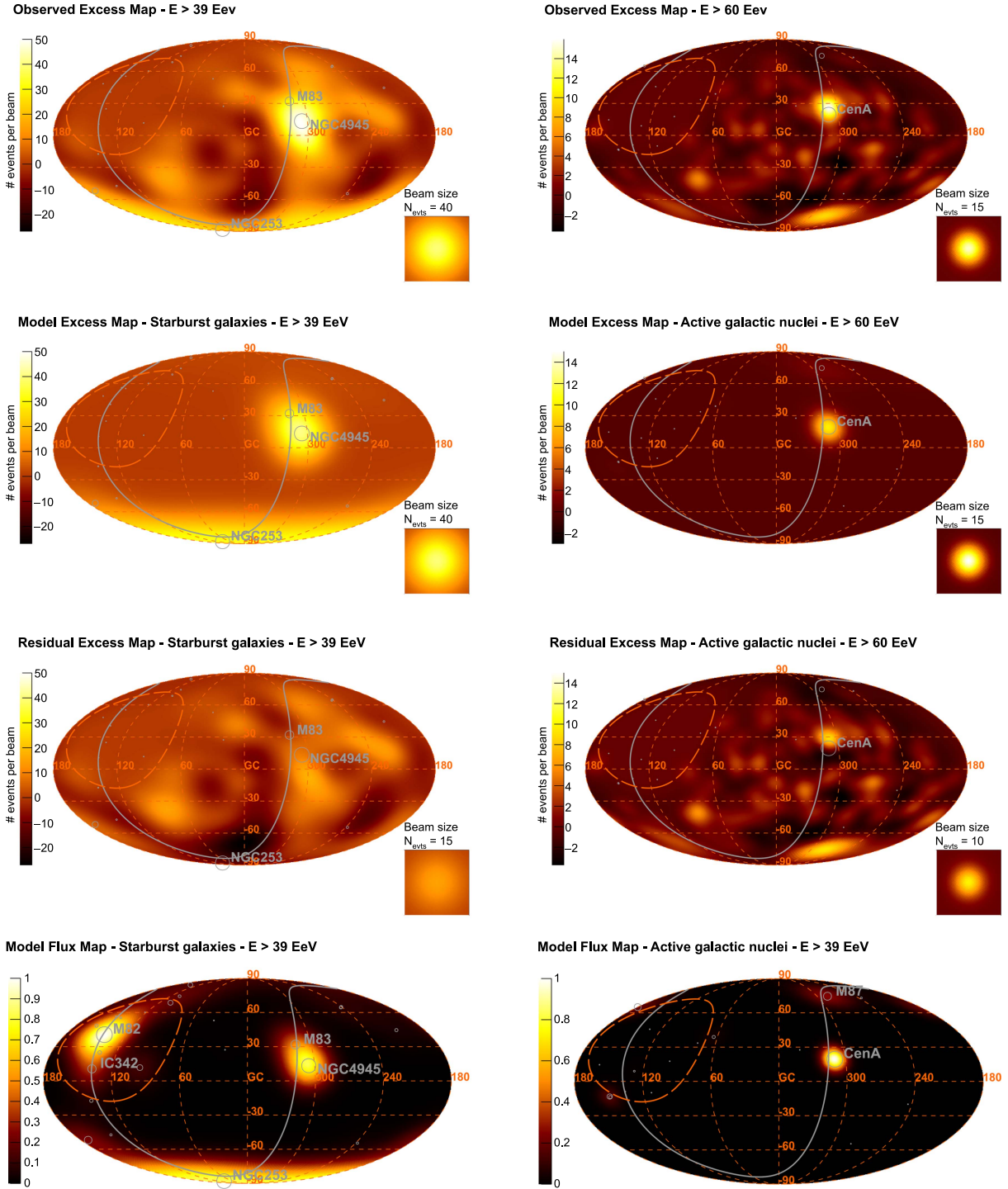


Figure 6: From top to bottom: (i) observed excess map, (ii) model excess map, (iii) residual map, and (iv) model flux map, for the best-fit parameters obtained with starburst galaxies above 39 EeV (left) and γ AGNs above 60 EeV (right). The excess maps (best-fit isotropic component subtracted) and residual maps (observed minus model) are smeared at the best-fit angular scale. The color scale indicates the number of events per smearing beam (see inset). The model flux map corresponds to a uniform full-sky exposure. The supergalactic plane is shown as a solid gray line. An orange dashed line delimits the field of view of the array. From Ref. [3]

yielding a statistical significance $\gtrsim 5\sigma$ [154]. However, caution must be exercised in all-sky comparisons [155]. Moreover, (48) combines a catalog-based cross-correlated search (Auger) with a blind search (TA). Therefore, (48) provides a rough estimate of the statistical significance under the strong assumption that M82 (which is at the border of the excess of TA events) is the only source contributing to the TA hot-spot. It is clear that new data are needed to confirm the suggested correlation.⁸

For γ AGNs, a compelling concentration of events is observed in the region around the direction of the nearest active galaxy, Centaurus A (Cen A). A separate analysis [32] shows that the maximum departure from isotropy occurs for a ring of 15° around the object, in which 19 (out of a total of 203) events with $E \geq 58$ EeV are observed compared to an expectation of 6.0 from isotropy. The significance of this excess can be obtained by penalizing for the scan in energy and angular scale. Performing such a process one obtains a statistical significance of $\sim 3.1\sigma$ [32]. There are no events coming from less than 15° around M87, which is almost 5 times more distant than Cen A and lies at the core of the Virgo cluster. The Auger exposure is 3 times smaller for M87 than for Cen A [157]. Using these two rough numbers and assuming equal luminosity, one expects 75 times fewer events from M87 than from Cen A. Hence, the lack of events in this region is not completely unexpected.

The Centaurus cluster lies 45 Mpc behind Cen A. An interesting question then is whether some of the events in the 15° circle could come from the Centaurus cluster rather than from Cen A. This does not appear likely because the Centaurus cluster is farther away than the Virgo cluster and for comparable CR luminosities one would expect a small fraction of events coming from Virgo [158].

It has been proposed that Fornax A could be the source of the apparent excess above 60 EeV right to the Galactic South pole in Fig. 6 [159]. However, if the Galactic magnetic field is approximated well by the JF model [116–118], then Fornax A is unlikely to be the source of the excess because the magnetic field would deflect UHECRs into a different location near the Galactic equator [160, 161].

The latest search for hot spot anisotropies is a joint effort by the two collaborations considering 840 events recorded by Auger with $E > E_{\text{th,Auger}} = 40$ EeV and 130 events recorded by TA with $E > E_{\text{th,TA}} = 53.2$ EeV [162]. The most significant excesses observed in a 20° search are at Galactic longitude and latitude: $(l, b) \approx (303.0^\circ, 12.9^\circ)$ and $(l, b) \approx (162.5^\circ, 44.4^\circ)$, with local Li-Ma statistical significance for the rejection of the null (background only) hypothesis of 4.7σ and 4.2σ , respectively. The Li-Ma significance map of this data-sample is shown in Fig. 7.

In addition, the TA Collaboration carried out an independent test of the reported correlation between the arrival directions of UHECRs and SBGs. The data sample used for this analysis includes CRs with $E > E'_{\text{th,TA}} = 43$ EeV detected by TA in a nine year period from May 2008 to May 2017. These data are compatible with isotropy to within 1.1σ and with Auger result to within 1.4σ , and so the TA Collaboration concluded that with their current statistics they cannot make a statistically significant corroboration or refutation of the reported possible correlation between UHECRs and SBGs [163]. It is important to stress, however, that $E'_{\text{th,TA}} < E_{\text{th,TA}}$. Most importantly, $E_{\text{th,TA}}$ is above the energy at which TA observes the suppression in the spectrum [164], but $E'_{\text{th,TA}}$ is below. This implies that the data sample of the test carried out by the TA Collaboration is most likely contaminated from the isotropic background of UHECRs emitted by far away sources, and consequently this would tend to reduce the significance of any possible correlation with nearby sources.

⁸First generation of UHECR observatories also pointed to a starburst origin for the highest energy events [156].

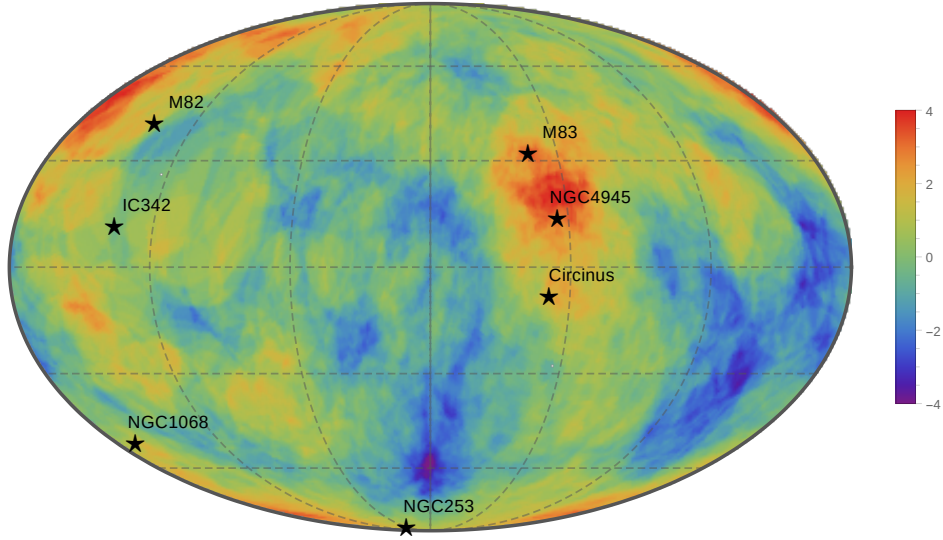


Figure 7: Skymap in Galactic coordinates of the Li-Ma significances of over-densities in 20° radius windows for 840 events recorded by Auger with $E > E_{\text{th,Auger}}$ and 130 events recorded by TA with $E > E_{\text{th,TA}}$. The color scale indicates the significance in units of standard deviations; negative values follow the convention of indicating the (positive) significance of deficits. Nearby SBGs providing a significant contribution to the UHECR correlation signal of Auger [3] and TA [163] are indicated by stars. From Ref. [161].

We end with two observations:

- It is important to keep in mind that if a source produces an anisotropy signal at energy E with cosmic ray nuclei of charge Ze , it should also produce a similar anisotropy pattern at energies E/Z via the proton component that is emitted along with the nuclei, given that the trajectory of cosmic rays within a magnetic field is only rigidity-dependent [165]. Moreover, secondary protons produced during propagation could also create an anisotropy pattern in the “low” energy regime [166]. This sets a constraint on the maximum distance to nucleus-emitting-sources. Making the extreme assumption that these sources do not emit any protons, the hypothetical source(s) responsible for anisotropies should lie closer than ~ 20 to 30, 80 to 100, and 180 to 200 Mpc, if the anisotropy signal is mainly composed of oxygen, silicon and iron nuclei, respectively [166]. This sets an interesting constraint on source models of UHECR nuclei and provides a distinctive signal to be tested by future data.
- It is also important to keep in mind that the anisotropies searches discussed above are all *a posteriori* studies, so *one cannot use them to determine a completely unbiased confidence level for anisotropy as the number of trials is unknown*.

In summary, the inaugural years of data taking at TA and the Pierre Auger Observatory have yielded a large, high-quality data sample. The enormous area covered by the Auger surface array together with an excellent fluorescence system and hybrid detection techniques have provided us with large statistics, good energy resolution, and solid control of systematic uncertainties. Presently, Auger is collecting some $7,000 \text{ km}^2 \text{ sr yr}$ of exposure each year, and is expected to run until 2025. New detector systems are being deployed, which will lower the energy detection threshold down to 10^8 GeV [167]. In particular, the addition of planar plastic scintillator of 4 m^2 area to each Cherenkov detector will provide baryonic-

sensitive observables for each shower enabling charge-discriminated studies with a duty cycle of nearly 100%. An experimental radio detection program is also co-located with the observatory and shows promising results [168, 169]. In addition, new surface and fluorescence detectors are planned to be constructed for the TA \times 4 experiment to cover 4 times larger area than TA to observe cosmic rays, especially with the highest energies using high statistics [170]. As always, the development of new analysis techniques is ongoing, and interesting new results can be expected.

3. Quest for the origin(s) of UHECRs

3.1. Acceleration processes

3.1.1. Phenomenological considerations

It is most likely that the bulk of the cosmic radiation is a result of some very general magneto-hydrodynamic (MHD) phenomenon in space which transfers kinetic or magnetic energy into CR energy. The details of the acceleration process and the maximum attainable energy depend on the particular physical situation under consideration. There are basically two types of processes that one might invoke. The first type assumes the particles are accelerated directly to very high energy by an extended electric field [171]. This idea can be traced back to the early '30s when Swann [172] pointed out that betatron acceleration may take place in the increasing magnetic field of a sunspot. These so-called ‘‘one-shot’’ mechanisms have been worked out in greatest detail, and the electric field in question is now generally associated with the rapid rotation of small, highly magnetized objects such as white dwarfs [173, 174], neutron stars (pulsars) [175–179], or black holes [180–182]. Electric field acceleration has the advantage of being fast, but suffers from the circumstance that the acceleration occurs in astrophysical sites of very high energy density, where many opportunities for energy loss exist. The second type assumes particles gain energy gradually through multiple stochastic encounters with moving magnetized plasmas. This idea was pioneered by Fermi [183, 184]. A variety of astrophysical environments have been suggested as sites of stochastic acceleration, including the interplanetary medium [185, 186], supernova remnants (SNRs) [187–192], the Galactic disk and halo [193–196], AGNs [197–199], large-scale jets and lobes of giant radio-galaxies (RG) [200–202], blazars [203–206], gamma-ray bursts (GRBs) [207, 208], starburst superwinds [4, 209], Galactic microquasar systems [210, 211], and clusters of galaxies [212–214]. Stochastic acceleration has the disadvantage of being slow, and it is also hard to keep the relativistic particles confined within the Fermi engine.

The length scale characterizing the propagation of an UHECR of energy E and charge Ze in a magnetic field B is the Larmor radius

$$r_L = \frac{1}{\sqrt{4\pi\alpha}} \frac{E}{ZB} = 1.1 \frac{1}{Z} \left(\frac{E}{10^9 \text{ GeV}} \right) \left(\frac{B}{\mu\text{G}} \right)^{-1} \text{ kpc}; \quad (49)$$

a greater Larmor radius implies a less curved trajectory. If the CR energy originates via an acceleration process, a general estimate of the maximal energy can be obtained by requiring the Larmor radius of the UHECR to be no larger than the linear size R of the accelerator. This constraint provides a qualitative criterion to identify potential sources of UHECRs by simply looking at the largest values of the product BR ; namely,

$$E \lesssim Z \left(\frac{R}{\text{kpc}} \right) \left(\frac{B}{\mu\text{G}} \right) \times 10^9 \text{ GeV}. \quad (50)$$

The limitation in energy is conveniently visualized in the “Hillas plot” [171] shown in Fig. 8, where the characteristic magnetic field B of candidate cosmic accelerators is plotted against their characteristic size R . It is striking that the potential accelerators range from neutron stars (for which $R \sim 10$ km), up to clusters of galaxies (for which $R \sim 1$ Mpc). Exceptions to the limit (50) may occur for astrophysical systems containing jets which move relativistically in the host-galaxy frame. Such relativistic jets are ubiquitous in astrophysical systems that contain compact objects, such as blazars, GRBs, and microquasars. The Hillas criterion is a necessary condition, but not sufficient. An important caveat is that (50) neglects the finite lifetime of the acceleration region and energy loss due to interactions with the environment, such as synchrotron radiation in the magnetic field and the production of secondary particles. For example, Gpc scale shocks from structure formation with \mathcal{O} (nG) magnetic fields would satisfy the Hillas criterion, but the acceleration at such shocks could be much too slow and consequently subject to large energy loss; see in Fig. 8 intergalactic medium.

Along these lines, in this section we will scrutinize some general constraints on UHECR accelerators. The essence of these constraints are briefly summarized in the following points [216]:

- geometry – the accelerated particle should need be kept inside the source while being accelerated;
- power – the source should possess the required amount of energy to give it to accelerated particles;
- radiation losses – the energy lost by a particle for radiation in the accelerating field should not exceed the energy gain;
- interaction losses – the energy lost by a particle in interactions with other particles should not exceed the energy gain;
- emissivity – the total number (density) and power of sources should be able to provide the observed UHECR flux;
- accompanying radiation of photons, neutrinos, and low-energy cosmic rays should not exceed the observed fluxes, both for a given source and for the diffuse background.

3.1.2. Unipolar induction

A neutron star is a compact object of radius $R_* \sim 10$ km, which evolved from the gravitational collapse of an ordinary massive star of radius $R_* \sim 10^6$ km, with a magnetic field $B_* \sim 1$ G, and a rotation period $P_* \sim 10 - 100$ yr, or else from white dwarfs that because of accretion exceeded the Chandrasekhar mass of $1.4M_\odot$, where M_\odot is the solar mass. The conservation of angular momentum, $MR_*^2\Omega_* = MR_*^2\Omega_*$, and magnetic flux, $R_*^2B_* = R_*^2B_*$, entail that when compressed to the size R_* the rotation period and the magnetic field of the neutron star are of order $P_* \sim (R_*/R_*)^2P_* \sim (0.01 - 1)$ s and $B_* \sim (R_*/R_*)^2B_* \sim 10^{12}$ G = 100 MT, where $\Omega_i = 2\pi/P_i$ is the angular velocity. Therefore, according to the Hillas criterion neutron stars can accelerate CRs to the maximum observed energies.

Neutron-star surfaces are thought to be composed of anisotropic, tightly-bound condensed matter. The crust of neutron stars extends down to about 1 km below the surface, with densities ranging from a few g/cm^3 on the exterior surface up to nuclear density 10^{14} g/cm^3 in the interior [217]. The outermost layers of the star are composed of long molecular chains of ^{56}Fe , with axes parallel to the magnetic field. ^{56}Fe ions can thus be stripped off the surface and be accelerated to extremely-high energies.

The acceleration process is Faraday’s unipolar induction, in which the rotational energy of the highly conducting plasma surrounding the homogeneously magnetized star is converted into electromagnetic energy. The electromagnetic force $F_{\text{em}} \sim ZeE$ acting on a CR of charge Ze and mass m near the neutron star

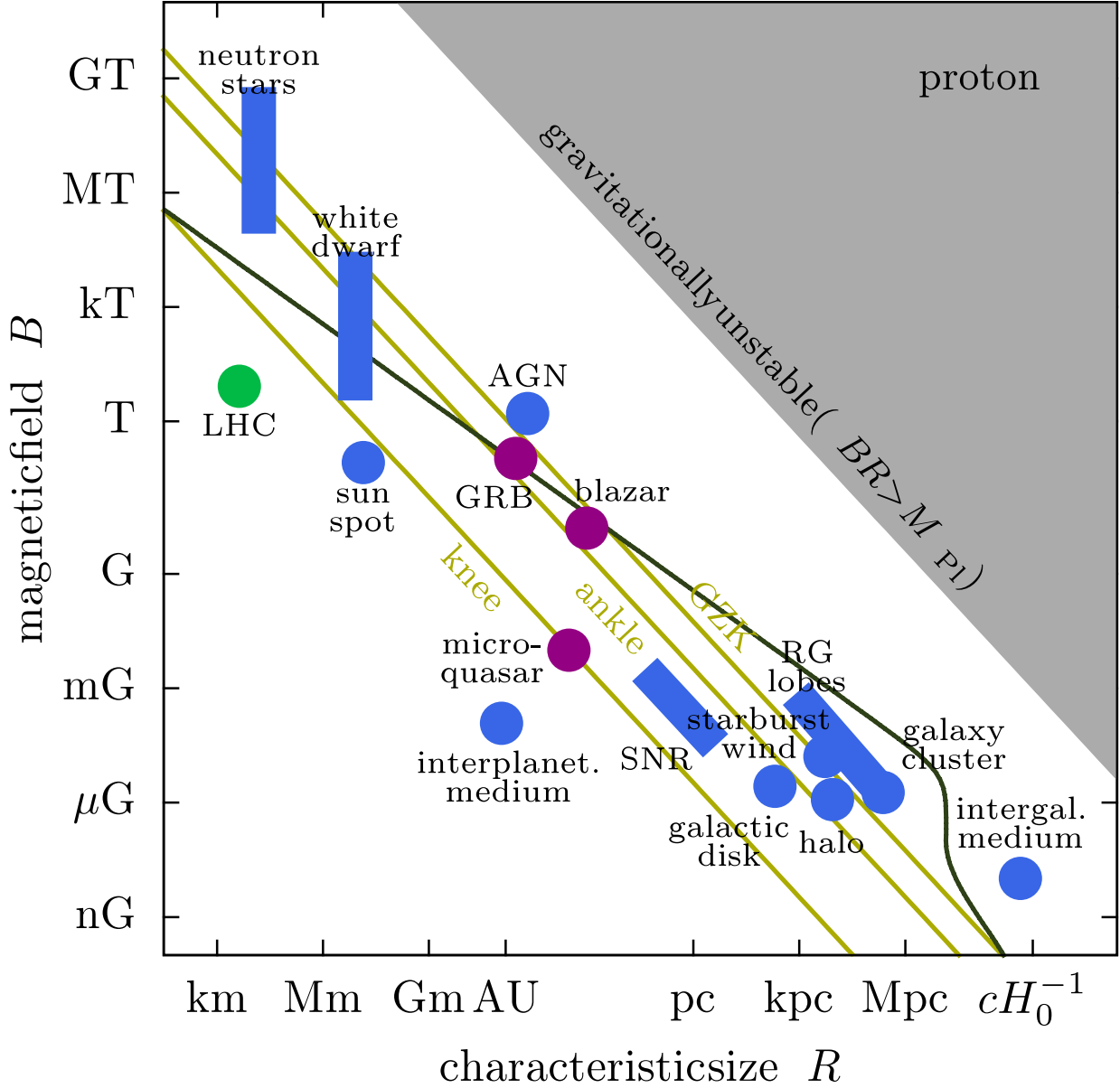


Figure 8: The “Hillas plot” for various CR source candidates, (blue areas). Also shown are jet-frame parameters for blazars, GRBs, and microquasars (purple areas). The corresponding point for the LHC beam is also shown. The straight lines show the *lower limit* for accelerators of protons at the *knee* ($E_{\text{knee}} \sim 10^{6.6}$ GeV), the *ankle* ($E_{\text{ankle}} \sim 10^{9.7}$ GeV), and the GZK suppression ($E_{\text{supp}} \sim 10^{10.6}$ GeV). The curve is the *upper limit* from synchrotron losses and proton interactions in the cosmic photon background ($R \gg 1$ Mpc). The grey area corresponds to astrophysical environments with extremely large magnetic field energy that would be gravitationally unstable. Here, AGN indicates the unipolar inductor which originates in the rotating accretion disk around a $10^8 M_{\odot}$ black hole; such a disk could draw in magnetic flux with the gas to give a magnetic field $B \sim 10^4$ G parallel to the rotation axis [182]. Blazars and RGs are AGNs that are oriented at different angles [15]. When the galaxy is oriented so that the jets of energy exiting the black hole are pointed toward Earth the objects is called a blazar. When the Earth is oriented perpendicular to the jet axis, the full extent of the jets may be seen particularly at low frequencies, giving rise to a morphology typical of RGs. For blazars and RG lobes, particle acceleration proceeds via Fermi mechanism [201, 202, 205]. From Ref. [215].

surface turns out to be many orders of magnitude greater than the gravitational force $F_g = GMm/R_*^2$. This condition allows us to disregard the electromagnetic field distortion connected with the space curvature in the vicinity of the neutron star. Therefore, the charges co-rotating with the star only experience the magnetic force, which is orthogonal to both the magnetic field and velocity. If unlimited plasma particles can be supplied into the system the electric charges move freely until the electric force and the magnetic force are equal and opposite,

$$\mathbf{E} + \mathbf{v} \times \mathbf{B} = \mathbf{0}. \quad (51)$$

The condition (51) simply implies that $\mathbf{E} \cdot \mathbf{B} = 0$. In other words, if the plasma surrounding the star is a perfect conductor, the electric field in the prime coordinate system co-rotating with the star is zero, $\mathbf{E}' = \mathbf{0}$.

Because of the presence of plasma in the pulsar magnetosphere condition (51) is, with adequate accuracy, satisfied not only in the interior of the neutron star but also in the whole magnetosphere. It is evident that the rigid co-rotation becomes impossible at large distances from the rotation axis. Indeed, the plasma rigidly co-rotates with the star within a zone $r < R_L$ limited by the finiteness of the speed of light. The so-called *light cylinder* defines the distance from the rotational axis at which a co-rotating particle would reach the speed of light; namely

$$R_L = \frac{c}{\Omega_*}, \quad (52)$$

where for clarity, we have written explicitly the speed of light while defining R_L ; hereafter we continue using natural units and we will drop c from our formulae. Note that R_L provides a natural scale to define the magnetosphere boundary. For ordinary pulsars, $R_L \sim 10^3 - 10^4$ km. This implies that the light cylinder is at distances several thousand times larger than the neutron star radius.

To discuss the generalities of the acceleration mechanism following [218] we consider the simplest case of a perfectly conducting neutron star rotating with angular velocity Ω_* . The star is endowed with a magnetic dipole moment aligned with the rotation axis, taken here in the vertical $\hat{\mathbf{z}}$ direction. The magnetic moment tends to be antiparallel (as opposed to parallel) to its spin angular momentum and has a magnitude $\mu = B_p R_*^3/2$, where B_p is the magnetic field strength at the pole. In spherical coordinates the components of the magnetic field are given by

$$B(r, \theta) = B_p \left(\frac{R_*}{r} \right)^3 \cos \theta \hat{\mathbf{r}} \quad (53a)$$

and

$$B(r, \theta) = \frac{B_p}{2} \left(\frac{R_*}{r} \right)^3 \sin \theta \hat{\boldsymbol{\theta}}. \quad (53b)$$

To first order approximation we can neglect the magnetic field contribution from magnetospheric currents, such that the magnetic field far from the neutron star surface is dominated by the star's own dipole field.

As one can see in Fig. 9, some magnetic field lines close inside the light cylinder, while those connected to the polar region cross it, and the particles moving along them cannot co-rotate. These *open field lines* define two *polar caps* on the stellar surface from which charged particles leaving the star can move along field lines and escape from the co-rotating magnetosphere by passing through the light cylinder. At the light cylinder the co-rotating magnetosphere carries one sign of net charge along an equatorial belt and the opposite sign above and below it. A (centrifugally induced) loss of charged particles out through the light cylinder would cause $\mathbf{E} \cdot \mathbf{B} \neq 0$. The separatrix is the line dividing the *co-rotating magnetosphere* from the

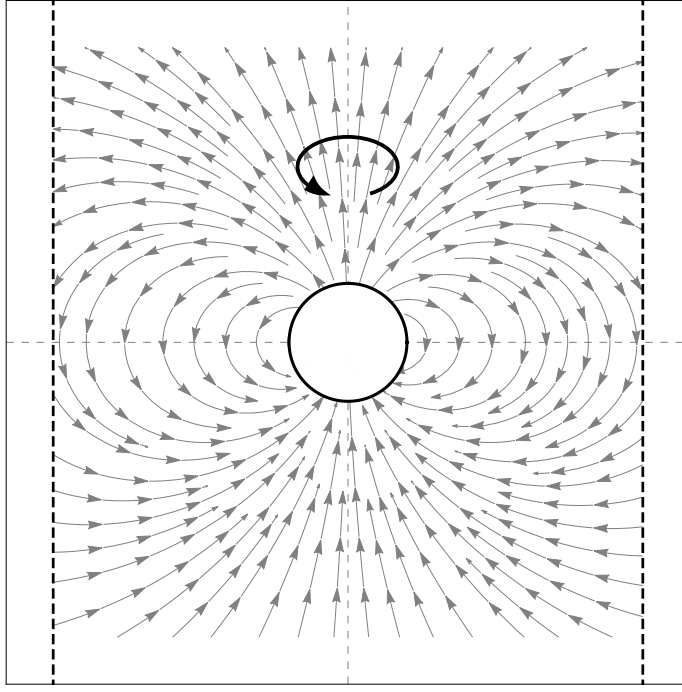


Figure 9: The axisymmetric magnetosphere structure of a neutron star. The rotating homogeneously magnetized star generates a dipole magnetic field. The open field lines coming out from the magnetic poles cross the light cylinder (dashed line).

open field lines region. The *polar cap* is defined as the portion of the star surface connected with the open field lines. The semi-opening angle for a dipolar magnetic field can be approximated by

$$\sin \theta_0 = \sqrt{\frac{R_*}{R_L}} = \sqrt{R_* \Omega_*}, \quad (54)$$

and so for $R_* = 10$ km, (54) leads to $\theta_0 \sim 0.8^\circ / \sqrt{P/\text{s}}$ [219].

A polar magnetospheric gap is formed that spans the open field lines from the stellar surface. In the gap $\mathbf{E} \cdot \mathbf{B} \neq 0$, although as we have seen the scalar product vanishes essentially everywhere else in the near magnetosphere. Co-rotation requires a Goldreich-Julian charge density,

$$\rho_{\text{GJ}} = \nabla \cdot \mathbf{E} = -\nabla \cdot (\boldsymbol{\Omega} \times \mathbf{r} \times \mathbf{B}) = -2\boldsymbol{\Omega} \cdot \mathbf{B} + \text{relativistic corrections} \sim B_p R_*^3 \Omega_*^3, \quad (55)$$

screening $\mathbf{E} \cdot \mathbf{B}$ [220]. Here, we have used $\nabla \times (\boldsymbol{\Omega} \times \mathbf{r}) = 2\boldsymbol{\Omega}$, (52), and (53b). The potential difference between the pole (p) and the point (c) at the edge of the polar cap (where the first open force line begins) is given by

$$\begin{aligned} \Delta\phi &= \int_p^c \mathbf{E} \cdot d\mathbf{s} = - \int_p^c (\mathbf{v} \times \mathbf{B}) \cdot d\mathbf{l} = \Omega_* R_* B_p \int_p^c [(\hat{\mathbf{z}} \times \hat{\mathbf{r}}) \times \hat{\mathbf{r}}] \cdot d\mathbf{l} = R_*^2 \Omega_* B_p \int_0^{\theta_0} \sin \theta d\theta \\ &= R_*^2 \Omega_* B_p (1 - \cos \theta_0), \end{aligned} \quad (56)$$

where $\hat{\mathbf{z}} = \cos \theta \hat{\mathbf{r}} - \sin \theta \hat{\boldsymbol{\theta}}$, $\hat{\mathbf{z}} \times \hat{\mathbf{r}} = \sin \theta \hat{\boldsymbol{\phi}}$, $(\hat{\mathbf{z}} \times \hat{\mathbf{r}}) \times \hat{\mathbf{r}} = \sin \theta \hat{\boldsymbol{\theta}}$, $d\mathbf{s} = R_* d\theta \hat{\boldsymbol{\theta}}$, and $\mathbf{v} = R_* \boldsymbol{\Omega}_* \times \hat{\mathbf{r}}$ is the velocity on the surface [221]. The integration goes over the contour on the pulsar surface where to a good

approximation the magnetic field is constant and in the radial direction, i.e., $\mathbf{B} \approx B_p \hat{\mathbf{r}}$. The gap continually breaks down (sparking) by forming e^+e^- pairs on a time scale of a few microseconds. The gap positrons move out along the open field lines, and the electrons flow to the stellar surface to close the pulsar's unipolar generator circuit.

For $\theta_0 \ll 1$, we have $\sin \theta_0 \approx \theta_0$ and because $(1 - \cos \theta_0) = 2 \sin^2(\theta_0/2)$ we can rewrite (56) as

$$\Delta\phi = \frac{1}{2} \Omega_* B_p R_*^2 \theta_0^2 \sim \frac{1}{2} B_p R_*^3 \Omega_*^2 \sim 6.6 \times 10^{19} \left(\frac{B_p}{10^{13} \text{ G}} \right) \left(\frac{R_*}{10 \text{ km}} \right)^3 \left(\frac{P_*}{1 \text{ ms}} \right)^{-2} \text{ V}. \quad (57)$$

Provided that particles of charge Ze can experience the total potential drop (57), they will be accelerated to the energy

$$E = Ze \Delta\phi, \quad (58)$$

which corresponds to a maximum achievable particle Lorentz factor of

$$\gamma_{\text{max}}^{\text{acc}} = \frac{Ze}{Am_N} \Delta\phi = 7 \times 10^{10} \frac{Z}{A} \left(\frac{B_p}{10^{13} \text{ G}} \right) \left(\frac{R_*}{10 \text{ km}} \right)^3 \left(\frac{P_*}{1 \text{ ms}} \right)^{-2}, \quad (59)$$

where $m_N \sim 1 \text{ GeV}$ is the nucleon mass and A the nucleus baryon number [176]. The fiducial value of P_* adopted in (57) corresponds to the exceptionally fast spinning young pulsars. The majority of pulsars are born spinning slower. Indeed, the distribution of pulsar-birth spin periods is Gaussian, centered at 300 ms, with standard deviation of 150 ms [222]. Note that most of the pulsars would accelerate heavy nuclei up a few 10^7 GeV . However, the period of a uniformly rotating neutron star could be as low as $P_* \approx 0.288 \text{ ms}$ [223]. Hence, proto-pulsars spinning initially with $P_* \approx 40 \text{ ms}$ would already reach $E \sim 10^9 \text{ GeV}$, which is roughly the maximum energy of Galactic cosmic rays [179].

In the real world, the maximum CR energy within the corotating region will be limited by energy loss. For example, within the potential drop the charged particles follow the curved magnetic field lines and so emit curvature-radiation photons. The energy loss rate or total power radiated away by a single cosmic ray is [224]

$$-\frac{dE}{dt} = \frac{2}{3} \frac{Z^2 e^2}{r_c^2} \gamma^4, \quad (60)$$

where r_c is the curvature radius of the magnetic field lines. Acceleration gains are balanced by radiative losses,

$$\dot{\gamma} = \frac{Ze \Delta\phi}{Am_N} \frac{2\pi}{\xi P_*} - \frac{8\pi^2}{3P_*^2} \frac{Z^2 e^2}{Am_N} \gamma^4, \quad (61)$$

where we have assumed that the total potential drop is available for particle acceleration over a gap of length ξR_L and that $r_c \sim R_L$. In the absence of other damping mechanisms, the radiation reaction limit turns out to be,

$$\gamma_{\text{max}}^{\text{rad}} = \left(\frac{3\pi B_p R_*^3}{2ZeP_*\xi} \right)^{1/4} \sim 1.1 \times 10^8 \left(\frac{Z}{26} \right)^{-1/4} \xi^{-1/4} \left(\frac{B_p}{10^{13} \text{ G}} \right)^{1/4} \left(\frac{P_*}{1 \text{ ms}} \right)^{-1/4} \left(\frac{R_*}{10 \text{ km}} \right)^{3/4}. \quad (62)$$

The actual maximum energy that particles can reach at any time within the corotating magnetosphere is found to be

$$\gamma_{\text{max}} = \min \{ \gamma_{\text{max}}^{\text{acc}}, \gamma_{\text{max}}^{\text{rad}} \}. \quad (63)$$

Before proceeding we note that $\gamma_{\max}^{\text{rad}}$ has a very weak dependence on the fraction ξ of R_L over which the gap extends, with $R_*/R_L < \xi < 1$. However, the acceleration time to a given energy is strongly dependent on the unknown ξ ; namely,

$$\dot{\gamma}^{-1} = \frac{Am_N \gamma \xi P_*}{Ze \Delta\phi 2\pi} = 5 \times 10^{-6} \text{ s} \left(\frac{\gamma}{10^9}\right) \left(\frac{A}{56}\right) \left(\frac{Z}{26}\right)^{-1} \left(\frac{B_p}{10^{13} \text{ G}}\right)^{-1} \left(\frac{R_*}{10 \text{ km}}\right)^{-3} \left(\frac{P_*}{1 \text{ ms}}\right)^3 \xi. \quad (64)$$

Note that for newly-born fast spinning pulsars,

$$\frac{R_*}{R_L} \sim 0.2 \left(\frac{R_*}{10 \text{ km}}\right) \left(\frac{P_*}{1 \text{ ms}}\right)^{-1}, \quad (65)$$

suggesting that $\xi = \mathcal{O}(1)$ and consequently that the gap cannot be far from the star surface.

UHECR nuclei could also suffer photodisintegration in the thermal radiation fields generated by the star and on the source environment. We will discuss these phenomena in detail in Sec. 3.4. We advance that for the most reasonable range of neutron star surface temperatures ($T < 10^7$ K), a large fraction of nuclei survive *complete* photo-disintegration in the hostile environment sustained by the thermal radiation field from the star [225]. However, the apparently inconsequential photo-disintegration losses could still be enough to produce a mixed nuclear composition at the source, with a non-negligible CNO component.

The spectrum of accelerated UHECRs is determined by the evolution of the rotational frequency. As the star spins down, the energy of the particles decreases. The total fluence of UHECRs between energy E and $E + dE$ is found to be

$$\frac{dN}{dE} = \frac{dN}{dt} \frac{dt}{d\Omega_*} \frac{d\Omega_*}{dE} dE, \quad (66)$$

where $\dot{N} = n_{\text{GJ}\pi} R_L c$ and $n_{\text{GJ}} = \rho_{\text{GJ}}/(Ze)$ [176]. It is easily seen that when the effect of the magnetosphere is taken into account the spin-down luminosity of the pulsar can be well approximated by $I\Omega_*\dot{\Omega}_* = \mu^2\Omega_*^4$, where $I \sim \frac{2}{5}MR_*^2 \sim 10^{45} \text{ g/cm}^2$ is the moment of inertia [226]. Finally, by differentiating (58) it follows that $dE/d\Omega_* = 2E/\Omega_*$. Therefore, (66) can be rewritten as

$$\frac{dN}{dE} \sim \frac{\pi I}{Ze\mu E}, \quad (67)$$

which explicitly shows that the total fluence of UHECRs accelerated in the neutron star magnetosphere yields a very hard spectrum $\propto E^{-1}$ [176]. Recall that simultaneously reproducing Auger data on the spectrum together with the observed nuclear composition requires hard source spectra [97].

Faraday's dynamo may also operate in the vicinity of a spinning super-massive black hole. The Blandford-Znajek model [180, 181] permits a direct calculation of the potential drop in polar cap regions of black hole magnetospheres, and can explain acceleration of UHECR nuclei with choice of parameters [227–229]. However, photo-nuclear interactions on the ambient photon fields surrounding the accelerator present formidable challenges for the model [230].

3.1.3. Fermi acceleration at shock waves

In his original analysis of the late '40s, Fermi [183] considered the scattering of CRs on moving magnetized clouds. A sketch of one of these encounters is shown in Fig. 10. Consider a CR entering into a single

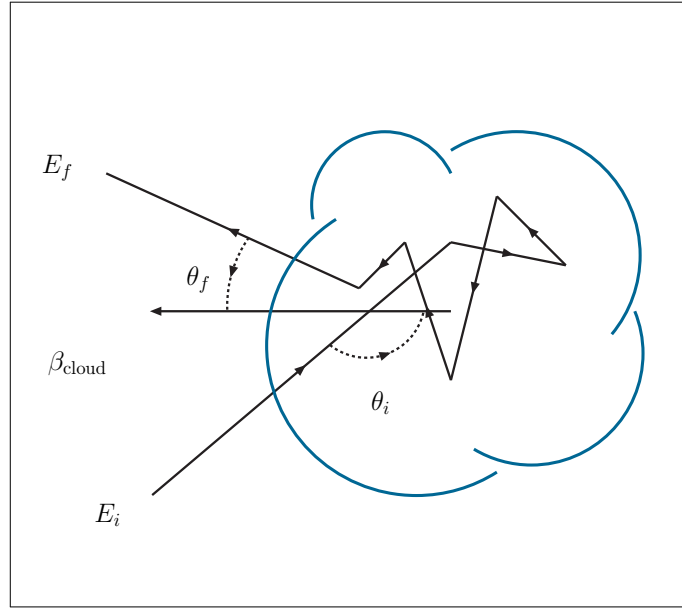


Figure 10: A sketch of 2nd order Fermi acceleration by scattering off magnetic clouds.

cloud with energy E_i and incident angle θ_i with the cloud's direction undergoing diffuse scattering on the irregularities in the magnetic field. After diffusing inside the cloud, the particle's average motion coincides with that of the gas cloud. The energy gain by the particle, which emerges at an angle θ_f with energy E_f , can be obtained by applying Lorentz transformations between the laboratory frame (unprimed) and the cloud frame (primed). In the rest frame of the moving cloud, the CR particle has a total initial energy

$$E'_i = \gamma_{\text{cloud}} E_i (1 - u_{\text{cloud}} \cos \theta_i), \quad (68)$$

where γ_{cloud} and u_{cloud} are the Lorentz factor and velocity of the cloud, respectively. In the frame of the cloud we expect no change in energy ($E'_i = E'_f$), because all the scatterings inside the cloud are due only to motion in the magnetic field (so-called collisionless scattering).⁹ There is elastic scattering between the CR and the cloud as a whole, which is much more massive than the CR. Transforming to the laboratory frame we find that the energy of the particle after its encounter with the cloud is

$$E_f = \gamma_{\text{cloud}} E'_f (1 + u_{\text{cloud}} \cos \theta_f). \quad (69)$$

The fractional energy change in the laboratory frame is then

$$\frac{\Delta E}{E} = \frac{E_f - E_i}{E_i} = \frac{1 - u_{\text{cloud}} \cos \theta_i + u_{\text{cloud}} \cos \theta_f - u_{\text{cloud}}^2 \cos \theta_i \cos \theta_f}{1 - u_{\text{cloud}}^2} - 1. \quad (70)$$

To determine the average energy gain one must obtain the average values of $\cos \theta_i$ and $\cos \theta_f$. Inside the cloud, the CR scatters off magnetic irregularities many times and its direction becomes randomized, so that

⁹In collision-dominated plasmas, particle-particle collisions drive the plasma to thermal equilibrium. If an individual particle gets more energy than average, it will immediately transfer energy via collisions to slower particles. Scatterings are inelastic. In collisionless plasmas, individual charged particles interact with the background magnetic field. Scatterings are nearly elastic.

$\langle \cos \theta_f \rangle = 0$. The average value of $\cos \theta_i$ depends on the rate at which CRs collide with clouds at different angles. The collisionless scattered particle will gain energy in a head-on collision ($\theta_i > \pi/2$) and lose energy by tail-end ($\theta_i < \pi/2$) scattering. The net increase of its energy is a statistical effect. The average value of $\cos \theta_i$ depends on the relative velocity between the cloud and the particle. The probability P per unit solid angle Ω of having a collision at angle θ_i is proportional to $(v - u_{\text{cloud}} \cos \theta_i)$, where v is the CR speed. In the ultrarelativistic limit, i.e., $v \sim 1$ (as seen in the laboratory frame),

$$\frac{dP}{d\Omega_i} \propto (1 - u_{\text{cloud}} \cos \theta_i), \quad (71)$$

so

$$\langle \cos \theta_i \rangle = \left\{ \int_0^\pi \cos \theta_i \frac{dP}{d\Omega_i} \right\} / \left\{ \int_0^\pi \frac{dP}{d\Omega_i} d\Omega_i \right\} = -\frac{u_{\text{cloud}}}{3}. \quad (72)$$

Now, inserting (72) into (70), one obtains for $u_{\text{cloud}} \ll 1$,

$$\frac{\langle \Delta E \rangle}{E} = \frac{1 + u_{\text{cloud}}^2/3}{1 - u_{\text{cloud}}^2} - 1 \approx \frac{4}{3} u_{\text{cloud}}^2. \quad (73)$$

Note that $\langle \Delta E \rangle / E \propto u_{\text{cloud}}^2$, so even though the average magnetic field may vanish, there can still be a net transfer of the macroscopic kinetic energy from the moving cloud to the particle. However, the average energy gain is very small, because $u_{\text{cloud}}^2 \ll 1$. This acceleration process is very similar to a thermodynamical system of two gases, which tries to come into thermal equilibrium [231]. Correspondingly, the spectrum of CRs should follow a thermal spectrum which might be in conflict with the observed power-law.

By the mid '50s, Fermi realized that a more efficient acceleration process may occur when particles scatter back and forth between two ends of a contracting magnetic bottle, as the particles would gain energy at every scattering [184]. Ever since the late '70s it became clear that a simple version of this acceleration process may occur in the vicinity of magnetized collisionless plasma shocks occurring in astrophysical environments [232–239]. These shocks originate in the sudden change of density ρ , temperature T , and pressure P that decelerate a supersonic flow. Before proceeding, we pause to introduce some notation. The state of a system in (local) thermodynamic equilibrium may be defined by any two intensive variables, such as T , P , the specific volume $v \equiv \rho^{-1}$, the internal energy per unit mass ε , or the entropy per unit mass s . The first law of thermodynamics may be stated that in going from state 1 to state 2, the change in internal energy per unit mass must equal the sum of the heat added per unit mass q to the work done per unit mass on the system, $d\varepsilon = Tds - Pdv$. This relation is valid for both reversible and irreversible processes. Any process in an open system which does not exchange heat with the environment is said to be adiabatic. If the process is furthermore reversible, it follows that $\delta q = 0$ in each infinitesimal step, so that the $\delta s = \delta q/T = 0$. The specific entropy must in other words stay constant in any reversible, adiabatic process. Such a process is for this reason called isentropic. The sound speed is defined as

$$c_s^2 = \left(\frac{\partial P}{\partial \rho} \right) \Big|_s = \frac{\gamma P}{\rho}, \quad (74)$$

where the derivative is taken isentropically so that $P\rho^{-\gamma} = \text{constant}$, with γ the adiabatic index. The value of the adiabatic index is $\gamma = 5/3$ for monatomic gases, $\gamma = 7/5$ for diatomic gases, $\gamma = 9/7$ for three-atomic gases with non-static bindings, and $\gamma = 4/3$ for a relativistic gas.

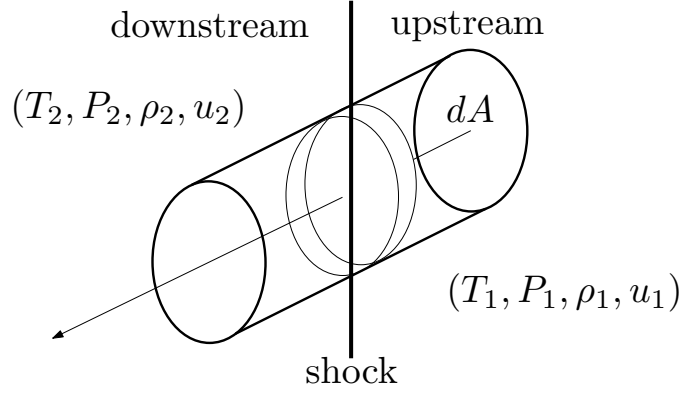


Figure 11: A sketch of a perpendicular shock.

Hereafter we assume that: (i) the gas density is low enough so particle-particle collisions are rare, and (ii) the gas passing through the shock is not dissociated, i.e., both the mass of a gas molecule and the adiabatic index remain unchanged. Then changes occur in ρ , T , P , and velocity. For simplicity, throughout we consider magnetized plasmas near a perpendicular shock, i.e. one in which the propagation direction of the shock is aligned with the incident magnetic field. The description of the plasma and fields near a parallel shock is considerably more complicated than that of a perpendicular shock and can be found in e.g., [240, 241]. At this stage, it is worthwhile to point out that despite the fact we cannot describe the way that the fluid behaves inside the shock (say, in a few mean free paths of the shock), we can portray how the fluid conditions differ from side to side of the shock, i.e., as a result of shock passing. We will show that this characterization is sufficient for the purpose of modeling UHECR acceleration.

Consider a propagating supersonic flow. In the rest frame of the shock, unshocked gas moving faster than its sound speed approaches the shock from the right direction. The preshock conditions are characterized by T_1 , P_1 , ρ_1 , u_1 , whereas the postshock conditions are described by T_2 , P_2 , ρ_2 , u_2 . For a steady shock, the mass contained in the cylinder shown in Fig. 11 is constant. This implies that the mass flux into the shock is the same as the mass flux out,

$$\rho_1 u_1 = \rho_2 u_2. \quad (75)$$

The momentum density contained in the cylinder is also constant. Thus, the net pressure force on the cylinder plus the net momentum flux into the cylinder must be zero, yielding

$$(P_1 dA - P_2 dA) + (\rho_1 u_1^2 dA - \rho_2 u_2^2 dA) = 0, \quad (76)$$

or equivalently

$$P_1 + \rho_1 u_1^2 = P_2 + \rho_2 u_2^2. \quad (77)$$

Finally, the energy contained in the cylinder is a constant. Therefore, the net flow of energy into the cylinder plus the work done on a gas in the cylinder is equal to zero. This leads to

$$\left[u_1 \left(\rho_1 \varepsilon_1 + \frac{1}{2} \rho_1 u_1^2 \right) dA - u_2 \left(\rho_2 \varepsilon_2 + \frac{1}{2} \rho_2 u_2^2 \right) dA \right] + (P_1 u_1 - P_2 u_2) dA = 0, \quad (78)$$

or equivalently,

$$u_1 \left[P_1 + \rho_1 \left(\varepsilon_1 + \frac{1}{2} \rho_1 u_1^2 \right) \right] = u_2 \left[P_2 + \rho_2 \left(\varepsilon_2 + \frac{1}{2} \rho_2 u_2^2 \right) \right]. \quad (79)$$

Substituting (75) into (79) it follows that

$$\varepsilon_1 + \frac{1}{2}u_1^2 + \frac{P_1}{\rho_1} = \varepsilon_2 + \frac{1}{2}u_2^2 + \frac{P_2}{\rho_2}. \quad (80)$$

Equations (75), (77), and (80) are the well-known Rankine-Hugoniot (RH) relations. Substituting (74) in (77) and (80) we obtain.

$$u_1 \left(1 + \frac{c_{s,1}^2}{\gamma u_1^2} \right) = u_2 \left(1 + \frac{c_{s,2}^2}{\gamma u_2^2} \right). \quad (81a)$$

and

$$\frac{1}{2}u_1^2 + \frac{c_{s,1}^2}{\gamma - 1} = \frac{1}{2}u_2^2 + \frac{c_{s,2}^2}{\gamma - 1}. \quad (81b)$$

It is easily seen that the entropy per unit mass of the matter entering the shock is lower than that of the gas leaving the shock: the shock produces a great disorganization of the gas.

The dimensionless number that characterizes the strength of a shock is the Mach number, the ratio of the unshocked gas speed to the upstream sound speed,

$$\mathcal{M} = \frac{u_1}{c_{s,1}} = \left(\frac{\rho_1 u_1^2}{\gamma P_1} \right)^{1/2}. \quad (82)$$

Given that $\mathcal{M} > 1$, it is straightforward to see that $\rho_2 > \rho_1$ (shocks compress), $u_2 < u_1$ (shocks decelerate), $P_2 > P_1$ (shocks increase pressure), and $T_2 > T_1$ (shocks heat). The latter may seem surprising, given that the shock is considered to be adiabatic: although the process has been adiabatic, in that $\delta q/dt = 0$, the gas has changed its adiabat; its entropy has increased as a consequence of the shock converting kinetic energy into thermal, internal energy.¹⁰ The total energy of the post-shock gas is lower (in the shock rest frame) because of the work done on the gas by *viscosity* and pressure in the shock. It is this aspect of the shock that causes irreversibility, thus defining an ‘‘arrow of time.’’

The compression ratio achieved by the shock is defined by

$$\zeta = \frac{\rho_2}{\rho_1} = \frac{u_1}{u_2}, \quad (83)$$

so that $\psi = \zeta^{-1}$ is the inverse compression ratio, and therefore $u_1 = c_{s,1}\mathcal{M}$ and $u_2 = c_{s,1}\psi\mathcal{M}$. Substituting these expressions in (81) leads to

$$\left(1 + \frac{1}{\gamma \psi \mathcal{M}^2} \right) = \psi \left(1 + \frac{c_{s,2}^2}{c_{s,1}^2} \frac{1}{\gamma \psi \mathcal{M}^2} \right) \quad (84a)$$

and

$$\frac{1}{2}\mathcal{M}^2 + \frac{1}{\gamma - 1} = \frac{1}{2}\psi^2\mathcal{M}^2 + \frac{1}{\gamma - 1} \frac{c_{s,2}^2}{c_{s,1}^2}, \quad (84b)$$

¹⁰A shock converts supersonic gas into denser, slower moving, higher pressure, subsonic gas. It increases the specific entropy of the gas. In another terminology, a shock shifts gas to a higher adiabat. An adiabat is a locus of constant entropy ($T \propto \rho^{\gamma-1}$) in the density-temperature plane. Gas can move adiabatically along an adiabat, while changes in entropy move it from one adiabat to another.

which can be rewritten as two expressions for $c_{s,2}^2/c_{s,1}^2$; namely,

$$\frac{c_{s,2}^2}{c_{s,1}^2} = \psi + \gamma\psi\mathcal{M}^2(1 - \psi) = 1 + \frac{\gamma - 1}{2}\mathcal{M}^2(1 - \psi^2). \quad (85)$$

Combining these two expressions yields an equation for ψ

$$(\psi - 1) + \gamma\psi\mathcal{M}^2(1 - \psi) - \frac{\gamma - 1}{2}\mathcal{M}^2(\psi + 1) = 0. \quad (86)$$

Note that if $\psi = 1$ there is no shock as $\rho_1 = \rho_2$, $u_1 = u_2$, and $P_1 = P_2$. Thus,

$$1 - \gamma\psi\mathcal{M}^2 + \frac{\gamma - 1}{2}\mathcal{M}^2(\psi + 1) = 0 \quad (87)$$

yielding

$$\psi = \frac{\gamma - 1}{\gamma + 1} + \frac{2}{\gamma + 1} \frac{1}{\mathcal{M}^2}. \quad (88)$$

We can now substitute (88) into (75), (77), and (80) to rewrite the RH jump conditions in a more useful form

$$\frac{\rho_1}{\rho_2} = \frac{u_2}{u_1} = \frac{\gamma - 1}{\gamma + 1} + \frac{2}{\gamma + 1} \frac{1}{\mathcal{M}^2}, \quad (89a)$$

$$\frac{P_2}{P_1} = \frac{2\gamma}{\gamma + 1}\mathcal{M}^2 - \frac{\gamma - 1}{\gamma + 1}, \quad (89b)$$

and

$$\frac{T_2}{T_1} = \frac{c_{s,2}^2}{c_{s,1}^2} = \frac{P_2 \rho_1}{P_1 \rho_2} = \left(\frac{2\gamma}{\gamma + 1}\mathcal{M}^2 - \frac{\gamma - 1}{\gamma + 1} \right) \left(\frac{\gamma - 1}{\gamma + 1} + \frac{2}{1 + \gamma} \frac{1}{\mathcal{M}^2} \right). \quad (89c)$$

Note that the thermodynamics variables depend on the Mach number of the upstream gas \mathcal{M} and the adiabatic index γ , which specify the way that energy is shared between the internal energy and the kinetic flow. For a very strong shock, $\mathcal{M} \rightarrow \infty$, yielding $\zeta \rightarrow (\gamma + 1)/(\gamma - 1)$ and $P_2/P_1 \rightarrow \infty$. Note also that $\gamma \rightarrow 1$ gives the maximum compression ratio, for which $\rho_2/\rho_1 \rightarrow \mathcal{M}^2$ and $T_1 \rightarrow T_2$, but P_2/P_1 can become arbitrarily large.

Suppose that a strong (nonrelativistic) shock wave propagates through the plasma as sketched in the left panel of Fig. 12. In the frame stationary with respect to the shock, the upstream flow approaches with speed u_1 and the downstream flow recedes with speed u_2 . The RH conservation relations imply that the upstream velocity u_1 (ahead of the shock) is much higher than the downstream velocity u_2 (behind the shock). Therefore, when measured in the upstream rest frame, the quantity $u = u_1 - u_2$ is the speed of the shocked fluid and $u_1 = u_{\text{shock}}$ is the speed of the shock. In the primed frame stationary with respect to the downstream fluid, $u_2 = u_{\text{shock}}$ and $u = u_1 - u_2$ is the speed of the upstream fluid. Hence, because of the converging flow – whichever side of the shock you are on, if you are moving with the plasma, the plasma on the other side of the shock is approaching you with velocity u – to first order there are only head-on collisions for particles crossing the shock front; see Fig. 12. The acceleration process, although stochastic, always leads to a gain in energy. In order to work out the energy gain per shock crossing, we can visualize magnetic irregularities on either side of the shock as clouds of magnetized plasma of Fermi's original theory. As one can see in Fig. 12 there is an asymmetry because upstream particles always return to the shock, whereas downstream particles may be advected and never come back to the shock.

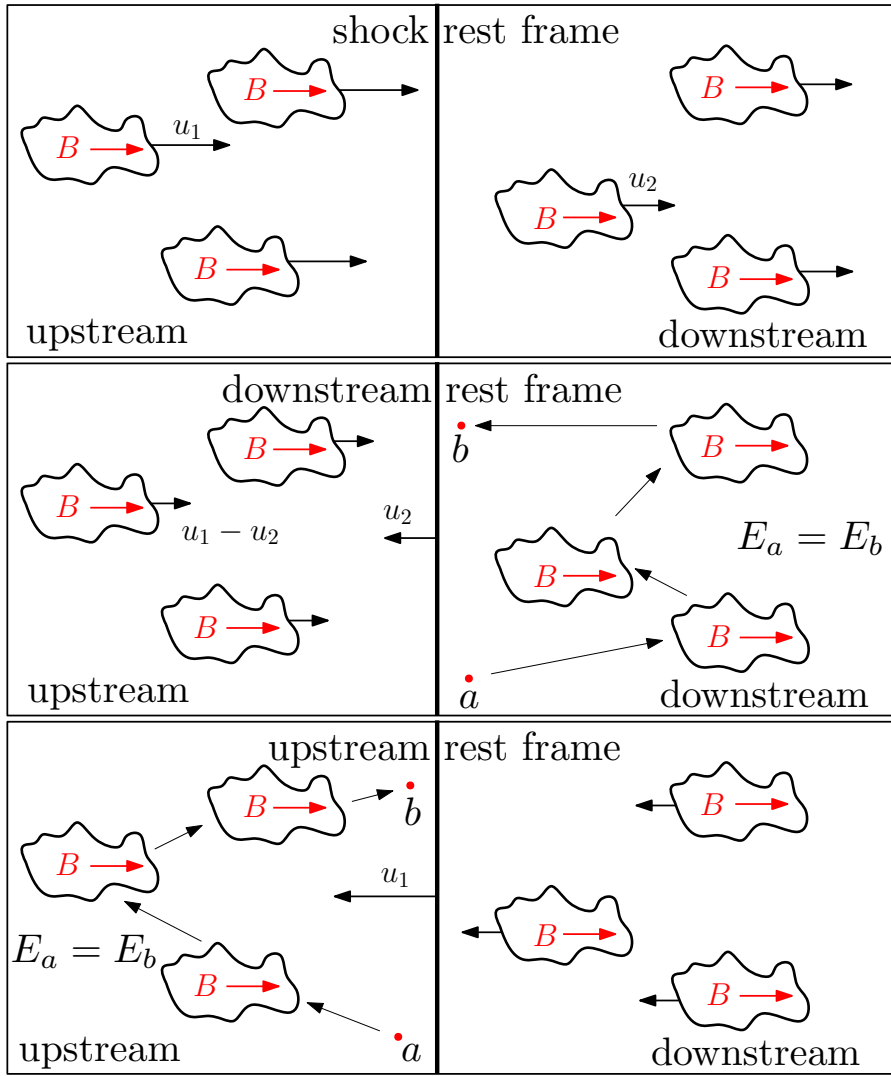


Figure 12: Different perspectives of 1st order Fermi acceleration by scattering off a plasma shock.

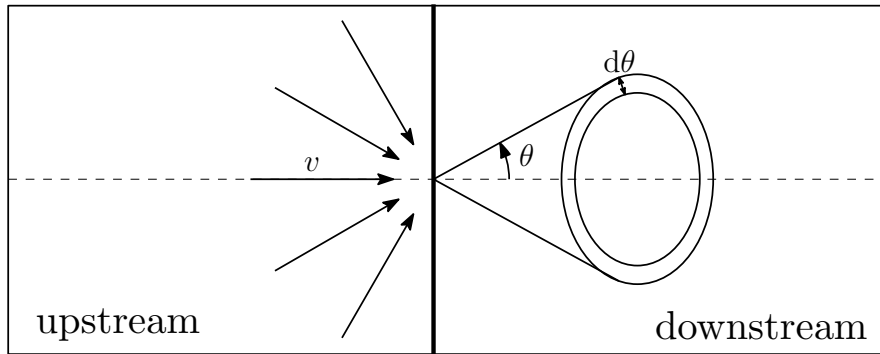


Figure 13: Properties of CRs undergoing diffusive shock acceleration. The number density of accelerated particles close to the shock is isotropic, $dn_{1,2} = n_{1,2} d\Omega / (4\pi)$. The rate at which particles cross the shock is proportional to $v \cos \theta$, with $0 < \theta < \pi/2$. The number of particles between θ and $\theta + d\theta$ is proportional to $\sin \theta d\theta$. The differential probability for an ultra-relativistic ($v \simeq c$) particle to cross the shock is $dP \propto \sin \theta \cos \theta d\theta$.

Consider an upstream particle that has initial energy E and initial momentum p . The particle “sees” the downstream flow with a velocity $u = u_1 - u_2$ and a Lorentz factor γ_u . To determine the energy of the particle in the downstream rest frame we perform a Lorentz transformation

$$E' = \gamma_u(E + u p \cos \theta), \quad (90)$$

where θ is the incident angle; see Fig. 13. Now, assume that the shock is non-relativistic (i.e., $\gamma_u \sim 1$) and that the particle is relativistic (i.e., $E = p$). Under these conditions the energy gain per half-cycle (say, upstream \rightarrow downstream) is

$$\frac{\delta E}{E} = u \cos \theta. \quad (91)$$

Assuming that the particles upstream and downstream of the shock are rapidly isotropized by magnetic field irregularities, the distribution function for particles crossing the shock is $f(\theta) \propto \sin \theta \cos \theta$; see Fig. 13. The total probability must equal unity, $\int_0^{\pi/2} f(\theta) d\theta = 1$, and so the normalized differential probability for a particle to cross the shock is found to be,

$$dP = 2 \sin \theta \cos \theta d\theta. \quad (92)$$

The average gain per half-cycle $\langle \delta E \rangle / E$ is (91) averaged over the differential probability distribution (92)

$$\frac{\langle \delta E \rangle}{E} = 2u \int_0^{\pi/2} d\theta \cos^2 \theta \sin \theta = \frac{2}{3}u. \quad (93)$$

Now, it is straightforward to see that $\langle \delta E \rangle / E|_{\text{up} \rightarrow \text{down}} = \langle \delta E \rangle / E|_{\text{down} \rightarrow \text{up}}$, and therefore for a full cycle up \rightarrow down and down \rightarrow up the energy gain is

$$\frac{\langle \Delta E \rangle}{E} = \frac{4}{3}u = \frac{4}{3}(u_1 - u_2). \quad (94)$$

Note this is first order in u , and is therefore more efficient than Fermi’s original mechanism.

An attractive feature of Fermi acceleration is its prediction of a power-law flux of CRs. Consider a test-particle with momentum p in the rest frame of the upstream fluid. The particle’s momentum distribution is isotropic in the fluid rest frame. For pitch angles $\pi/2 < \theta_i < \pi$ relative to the shock velocity vector the particle enters the downstream region and has *on average* the relative momentum $p[1 + 2(u_1 - u_2)/3]$. Subsequent diffusion in the downstream region ‘re-isotropizes’ the particle’s momentum distribution in the fluid rest frame. As the particle diffuses back into the upstream region (for pitch angles $0 < \theta_f < \pi/2$) it has *gained* an average momentum of $\langle \Delta p \rangle / p \simeq 4(u_1 - u_2)/3$. This means that the momentum gain of a particle per time is proportional to its momentum,

$$\dot{p} = p/t_{\text{gain}}. \quad (95)$$

On the other hand, the loss of particles from the acceleration region is proportional to the CR distribution function

$$\dot{f} = -f/t_{\text{loss}}. \quad (96)$$

Therefore, taking the ratio (95)/(96) we first obtain

$$df/dp = -\alpha f/p, \quad (97)$$

and after integration $f(p) \propto p^{-\alpha}$, with $\alpha = t_{\text{gain}}/t_{\text{loss}}$. If the acceleration cycle across the shock takes the time Δt we have already identified $\Delta t/t_{\text{gain}} = \langle \Delta p \rangle / p \simeq 4(u_1 - u_2)/3$. Now, $\Delta t/t_{\text{loss}}$ represents the probability that the particle leaves the accelerator after each cycle. This is given by

$$\frac{\Delta t}{t_{\text{loss}}} \simeq \frac{R_{\text{out}}}{R_{\text{in}}}, \quad (98)$$

where R_{in} is the number of particles per unit time (rate) that begins a cycle and R_{out} is the number of particles per unit time that leaves the system. The rate at which CRs cross from upstream to downstream is given by the projection of the isotropic CR flux onto the plane shock front

$$R_{\text{in}}(\text{up} \rightarrow \text{down}) = \int_{\text{up} \rightarrow \text{down}} dn_1 v \cos \theta = \frac{v n_1}{4\pi} \int_0^{2\pi} d\phi \int_0^1 d \cos \theta = \frac{1}{4} v n_1, \quad (99)$$

see Fig. 13. The particle lost rate (advected) downstream is $R_{\text{out}} = n_2 u_2$, and so taking $v \simeq c$

$$\frac{R_{\text{out}}}{R_{\text{in}}} = \frac{4n_1 u_2}{n_2} = 4u_1 \ll 1, \quad (100)$$

showing that most of the particles perform many cycles. Putting all this together,

$$\alpha \simeq \frac{3u_1}{u_1 - u_2} = \frac{3\zeta}{\zeta - 1}. \quad (101)$$

The differential energy spectrum $dN/dE \propto E^{-\gamma}$ is related to the phase space distribution in momentum space by $dN = 4\pi p^2 f(p) dp$ and hence $\gamma = \alpha - 2$.

All in all, the steepness of the power-law spectrum at the sources depends on the shock compression ratio via the adiabatic index. The different regions of the parameter space can be easily visualized with a simple phenomenological argument [242]. Consider an expanding shell that magnetically confines UHECRs. Assuming that the CRs are isotropically distributed in the shell, the number of escaping particles is proportional to the volume. The shell width expands as $\delta r \propto r$. This implies that the volume of the plasma increases as $V \propto r^3$ and the total energy scales as $U \propto V^{-(\gamma-1)} \propto r^{-3(\gamma-1)}$. Now, using the scaling of the volume and the total energy we can derive the scaling of the magnetic field inside the plasma $B \propto \sqrt{U/V} \propto r^{-3\gamma/2}$. If we further assume that the energy of a single particle in the plasma scales in the same way as the total energy of the plasma, then the Larmor radius of the particle changes with time (or radius) as $r_L \propto E/B \propto r^{-3(\gamma-2)/2}$. For a relativistic gas, $\gamma = 4/3$ yielding $r_L \propto r$, and so the ratio $r_L/\delta r$ is constant. This means that a relativistic gas provides a critical balance for stability between losses and escape. For $\gamma > 4/3$, the adiabatic energy loss is faster than the escape, and the particles are more strongly confined for larger radii. For $\gamma < 4/3$, the Larmor radius increases faster than the particles lose energy, and the particles are getting less confined at larger radii. For a monoatomic gas, $\zeta = 4$ and the spectral index becomes $\gamma = 2$. For a three-atomic gas with non-static bindings $\zeta = 8$, yielding a hard source spectrum with spectral index $\gamma = 1.4$.

The acceleration time scale is given by

$$\left(\frac{1}{E} \frac{dE}{dt} \right)^{-1} = \frac{t_{\text{cycle}}}{\langle \Delta E \rangle / E}, \quad (102)$$

where t_{cycle} is the cycle time for one back-and-forth encounter. Diffusion takes place in the presence of advection at speed u_2 in the downstream direction. The characteristic distance a CR diffuses in time t_D

is $l_D = \sqrt{D_2 t_D}$ where D_2 is the diffusion coefficient in the downstream region. The distance advected in this time is simply $u_2 t_D$. If $\sqrt{D_2 t_D} \gg u_2 t_D$ the CR has a very high probability of returning to the shock, whereas if $\sqrt{D_2 t_D} \ll u_2 t_D$ the CR has a very high probability of never returning to the shock (i.e. it has effectively escaped downstream). So, we set $\sqrt{D_2 t_D} = u_2 t_D$ to characterize the diffusion time $t_D = D_2/u_2^2$ and define a distance $l_D = D_2/u_2$ downstream of the shock which is effectively a boundary between the region closer to the shock where the particles will usually return to the shock and the region farther from the shock in which the particles will usually be advected downstream never to return. There are $n_2 D_2/u_2$ particles per unit area of shock between the shock and this boundary. Dividing this by $R_{\text{in}}(\text{down} \rightarrow \text{up})$ we obtain the average time spent downstream before returning to the shock

$$t_2 \approx \frac{4}{v} \frac{D_2}{u_2}. \quad (103)$$

Now, we must consider the other half of the cycle, after the CR has crossed the shock from downstream to upstream until it returns to the shock. In this case we can define a boundary at a distance D_1/u_1 upstream of the shock such that nearly all particles upstream of this boundary have never encountered the shock, and nearly all the particles between this boundary and the shock have diffused there from the shock. Then dividing the number of particles per unit area of shock between the shock and this boundary, $n_1 D_1/u_1$, by $R_{\text{in}}(\text{up} \rightarrow \text{down})$ we obtain the average time spent upstream before returning to the shock

$$t_1 \approx \frac{4}{v} \frac{D_1}{u_1}, \quad (104)$$

and hence the time for a full cycle is

$$t_{\text{cycle}} \approx \frac{4}{v} \left(\frac{D_1}{u_1} + \frac{D_2}{u_2} \right). \quad (105)$$

To proceed we must estimate the diffusion coefficient, which can be interpreted as

$$D = \frac{1}{3} \lambda_D v, \quad (106)$$

where v is the particle velocity and λ_D the diffusion mean free path. The diffusion length cannot be smaller than the Larmor radius because energetic particles cannot respond to irregularities in the magnetic field smaller than the particle gyroradius [237]. The minimum diffusion coefficient, which gives the maximum possible acceleration rate, corresponds to the Bohm diffusion limit. Substituting (49) into (106) gives

$$D_{\text{min}} = \frac{r_L v}{3} \sim \frac{1}{3} \frac{E v}{Z \sqrt{4\pi \alpha} B}. \quad (107)$$

Taking $D_1 = D_2 = D_{\text{min}}$ in (105), and inserting the output into (102) yields an expression for the acceleration rate, which does not depend on the CR energy because $t_{\text{cycle}} \propto E$. Assuming that the acceleration is continuous, the constraint due to the finite lifetime τ of the shock yields,

$$E \lesssim \varkappa(\zeta) Z \sqrt{4\pi \alpha} B u_1^2 \tau, \quad (108)$$

where $\varkappa(\zeta) = 3/20$ for a monoatomic classic gas [243], and $\varkappa(\zeta) = 1/12$ for a three atomic gas with non-static bindings [209]. At this stage, it is worthwhile to remind the reader that in the preceding discussion it was implicitly assumed that the magnetic field is parallel to the shock normal. Injecting additional hypotheses into the model may reduce [195, 244] or increase [245, 246] the maximum achievable energy.

For a relativistic outflow, with $\gamma_u \equiv (1 - u_1^2)^{-1/2} \gg 1$, the calculation is somewhat more complicated, because the CR is allowed to be accelerated only over a fraction of the characteristic length of the accelerator, which is comparable to R/γ_u [207, 247]. To visualize this, one must realize that as the plasma expands, its magnetic field decreases, and consequently the time available for acceleration corresponds to the time of expansion from R to, say, $2R$. In the observer frame this time is R/u_1 , while in the plasma rest frame it is $R/(\gamma_u u_1)$. Therefore, a CR moving with the magnetized plasma can only be accelerated over a transverse distance $\sim R/\gamma_u$. This shows that the maximal energy is also inversely proportional to the Lorentz factor,

$$E \lesssim \varkappa(\zeta) Z \sqrt{4\pi\alpha} B \frac{u_1}{\gamma_u} R. \quad (109)$$

When a GRB erupts, the internal plasma is accelerated to ultra-relativistic velocities, making GRBs premium astrophysical sites to explore how relativistic collisionless shocks can accelerate UHECRs [207, 208]. For typical source parameters, the plasma is opaque to the propagation of UHECR nuclei [250], and so it appears that these powerful compact objects would only accelerate protons up to ultra-high energies; see, however, [251–255].

For the generic case of acceleration in an outflow, one can compare (109) with the magnetic luminosity L_B to set a lower bound on the luminosity that a source must possess to accelerate UHECRs. Namely, the magnetic field carries with it an energy density $B^2/2$ and the flow carries with it an energy flux $> vB^2/2$ so (109) sets a lower limit on the rate

$$L_B > \frac{1}{8\pi\alpha} \frac{1}{\varkappa^2(\zeta)} \frac{\gamma_u^2}{u_1} E_p^2 \sim 10^{42} \frac{1}{\varkappa^2(\zeta)} \frac{\gamma_u^2}{u_1} \left(\frac{E_p}{10^{10}\text{GeV}} \right)^2 \text{ erg/s} \quad (110)$$

at which the energy must be carried by the outflowing plasma to accelerate a nucleus to a given rigidity E_p [159]. The Poynting luminosity of the accelerator [207, 247, 248] is found to be a factor of 2 larger [249]. Only the brightest AGNs and GRBs are known to satisfy the (110) power requirement while reaching $E_p \sim 10^{10}$ GeV [207, 256, 257]. We will see in Sec. 3.3, however, that there are ways to escape this constraint.

3.2. Energy loss

3.2.1. Interaction rate of UHECRs on photon fields

Thus far we have considered acceleration processes in astrophysical environments without paying attention to the CR energy loss through interactions with the source's photon backgrounds. Moreover, as UHECRs propagate *en route* to Earth they also lose energy scattering off the pervasive radiation fields permeating the universe. Before we estimate the UHECR mean free path of these collisions we review some basic phenomenology of collider physics.

For both an incident beam on a fixed target or two colliding beams, the interaction rate R is proportional to the number density of particles n_1 and n_2 that approach each other with a certain relative velocity. The natural definition of the relativistic invariant flux is

$$\mathcal{F} = (J_1 \cdot J_2) v_{\text{rel}}, \quad (111)$$

where

$$J_i = (n_i, n_i \mathbf{v}_i) = n_i^0 (\gamma_i, \gamma_i \mathbf{v}_i) = n_i^0 u_i, \quad (112)$$

is a 4-vector current ($i = 1, 2$), and where n_i^0 is the number density in the rest frame and u_i the 4-velocity $u_i = \gamma_i(1, \mathbf{v}_i)$, with $u_i^2 = 1$ and γ_i the Lorentz factor [258]. One can check by inspection that this expression is a Lorentz scalar. For massless particles, the velocity vector becomes the unitary vector in the direction of propagation and if at least one massless particle is involved in the collision then $v_{\text{rel}} = 1$, yielding

$$\mathcal{F} = J_1 \cdot J_2 = n_1 n_2 (1 - \mathbf{v}_1 \cdot \mathbf{v}_2). \quad (113)$$

For two massless particles, the flux can be rewritten as $\mathcal{F} = n_1 n_2 (1 - \cos \theta)$, where θ is the angle between the 3-momenta $\hat{\mathbf{k}}_1$ and $\hat{\mathbf{k}}_2$ of the incoming particles. For collisions of a massless with a massive particle, the incident flux is found to be $\mathcal{F} = n_1 n_2 (1 - v_2 \cos \theta)$. The physical quantity that gives the intrinsic quantum probability for an interaction is the cross section, defined by the ratio $\sigma = R/\mathcal{F}$.

The interaction rate for a highly relativistic ($v \sim 1$) cosmic ray (with baryon number A and energy $E = \gamma A$ GeV) propagating through an isotropic photon background with energy ε and spectrum $n(\varepsilon)$, normalized so that the total number of photons in a box is $\int n(\varepsilon) d\varepsilon$, can be derived assuming one of the densities in the scattering process collapses into a delta function,

$$\begin{aligned} R &= \frac{1}{4\pi} \int_0^\infty d\varepsilon n(\varepsilon) \int d\Omega \sigma(\varepsilon') (1 - \cos \theta) = \frac{1}{2} \int_0^\infty d\varepsilon n(\varepsilon) \int_{-1}^{+1} d \cos \theta \sigma(\varepsilon') (1 - \cos \theta) \\ &= \frac{1}{2\gamma^2} \int_0^\infty \frac{d\varepsilon}{\varepsilon^2} n(\varepsilon) \int_0^{2\gamma\varepsilon} d\varepsilon' \varepsilon'^2 \sigma(\varepsilon'), \end{aligned} \quad (114)$$

where $\sigma(\varepsilon')$ is the cross section for UHECR interaction with a photon of energy ε' in the rest frame of the CR [23]. The Mandelstam invariant,

$$s = m^2 + 2m\varepsilon' = m^2 + 2(E\varepsilon - \mathbf{k} \cdot \mathbf{p}), \quad (115)$$

relates quantities in the rest frame of the UHECR and the CMB frame, respectively. This leads to

$$\varepsilon' = \frac{E\varepsilon - \mathbf{k} \cdot \mathbf{p}}{m} = \frac{E}{m} \varepsilon (1 - \frac{p}{E} \cos \theta) = \gamma \varepsilon (1 - v \cos \theta) \quad (116)$$

and

$$d\varepsilon' = -\gamma \varepsilon v d \cos \theta, \quad (117)$$

where $m = A$ GeV, $k = \varepsilon$, $p/E = v$.

We begin discussing the energy loss by considering UHECR collisions with the pervasive photon backgrounds permeating the universe. After that, when we discuss the potential classes of sources which are able to emit UHECRs in our cosmic backyard, we will address the limitation of CR collisions with thermal photons inside the acceleration region.

3.2.2. Opacity of the CMB to UHECR protons

On the way to Earth, UHECR protons degrade their energy through Bethe-Heitler (BH) pair production and photopion production, each successively dominating as the proton energy increases. The fractional energy loss due to interactions with the universal photon fields at a redshift $z = 0$ is determined by the integral of the proton energy loss per collision multiplied by the probability per unit time for a proton

collision in an isotropic gas of photons [259]. Introducing the inelasticity in (114), this integral can be explicitly written as

$$\begin{aligned} -\frac{1}{E} \frac{dE}{dt} &= \frac{1}{2\gamma^2} \sum_j \int_0^\infty d\varepsilon n_j(\varepsilon) \frac{1}{\varepsilon^2} \int_0^\infty d\varepsilon' \langle y(\varepsilon') \rangle_j \sigma_j(\varepsilon') \varepsilon' \Theta(2\gamma\varepsilon - \varepsilon') \\ &= \frac{1}{2\gamma^2} \sum_j \int_0^\infty d\varepsilon' \langle y(\varepsilon') \rangle_j \sigma_j(\varepsilon') \varepsilon' \int_{\frac{\varepsilon'}{2\gamma}}^\infty d\varepsilon n_j(\varepsilon) \frac{1}{\varepsilon^2} \end{aligned} \quad (118)$$

where ε' is the photon energy in the rest frame of the nucleon, $\langle y(\varepsilon') \rangle_j$ is the average fraction of the energy lost by the nucleon for the j th reaction channel, $n_j(\varepsilon)d\varepsilon$ stands for the number density of photons with energy between ε and $\varepsilon + d\varepsilon$, $\sigma_j(\varepsilon')$ is the total cross section of the j th interaction channel, and γ is the Lorentz factor of the nucleon. The sum is carried out over all relevant channels: $p\gamma \rightarrow pe^+e^-$, $p\gamma \rightarrow \pi^0p$, $p\gamma \rightarrow \pi^+n$, $p\gamma \rightarrow \text{multi-}\pi p$, and $p\gamma \rightarrow \text{multi-}\pi n$.

Pair production and photopion production processes are only of importance for interactions with the CMB (collisions with optical and infrared photons give a negligible contribution) [260, 261]. For interactions with the CMB, the photon density is that of a Planck spectrum

$$n(\varepsilon) = (\varepsilon/\pi)^2 [e^{\varepsilon/T} - 1]^{-1}, \quad (119)$$

and so the fractional energy loss is given by

$$-\frac{1}{E} \frac{dE}{dt} = -\frac{T}{2\pi^2\gamma^2} \int_{\varepsilon'_{\text{th}}}^\infty d\varepsilon' \sigma_j(\varepsilon') \langle y(\varepsilon') \rangle_j \varepsilon' \ln \left[1 - e^{-\varepsilon'/(2\gamma T)} \right], \quad (120)$$

where ε'_{th} is the threshold energy in the rest frame of the nucleon and $T = 2.7255(6)$ K [262].

For $E \lesssim 10^9$ GeV, the BH pair production process proceeds through the ‘‘high-energy’’ photons on the tail of the Planck distribution. Hence, the inelasticity and the cross section can be approximated by their values at threshold; i.e., $\langle y \rangle = 2m_e/m_p$ and $\sigma(\varepsilon') = \frac{\pi}{12} \alpha r_0^2 (\varepsilon'/m_e - 2)^3$, where α is the fine structure constant, r_0 is the classical radius of the electron, m_e and m_p the mass of the electron and the proton [260, 261]. This leads to

$$-\frac{1}{E} \frac{dE}{dt} = \frac{16}{\pi} \frac{m_e}{m_p} \alpha r_0^2 T^3 \left(\frac{\gamma T}{m_e} \right)^2 \exp \left(-\frac{m_e}{\gamma T} \right). \quad (121)$$

At higher energies, say $E \gtrsim 10^{10}$ GeV, the characteristic time for the energy loss due to pair production is $-E/(dE/dt) \approx 5 \times 10^9$ yr [263, 264], and the photopion production processes $p\gamma \rightarrow p\pi^0$ and $p\gamma \rightarrow \pi^+n$ give the main contribution to proton energy loss. The cross sections of these processes are well known and the kinematics is simple.

Photopion production turns on at a photon energy in the proton rest frame of 145 MeV with a strongly increasing cross section at the $\Delta(1232)$ resonance, which decays into the one pion channels π^+n and π^0p . With increasing energy, heavier baryon resonances occur and the proton (or instead a neutron) might reappear only after successive decays of resonances [265]. The most important channel of this kind is $p\gamma \rightarrow \Delta^{++}\pi^-$ with intermediate Δ^{++} states leading finally to $\Delta^{++} \rightarrow p\pi^+$. Δ^{++} examples in this category are the $\Delta(1620)$ and $\Delta(1700)$ resonances. The cross section in this region can be described by either a sum or

a product of Breit-Wigner distributions over the main resonances produced in $p\gamma$ collisions considering final states with pions, kaons, and a single nucleon: πN , $\pi\pi N$ and $K\Lambda$ ($\Lambda \rightarrow N\pi$) [11]. At high energies, $3.0 \text{ GeV} < \varepsilon' < 183 \text{ GeV}$, the CERN-HERA and COMPAS Groups have made a fit to the $p\gamma$ cross section [266]. The parameterization is

$$\sigma(\varepsilon') = A + B \ln^2 \left(\frac{\varepsilon'}{\text{GeV}} \right) + C \ln \left(\frac{\varepsilon'}{\text{GeV}} \right) \text{ mb}, \quad (122)$$

where $A = 0.147 \pm 0.001$, $B = 0.0022 \pm 0.0001$, and $C = -0.0170 \pm 0.0007$.

We turn now to the kinematics of proton-photon interactions. The inelasticity $\langle y \rangle$ depends not only on the outgoing particles but also on the kinematics of the final state. Nevertheless, averaging over final state kinematics leads to a good approximation of $\langle y \rangle$. The c.m. system quantities (denoted by $*$) are determined from the relativistic invariance of the square of the total 4-momentum $p_\mu p^\mu$ of the proton-photon system. From (115), this invariance leads to the relation

$$s = (\varepsilon^* + E^*)^2 = m_p^2 + 2m_p \varepsilon'. \quad (123)$$

The c.m. system energies of the particles are uniquely determined by conservation of energy and momentum. For $p\gamma \rightarrow p\pi$, the mean energy of the outgoing proton and pion are given by

$$\langle E_p^* \rangle = \frac{(s + m_p^2 - m_\pi^2)}{2\sqrt{s}} \quad (124a)$$

and

$$\langle E_\pi^* \rangle = \frac{(s + m_\pi^2 - m_p^2)}{2\sqrt{s}}, \quad (124b)$$

or in the lab frame by

$$\langle E_p \rangle = \gamma_{\text{c.m.}} \frac{(s + m_p^2 - m_\pi^2)}{2\sqrt{s}} = \frac{E(s + m_p^2 - m_\pi^2)}{2s} \quad (125a)$$

and

$$\langle E_\pi \rangle = \gamma_{\text{c.m.}} \frac{(s + m_\pi^2 - m_p^2)}{2\sqrt{s}} = \frac{E(s + m_\pi^2 - m_p^2)}{2s}, \quad (125b)$$

where $\gamma_{\text{c.m.}} = (E + \varepsilon)/\sqrt{s} \simeq E/\sqrt{s}$ is the Lorentz factor between the c.m. and lab frames [259]. The mean inelasticity is given by

$$\langle y(\varepsilon') \rangle = 1 - \frac{\langle E_p \rangle}{E} = \frac{1}{2} \left(1 + \frac{m_\pi^2 - m_p^2}{m_p^2 + 2m_p \varepsilon'} \right). \quad (126)$$

It is well established experimentally that at very high energies ($\sqrt{s} \gtrsim 3 \text{ GeV}$) the incoming particles lose only one-half their energy via pion photoproduction independently of the number of pions produced, i.e., $\langle y \rangle \sim 1/2$ [267]. This *leading particle effect* is consistent with (126).

Numerical integration of (120) is carried out taking into account the aforementioned resonance decays and the production of multipion final states at high c.m. energies. For $\sqrt{s} < 2 \text{ GeV}$, a χ^2 fit of the numerical results, using the exponential behavior

$$-\frac{1}{E} \frac{dE}{dt} = A \exp[-B/E] \quad (127)$$

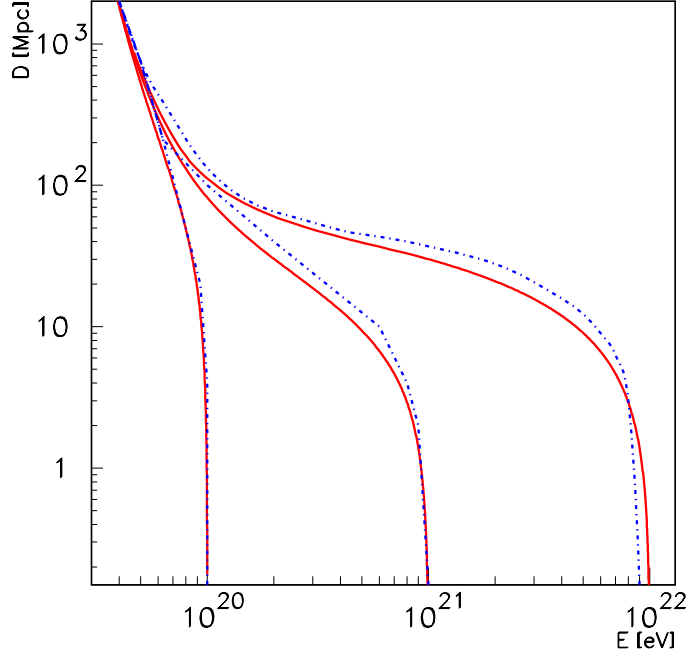


Figure 14: Energy attenuation length of protons in the intergalactic medium. The solid-lines indicate the results from the continuous energy loss approximation, whereas the dashed-lines correspond to the results of a Monte Carlo simulation [264]. Note that after a distance of ~ 100 Mpc, or propagation time $\sim 3 \times 10^8$ yr, the mean energy is essentially independent of the initial energy of the protons, with a critical energy around 10^{20} eV. From Ref. [271].

derived in [261] approximating both the cross section and the fractional energy loss by their threshold values, gives

$$A = (3.66 \pm 0.08) \times 10^{-8} \text{ yr}^{-1} \text{ and } B = (2.87 \pm 0.03) \times 10^{11} \text{ GeV}, \quad (128)$$

with $\chi^2/\text{dof} = 3.9/10$ [268, 269]. The fractional energy loss due to production of multipion final states at higher c.m. energies ($\sqrt{s} \gtrsim 3$ GeV) is roughly a constant,

$$-\frac{1}{E} \frac{dE}{dt} = C = (2.42 \pm 0.03) \times 10^{-8} \text{ yr}^{-1}. \quad (129)$$

From the values determined for the fractional energy loss, it is straightforward to compute the energy degradation of UHECRs in terms of their flight time. This is given by,

$$At - \text{Ei}(B/E) + \text{Ei}(B/E_0) = 0, \quad \text{for } 10^{10} \text{ GeV} \lesssim E \lesssim 10^{12} \text{ GeV}, \quad (130)$$

and

$$E(t) = E_0 \exp[-Ct], \quad \text{for } E \gtrsim 10^{12} \text{ GeV}, \quad (131)$$

where $\text{Ei}(x)$ is the exponential integral [270]. In Fig. 14 we show the proton energy degradation as a function of the mean flight distance. It is evident from this figure that the CR energy degradation resulting from the preceding semi-analytic calculation within the context of a continuous energy loss approximation is consistent with that obtained through numerical simulations [264]. Note that independent of the initial energy, the mean energy values approach 10^{11} GeV after the proton propagates a distance of about 100 Mpc.

3.2.3. Photonuclear interactions

The relevant mechanisms for the energy loss that extremely high energy nuclei suffer during their trip to Earth are: Compton interactions, pair production in the field of the nucleus, photodisintegration, and hadron photoproduction. The Compton interactions have no threshold energy. In the nucleus rest-frame, pair production has a threshold at ~ 1 MeV, photodisintegration is particularly important at the peak of the GDR (15 to 25 MeV), and photomeson production has a threshold energy of ~ 145 MeV.

Compton interactions result in only a negligibly small energy loss for the nucleus given by

$$-\frac{dE}{dt} = \frac{Z^4}{A^2} \epsilon_\gamma \left(\frac{E}{Am_p} \right)^2 \text{ eV s}^{-1} \quad (132)$$

where ϵ_γ is the energy density of the ambient photon field in eV cm^{-3} [24]. The energy loss rate due to photopair production is Z^2/A times higher than for a proton of the same Lorentz factor [272], whereas the energy loss rate due to photomeson production remains roughly the same. The latter is true because the cross section for photomeson production by nuclei is proportional to the baryon number A [273], while the inelasticity is proportional to $1/A$. However, it is photodisintegration rather than photopair and photomeson production that determines the energetics of UHECR nuclei. During this process some fragments of the nuclei are released, mostly single neutrons and protons [274, 275]. Experimental data of photonuclear interactions are consistent with a two-step process: photoabsorption by the nucleus to form a compound state, followed by a statistical decay process involving the emission of one or more nucleons, followed by immediate photo-emission from the excited daughter nuclei. For brevity, we label the photonuclear process $A_i\gamma \rightarrow A_f^*N$, followed by $A_f^* \rightarrow A_f + \gamma$ -ray as “ A^* .” In the energy region which extends from threshold for single-nucleon emission ~ 10 MeV up to ~ 30 MeV the GDR dominates the A^* process. The GDR typically de-excites by the statistical emission of a single nucleon. Above the GDR region, and up to the photo-pion production threshold, the non-resonant A^* processes provide a much smaller cross section with a relatively flat dependence on energy. The photodisintegration cross section for all the different nuclear species has been obtained through a direct fit to data [24, 276, 277]; the associated uncertainties have been studied in [278].

For $A > 4$ the cross section for losing one nucleon can be described by a Breit-Wigner form

$$\sigma_A(\varepsilon') = \begin{cases} \sigma_0 \frac{\varepsilon'^2 \Gamma^2}{(\varepsilon_0^2 - \varepsilon'^2)^2 + \varepsilon'^2 \Gamma^2} & \text{for } \varepsilon' \leq 30 \text{ MeV} \\ \frac{A}{8} \text{ mb} & \text{for } \varepsilon' > 30 \text{ MeV} \end{cases}, \quad (133)$$

where $\Gamma = 8$ MeV is the width, $\varepsilon_0 = 42.65 A^{-0.21}$ MeV is the central value of the GDR energy band, and $\sigma_0 = 1.45 A$ mb is the normalization [279]. The GDR cross section can be safely approximated by the single pole of the narrow-width approximation (NWA),

$$\sigma_A(\varepsilon') = \varpi \delta(\varepsilon' - \varepsilon_0), \quad (134)$$

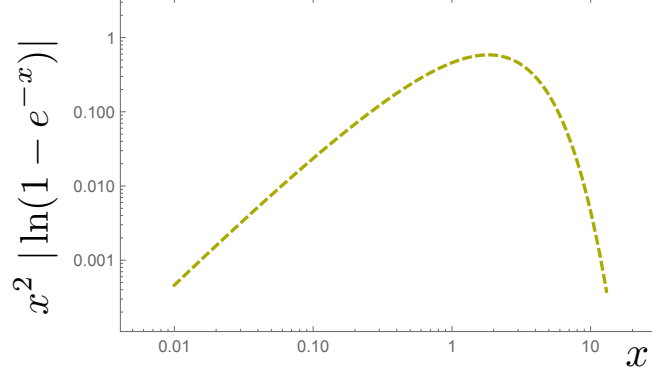
where $\varpi = \pi \sigma_0 \Gamma/2$; the factor of 1/2 is introduced to match the integral (i.e. total cross section) of the Breit-Wigner and the delta function [280].

For $A \leq 4$, the photodisintegration cross section can be described by the shifted log-normal distribution,

$$\sigma_A(\varepsilon') = \sigma_0 \exp \left\{ -\frac{\ln^2 [(\varepsilon' - \varepsilon'_{\text{th}})/(\varepsilon_0 - \varepsilon'_{\text{th}})]}{2\Gamma^2} \right\}, \quad (135)$$

Table 2: Parameters of the photo-disintegration cross-section.

A	σ_0 (mb)	ε_0 (MeV)	ε'_{th} (MeV)	Γ	ϖ (mb MeV)
4	3.22 ± 0.05	26.6 ± 0.4	20.1 ± 0.4	0.94 ± 0.08	77 ± 3
3	1.82 ± 0.05	15.3 ± 0.4	5.1 ± 0.2	0.93 ± 0.04	67 ± 2
2	2.60 ± 0.09	3.87 ± 0.09	2.42 ± 0.05	1.48 ± 0.04	42.2 ± 0.4


 Figure 15: The scaling functions $x^2 |\ln(1 - e^{-x})|$, proportional to the photodisintegration rate in (140). Adapted from [282].

where ε_0 is the central value of the GDR energy band (with threshold ε'_{th}), σ_0 is the cross section at $\varepsilon = \varepsilon_0$, and Γ is a measurement of the dispersion around ε_0 ; the cross section parameters are given in Table 2 [281]. For analytical order of magnitude estimates, the cross section can take the form (134) of the NWA, with $\varpi = \sqrt{2\pi} \sigma_0 \Gamma (\varepsilon_0 - \varepsilon'_{\text{th}}) e^{\Gamma^2/2}$.

The general formula for the inverse photodisintegration mean-free-path (mfp) for a highly relativistic nucleus with energy $E = \gamma A$ GeV propagating through an isotropic photon background with energy ε and spectrum $n(\varepsilon)$ is given by

$$\lambda^{-1}(A) = \frac{1}{2\gamma^2} \int_0^\infty \frac{n(\varepsilon)}{\varepsilon^2} d\varepsilon \int_{\varepsilon'_{\text{th}}}^{2\gamma\varepsilon} \varepsilon' \sigma(\varepsilon') d\varepsilon', \quad (136)$$

where ε'_{th} is the GDR energy threshold. Note that $\lambda(A) = \tau(A)$ is also the mean survival time, so $\lambda^{-1}(A)$ is also the photodisintegration rate per nucleus $R(A)$ given in (114). The outer integral running over $\varepsilon \in [0, \infty)$ can be splitted into two parts, $\varepsilon \in [0, \varepsilon'_{\text{th}}/(2\gamma)]$ and $\varepsilon \in [\varepsilon'_{\text{th}}/(2\gamma), \infty)$, and so (136) can be rewritten as

$$\lambda^{-1}(A) = \frac{1}{2\gamma^2} \int_0^{\varepsilon'_{\text{th}}/2\gamma} \frac{n(\varepsilon)}{\varepsilon^2} d\varepsilon \int_{\varepsilon'_{\text{th}}}^{2\gamma\varepsilon} \varepsilon' \sigma(\varepsilon') d\varepsilon' + \frac{1}{2\gamma^2} \int_{\varepsilon'_{\text{th}}/2\gamma}^\infty \frac{n(\varepsilon)}{\varepsilon^2} d\varepsilon \int_{\varepsilon'_{\text{th}}}^{2\gamma\varepsilon} \varepsilon' \sigma(\varepsilon') d\varepsilon'. \quad (137)$$

Note that the first term has no contribution to $\lambda^{-1}(A)$, because since $\varepsilon \in [0, \varepsilon'_{\text{th}}/(2\gamma)]$ the upper limit of the integral over $d\varepsilon'$ remains always below the cross section energy threshold, i.e., $0 \leq 2\gamma\varepsilon \leq \varepsilon'_{\text{th}}$.

Inserting (134) into (137) the integral over $d\varepsilon'$ becomes

$$\begin{aligned} \int_{\varepsilon'_{\text{th}}}^{2\gamma\varepsilon} \varepsilon' \sigma(\varepsilon') d\varepsilon' &= \int_{-\infty}^{+\infty} \Theta(\varepsilon' - \varepsilon'_{\text{th}}) \Theta(2\gamma\varepsilon - \varepsilon') \varepsilon' \sigma(\varepsilon') d\varepsilon' \\ &= \varpi \int_{-\infty}^{+\infty} \Theta(\varepsilon' - \varepsilon'_{\text{th}}) \Theta(2\gamma\varepsilon - \varepsilon') \varepsilon' \delta(\varepsilon' - \varepsilon_0) d\varepsilon' = \varpi \Theta(2\gamma\varepsilon - \varepsilon_0) \varepsilon_0, \end{aligned} \quad (138)$$

because $\Theta(\varepsilon_0 - \varepsilon'_{\text{th}}) = 1$ for $\varepsilon_0 > \varepsilon'_{\text{th}}$. This means that in the NWA the reciprocal mfp is given by

$$\lambda^{-1}(A) = \frac{\varpi \varepsilon_0}{2\gamma^2} \int_{\frac{\varepsilon'_{\text{th}}}{2\gamma}}^{\infty} \frac{n(\varepsilon)}{\varepsilon^2} \Theta(2\gamma\varepsilon - \varepsilon_0) d\varepsilon = \frac{\varpi \varepsilon_0}{2\gamma^2} \int_{\frac{\varepsilon_0}{2\gamma}}^{\infty} \frac{n(\varepsilon)}{\varepsilon^2} d\varepsilon \quad (139)$$

because $(2\gamma\varepsilon - \varepsilon_0) > 0$ for $\varepsilon > \varepsilon_0/(2\gamma)$. For a nucleus passing through a region where the photon density is described by a Bose-Einstein distribution (119), the photodisintegration rate is given by

$$\lambda_{\text{BE}}^{-1}(A) \approx \frac{\varpi \varepsilon_0 T}{2\gamma^2 \pi^2} |\ln(1 - e^{-\varepsilon_0/2\gamma T})| = \frac{2 \varpi T^3}{\pi^2 \varepsilon_0} x^2 |\ln(1 - e^{-x})|, \quad (140)$$

where we have defined a dimensionless scaling variable $x \equiv \varepsilon_0/(2\gamma T)$. From the pre-factor, we learn that for $A > 4$ the peak of $\lambda_{\text{BE}}^{-1}(A)$ scales in A as $\sigma_0/\varepsilon_0 \sim A^{1.21}$, and the value of γ at the peak scales as $\varepsilon_0 \sim A^{-0.21}$. The scaling function $x^2 |\ln(1 - e^{-x})|$ is shown in Fig. 15. Approximations to the $|\ln|$ term yield e^{-x} for $x > 2$, and $|\ln x|$ for $x \ll 1$. Thus, the exponential suppression of the process appears for $\varepsilon_0 > 4\gamma T$, and the small x region presents a mfp that scales as $x^2 |\ln x|$. The peak region provides the smallest inverse mfp, and so this region dominates the A^* -process. In the peak region, x is of order one, which implies that $2\gamma T \sim \varepsilon_0$. When this latter relation between the nuclei boost and the ambient photon temperature is met, then the photo-disintegration rate is optimized.

In Fig. 16 we show the nucleus mfp from a numerical integration of (136) using precise cross section curves fitted to data for single-nucleon and multi-nucleon emission. For the nitrogen, silicon, and iron calculations we adopted a numerical integration of ‘‘TALYS-1.6 (restored)’’ cross sections (as described in Appendix A of [283]), using the optical and infrared backgrounds estimated in [284], as well as the CMB Planckian spectrum. For helium, we used the fit to photodisintegration cross section data of [281]. For iron nuclei, $\varepsilon_0 \sim 18$ MeV, and since the CMB temperature is $T \sim 0.2348$ meV the maximum of the scaling function $x \sim 1$ corresponds to a Lorentz factor $\gamma \sim 10^{10.6}$. The critical value of the scaling function, $x < 2$, implies that interactions with the CMB are exponentially suppressed for $\gamma < 10^{10.3}$. These phenomenological estimates are visible in Fig. 16. Actually, for $10^9 \lesssim \gamma \lesssim 10^{9.5}$ interactions with the infrared background dominate the A^* -rate for iron nuclei, and the approximation given in (140) breaks down. This corresponds to $E \lesssim 10^{11.2}$ GeV.

For $2 \times 10^{-3} < \varepsilon/\text{eV} < 0.8$, the spectral density of the cosmic infrared background can be parametrized by [285]

$$n(\varepsilon) \simeq 1.1 \times 10^{-4} \left(\frac{\varepsilon}{\text{eV}} \right)^{-2.5} \text{cm}^{-3} \text{eV}^{-1}. \quad (141)$$

A comparison of this parametrization and the estimate of $n(\varepsilon)$ given in [284] is shown in Fig. 17. Substitution of (141) into (139) leads to the mfp of a nucleus scattering off the infrared photons

$$\lambda^{-1}(A) \approx \frac{\varpi \varepsilon_0}{2\gamma^2} \int_{\frac{\varepsilon_0}{2\gamma}}^{\varepsilon_{\text{max}}} \frac{n(\varepsilon)}{\varepsilon^2} d\varepsilon \sim 8.4 \times 10^{20} \left(\frac{\sigma_0}{\text{cm}^2} \right) \left(\frac{\Gamma}{\text{eV}} \right) \left(\frac{\varepsilon_0}{\text{eV}} \right)^{-2.5} \gamma^{1.5} \text{Mpc}^{-1}, \quad (142)$$

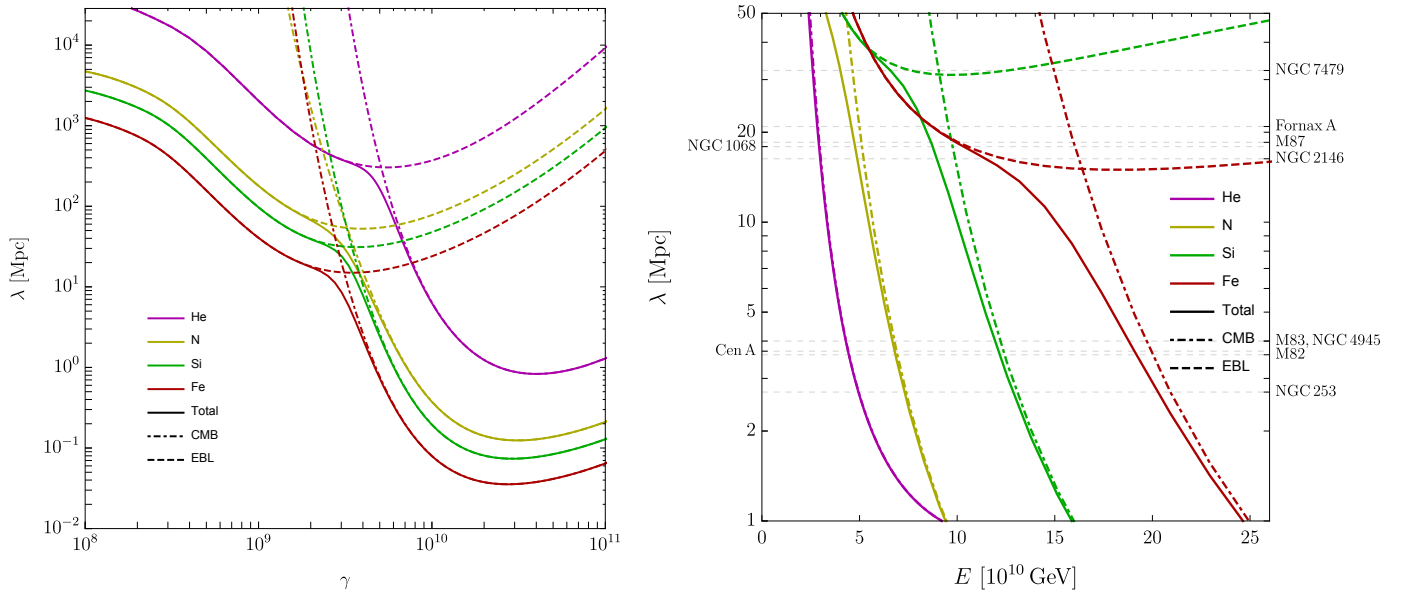


Figure 16: Photodisintegration mfp on the CMB and EBL as a function of the Lorentz factor γ (left) and nucleus energy E (right). The horizontal dashed lines indicate the distance to nearby starbursts and radio-galaxies. This figure is courtesy of Jorge Fernandez Soriano.

where $\varepsilon_{\max} = 0.8$ eV. Note that $\varepsilon_{\min} = 2 \times 10^{-3}$ eV sets an upper bound on the nucleus Lorentz factor, $\gamma < \varepsilon_0 / (2\varepsilon_{\min})$. For an iron nucleus, this translates to $\gamma < 4.5 \times 10^9$ or equivalently $E < 10^{11.4}$ GeV.

At this stage it is worthwhile to point out that since the Lorentz factor is conserved in the photodisintegration process, the surviving fragment A_f sees the photons of the thermal background at the same energy of the parent nucleus A_i . This implies that A_f would never reach the GDR threshold and the A^* process must continue until the primary nucleus photodisintegrates completely. In contrast, the BH pair production and photopion production processes, involve the creation of new particles that carry off energy, yielding baryons with energies ever closer to the photopion or pair production thresholds. This implies that if UHECRs are dominantly protons and the observed suppression originates in the GZK interactions, then an enhancement of the flux (visible as a bump in the spectrum) would occur before the GZK cutoff as a consequence of the pile-up of energy degraded protons recoiling down from higher energies and ending up approximately below threshold to undergo further photoproduction reactions [286, 287]. Although nuclei undergoing photodisintegration never reach the threshold of the GDR, a bump in the spectrum would be expected, too [288]. The source of the bump originates in a distinct property of the photodisintegration process: after the same propagation distance, the surviving fragments of two identical nuclei of baryon number A emitted with different energies can reach the Earth with the same energy, but different baryon number. Therefore, the observation of a bump in the spectrum (just before the cutoff) will be a clear indication that GZK interactions are at play.

During the A^* process, production of e^+e^- pairs tend to reduce the nucleus Lorentz factor and mitigate the rate of photodisintegration. For $10^{10.5} \lesssim E/\text{GeV} \lesssim 10^{11.5}$ and propagation distances $\lesssim 50$ Mpc, the effect of e^+e^- pair and photopion production can be safely neglected [263]. One sees in Fig. 16 that for $E > E_{\text{supp}}$, the interaction mfp decreases rapidly with increasing energy, and increases rapidly with increasing nuclear composition:

- at $E = 10^{10.7}$ GeV, the mfp for ionized helium (^4He) is about 3 Mpc, while at $10^{10.9}$ GeV it is nil;

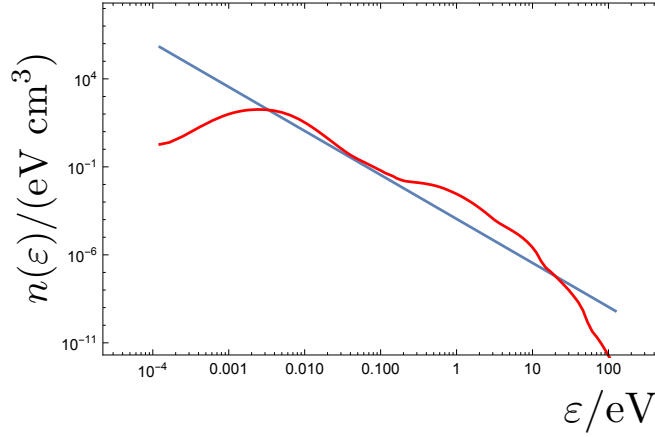


Figure 17: Comparison of the density of infrared photons as parametrized in (141) and estimated in [284].

- at $E = 10^{10.9}$ GeV, the mfp for ionized nitrogen (^{14}N) is about 4 Mpc, while at 10^{11} GeV it is nil;
- at $E = 10^{11.1}$ GeV, the mfp for ionized silicon (^{28}Si) is about 2.5 Mpc, while at $10^{11.2}$ GeV it is nil;
- etcetera, until finally we reach ionized iron (^{56}Fe) where the mfp at $E = 10^{11.3}$ GeV is about 3 Mpc, while at $10^{10.4}$ GeV it too is nil.

Altogether, the nearby Universe behaves as a *cosmic mass spectrometer* [154]. From sources at increasing distance, fewer and heavier nuclei at highest energies are expected to reach Earth. The main features in the energy evolution of the abundance of various nuclear species on Earth can be summarized as follows:

- the contribution of ^4He should decrease with rising energy and then essentially disappear above about $10^{10.8}$ GeV;
- on average, only species heavier than ^{14}N can contribute to the observed flux on Earth above 10^{11} GeV, with nuclear species lighter than ^{28}Si highly suppressed at $10^{11.2}$ GeV;
- the mean flux of iron nuclei becomes suppressed somewhat below $10^{11.4}$ GeV.

The three considerations enumerated above are similar to those obtained assuming a continuous source distribution, with cutoff at about 3 Mpc [289–291].

In the limit of small deflections (expected for nG field strength [131]) the typical deflection of UHECRs in the extragalactic magnetic field can be estimated to be

$$\delta\theta_{\text{extragalactic}} \approx 1.5^\circ Z \sqrt{\frac{d}{3.8 \text{ Mpc}} \frac{\lambda}{0.1 \text{ Mpc}} \left(\frac{B}{\text{nG}}\right) \left(\frac{E}{10^{10} \text{ GeV}}\right)^{-1}}, \quad (143)$$

where d is the source distance, Z is the charge of the UHECR in units of the proton charge, and λ the magnetic field coherence length [292, 293]. It is then reasonable to assume that extragalactic deflections would generally be much smaller than those arising from the Galactic magnetic field.

The Galactic magnetic field is not well constrained by current data, but if we adopt our benchmark JF model [116–118] typical values of the deflections of UHECRs crossing the Galaxy are

$$\delta\theta_{\text{Galactic}} \sim 10^\circ Z \left(\frac{E}{10^{10} \text{ GeV}}\right)^{-1}, \quad (144)$$

depending on the direction considered [294]. When the average magnetic field deflection is combined with the energy loss during propagation shown in Fig. 16 one can anticipate that the energy dependence of the hot-spot contour produced by a pure-proton source would be different from that of a source emitting a mixed composition of nuclei [154]. The difference can be easily pictured when considering the main properties characterizing the acceleration and propagation of a nucleus of charge Ze and baryon number A : (i) the maximum energy of acceleration capability of the sources grows linearly in Z , (ii) the energy loss per distance traveled decreases with increasing A , and (iii) the bending of the cosmic ray decreases as Z/E with rising energy. This implies that the pointing of UHECR nuclei to their nearest extragalactic sources would only be expected for $10^{10.6} \lesssim E/\text{GeV} \lesssim 10^{11}$. Actually, the less deflected ${}^4\text{He}$ nuclei could only contribute to the anisotropy hot-spot if $E \lesssim 10^{10.8}$ GeV. In contrast, sources of UHECR protons exhibit anisotropy patterns which become denser and compressed with rising energy. An intuitive description with analogy to the peeling of an onion, which portrays the hot-spot differences, is as follows: while peeling a hot-spot produced by a pure-proton source one would be probing higher and higher energies, whereas when peeling a hot-spot produced by source that emits a mixed-composition of nuclei one would be probing lower and lower energies. When effects of the regular component of the Galactic magnetic field are included, the hot-spots are elongated depending on their location in the sky [161]. Stock-still the variation in (shape and size) of the expected “squeezed onion layers” provides a powerful discriminator of the baryonic composition.

A point worth recalling at this juncture is that the TS scan over the threshold energy in the most recent Auger anisotropy analysis gives a maximum signal for SBGs when considering UHECRs with $E > 39$ EeV and for γ AGNs when considering UHECRs with $E > 60$ EeV [3]. Then the previous considerations on the energy dependence of the hot-spot contour allows one to speculate that γ AGNs are most likely associated with pure-proton sources, while SBGs are more likely sources emitting a mixed composition of nuclei.

3.3. Plausible sources in our cosmic backyard

3.3.1. γ AGNs

AGNs are composed of an accretion disk around a central super-massive black hole and are sometimes associated with jets terminating in lobes, which can be detected in radio. One can classify these objects into two categories: radio-quiet AGN with no prominent radio emission nor jets, and radio-loud objects presenting jets. All of the AGNs with MeV-GeV-TeV γ -ray emission identified so far are radio-loud galaxies.

Fanaroff-Riley II (FR II) galaxies [295] are a sub-class of radio-loud sources. Localized regions of intense synchrotron emission, known as hot-spots, are observed within their lobes. These regions are presumably produced when the bulk kinetic energy of the jets ejected by a central active nucleus is reconverted into relativistic particles and turbulent fields at a *working surface* in the head of the jets [296]. Specifically, the speed $u_{\text{head}} \approx u_{\text{jet}} [1 + (n_e/n_{\text{jet}})^{1/2}]^{-1}$, with which the head of a jet advances into the intergalactic medium of particle density n_e can be obtained by balancing the momentum flux in the jet against the momentum flux of the surrounding medium; where n_{jet} and u_{jet} are the particle density and the velocity of the jet flow, respectively (for relativistic corrections, see [297]). For $n_e \geq n_{\text{jet}}$, $u_{\text{jet}} > u_{\text{head}}$ so that that the jet decelerates. The result is the formation of a strong collisionless shock, which is responsible for particle reacceleration and magnetic field amplification [298]. The acceleration of particles up to ultrarelativistic energies in the hot-spots is the result of repeated scattering back and forth across the shock front, similar to that discussed in Sec. 3.1.3. The particle deflection in this mechanism is dominated by the turbulent magnetic field with wavelength k equal to the Larmor radius of the particle concerned [238]. A self-consistent (although possibly

not unique) specification of the turbulence is to assume that the energy density per unit of wave number of MHD turbulence is of the Kolmogorov type, $I(k) \propto k^{-5/3}$, just as for hydrodynamical turbulence [299]. With this in mind, to order of magnitude accuracy using effective quantities averaged over upstream (jet) and downstream (hot-spot) conditions (considering that downstream counts a fraction of 4/5) the acceleration timescale at a shock front is found to be

$$\left(\frac{1}{E} \frac{dE}{dt}\right)^{-1} \sim \frac{20 D_K(E)}{u_{\text{jet}}^2}, \quad (145)$$

where

$$D_K(E) = \frac{2}{\pi \varrho} \left(\frac{E}{ZeB}\right)^{1/3} R^{2/3} \quad (146)$$

is the Kolmogorov diffusion coefficient, ϱ is the ratio of turbulent to ambient magnetic energy density in the region of the shock (of radius R), and B is the total magnetic field strength [201]. Note that (145) follows from (94), (102), and (105) taking a strong shock with compression ratio $\zeta = 4$ (corresponding to $u_{\text{jet}} = u_{\text{head}}/4$) and $D_1 = D_2 = D_K$. On the basis of the discussion given in Sec. 3.2.3, it is reasonable to set $Z = 1$ for γ AGNs.

The acceleration process will be efficient as long as the energy losses by synchrotron radiation and/or pion-producing interactions do not become dominant. The synchrotron loss time for protons is given by

$$-\left(\frac{1}{E} \frac{dE}{dt}\right)^{-1} \sim \frac{6\pi m_p^3 c}{\sigma_T m_e^2 \gamma B^2}, \quad (147)$$

where σ_T is the Thomson cross section and $\gamma = E/m_p$ is Lorentz factor [36, 200].

For typical hot-spot conditions, the number density of photons per unit energy interval follows a power-law spectrum

$$n(\varepsilon) = \begin{cases} (N_r/\varepsilon_r) (\varepsilon/\varepsilon_r)^{-2} & \varepsilon_r \leq \varepsilon \leq \varepsilon_g \\ 0 & \text{otherwise} \end{cases} \quad (148)$$

where N_r is the normalization constant and ε_r and ε_g correspond to radio and gamma rays energies, respectively [200]. Straightforward substitution of (148) into (118) leads to the fractional energy loss due to photopion production

$$-\left(\frac{1}{E} \frac{dE}{dt}\right)^{-1} = \frac{4}{3} N_r \frac{\varepsilon_r}{\varepsilon'_{\text{th}}} \gamma \int_1^\infty \langle y(x\varepsilon'_{\text{th}}) \rangle \sigma(x\varepsilon'_{\text{th}}) x^{-2} dx \sim \frac{2}{3} a \gamma \left[\frac{\langle \sigma_{\gamma p} \rangle}{\ln(\varepsilon_g/\varepsilon_r)} \right] \left(\frac{B^2}{m_p}\right), \quad (149)$$

where

$$a = \frac{N_r \varepsilon_r \ln(\varepsilon_g/\varepsilon_r)}{B^2/2} \quad (150)$$

is the ratio of photon to magnetic energy density,

$$\int_1^\infty \langle y(x\varepsilon'_{\text{th}}) \rangle \sigma(x\varepsilon'_{\text{th}}) x^{-2} dx \sim \frac{m_\pi}{m_p} \langle \sigma_{\gamma p} \rangle \sim 900 \frac{m_\pi}{m_p} \mu\text{b}, \quad (151)$$

and $\varepsilon'_{\text{th}} = m_\pi$ [200]. The time scale of the energy loss for protons, including synchrotron and photon interaction losses, can be approximated by

$$-\left(\frac{1}{E} \frac{dE}{dt}\right)^{-1} \sim \frac{2}{3} \frac{m_p^4}{\sigma_T m_e^2 B^2 (1 + Aa)} E^{-1}, \quad (152)$$

where

$$A = \frac{\langle \sigma_{\gamma p} \rangle}{\sigma_T} \frac{(m_p/m_e)^2}{\ln(\varepsilon_g/\varepsilon_r)} \approx 1.6 \times 10^5 \frac{\langle \sigma_{\gamma p} \rangle}{\sigma_T} \approx 200. \quad (153)$$

gives a measure of the relative strength of γp interactions versus the synchrotron emission. Note that $p\gamma \rightarrow \pi^+ n$ involves the creation of ultrarelativistic neutrons that can readily escape the system and provide a directional signal for nearby sources [300, 301]. The maximum attainable energy can be obtained by balancing the energy gains and losses [302]

$$E = 1.4 \times 10^{16} \left(\frac{B}{\mu\text{G}} \right)^{-5/4} u_{\text{jet}}^{3/2} \varrho^{3/4} \left(\frac{R}{\text{kpc}} \right)^{-1/2} (1 + Aa)^{-3/4} \text{ GeV}, \quad (154)$$

It is of interest to apply the acceleration conditions to the nearest γ AGN. It is this that we now turn to study.

As the closest radio-loud galaxy to Earth, Cen A (identified at optical frequencies with the galaxy NGC 5128) is the perfect *cosmic laboratory* to study the physical processes responsible for UHECR acceleration. Radio observations at different wavelengths have revealed a rather complex morphology of this FRI source [303]. It comprises a compact core, a jet (with subluminal proper motions $u_{\text{jet}} \sim 0.5$ [304]) also visible at X-ray frequencies, a weak counter-jet, two inner lobes, a kpc-scale middle lobe, and two giant outer lobes. The jet would be responsible for the formation of the northern inner and middle lobes when interacting with the interstellar and intergalactic media, respectively. There appears to be a compact structure in the northern lobe, at the extrapolated end of the jet. This structure resembles the hot-spots such as those existing at the extremities of FRII galaxies. However, at Cen A it lies at the side of the lobe rather than at the most distant northern edge, and the brightness contrast (hot-spot to lobe) is not as extreme [305].

EGRET observations of the γ -ray flux for energies > 100 MeV allow an estimate $L_\gamma \sim 10^{41}$ erg s $^{-1}$ for Cen A [306]. This value of L_γ is consistent with an earlier observation of photons in the TeV-range during a period of elevated X-ray activity [307], and is considerably smaller than the estimated bolometric luminosity $L_{\text{bol}} \sim 10^{43}$ erg s $^{-1}$ [303]. During the first 3-months of science operation, the *Fermi*-LAT confirmed the EGRET detection of Cen A [308, 309]. Besides, data from H.E.S.S. have confirmed Cen A as a TeV γ -ray emitting source [310]. Extrapolating the spectrum measured by *Fermi*-LAT in the GeV regime to very-high energies roughly matches the H.E.S.S. spectrum [311]. Data from *Fermi*-LAT established that a large fraction ($> 1/2$) of the total > 100 MeV emission from Cen A emanates from the lobes [312]. However, a combined analysis of H.E.S.S. and *Fermi* data shows that the very-high energy γ -ray emission comes from the core of Cen A with 12σ significance [313].

Estimates of the radio spectral index of synchrotron emission in the hot-spot and the observed degree of linear polarization in the same region suggests that the ratio of turbulent to ambient magnetic energy density in the region of the shock is $\varrho \sim 0.4$ [202]. The broadband radio-to-X-ray jet emission yields an equipartition magnetic field $B \sim 100 \mu\text{G}$ [314].¹¹ The radio-visible size of the hot-spot can be directly measured from the large scale map $R \simeq 2$ kpc [315]. The actual size can be larger because of uncertainties in the angular projection of this region along the line of sight.¹² Substituting these fiducial values in (50)

¹¹The usual way to estimate the magnetic field strength in a radio source is to minimize its total energy. The condition of minimum energy is obtained when the contributions of the magnetic field and the relativistic particles are approximately equal (equipartition condition). The corresponding B -field is commonly referred to as the equipartition magnetic field.

¹²For example, an explanation of the apparent absence of a counter-jet in Cen A via relativistic beaming suggests that the angle of the visible jet axis with respect to the line of sight is at most 36° [305], which could lead to a doubling of the hot-spot radius. It should be remarked that for a distance of 3.4 Mpc, the extent of the entire source has a reasonable size even with this small angle.

and (154) it is easily seen that if the ratio of photon to magnetic energy density $a \lesssim 0.4$, it is plausible that Cen A can accelerate protons up to the maximum observed energies: $E_{p,\max} \sim 10^{11}$ GeV.

In order to ascertain the capability of Cen A to accelerate UHECR protons up to 10^{11} GeV one must crosscheck the lower limit on the rate at which the energy is carried by the out-flowing plasma (110), which must be provided by the source. The minimum total power of the jets inflating the giant lobes of Cen A is estimated to be $\approx 8 \times 10^{43}$ erg/s [205]. This argument provides a conservative upper limit for the magnetic field in the jet with kpc-scale radius, $B \lesssim 50 \mu\text{G}$, and through (50) leads to $E \lesssim 10^{10.7}$ GeV. The jet power required to maintain these extreme B values of $\mathcal{O}(\mu\text{G})$ and R of $\mathcal{O}(\text{kpc})$ can be reached during flaring intervals [205]. Acceleration of UHECR protons up to somewhat beyond 10^{11} GeV is therefore in principle possible during powerful episodes of jet activity.

Alternatively, shear acceleration [316] could help push proton energies up to and beyond 50 EeV [317]. The limb-brightening in the X -ray jet together with the longitudinal magnetic field polarization in the large scale jet might be indicative of internal jet stratification, *i.e.* a fast spine surrounded by slower moving layers. Energetic particles scattered across such a shear flow can sample the kinetic difference in the flow and will naturally experience an additional increase in energy. In particular, protons that diffuse from the inner shock region into the outer shear layers charge-exchange to produce neutrons with $E \sim 10^{11}$ GeV, which would escape the source. Finally, it has been noted that the jet powers in local radio galaxies could feasibly have been different in the past [159]. Indeed, there seems to be evidence in Cen A for enhanced activity within the last ~ 100 Myr [318, 319]. Altogether, one can conclude that Cen A and other nearby radiogalaxies (like M87 and Fornax A) can accelerate protons up to about 10^{11} GeV.

We cannot go without noticing that AGN flares resulting from the tidal disruption of a star or from a disk instability also meet the UHECR acceleration requirements [320]. Interestingly, such tidal disruption events can generate the luminosity required to account for the full-sky UHECR intensity [321], and may accommodate the intermediate scale anisotropies which seem to be emerging in TA and Auger data [152]. However, it is not clear whether they can accommodate the observed mixed composition, which appears to dominate the UHECR intensity above the ankle [322–324].

3.3.2. SBGs

Starbursts are galaxies (sometimes, the term also refers only to particular regions of galaxies) undergoing a large-scale star formation episode. The universal fast star formation in starburst galaxies is directly correlated with the efficient ejection of gas, which is the fuel for star formation. This happenstance generates a galactic-scale superwind, which is powered by the momentum and energy injected by massive stars in the form of supernovae, stellar winds, and radiation [325, 326]. Multi-wavelength observations seem to indicate that these superwinds are genuinely multi-phase: with hot, warm, cold, and relativistic (cosmic rays) phases. These observations also suggest a pervasive development of the hot ($T \sim 10^7$ K) and warm diffuse ionized ($T \sim 10^4$ K) phases. Namely, experiment shows that the hot and warm large-scale supersonic outflows escalate along the rotation axis of the disk to the outer halo area in the form of local chimneys. Such a supersonic outflow, however, does not extend indefinitely. As the superwind expands adiabatically out beyond the confines of the starburst region, its density decreases. At a certain radial distance the pressure would become too small to further support a supersonic flow. Whenever the flow is slowed down to subsonic speed a termination shock stops the superwind. The shocked gas continues as a subsonic flow. The termination shock would remain in steady state as long as the starburst lasts. This set up clearly provides a profitable arena for acceleration of UHECRs [4].

Because of the high prevalence of supernovae, starbursts should possess a large density of newly-born pulsars [327]. Due to their important rotational and magnetic energy reservoirs these young neutron stars, with their metal-rich surfaces, have been explored as a potential engine for UHECR acceleration [176–178]. As we discussed already in Sec. 3.1.2, the combination of the fast star rotation and its strong magnetic field can induce large potential differences in the out-flowing relativistic plasma for UHECR acceleration.

There are numerous indications that long GRBs are extreme supernova events, which arise from the death of massive stars [328]. Starburst galaxies are characterized by high star-formation rates per unit area, of the order of 15 to 20 $M_{\odot} \text{ yr}^{-1} \text{ kpc}^{-2}$ [325]. This is up to several hundred times larger than the characteristic value normally found in gas-rich galaxies like the Milky Way. The observed supernova rate in starbursts is also higher than average, and so it seems only natural to expect a high rate of long GRBs too [329, 330]. However, the star formation rates per unit stellar mass of GRB host galaxies are found to be higher than for typical nearby starburst galaxies [331]. Moreover, stronger and stronger experimental evidence has been accumulating that implies GRB hosts are low mass irregular galaxies and have low metallicity, see e.g. [332–334]. Altogether, this makes the GRB \Leftrightarrow (metal-rich) starburst connection highly unlikely.¹³

The acceleration of particles in starburst galaxies may alternatively proceed in a two-stage process [4]. First, ions are diffusively accelerated at single SNRs within the nuclear region of the galaxy. Energies up to about 50 PeV can be achieved in this stage [336]. Collective plasma motions force the CR gas to stream along from the starburst region. Some nuclei then escape through the disk in opposite directions along the symmetry axis of the system and experience supplementary acceleration at the terminal shock of the galactic-scale superwind. To picture the specifics of diffuse shock acceleration in SBGs, consider a spherical cavity where core-collapse supernovae and stellar winds inject kinetic energy. This kinetic energy then thermalizes and drives a super-heated outflow that escapes the sphere. To a first approximation we ignore gravity, radiative cooling, and other effects [337]. In this approximation energy conservation leads to the asymptotic speed of the outflow

$$u_{\infty} \approx \sqrt{\frac{2\dot{E}_{\text{sw}}}{\dot{M}_{\text{sw}}}} \sim 10^3 \sqrt{\frac{\epsilon}{\beta}} \text{ km s}^{-1}, \quad (155)$$

where \dot{E}_{sw} and \dot{M}_{sw} are respectively the energy and mass injection rates inside the spherical volume of the starburst region, and where β is the mass loading factor, i.e. the ratio of the mass injection rate to the star formation rate. In the second rendition we have scaled the energy injection rate expected from core-collapse supernovae considering a thermalization efficiency ϵ . For this order of magnitude calculation, we have assumed that in total a $100M_{\odot}$ star injects $\mathcal{O}(10^{51} \text{ erg})$ into its surroundings during the wind phase.

As the cavity expands adiabatically a strong shock front is formed on the contact surface with the cold gas in the halo. At the region where this occurs, the inward ram pressure is balanced by the pressure inside the halo, P_{halo} . A point worth noting at this juncture is that the difference in pressure between the disk and the halo manifestly breaks the symmetry, and so the outflowing fluid which escapes from the starburst region features back-to-back chimneys with conic profiles. Rather than considering a spherical shock we assume the outflow cones fill a solid angle Ω , and hence the ram pressure at radius r is found to be

$$P_{\text{ram}} = \frac{\rho_{\text{sw}} u_{\infty}^2}{2} = \frac{\dot{p}_{\text{sw}}}{2\Omega r^2} = \frac{\dot{M}_{\text{sw}} u_{\infty}}{2\Omega r^2} = \frac{\sqrt{2 \dot{E}_{\text{sw}} \dot{M}_{\text{sw}}}}{2\Omega r^2}, \quad (156)$$

¹³Similar considerations apply to hypernova host galaxies [335].

where $\rho_{\text{sw}} = \dot{M}_{\text{sw}}/(\Omega u_{\infty} r^2)$ is the density of the outflow and $\dot{p}_{\text{sw}} = \dot{M}_{\text{sw}} u_{\infty}$ is the asymptotic momentum injection rate of the superwind [338]. The agitated superwind gas inside the shock is in pressure equilibrium with the outside gas at a radius

$$R_{\text{sh}} \sim \sqrt{\frac{\dot{M}_{\text{sw}} u_{\infty}}{2\Omega P_{\text{halo}}}}. \quad (157)$$

In (156) and (157) it was implicitly assumed that the magnetic field is parallel to the shock normal. Recall that for a flow-aligned field, the fluid motion decouples from the field. The termination shock is a steady-state feature, present even if the starburst wind has always been active.

To develop some sense of the orders of magnitude involved, we assume that the prominent M82 typifies the nearby starburst population. For a standard Kroupa initial mass function [339], our archetypal starburst has a star formation rate $\sim 10M_{\odot} \text{ yr}^{-1}$ and a radius of about 400 pc.¹⁴ Hard X-ray observations provide direct observational evidence for a hot-fluid phase. The inferred gas temperature range is $10^{7.5} \lesssim T/\text{K} \lesssim 10^{7.9}$, the thermalization efficiency $0.3 \lesssim \epsilon \lesssim 1$, and the mass loading factor $0.2 \lesssim \beta \lesssim 0.6$. Substituting for ϵ and β into (155) we obtain $1.4 \times 10^3 \lesssim u_{\infty}/(\text{km s}^{-1}) \lesssim 2.2 \times 10^3$ [340]. The warm fluid has been observed through nebular line and continuum emission in the vacuum ultraviolet, as well as through mid- and far-infrared fine-structure line emission excitations [341–344]. High-resolution spectroscopic studies seem to indicate that the warm ($T \sim 10^4$ K) gas has emission-line ratios consistent with a mixture of photo-ionized gas by radiation leaking out of the starburst and shock-heated by the outflowing superwind fluid generated within the starburst [345]. The kinematics of this gas, after correcting for line-of-sight effects, yields an outflow speed of the warm ionized fluid of roughly 600 km s^{-1} . The velocity field, however, shows rapid acceleration of the gas from the starburst itself out to a radius of about 600 pc, beyond which the flow speed is roughly constant. The inferred speed from cold and warm molecular and atomic gas observations [346, 347] is significantly smaller than those observed from the warm ionized phase. This is also the case for the starburst galaxy NGC 253: ALMA observations of CO emission imply a mass loading factor of at least 1 to 3 [348]. However, it is important to stress that the emission from the molecular and atomic gas most likely traces the interaction of the superwind with detached relatively denser ambient gas clouds [325], and as such it is not the best gauge to characterize the overall properties of the superwind plasma [349]. (See [244] for a different perspective.) Herein, we adopt the properties of the hot gas detected in hard X-rays to determine the shock terminal velocity. We take an outflow rate of $\dot{M}_{\text{sw}} \sim 3M_{\odot} \text{ yr}^{-1}$, which is roughly 30% of the star-formation rate ($\beta \sim 0.3$), yielding $\dot{E}_{\text{sw}} \sim 3 \times 10^{42} \text{ erg s}^{-1}$ [325]. For $\Omega \sim \pi$, this leads to $u_{\infty} \sim 1.8 \times 10^3 \text{ km s}^{-1}$ and $R_{\text{sh}} \sim 8 \text{ kpc}$, where we have taken $P_{\text{halo}} \sim 10^{-14} \text{ erg cm}^{-3}$ [350].

Radio continuum and polarization observations of M82 provide an estimate of the magnetic field strength in the core region of $98 \mu\text{G}$ and in the halo of $24 \mu\text{G}$; averaging the magnetic field strength over the whole galaxy results in a mean equipartition field strength of $35 \mu\text{G}$ [351]. Comparable field strengths have been estimated for NGC 253 [352–355] and other starbursts [356]. Actually, the field strengths could be higher if the cosmic rays are not in equipartition with the magnetic field [357–359]. If this were the case, e.g., the magnetic field strength in M82 and NGC 253 could be as high as $300 \mu\text{G}$ [360–362].

The duration of the starburst phenomenon is subject to large uncertainties. The most commonly cited timescale for a starburst is 5 to 10 Myr, comparable to the lifetime of massive stars [363–365]. However, it has been suggested that the starburst phenomenon can be a longer and more global event than related by

¹⁴The initial mass function is an empirical function that describes the distribution of initial masses for a population of stars.

the lifetime of individual massive stars or pockets of intense star formation [366–368]. In this alternative viewpoint the short duration timescales are instead interpreted as a measure of the *flickering* created by currently active pockets of star formation that move around the galaxy. Measuring the characteristics of just one of these flickers reveals much about an individual star formation region but of course does not measure the totality of the starburst phenomenon in the galaxy. If starbursts are indeed a global phenomenon, then the events are longer than the lifecycle of any currently observable massive star or area of intense star formation and the bursts are not instantaneous. An observation that measures currently observable star formation activity will therefore only measure the *flickering* associated with a starburst pocket and not the entire phenomenon. This aspect, frequently denied or not yet sufficiently emphasized, may bring still another rewarding dimension to the problem at hand.

A measurement of the starburst phenomenon in twenty nearby galaxies from direct evaluation of their star formation histories reconstructed using archival Hubble Space Telescope observations suggests the average duration of a starburst is between 450 and 650 Myr [368].

Since the large-scale terminal shock is far from the starburst region, the photon field energy density in the acceleration region drops to values of the order of the CMB. Now, for $E \lesssim 10^{11}$ GeV and $Z \gtrsim 10$, the energy attenuation length $\gtrsim 30$ Mpc [290]. Therefore, we will restrict ourselves to $\tau \lesssim 100$ Myr. This duration range is in good agreement with the overall star formation history of M82 [369, 370] and NGC 253 [371, 372], and it is also consistent with the upper limit on the starburst age of these galaxies derived in [373].

In toto, substituting $u_\infty \sim 1.8 \times 10^3$ km s⁻¹, $B \sim 300$ μ G, and $\tau \sim 40$ Myr into (108) we obtain [209]

$$E \lesssim Z 10^{10} \text{ GeV} . \quad (158)$$

Note that (158) is consistent with the Hillas criterion [171], as the maximum energy of confined baryons at a shock distance of R_{sh} is found to be

$$E \lesssim 10^9 Z \left(\frac{B}{\mu\text{G}} \right) \left(\frac{R_{\text{sh}}}{\text{kpc}} \right) \text{ GeV} . \quad (159)$$

To accommodate a hard emission spectrum, as required by Auger data, the maximum energy at the accelerator is driven by UHECR leakage from the boundaries of the shock (a.k.a. direct escape [242]), which corresponds to $\varkappa(\zeta) = 1/12$ [209].

Note, however, that starburst large-scale superwinds struggle to meet the power constraint (110), because $\dot{E}_{\text{sw}} < 10^{43}$ erg s⁻¹ and they have low shock velocities ($< 10^{3.5}$ km s⁻¹) [159]. Amplified magnetic fields close to the shock, as observed in supernova remnants [374–376], may offer a window to escape this constraint. Theoretical studies seem to indicate that streaming CRs may excite MHD turbulence, at least in principle, to amplify the magnetic field by orders of magnitude from its initial seed value [377–380]. Even though many complex, highly nonlinear microscopic processes remain to be explored, there is the possibility that non-linear interactions between CRs and the magnetic field could provide a peculiar scheme where the CRs themselves provide the magnetic field necessary for their acceleration to ultra-high energies. Whichever point of view one may find more convincing, it seems most conservative at this point to depend on experiment (if possible) to resolve the issue.

Superwinds of galactic-scale have also been observed in the other nearby SBGs contributing to the UHECR correlation signal of Auger [3] and TA [163]. Indeed, it has long been suspected that the observed properties of NGC 4945 can best be understood in the framework of a starburst-driven superwind

scenario [381]. NGC 4945 also hosts of a very peculiar X-ray-luminous AGN that is probably heavily obscured along all lines of sight [382, 383]. Despite the fact this galaxy has an X-ray and H nuclear outflow cone similar to NGC 253, it is lacking in diffuse X-ray or H emission when compared to a starburst of the same *total* galactic bolometric luminosity, $\log L_{X,\text{tot}}/L_{\text{bol}} = -4.25$ [384]. However, the AGN may dominate L_{bol} . If we assume that the diffuse X-ray emission is due to a starburst-driven wind alone, then the starburst must only account for 20% of L_{bol} . In general, the large-scale soft X-ray emission in starburst composite galaxies is consistent with a purely-starburst origin [385–387]. Thus, for a given total bolometric luminosity it appears that supernovae are more effective at driving galactic-scale winds than AGN [388]. This does not imply that AGN-driven galactic winds do not exist. There clearly are galaxies with AGN but lacking starbursts that have galactic-scale (i.e. of order 10 kpc) outflows [389, 390], but their local space density is lower than typical starburst superwind galaxies. Evidence for a galactic-scale superwind has also been observed in NGC 1068 [391], M83 [392, 393], and Circinus [394, 395].

In the TA search for correlations of UHECRs and SBGs, IC 342 provides the second relative source contribution weighted by the directional exposure, whereas M82 provides the leading contribution to the correlation signal [163]. IC 342 is a late-type spiral galaxy and is located at a distance of about 4 Mpc, though derived distances have varied between 2 Mpc and 4 Mpc [396–399]. This discrepancy arises because IC 342 is located close to the galactic disk, and so its light is dimmed by the Milky Way’s intervening clouds. The discrepancy in derived distances to IC 342 must be kept in mind when discussing distance-dependent quantities. High-resolution interferometric observations of the CO and HCN molecules seem to indicate that stellar winds and/or supernova shocks originating in the central starburst region are pushing outward the in-falling molecular gas [400]. X-ray observations with the ROSAT High Resolution Imager support this picture, suggesting that IC 342 may be a starburst galaxy early in its development [401].

3.4. *Fitting simultaneously the UHECR spectrum and its nuclear composition*

Thus far we have concentrated in semi-analytical calculations to elucidate the underlying phenomenology. Given that Auger has been taking high-quality data for over a decade, at this stage it becomes necessary to resort to numerical simulations to acquire enough theoretical precision to interpret the data. The subsequent discussion is based on the ideas developed in [94] to simultaneously fit the UHECR spectrum and its nuclear composition, including effects during CR propagation on the source environment and on the trip to Earth.

The flux and nuclear composition of UHECRs depend on the cosmic distribution of their sources. As our knowledge of source distributions and properties is limited, it is common practice to assume spatially homogeneous and isotropic CR emissions, and compute a mean spectrum based on this assumption. In reality, of course, this assumption cannot be correct, especially at the highest energies where the GZK effect severely limits the number of sources visible to us [402]. It is always interesting to quantify the possible deviation from the mean prediction based on the knowledge we do have on the source density and the possible distance to the closest source populations. This next statistical moment beyond the mean prediction is referred to as the ensemble fluctuation [403]. It depends on, and thus provides information on, the distribution of discrete local sources, source composition, and energy losses during propagation. This ensemble fluctuation in the energy spectrum is one manifestation of the cosmic variance, which should also appear directly through eventual identification of nearby source populations. In fact, once statistics become sufficiently large, it will be interesting to try to identify the ensemble fluctuations in the energy

spectrum [404]. For simplicity, herein consideration will be given to a minimal model (i.e. minimal number of free parameters in the fit) adopting the canonical hypothesis of a uniform source distribution.

The number of UHECR per unit volume and energy in the present universe is equal to the number of particles accumulated during the entire history of the universe and is comprised of both primary particles emitted by the sources and secondaries produced in the photodisintegration process. The co-moving space density of CRs (7) of mass A from a population of uniformly distributed sources with (possibly age-dependent) emission rate per volume $\mathcal{Q}(E', A', t)$ is given by

$$n(E, A, A') \equiv \frac{dN}{dE dV} = \int_E^\infty \int_0^{t_H} \frac{d\mathcal{P}_{AA'}(E', E, t)}{dE} \mathcal{Q}(E', A', t) \xi(t) dE' dt, \quad (160)$$

where the variable t characterizes a particular age of the universe and t_H indicates its present age, and where $d\mathcal{P}_{AA'}/dE$ is the expectation value for the number of nuclei of mass A in the energy interval $(E, E + dE)$ which derive from a parent of mass A' and energy E' emitted at time t . Here, $\xi(t)$ is the ratio of the product of co-moving source density and $\mathcal{Q}(E', A', t)$, relative to the value of that product today. A semi-analytical approximation of $d\mathcal{P}_{AA'}/dE$ indicates that not only the LO single nucleon emission [408], but also NLO corrections from two-nucleon emission are relevant to interpret the high-quality data [409]. Note that $d\mathcal{P}_{AA'}/dE$ includes propagation effects both at the source environment and on the way to Earth.

Two additional assumptions will be exercised to fit the data. Firstly, that the UHECR emission rate is the same for all sources and the spectrum and composition is independent of the age of the universe, so that evolution of the volumetric emission rate with cosmological time can be described by an overall source evolution factor, $\xi(t)$. The cosmological evolution of the source density per co-moving volume is parametrized as

$$n_s(z) = n_0 \xi(z) \quad (161)$$

with $\xi(z=0) = 1$. The evolution of sources follows the star formation rate with

$$\xi(z) = \frac{(1+z)^a}{1 + [(1+z)/b]^c} \quad (162)$$

where $a = 3.26 \pm 0.21$, $b = 2.59 \pm 0.14$, and $c = 5.68 \pm 0.19$ [405]. Secondly, that the emission rate is fairly well described by a power-law spectrum. Under these very general assumptions the source emission rate per volume takes the form

$$\mathcal{Q}(E', A') = \mathcal{Q}_0 \left(\frac{E'}{E_0} \right)^{-\gamma} \exp \left(-\frac{E'}{Z' E_p^{\max}} \right), \quad (163)$$

where E_p^{\max} is the maximal energy of emitted protons, i.e., maximum rigidity of the accelerator, Z' is the nucleus' atomic number, E_0 is some reference energy, and

$$\mathcal{Q}_0 = \begin{cases} \dot{n}_0 \frac{dN_{A'}}{dE'} \Big|_{E'=E_0}, & \text{for bursting sources} \\ n_0 \frac{dN_{A'}}{dE' dt} \Big|_{E'=E_0}, & \text{for steady sources} \end{cases}, \quad (164)$$

and where \dot{n}_0 is the number of bursts per unit volume per unit time and $dN_{A'}/dE'$ is the spectrum of particles produced by each burst, or for a steady source n_0 is the number density of sources at $z=0$, and

$Q_0 \equiv dN_{A'}/dE'dt$ is the UHECR production rate per unit energy per source. The cosmic ray power density above a certain energy E'_{\min} is given by

$$\begin{aligned}
\dot{\epsilon}_{\text{CR}}(> E_{\min}) &= \int_{E'_{\min}}^{\infty} E' Q(E', A') dE' = Q_0 \int_{E'_{\min}}^{\infty} E' \left(\frac{E'}{E_0}\right)^{-\gamma} \exp\left(-\frac{E'}{Z' E_p^{\max}}\right) dE' \\
&= Z' E_p^{\max} \left(\frac{Z' E_p^{\max}}{E_0}\right)^{-\gamma+1} \int_{E'_{\min}/(Z' E_p^{\max})}^{\infty} t^{-\gamma+1} e^{-t} dt \\
&= Q_0 E_0^2 \left(\frac{Z' E_p^{\max}}{E_0}\right)^{-\gamma+2} \Gamma\left(-\gamma+2, \frac{E'_{\min}}{Z' E_p^{\max}}\right), \tag{165}
\end{aligned}$$

where $\Gamma(x)$ denotes the upper incomplete gamma function.

For a given spectrum of injected nuclei of mass A' , the space density of cosmic rays at Earth with energy E and mass A is given by (160). For an isotropic arrival direction distribution the relation between the spectrum and the cosmic ray density follows from (7) and is given by

$$J(E, A, A') \equiv \frac{dN}{dE dA dt d\Omega} = \frac{1}{4\pi} n(E, A, A'), \tag{166}$$

Note that discretization of (160) allows a numerical treatment of the problem. For details of the discretization procedure, see [94].

Before discussing the results of the fit, we pause to discuss some interesting phenomenological aspects of the source environment. To visualize the *high-pass filter* mechanism advertised in Sec. 2.2, envision a source in which the escape and interaction times are both power laws in energy,

$$\tau_{\text{esc}} = a (E/E_0)^\delta \quad \text{and} \quad \tau_{\text{int}} = b (E/E_0)^\zeta. \tag{167}$$

Thus, a fraction

$$\eta_{\text{esc}}(E) = (1 + \tau_{\text{esc}}/\tau_{\text{int}})^{-1} = [1 + R_0 (E/E_0)^{\delta-\zeta}]^{-1} \tag{168}$$

of the particles escape without interaction and the rest interact before escaping, so $\eta_{\text{int}} = 1 - \eta_{\text{esc}}$, with $R_0 = a/b$ the ratio of the escape and interaction time at reference energy E_0 . Note that η_{esc} and η_{int} depend only on the ratio of the escape and interaction times, but not on the absolute value of either of them. When $\delta > \zeta$, the source environment acts as a *low-pass filter* on the particles injected from the accelerator, leading to a cutoff in the escaping spectrum at high energies. This situation is typical of leaky box models of diffuse acceleration at time-independent shocks [410, 411] where $\delta > 0$ because the higher the energy of the particle, the longer it needs to stay in the accelerator to reach its energy. By contrast, if the escape time decreases with energy, as in the case of diffusion in turbulent magnetic fields outside the accelerator, then it is possible to have $\delta < \zeta$ leading to a *high-pass filter* on the energy spectrum of injected nuclei: the lower the energy, the more time the nuclei have to interact before escaping, leading to a hardening of the spectrum and lightening of the composition of nuclei escaping the region surrounding the source. The spallated nucleons have energies of E/A ; these nucleons are most abundant at low energies and have a steeper spectrum than the parent nuclei. Thus, the *high-pass filter* leads naturally to an ankle-like feature separating the nucleonic fragments from the remaining nuclei. The normalization and slope of the spectrum of spallated nucleons relative to that of the primary nuclei is determined by how thoroughly the primary nuclei are disintegrated, which is governed by the ratio of escape and interaction lengths of the most abundant primaries.

To obtain a more realistic treatment of the interaction time, one must specify the shape of the spectrum of the target photons. The simple representative photon background of non-thermal emission adopted here is a broken power-law,

$$n(\varepsilon) = n_* \begin{cases} (\varepsilon/\varepsilon_*)^\alpha & \varepsilon < \varepsilon_* \\ (\varepsilon/\varepsilon_*)^\beta & \text{otherwise} \end{cases}, \quad (169)$$

where ε is the photon energy and the maximum of the number density is at an energy of ε_* [410]. For such peaky photon spectra, the interaction time does not have the simple representation of (167) but it does have a rather universal structure. Substituting (169) into (139) yields:

$$\frac{1}{\tau_{\text{int}}(E)} = \frac{1}{\tau_b} \begin{cases} (E_b/E)^{\beta+1} & E \leq E_b \\ (1-\beta)/(1-\alpha) [(E_b/E)^{\alpha+1} - (E_b/E)^2] + (E_b/E)^2 & E > E_b \end{cases}, \quad (170)$$

where

$$\tau_b = \frac{E_b (1-\beta)}{c \varpi A m_p n_*} \quad \text{and} \quad E_b = \frac{\varepsilon_0 A m_p}{2\varepsilon_*}. \quad (171)$$

In the NWA the photopion production cross section can be described by (134) with the following parameters: $\sigma_0 \simeq 0.5 A$ mb, $\Gamma = 150$ MeV, and $\varepsilon_0 = (m_\Delta^2 - m_p^2)/(2m_p) \simeq 340$ MeV [11].

As can be seen in Fig. 18 the folding of a single resonance in the NWA with a broken power-law spectrum leads to a “V” shape curve for τ_{int} in a log-log plot for both photo-disintegration (top panel) and photopion production (middle panel). Combining both processes in the NWA yields an interaction time with a “W” shape, while numerical integration of (136) using precise cross section curves fitted to data (including the plateau for multi-pion production) softens the “W” to what we shall refer to as an “L” shape for brevity, as shown in the bottom panel of Fig. 18. As evident from Fig. 18, below the inflection point for photodisintegration E_b , the NWA provides a good representation of the data, while from the full numerical integration in the high-energy region τ_{int} is roughly constant. Hence we can write an approximate representation of the interaction time

$$\tau_{\text{int}}(E) \approx \tau_b \begin{cases} (E/E_b)^{\beta+1} & E \leq E_b \\ 1 & E > E_b \end{cases}. \quad (172)$$

Returning to the discussion of τ_{int} , now (167) with (172) together yield the fraction of nuclei which escape without interaction in a peaky photon spectrum. It is straightforward to see that if $\delta < 0$ and the interaction time is described by an L-shaped curve, then η_{esc} has the properties of a high-pass filter. These conclusions do not depend on the exact shape of the photon spectrum. As one can guess from Fig. 15, if the photon density is assumed to follow a black body spectrum, then each interaction time in the NWA would have a V shape and the total interaction time would flatten to an L-curve as well, modulated by the cross section plateau of multi-pion production [94].

Motivated by the energy dependence of the diffusion coefficient for propagation in a turbulent magnetic field, one can model τ_{esc} as a power law in rigidity E/Z ,

$$\tau_{\text{esc}} = \tau_0 (EZ^{-1}/E_0)^\delta. \quad (173)$$

Since only the ratio of escape and interaction times matters, and the $\{E, A, Z\}$ dependence of this ratio is entirely determined once the spectral index of the escape time δ is specified, the remaining freedom in characterizing the source environment can be encoded by specifying the ratio of escape to interaction time

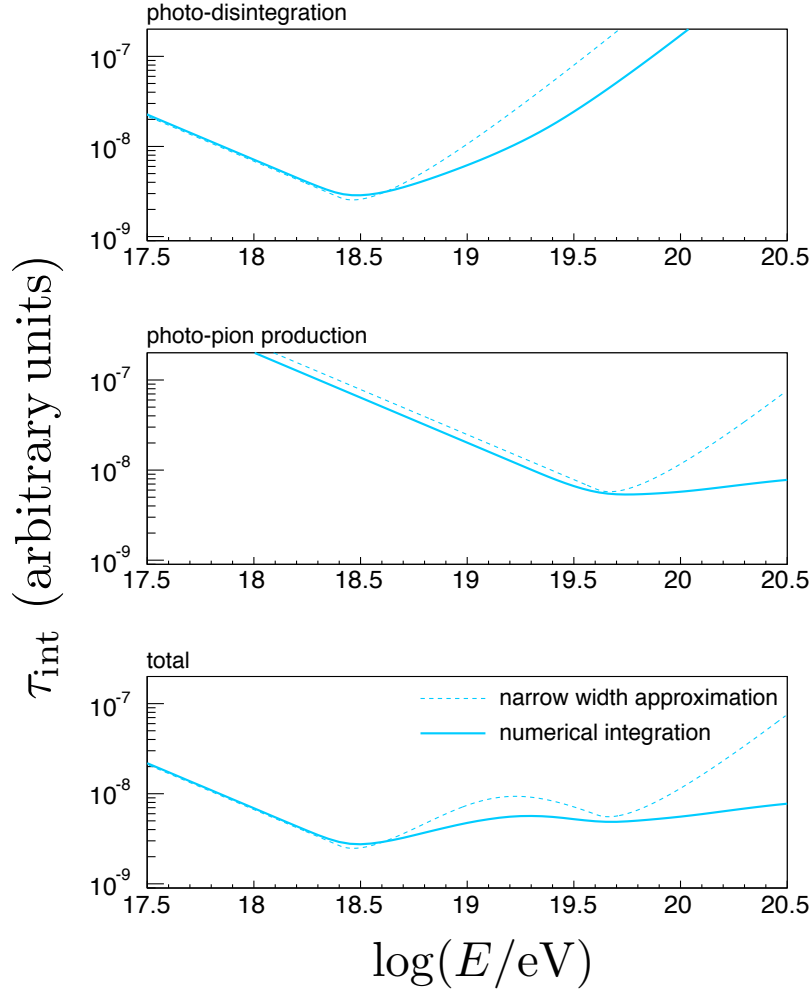


Figure 18: Interaction times of ^{28}Si in a broken power-law photon field with parameters $\alpha = 3/2$, $\beta = -1$ and $\varepsilon_* = 0.11$ eV. Top panel: photo-disintegration, middle panel: photo-pion production, bottom panel: sum of the two processes. The results of numerical integration using detailed cross sections are shown as thick solid lines, while those of the NWA are displayed with thin dashed lines. From Ref. [94].

for a particular choice of $\{E, A, Z\}$, say at $E = 10^{10}$ GeV for iron nuclei, denoted R_{10}^{Fe} . In application to a particular source candidate, R_{10}^{Fe} depends on the density of photons and the properties of the turbulent magnetic field that delays the escape of the UHECRs from the environment of their source.

Figure 19 shows a comparison of the extragalactic all-particle spectrum (obtained by combining contributions from photodisintegration in the source environment and on the way to Earth) with both the Auger measured flux above $10^{8.5}$ GeV [412] and the mean and variance of the distribution of the logarithm of the baryon number on top of the atmosphere, $\langle \ln A \rangle$ and $V(\ln A)$ [51, 412, 413]. The source spectra are modelled using a mixed composition, which follows the abundances of Galactic nuclei at a nucleus energy of 1 TeV. The corresponding nucleus fractions are: 0.365, 0.309, 0.044, 0.077, 0.019, 0.039, 0.039, 0.0096, 0.014, 0.084 for H, He, C, O, Ne, Mg, Si, S, Ar+Ca, Fe, respectively. The best fit values of the free parameters are: (i) the power law index of the injected nuclei $\gamma = 1.25 \pm 0.02$, (ii) the cutoff rigidity $\log(E_p^{\text{max}}/\text{GeV}) = 9.60 \pm 0.01$, (iii) the power law index of the escape length $\delta = -1.01 \pm 0.03$, (iv) the

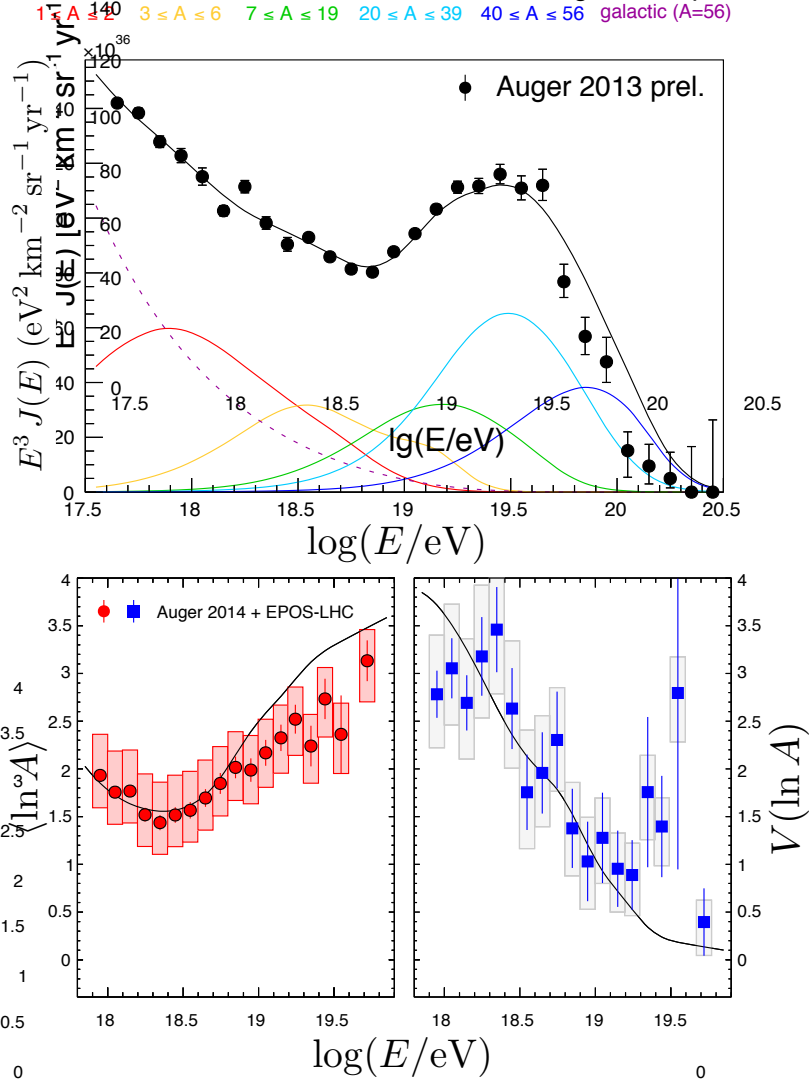


Figure 19: Spectrum and composition at Earth produced by a distribution of sources endowed with a *high-pass filter*. The data points are from the Pierre Auger Observatory [51, 412] *shifted by plus one sigma of systematic uncertainty for the energy scale and minus one sigma for the X_{\max} scale*. Error bars denote the statistical uncertainties and the shaded boxes illustrate the experimental systematic uncertainties of the composition. The composition estimates are based on an interpretation of air shower data with the EPOS-LHC event generator [414]. From Ref. [94].

ratio of interaction and escape time $\log(R_{10}^{\text{Fe}}) = 2.57 \pm 0.02$, (v) the flux fraction of Galactic cosmic rays $f = 0.686 \pm 0.01$, and (vi) the power law index index of the Galactic cosmic ray spectrum $\propto E^{-\gamma_{\text{gal}}}$, assumed to be dominated by iron nuclei: $\gamma_{\text{gal}} = 3.71 \pm 0.02$ [94]. The energy of maximum of the photon field density was fixed at $\varepsilon_* = 0.09$ eV. Substituting the corresponding fit parameters in (165) one infers a comoving volumetric energy injection rate in CRs at $z = 0$ of

$$\dot{\epsilon}_{\text{CR}}(> 10^{8.5} \text{ GeV}) = 1.5 \times 10^{45} \text{ erg Mpc}^{-3} \text{ yr}^{-1}. \quad (174)$$

There is a good overall agreement between the model and the data. The shape of the spectrum is described well, including the ankle and the flux suppression. The model also qualitatively reproduces the increase of

the average logarithmic mass with energy and the decrease of its variance. GRBs [415], SBGs [416], and AGNs [417] have been proposed as astrophysical sites that can accommodate a high-pass filter.

Alternative evolutions of the source luminosity density can be described by the simple one-parameter functional form

$$\xi(z) = \begin{cases} (1+z)^m & z < z_0 \\ (1+z_0)^m \exp(-(z-z_0)) & \text{otherwise} \end{cases}, \quad (175)$$

with $z_0 = 2$ and m ranging from -4 to $+4$. $m = 0$ yields a uniform source luminosity distribution, $m = +4$ corresponds to a strong evolution similar to the one of AGNs [418, 419], and negative values result in sources that are most abundant or most luminous within the low-redshift universe [420]. One interesting source class for which the number of objects increases at low redshifts are low-luminosity γ -ray BL Lacertae (BL Lac) objects.¹⁵ While Fermi measurements have revealed that the number density of bright BL Lacs peaks at a fairly high redshift of $z \simeq 1.2$, the more numerous low-luminosity ($L_\gamma < 10^{44}$ erg s⁻¹) and high-synchrotron peaked members of this population exhibit negative source evolution, and thus are overwhelmingly distributed at low redshifts [421]. The resulting variations on the fit parameters that simultaneously accommodate the shape of the UHECR spectrum and its nuclear composition are as follows [94]:

- $\gamma = 2$ gives a poor description of the data for $m \gtrsim 0$, but is a viable choice for closeby sources;
- for positive values of m , a fixed value of $\gamma = 1$ gives a similar fit quality as the freely floating γ , but the latter converges to values larger than 1 for source evolutions with $m > 2$;
- for the “traditional” source evolutions with $m \geq 0$ and fixed $\gamma = 1$, most of the parameters exhibit only a minor variation with m , with the exception of the power-law index of the escape time δ and the power density $\dot{\epsilon}_{\text{CR}} (> 10^{8.5}$ GeV).

This implies that the fit to Auger data does not critically depend on the choice of the source evolution, but that for a given choice of m one can constrain the allowed values of γ , δ and $\dot{\epsilon}_{\text{CR}} (> 10^{8.5}$ GeV).

3.5. Impact of ν and γ -ray observations on UHECR models

In the late '90s, Waxman and Bahcall (WB) envisioned the CR engines as machines where protons are accelerated and (possibly) permanently confined by the magnetic fields of the acceleration region [422]. The production of neutrons and pions and subsequent decay produces neutrinos, γ -rays, and CRs. If the neutrino-emitting source also produces high- or ultra-high-energy CRs, then *pion production must be the principal agent for the high energy cutoff on the proton spectrum*. Conversely, since the protons must undergo sufficient acceleration, inelastic pion production needs to be small below the cutoff energy; consequently, the plasma must be optically thin. Since the interaction time for protons is greatly increased over that of neutrons due to magnetic confinement, the neutrons escape before interacting, and on decay give rise to the observed CR flux. The foregoing can be summarized as three conditions on the characteristic nucleon interaction time scale τ_{int} ; the neutron decay lifetime τ_n ; the characteristic cycle time of confinement τ_{cycle} ; and the total proton confinement time τ_{conf} : (i) $\tau_{\text{int}} \gg \tau_{\text{cycle}}$; (ii) $\tau_n > \tau_{\text{cycle}}$; (iii) $\tau_{\text{int}} \ll \tau_{\text{conf}}$. The first condition

¹⁵From the viewpoint of AGN classification, BL Lacs are a blazar subtype. The blazar category encompasses all quasars oriented with the relativistic jet directed at the observer giving a unique radio emission spectrum. This includes both radio quiet AGN (BL Lacs) and optically violent variable quasars.

ensures that the protons attain sufficient energy. Conditions (i) and (ii) allow the neutrons to escape the source before decaying. Condition (iii) permits sufficient interaction to produce neutrons and neutrinos. These three conditions together define an optically thin source [423]. A desirable property to reproduce the almost structureless energy spectrum is that a single type of source will produce cosmic rays with a smooth spectrum across a wide range of energy.

The UHECR intensity just below E_{supp} is often summarized as “one particle per kilometer square per year per steradian.” This can be translated into an energy intensity [424]

$$E \{E J(E)\} = \frac{10^{10.5} \text{ GeV}}{(10^{10} \text{ cm}^2)(10^{7.5} \text{ s}) \text{ sr}} = 10^{-7} \text{ GeV cm}^{-2} \text{ s}^{-1} \text{ sr}^{-1}. \quad (176)$$

From this we can derive the energy density ϵ_{CR} in UHECRs using intensity = velocity \times density, or

$$4\pi \int dE \{E J(E)\} = v \epsilon_{\text{CR}}. \quad (177)$$

This leads to

$$\epsilon_{\text{CR}} = \frac{4\pi}{v} \int_{E_{\text{min}}}^{E_{\text{max}}} \frac{10^{-7}}{E} dE \frac{\text{GeV}}{\text{cm}^2 \text{ s}} \simeq 10^{-19} \frac{\text{TeV}}{\text{cm}^3}, \quad (178)$$

taking the extreme energies of the accelerator(s) to be $E_{\text{min}} \simeq 10^{10} \text{ GeV}$ and $E_{\text{max}} = 10^{12} \text{ GeV}$, and $v \sim c$. The power required for a population of sources to generate this energy density over the Hubble time ($t_H \approx 10^{10} \text{ yr}$) is: $\dot{\epsilon}_{\text{CR}}^{[10^{10}, 10^{12}]} \sim 5 \times 10^{44} \text{ TeV Mpc}^{-3} \text{ yr}^{-1} \simeq 3 \times 10^{37} \text{ erg Mpc}^{-3} \text{ s}^{-1}$. This works out to roughly (i) $L \approx 3 \times 10^{39} \text{ erg s}^{-1}$ per galaxy, (ii) $L \approx 3 \times 10^{42} \text{ erg s}^{-1}$ per cluster of galaxies, (iii) $L \approx 2 \times 10^{44} \text{ erg s}^{-1}$ per active galaxy, or (iv) $\int L dt \approx 10^{52} \text{ erg}$ per cosmological GRB [424]. The coincidence between these numbers and the observed output in electromagnetic energy of these sources explains why they have emerged as the leading candidates for accelerators of UHECR protons.

The energy production rate of protons derived professionally, assuming a cosmological distribution of proton sources, with injection spectrum $\propto E^{-2}$, is [425]

$$\dot{\epsilon}_{\text{CR}}^{[10^{10}, 10^{12}]} \sim 5 \times 10^{44} \text{ erg Mpc}^{-3} \text{ yr}^{-1}. \quad (179)$$

This is within a factor $\mathcal{O}(1)$ of our back-of-the-envelope estimate (1 TeV \simeq 1.6 erg). The energy-dependent generation rate of CRs is therefore given by

$$E^2 \dot{n}(E) = \frac{\dot{\epsilon}_{\text{CR}}^{[10^{10}, 10^{12}]}}{\ln(10^{12}/10^{10})} \approx 10^{44} \text{ erg Mpc}^{-3} \text{ yr}^{-1}.$$

The energy density of neutrinos produced through $p\gamma$ interactions of these protons can be directly tied to the injection rate of CRs

$$E_\nu^2 n(E_\nu) \approx \frac{3}{8} \epsilon_\pi t_H E^2 \dot{n}(E), \quad (180)$$

where ϵ_π is the fraction of the energy which is injected in protons lost into photopion interactions. The factor of 3/8 comes from the fact that, close to threshold, roughly half the pions produced are neutral, thus not generating neutrinos, and one quarter of the energy of charged pion decays ($\pi^+ \rightarrow e^+ \nu_e \nu_\mu \bar{\nu}_\mu$ and the conjugate process) goes to electrons rather than neutrinos. Namely, resonant $p\gamma$ interactions produce twice

as many neutral pions as charged pions. Direct pion production via virtual meson exchange contributes only about 20% to the total cross section, but is almost exclusively into π^+ . Hence, $p\gamma$ interactions produce roughly equal numbers of π^+ and π^0 . The average neutrino energy from the direct pion decay is found to be $\langle E_\nu \rangle^\pi = (1 - r) E_\pi/2 \simeq 0.22 E_\pi$ and that of the muon is $\langle E_\nu \rangle^\mu = (1 + r) E_\pi/2 \simeq 0.78 E_\pi$, where r is the ratio of muon to the pion mass squared. In muon decay, all secondaries can be considered massless and so each of the neutrinos has about 1/3 of the muon energy. This gives an average neutrino energy of $\langle E_\nu \rangle^\mu = (1 + r) E_\pi/6 = 0.26 E_\pi$, and so $\langle E_\nu \rangle \sim E_\pi/4$.

The WB-bound is defined by the condition $\epsilon_\pi = 1$

$$E_\nu^2 \Phi_{\nu_{\text{all}}}^{\text{WB}}(E_\nu) \approx \frac{3}{8} \xi_z \epsilon_\pi t_H \frac{c}{4\pi} E^2 \dot{n}(E) \approx 2.3 \times 10^{-8} \epsilon_\pi \xi_z \text{ GeV cm}^{-2} \text{ s}^{-1} \text{ sr}^{-1}, \quad (181)$$

where

$$\xi_z = \int_0^\infty dz \frac{(1+z)^{-\gamma}}{\sqrt{\Omega_m(1+z)^3 + \Omega_\Lambda}} \xi(z) \quad (182)$$

accounts for the effects of source evolution with redshift [422]. For $\gamma = 2$ and no source evolution in the local ($z < 2$) universe, $\xi(z) = 1$ and $\xi_z \simeq 0.5$ [426]. For sources (with $\gamma = 2$) following the star-formation rate, $\xi(z)$ is given by (162) and $\xi_z \sim 3$. For interactions with the ambient gas (i.e. pp rather than $p\gamma$ collisions), the average fraction of the total pion energy carried by charged pions is about 2/3, compared to 1/2 in the photopion channel. In this case, the upper bound given in (181) is enhanced by 33% [423]. Electron antineutrinos can also be produced through neutron β -decay [427]. The β -decay contribution to the diffuse neutrino flux, however, turns out to be negligible.

The actual value of the neutrino flux depends on what fraction of the proton energy is converted to charged pions (which then decay to neutrinos), i.e. ϵ_π is the ratio of charged pion energy to the *emerging* nucleon energy at the source. For resonant photoproduction, the inelasticity is kinematically determined by requiring equal boosts for the decay products of the Δ^+ , giving $\epsilon_\pi = E_{\pi^+}/E_n \approx 0.28$, where E_{π^+} and E_n are the emerging charged pion and neutron energies, respectively. For $pp \rightarrow NN + \text{pions}$, where N indicates a final state nucleon, the inelasticity is ≈ 0.6 [428]. This then implies that the energy carried away by charged pions is about equal to the emerging nucleon energy, yielding (with our definition) $\epsilon_\pi \approx 1$.

At production, if all muons decay, the neutrino flux consists of equal fractions of ν_e , ν_μ and $\bar{\nu}_\mu$. Originally, the WB-bound was presented for the sum of ν_μ and $\bar{\nu}_\mu$ (neglecting ν_e), motivated by the fact that only muon neutrinos are detectable as track events in neutrino telescopes. Since oscillations in the neutrino sector mix the different species, we chose instead to discuss the sum of all neutrino flavors ν_{all} . When the effects of oscillations are accounted for, *nearly* equal numbers of the three neutrino flavors are expected at Earth [429].

If UHECR include nuclei heavier than hydrogen, then the neutrino intensity expected from the cosmic ray sources may be modified. Nuclei undergoing acceleration can produce pions, just as protons do, through interactions with the ambient gas, so the WB argument would be unchanged in this case. However, if interactions with radiation fields dominate over interactions with matter, the neutrino flux would be suppressed if the cosmic rays are heavy nuclei. This is because the photodisintegration of nuclei dominates over pion production at all but the very highest energies.

The diffuse intensity of astrophysical neutrinos has an additional component originating in the energy loss of UHECRs travelling to Earth [430]. The accumulation of these neutrinos over cosmological time is

known as the cosmogenic neutrino flux. The GZK reaction chain generating cosmogenic neutrinos is well known [431]. The intermediate state of the reaction $p\gamma \rightarrow n\pi^+/p\pi^0$ is dominated by the Δ^+ resonance, because the neutron decay length is smaller than the nucleon mean free path on the CMB. Gamma-rays, produced via π^0 decay, subsequently cascade electromagnetically on intergalactic radiation fields through e^+e^- pair production followed by inverse Compton scattering. The net result is a pile up of γ -rays at GeV–TeV energies, just below the threshold for further pair production on the diffuse optical background. Meanwhile each π^+ decays to 3 neutrinos and a positron; the e^+ readily loses its energy through inverse Compton scattering on the diffuse radio background or through synchrotron radiation in intergalactic magnetic fields. As we have seen, the neutrinos carry away about 3/4 of the π^+ energy, therefore the energy in cosmogenic neutrinos is about 3/4 of that produced in γ -rays. The functional form of the cosmogenic neutrino intensity depends on the source spectra, the source evolution, and on the UHECR nuclear composition [432–440]. For proton primaries, the energy-squared-weighted intensity $E_\nu^2\Phi_\nu(E_\nu)$ peaks between $10^{9.6}$ and 10^{10} GeV, where the magnitude is around 1 in WB units.¹⁶ For heavy nuclei, the peak is at much lower energy (around $10^{8.7}$ GeV) and the magnitude is about 0.1 to 0.01 WB, depending on source evolution. The magnitude of the γ -ray pile up currently provides the most stringent bound on the intensity of cosmogenic neutrinos [441].

High- and ultra-high-energy neutrino detection has been one of the experimental challenges in particle astrophysics. It is widely believed that one of the most appropriate techniques for neutrino detection consists of measuring the Cherenkov light from muons or showers produced by the neutrino interactions in underground water or ice [442–445]. This allows instrumentation of large enough volumes to compensate for both the low neutrino cross section and the low fluxes expected. There are several projects under way to build sufficiently large detectors to measure the expected signals from a variety of neutrino sources. The IceCube facility, deployed near the Amundsen-Scott station, is the largest neutrino telescope in the world [446]. It comprises a cubic-kilometer of ultra-clear ice about a mile below the South Pole surface, instrumented with long strings of sensitive photon detectors which record light produced when neutrinos interact in the ice.

Neutrino (antineutrino) interactions in the Antarctic ice sheet can be reduced to three categories: (i) In charge current (CC) interactions the neutrino becomes a charged lepton through the exchange of a W^\pm with some nucleon N , $\nu_\ell(\bar{\nu}_\ell) + N \rightarrow \ell^\pm + \text{anything}$, where lepton flavor is labeled as $\ell \in \{e, \mu, \tau\}$. (ii) In neutral current (NC) interactions the neutrino interacts via a Z transferring momentum to jets of hadrons, but producing a neutrino rather than a ℓ^\pm in the final state: $\nu_\ell(\bar{\nu}_\ell) + N \rightarrow \nu_\ell(\bar{\nu}_\ell) + \text{anything}$. The scattered ν_ℓ exits the detector, carrying away energy, and so the observed energy presents a lower bound for the incident ν_ℓ energy. All three neutrino flavors exhibit a NC. These two possibilities are then projected onto two kinds of IceCube topologies to yield the three final possibilities: (i) “Shower” (\oplus) events result from all three flavors of NC events, and from the CC events of the electron and tau neutrinos below ~ 2 PeV. Shower events (also called “cascade” events) refer to the fact that energy is deposited no charged tracks (produced by muons or taus) are observed. (ii) Below a few PeV, “track” (\odot) events are produced only by the muon neutrino CC. The ν_μ CC creates a muon and a hadronic shower within the IceCube detector, the muon track contributes to the deposited energy, but then the muon is seen to exit the detector as a single track of unknown energy. The deposited energy is only a lower bound to the incident muon neutrino energy. (iii) At ν_τ energies above 3 PeV, ν_τ CC interactions begin to produce separable *double bang* events [429], with one smaller-energy shower produced by the initial ν_τ collision in the ice, and the second larger-energy shower resulting from the subsequent τ decay.

¹⁶Recall that 1 WB = 10^{-8} GeV (cm² sr)⁻¹.

UHECR experiments, like Auger, provide a complementary technique for ultra-high-energy cosmic neutrino (UHEC ν) detection by searching for deeply-developing, large zenith angle ($> 75^\circ$) showers [447]. At these large angles, hadron-induced showers traverse the equivalent of several atmospheres before reaching detectors at the ground. Beyond about 2 atmospheres, most of the electromagnetic component of a shower is extinguished and only very high energy muons survive. Consequently, a hadron-induced shower front is relatively flat and the shower particles arrive within a narrow time window. In contrast, a neutrino shower exhibits characteristics similar to those of a vertical shower, which has a more curved front and a wider distribution in particle arrival times due to the large number of lower energy electrons and photons. Furthermore, the “early” part of the shower will tend to be dominated by the electromagnetic component, while “late” portion will be enriched with tightly bunched muons. Using these characteristic features, it is possible to distinguish neutrino induced events from background hadronic showers. Moreover, because of full flavor mixing, tau neutrinos are expected to be as abundant as other species in the cosmic flux. Tau neutrinos can interact in the Earth’s crust, producing τ leptons which may decay above the ground-based detectors [448–452]. Details on how such neutrino events can be selected at the Pierre Auger Observatory are discussed in [453–458].

Because the shape of the astrophysical neutrino intensity is unknown, it is convenient to define a procedure to set model-independent limits on the total neutrino flux [459]. To this end, we first write a generic expression for the neutrino event rate

$$N = \sum_{i,X} \int dE_i N_A \Phi_i(E_i) \sigma_{iN \rightarrow X}(E_i) \mathcal{E}(E_i), \quad (183)$$

where the sum is over all neutrino species $i = \nu_e, \bar{\nu}_e, \nu_\mu, \bar{\nu}_\mu, \nu_\tau, \bar{\nu}_\tau$, and all final states X . $N_A = 6.022 \times 10^{23}$ is Avogadro’s number, and Φ_i is the source flux of neutrino species i , σ as usual denotes the cross section, and \mathcal{E} is the exposure measured in cm^3 w.e. sr time. We assume the simplest scenario in which there are no events that unambiguously pass all the experimental cuts, with zero events expected from background. This implies an upper bound of 2.4 events at 90%CL from neutrino fluxes [11]. Poisson intervals for more complex combinations of detection and background events are summarized in [460]. Note that if the number of events integrated over energy is bounded by 2.4, then it is certainly true bin by bin in energy. Thus, using (183) one obtains

$$\sum_{i,X} \int_{\Delta} dE_i N_A \Phi_i(E_i) \sigma_{iN \rightarrow X}(E_i) \mathcal{E}(E_i) < 2.4, \quad (184)$$

at 90% CL for some interval Δ . Here, the sum over X takes into account charge and neutral current processes. In a logarithmic interval Δ where a single power law approximation

$$\Phi_i(E_i) \sigma_{iN \rightarrow X}(E_i) \mathcal{E}(E_i) \sim E_i^\alpha \quad (185)$$

is valid, a straightforward calculation shows that

$$\int_{\langle E \rangle e^{-\Delta/2}}^{\langle E \rangle e^{\Delta/2}} \frac{dE_i}{E_i} E_i \Phi_i \sigma_{iN \rightarrow X} \mathcal{E} = \langle \sigma_{iN \rightarrow X} \mathcal{E} E_i \Phi_i \rangle \frac{\sinh \delta}{\delta} \Delta, \quad (186)$$

where $\delta = (\alpha + 1)\Delta/2$ and $\langle A \rangle$ denotes the quantity A evaluated at the center of the logarithmic interval. The parameter $\alpha = 0.363 + \beta - \gamma$, where 0.363 is the power law index of the SM neutrino cross section [461]

Table 3: All-flavor differential 90% CL upper limit based on the nine-year sample of IceCube data [462].

$\log_{10}(E_\nu/\text{GeV})$	$\log_{10}[E_\nu^2 \Phi_{\nu\text{all}}(E_\nu)/(\text{GeVcm}^{-2} \text{s}^{-1} \text{sr}^{-1})]$
7.0	-7.86
7.5	-7.71
8.0	-7.69
8.5	-7.75
9.0	-7.66
9.5	-7.45
10.0	-7.20

and β and $-\gamma$ are the power law indices (in the interval Δ) of the exposure and flux Φ_i , respectively. Since $\sinh \delta/\delta > 1$, a conservative bound may be obtained from (184) and (186):

$$N_A \sum_{i,X} \langle \sigma_{iN \rightarrow X}(E_i) \rangle \langle \mathcal{E}(E_i) \rangle \langle E_i \Phi^i \rangle < 2.4/\Delta . \quad (187)$$

By taking $\Delta = 1$ as a likely interval in which the single power law behavior is valid (this corresponds to one e -folding of energy), it is straightforward to obtain upper limits on the neutrino flux. The model-independent upper limits on the total neutrino flux, derived using the nine-year sample of IceCube data are collected in Table 3 [462]. The sensitivity of existing neutrino-detection facilities is about to reach 1 WB, challenging cosmic-ray models for which the highest energies are proton-dominated [463–467].

The multi-messenger program will also help discriminate among UHECR acceleration models. As an illustration, we consider the two main mechanisms proposed to accelerate UHECRs in starburst galaxies: unipolar induction in newly-born pulsars and Fermi shock acceleration in the galactic scale superwind. On the one hand, UHECRs crossing the supernova ejecta surrounding neutron stars would experience an effective optical depth to hadronic interactions which is larger than unity, and so one expects guaranteed fluxes of neutrinos in the energy range $10^8 \lesssim E_\nu/\text{GeV} \lesssim 10^9$ [468]. Actually, the differential upper limits on the diffuse neutrino flux from IceCube already constrain models of UHECR acceleration in the core of starburst galaxies [469]. Recall that for SBGs, the anisotropy signal has been observed for only a fraction $f_{\text{sig}} = (10 \pm 4)\%$ of the UHECR sample, so a small window of the parameter space still remains opened. On the other hand, if UHECRs are accelerated at the terminal shock of the starburst superwind, we expect the maximum energy to be constrained by direct escape of the nuclei, and so the flux of photons and neutrinos accompanying the starburst UHECR emission would be strongly suppressed. Indeed, if this were the case, the neutrino emission from starbursts would cutoff somewhat above 10^7 GeV, as entertained in [470].

After this discussion it appears evident the importance of multi-messenger observations to narrow the search for the UHECR origin(s). Next generation IceCube detector will play a key role in this endeavor [471].

3.6. Grand unified spectrum of diffuse extragalactic background radiation

The diffuse extragalactic background radiation (DEBRA) is an indicator of the integrated luminosity of the universe [472]. The analysis of the different components of DEBRA leads to the grand unified spectrum, covering roughly 34 decades of energy. This spectrum is continuously updated thanks to the

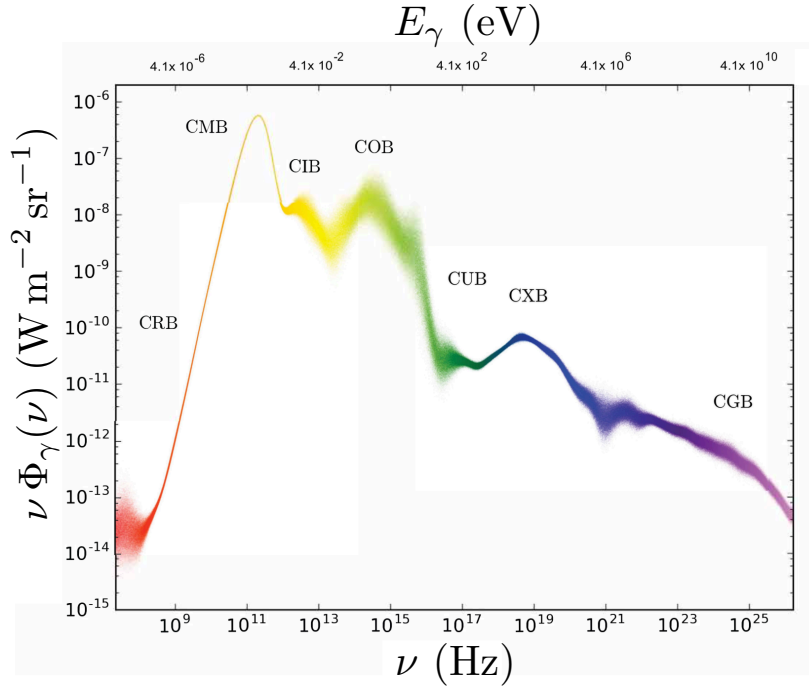


Figure 20: Frequency-weighted intensity of the EBL as measured in radio (CRB), microwave, infrared (CIB), optical (COB), UV (CUB), X-rays (CXB), and γ -rays (CGB). From Ref. [473].

numerous space- and ground-based multi-frequency experiments observing different cosmic messengers. In this section we review a series of simultaneous and coordinated multi-frequency observations which can help elucidate the UHECR origin(s).

The intensity of the extragalactic background light (EBL) spans close to 20 decades in photon frequency; see Fig 20. Across this whole range, the EBL spectrum captures cosmological backgrounds associated with either primordial phenomena, such as the CMB, or photons emitted by stars, galaxies, and AGNs due to nucleosynthesis or other radiative processes, including dust scattering, absorption and reradiation. It has been known since the early '60s that high-energy γ -rays from sources at cosmological distances will be absorbed along the way by the diffuse background of softer photons via electron-positron pair production [474–476]. Roughly speaking, photons originating at a redshift z will be absorbed above about an energy $\sim 100(1+z)^{-2}$ TeV [477, 478]. This implies that the intensity of extragalactic γ -rays has to be suppressed above about 1 TeV, see Fig. 20.

In 2012, the IceCube Collaboration famously announced the observation of two ~ 1 PeV neutrinos discovered in a search for the nearly guaranteed cosmogenic neutrinos [479]. The search technique was refined to extend the neutrino sensitivity to lower energies [480, 481], resulting in the discovery of additional “high-energy starting events” (HESEs), i.e. events initiated within the IceCube detector volume by entering neutrinos [482–484]. At the time of writing, 82 HESEs (including showers and tracks) have been reported from six years of IceCube data taking (2078 days between 2010 to early 2016) [485]. The HESE signal has been confirmed via a complementary measurement using CC interactions of $\nu_\mu + \bar{\nu}_\mu$, for which the interaction vertex can be outside IceCube instrumented volume [486–488].

A myriad of models have been proposed to interpret the data [489–491], but the origin of IceCube events

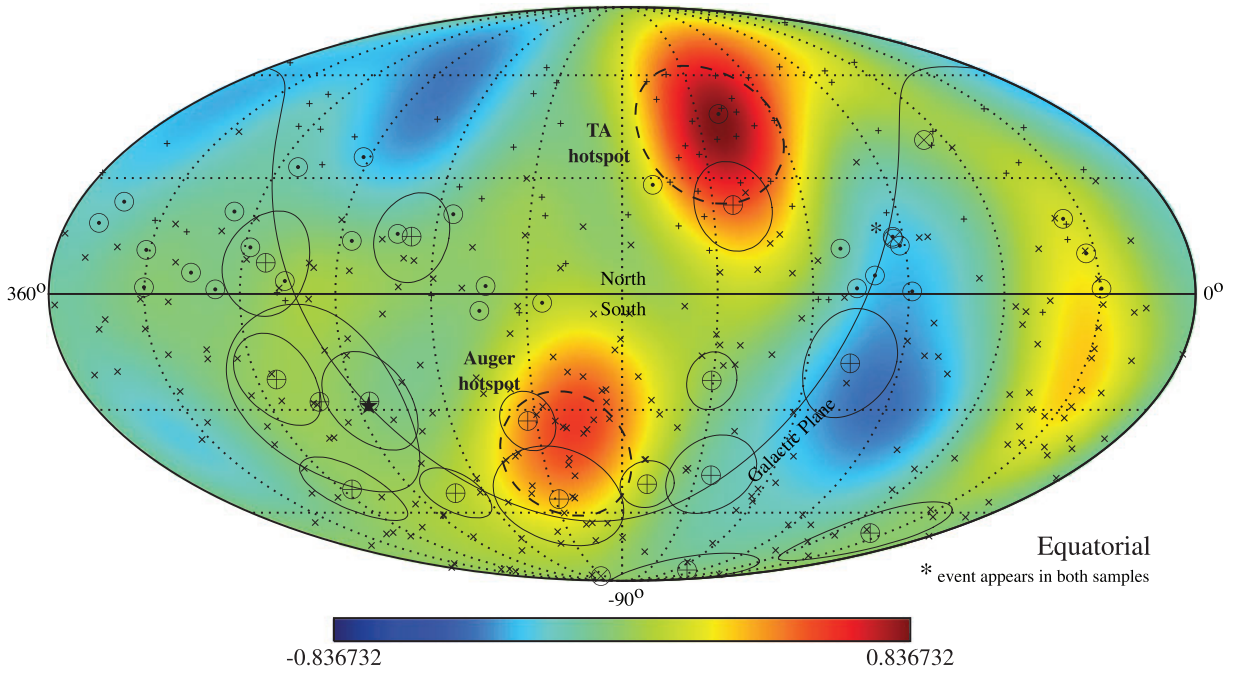


Figure 21: Mollweide projection of the arrival direction of IceCube neutrinos and UHECRs. The neutrino sample is from the six-year upgoing track analysis and the four-year HESE analysis (tracks \odot and cascades \oplus). Cascade events are indicated together with their median angular uncertainty (thin circles). One event ($*$) appears in both event samples. The Auger sample (\times) consists of events recorded between 1 January 2004 and 31 March 2014 with $E > 52$ EeV and $\theta < 80^\circ$ [102]. The TA sample ($+$) consists of events recorded between 11 May 2008 and 4 May 2013 with $E > 57$ EeV and $\theta < 55^\circ$ [100]. The background shows the anisotropy of the combined UHECR map derived by smoothing the events at best-fit position $\hat{\mathbf{n}}_i$ over the sphere with unit vector $\hat{\mathbf{n}}$ following a Fisher-Von Mises distribution $\mathfrak{F}(\hat{\mathbf{n}}, \hat{\mathbf{n}}_i; \varkappa)$. The parameter \varkappa is fixed to 11.5 such that 50% of the distribution is contained within an opening angle of 20° . From the smoothed event distribution $f(\mathbf{n}) = \sum_i \mathfrak{F}(\hat{\mathbf{n}}, \hat{\mathbf{n}}_i; \varkappa)$, the anisotropy is defined as $\delta J(\hat{\mathbf{n}}) = f(\hat{\mathbf{n}}) / \langle f(\delta(\hat{\mathbf{n}})) \rangle - 1$, where $\langle f(\delta(\hat{\mathbf{n}})) \rangle$ is the average of the distribution f in each declination bin δ . This simple procedure ensures that spurious anisotropies coming from the detector exposures that depend mostly on declination are corrected from the map. The dashed circles indicate excess regions in Auger (sampling radius of 15° ; post-trial p -value of 1.4×10^{-2}) and TA (sampling radius of 20° ; post-trial p -value of 3.7×10^{-4}) data samples. From Ref. [500].

remains unknown. The distribution of arrival directions is compatible with isotropy, without any hints of concentrations towards either the Galactic center or plane [492].¹⁷ Neither is there any significant correlation with the arrival direction of UHECRs observed by Auger and/or TA [499]; see Fig. 21. Even though there is no significant correlation with any type of extragalactic sources, the isotropicity of the neutrino flux strongly suggests the working assumption that it is of extragalactic origin.¹⁸ The Earthly flavor ratio $\nu_e : \nu_\mu : \nu_\tau$ is compatible with a 1 : 1 : 1 distribution [504–508]. This seems to indicate that IceCube neutrinos originate via pion decay in optically thin sources and experience vacuum oscillations across cosmological distances.

¹⁷See, however, [493–498].

¹⁸IceCube has identified the blazar TKS 0506+056 as a neutrino source [501]. However, IceCube searches constrain the maximum contribution of blazars in the *Fermi*-LAT 2LAC catalogue [502] to the observed astrophysical neutrino flux to be 27% or less between around 10 TeV and 2 PeV, assuming equipartition of flavors at Earth and a single power-law spectrum $\propto E_\nu^{-2.5}$ [503]. The search also excludes that the 2LAC blazars (and sub-populations) emit more than 50% of the observed neutrinos for a harder spectrum $\propto E_\nu^{-2.2}$ in the same energy range.

The most immediate impact of the discovery of astrophysical neutrinos is that the intensity level observed is exceptionally high by astronomical standards. The magnitude of the observed flux per steradian is at a level of the WB bound, which applies to neutrino production in proton sources that are also responsible for UHECRs. However, it is important to *stress* that the IceCube events have energies $E_\nu \lesssim 5$ PeV, and therefore the energy per nucleon of the parent CRs must be $E_p \lesssim 500$ PeV. Recall that efficient production of neutrinos at this energy would prevent acceleration of the parent protons to ultra-high energies, because of the 4th constraint (interaction losses) on particle acceleration; see Sec. 3.1.1. Under the optimal combination of parameters after fine tuning, the 3 conditions that define an optically thin source ($\tau_{\text{int}} \gg \tau_{\text{cycle}}, \tau_n > \tau_{\text{cycle}}, \tau_{\text{int}} \ll \tau_{\text{conf}}$) would of course hold. Only for such a particular case, the sources producing the neutrinos observed by IceCube would also emit UHECR protons. Such cosmic accelerators produce equal numbers of neutral, positive and negatively charged pions in the proton-proton beam dump. The neutral pions accompanying the charged parents of the neutrinos decay promptly into photons that could only be observed indirectly after propagation in the extragalactic background light. Losing energy, these photons cascade down to energies below 1 TeV where they can be observed with the *Fermi*-LAT satellite. The uncomplicated assumptions that IceCube’s neutrinos are produced via pion decay in optically thin sources and the neutrino spectrum follows an unbroken power law creates a tension between the relative magnitudes of the diffuse γ -ray flux detected by the *Fermi*-LAT satellite and the high energy neutrino flux per steradian detected at the South Pole [509]. The tension can be somewhat relaxed if there is a break in the spectrum, but still most of the γ -ray energy in the non-thermal universe must be produced in the hadronic accelerators responsible for IceCube’s neutrinos. This further constrains cosmogenic neutrino models [441] and the proton fraction of UHECRs, as *Fermi*-LAT photons cannot be counted twice. Mixed composition models, however, are safely below the bounds [510, 511].

Adding to the story, during its first observing run on 2015, the Advanced LIGO detectors recorded gravitational waves from the coalescence of two stellar-mass black holes (BBHs), GW150914 and GW151226, with a third candidate LVT151012 also likely to be a BBH system [512–515]. GW150914 and GW151226 have comparable luminosity distance estimates: $D_L = 420_{-180}^{+150}$ Mpc ($z = 0.09_{-0.04}^{+0.03}$) and $D_L = 440_{-190}^{+180}$ Mpc ($z = 0.09_{-0.04}^{+0.03}$), respectively. LVT151012 is the quietest signal and is inferred to be at a greater distance $D_L = 1000_{-500}^{+500}$ Mpc ($z = 0.20_{-0.09}^{+0.09}$). The broadband frequency spans the spectrum from below 35 Hz to above 450 Hz. BBH mergers have extremely high gravitational-wave luminosities: for GW150914, LVT151012, and GW151226 the peak values are respectively $3.6_{-0.4}^{+0.5} \times 10^{56}$ erg/s, $3.1_{-1.8}^{+0.8} \times 10^{56}$ erg/s, and $3.3_{-1.6}^{+0.8} \times 10^{56}$ erg/s. A direct comparison of these luminosities with the power requirements of (110) seems to indicate that binary BBH mergers could provide a profitable arena for UHECR acceleration, provided there are magnetic fields and disk debris remaining from the formation of the black holes. Moreover, it is also reasonable to suspect that if this were the case, then the accelerated CRs would interact with the surrounding matter or radiation to produce UHEC ν [516–518]. Unfortunately, a targeted search for these neutrinos yielded no candidates in Auger data [519].

During the second observing run, the LIGO-Virgo detector network observed a gravitational-wave signal (GW170817) from the inspiral of two low-mass compact objects consistent with a binary neutron star merger [520]. Nearly simultaneously, the *Fermi*-LAT and INTEGRAL telescopes detected a gamma-ray transient, GRB170817A, both spatially and temporally coincident with GW170817 [521]. Within about 12 hours of the gravitational wave trigger the host galaxy and post-merger electromagnetic transient was identified [522–526], and intensive programs of X-ray, optical/infrared, and radio observations soon followed [527–532]. Light curves measured over the next several weeks identified the hallmarks of a kilonova,

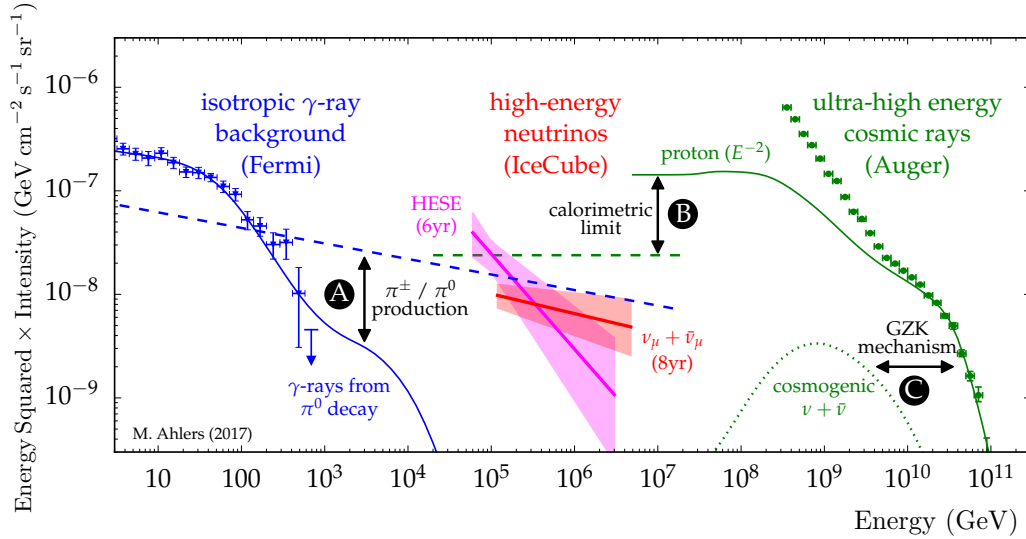


Figure 22: Multi-messenger interfaces. The neutrino intensity $\Phi_\nu(E_\nu)$ inferred from the eight-year upgoing track analysis (red fit) and the six-year HESE analysis (magenta fit) compared to the intensity of unresolved extragalactic γ -ray sources $\Phi_\gamma(E_\gamma)$ (blue data) and UHECRs $J(E)$ (green data). The neutrino spectra are indicated by the best-fit power-law (solid line) and 1σ uncertainty range (shaded range). Various multi-messenger interfaces are specified. **A:** The joined production of charged pions (π^\pm) and neutral pions (π^0) in CR interactions leads to the emission of neutrinos (dashed blue) and γ -rays (solid blue), respectively. **B:** CR emission models (solid green) of the most energetic cosmic rays imply a maximal WB-intensity (calorimetric limit) of neutrinos from the same sources (green dashed). **C:** UHECR models also predict the guaranteed emission of cosmogenic neutrinos from the collision with cosmic background photons (GZK effect). From Ref. [426].

i.e. emission driven by neutron-rich ejected material undergoing r-process nucleosynthesis [533, 534]. However, no neutrino events signaling the acceleration of CRs have been observed [535].¹⁹

The latest chapter in the story is courtesy of Auger. As alluded to already in Sec. 2.3, in 2017 the Auger Collaboration reported the observation of a large scale dipole anisotropy for events with $E > 8$ EeV [115]. The direction of the reconstructed dipole lies about 125° from the Galactic center. This suggests an extragalactic origin of UHECRs. The high and ultra-high energy components of DEBRA, together with the interconnections among the cosmic messengers, are summarized in Fig 22. Note that the lower-energy CRs are Galactic and so would not be measured in intergalactic space.

4. Phenomenology of UHECR air showers

4.1. Nature’s calorimeter

In this section we focus on UHECR phenomenology from the top of the atmosphere to the Earth’s surface. Unlike man-made calorimeters, the atmosphere is a calorimeter whose properties vary in a predictable way with altitude, and in a relatively unpredictable way with time. Beginning with the easier of the two variations, we note that the density and pressure depend strongly on the height, while the temperature does

¹⁹Neutrino emission from binary neutron star mergers has been studied in [536]. It was also noted that nucleus photodisintegration within binary neutron star merger remnants could produce the population of CRs below the “ankle” [537].

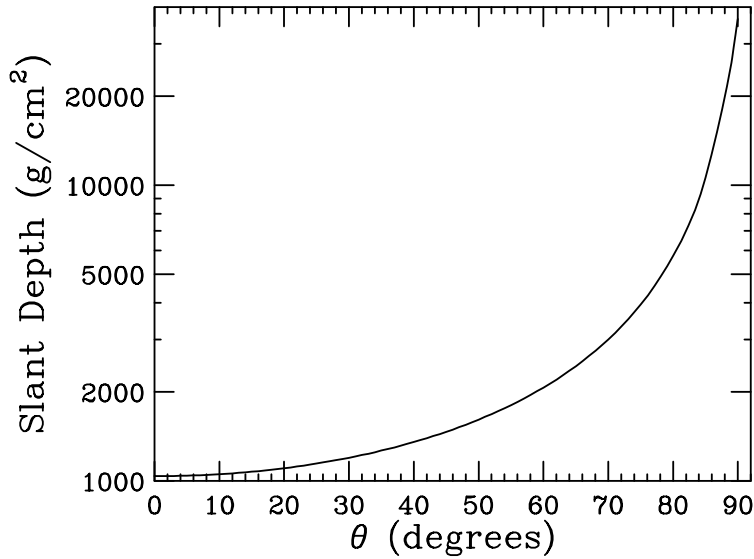


Figure 23: Slant depths corresponding to various zenith angles θ considering the curvature of the Earth. From Ref. [16].

not change by more than about 30% over the range 0–100 km above sea level. Therefore we can get a reasonable impression of the density variation by assuming an isothermal atmosphere, in which case the density $\rho_{\text{atm}}(h) \approx \rho_0 e^{-h/h_0}$, where $\rho_0 \approx 1.225 \text{ kg/m}^3$ and $h_0 = RT/(\mu g) \approx 8.4 \text{ km}$ is known as the scale-height of the atmosphere, R being the ideal gas constant, μ the average molecular weight of air, g the acceleration due to gravity and $T \approx 288 \text{ K}$. Of course, reading out such a natural calorimeter is complicated by the effects of varying aerosol and molecular attenuation and scattering.

The quantity that most intuitively describes the varying density of the atmospheric medium is the vertical atmospheric depth, $X_v(h) = \int_h^\infty \rho_{\text{atm}}(z) dz$, where z is the height. However, the quantity most relevant in air shower simulations is the slant depth, X , which defines the actual amount of air traversed by the shower. The variation of the slant depth with zenith angle is shown in Fig. 23. If the Earth curvature is not taken into account, then $X = X_v(h)/\cos \theta$, where θ is the zenith angle of the shower axis. For $\theta \lesssim 80^\circ$, the error associated with this approximation is less than 4%.

The atmospheric medium is endowed with a magnetic field. In general, the geomagnetic field is described by 3 parameters, its strength B , its inclination ι , and its declination δ . The inclination is defined as the angle between the local horizontal plane and the \mathbf{B} -field. The declination is defined as the angle between the horizontal component of the field B_\perp (i.e., perpendicular to the arrival direction of the air shower) and the geographical North (direction of the local meridian). The angle ι is positive when \mathbf{B} points downward and δ is positive when B_\perp is inclined towards the East.

4.2. Systematic uncertainties in air shower measurements from hadronic interaction models

Uncertainties in hadronic interactions at ultra-high energies constitute one of the most problematic sources of systematic error in the analysis of air showers. This section will explain the two principal schools of thought for extrapolating collider data to ultrahigh energies.

Soft multiparticle production with small transverse momenta with respect to the collision axis is a dominant feature of most hadronic events at c.m. energies $10 \text{ GeV} < \sqrt{s} < 62 \text{ GeV}$ (see e.g., [538, 539]).

Despite the fact that strict calculations based on ordinary QCD perturbation theory are not feasible, there are some phenomenological models that successfully take into account the main properties of the soft diffractive processes. These models, inspired by $1/N$ QCD expansion are also supplemented with generally accepted theoretical principles like duality, unitarity, Regge behavior, and parton structure. The interactions are no longer described by single particle exchange, but by highly complicated modes known as Reggeons. Up to about 62 GeV, the slow growth of the cross section with \sqrt{s} is driven by a dominant contribution of a special Reggeon, the Pomeron.

At higher energies, semihard (SH) interactions arising from the hard scattering of partons that carry only a very small fraction of the momenta of their parent hadrons can compete successfully with soft processes [540–547]. These semihard interactions lead to the “minijet” phenomenon, i.e. jets with transverse energy ($E_T = |p_T|$) much smaller than the total c.m. energy. Such low- p_T processes cannot be identified by jet finding algorithms, but (unlike soft processes) still they can be calculated using perturbative QCD. The cross section for SH interactions is described by

$$\sigma_{\text{QCD}}(s, p_T^{\text{min}}) = \sum_{i,j} \int \frac{dx_1}{x_1} \int \frac{dx_2}{x_2} \int_{Q_{\text{min}}^2}^{\hat{s}/2} d|\hat{t}| \frac{d\hat{\sigma}_{ij}}{d|\hat{t}|} x_1 f_i(x_1, |\hat{t}|) x_2 f_j(x_2, |\hat{t}|) , \quad (188)$$

where x_1 and x_2 are the fractions of the momenta of the parent hadrons carried by the partons which collide, $d\hat{\sigma}_{ij}/d|\hat{t}|$ is the cross section for scattering of partons of types i and j according to elementary QCD diagrams, f_i and f_j are parton distribution functions (PDFs), $\hat{s} = x_1 x_2 s$ and $-\hat{t} = \hat{s}(1 - \cos\vartheta^*)/2 = Q^2$ are the Mandelstam variables for this parton-parton process, and the sum is over all parton species. Here,

$$p_T = E_{\text{jet}}^{\text{lab}} \sin\vartheta_{\text{jet}} = \frac{\sqrt{\hat{s}}}{2} \sin\vartheta^* , \quad (189)$$

and

$$p_{\parallel} = E_{\text{jet}}^{\text{lab}} \cos\vartheta_{\text{jet}} , \quad (190)$$

where $E_{\text{jet}}^{\text{lab}}$ is the energy of the jet in the lab frame, ϑ_{jet} the angle of the jet with respect to the beam direction in the lab frame, and ϑ^* is the angle of the jet with respect to the beam direction in the c.m. frame of the elastic parton-parton collision. This implies that for small ϑ^* , $p_T^2 \approx Q^2$. The integration limits satisfy

$$Q_{\text{min}}^2 < |\hat{t}| < \hat{s}/2 , \quad (191)$$

where $Q_{\text{min}} = 1 - 2$ GeV is the minimal momentum transfer. The measured minijet cross sections indicate that the onset of SH interactions has just occurred by CERN SPS energies, $\sqrt{s} > 200$ GeV [548].

A first source of uncertainty in modeling cosmic ray interactions at ultra-high energy is encoded in the extrapolation of the measured parton densities several orders of magnitude down to low x . Primary protons that impact on the upper atmosphere with energy $\sim 10^{11}$ GeV yield partons with $x \equiv 2p_{\parallel}^*/\sqrt{s} \sim m_{\pi}/\sqrt{s} \sim 10^{-7}$, whereas current data on quark and gluon densities are only available for $x \gtrsim 10^{-5}$ to within an experimental accuracy of few percent for $Q^2 \approx 100$ GeV² [11]. In addition, extrapolation of HERA and LHC data to UHECR interactions assumes universality of the PDFs. This assumption, based on the QCD factorization conjecture (the cross section (188) can always be written in a form which factorizes the parton densities and the hard interaction processes irrespective of the order in perturbation theory and the particular hard process) holds in the limit $Q^2 \gg \Lambda_{\text{QCD}}$, where $\Lambda_{\text{QCD}} \sim 200$ MeV is the QCD renormalization scale.

For large Q^2 and not too small x , the Dokshitzer-Gribov-Lipatov-Altarelli-Parisi (DGLAP) equations [549–552]

$$\frac{\partial}{\partial \ln Q^2} \begin{pmatrix} q(x, Q^2) \\ g(x, Q^2) \end{pmatrix} = \frac{\alpha_s(Q^2)}{2\pi} \begin{pmatrix} P_{qq} & P_{qg} \\ P_{gq} & P_{gg} \end{pmatrix} \otimes \begin{pmatrix} q(x, Q^2) \\ g(x, Q^2) \end{pmatrix} \quad (192)$$

successfully predict the Q^2 dependence of the quark and gluon densities (q and g , respectively). Here, $\alpha_s = g^2/(4\pi)$, with g the strong coupling constant. The splitting functions P_{ij} indicate the probability of finding a daughter parton i in the parent parton j with a given fraction of parton j momentum. This probability will depend on the number of splittings allowed in the approximation. In the double-leading-logarithmic approximation, that is $\lim_{x \rightarrow 0} \ln(1/x)$ and $\lim_{Q^2 \rightarrow \infty} \ln(Q^2/\Lambda_{\text{QCD}})$, the DGLAP equations predict a steeply rising gluon density, $xg \sim x^{-0.4}$, which dominates the quark density at low x . HERA data are found to be consistent with a power law, $xg(x, Q^2) \sim x^{-\Delta_H}$, with an exponent Δ_H between 0.3 and 0.4 [553, 554].

The high energy minijet cross section is then determined by the dominant gluon distribution

$$\sigma_{\text{QCD}}(s, p_T^{\text{min}}) \approx \int \frac{dx_1}{x_1} \int \frac{dx_2}{x_2} \int_{Q_{\text{min}}^2}^{\hat{s}/2} d|\hat{t}| \frac{d\hat{\sigma}}{d|\hat{t}|} x_1 g(x_1, |\hat{t}|) x_2 g(x_2, |\hat{t}|), \quad (193)$$

where the integration limits satisfy

$$x_1 x_2 s > 2|\hat{t}| > 2Q_{\text{min}}^2. \quad (194)$$

Furthermore, because $d\hat{\sigma}/d|\hat{t}|$ is peaked at the low end of the $|\hat{t}|$ integration (see e.g [555]), the high energy behavior of σ_{QCD} is controlled (via the lower limits of the x_1, x_2 integrations) by the small- x behavior of the gluons [556]

$$\sigma_{\text{QCD}}(s) \propto \int_{2Q_{\text{min}}^2/s}^1 \frac{dx_1}{x_1} x_1^{-\Delta_H} \int_{2Q_{\text{min}}^2/x_1 s}^1 \frac{dx_2}{x_2} x_2^{-\Delta_H} \sim s^{\Delta_H} \ln s \underset{s \rightarrow \infty}{\sim} s^{\Delta_H}. \quad (195)$$

This estimate is, of course, too simplistic. At sufficiently small x , gluon shadowing corrections suppress the singular $x^{-\Delta_H}$ behavior of xg and hence suppress the power growth of σ_{QCD} with increasing s .

Although we have shown that the onset of semihard processes is an unambiguous prediction of QCD, in practice it is difficult to isolate these contributions from the soft interactions. Experimental evidence indicates that SH interactions can essentially be neglected up to and throughout the CERN ISR energy regime, $\sqrt{s} < 62$ GeV. Therefore, measurements made in this energy region can be used to model the soft interactions. A reasonable approach introduced in [557] is to base the extrapolation of the soft interactions on the assumption of geometrical scaling [558], which is observed to be true throughout the ISR energy range [559, 560]. We adopt the standard partial-wave amplitude in impact-parameter space $f(s, b)$, which is the Fourier transform of the elastic pp (or $p\bar{p}$) scattering amplitude. (We neglect any difference between pp and $p\bar{p}$ for $\sqrt{s} > 200$ GeV.) Geometrical scaling (GS) corresponds to the assumption that f , which *a priori* is a function of two dimensional variables b and s , depends only upon one dimensional variable $\beta = b/R(s)$, where R is the energy dependent radius of the proton, *i.e.*

$$f(s, b) = f_{\text{GS}}(\beta = b/R(s)). \quad (196)$$

Physically, this means that the opaqueness of the proton remains constant with rising energy and that the increase of the total cross section, σ_{tot} , in the ISR energy range reflects a steady growth of the radius $R(s)$. An immediate obvious consequence of GS is that the partial wave at $b = 0$ should be independent of energy

$$f(s, b = 0) = f_{\text{GS}}(\beta = 0). \quad (197)$$

Another consequence is that the ratio of elastic scattering to total cross section, $\sigma_{\text{el}}(s)/\sigma_{\text{tot}}(s)$, should be energy independent. This follows from

$$\sigma_{\text{tot}} = 8\pi \int \text{Im} f(s, b) b db \stackrel{\text{GS}}{=} 8\pi R^2(s) \int \text{Im} f_{\text{GS}}(\beta) \beta d\beta, \quad (198a)$$

and

$$\sigma_{\text{el}} = 8\pi \int |f(s, b)|^2 b db \stackrel{\text{GS}}{=} 8\pi R^2(s) \int |f_{\text{GS}}(\beta)|^2 \beta d\beta. \quad (198b)$$

To determine the gross features at high energies we can assume that the elastic amplitude has a simple form

$$F(s, t) = i \sigma_{\text{tot}}(s) e^{Bt/2}, \quad (199)$$

with B the slope parameter that measures the size of the proton [561]. This is a reasonable assumption: the amplitude is predominantly imaginary, and the exponential behavior observed for $|t| \lesssim 0.5 \text{ GeV}^2$ gives the bulk of the elastic cross section. Now, the Fourier transform $f(s, b)$ of the elastic amplitude $F(s, t)$ given by (199) has a Gaussian form in impact parameter space

$$f(s, b) = \frac{i\sigma_{\text{tot}}(s)}{8\pi B} e^{-b^2/2B}, \quad (200)$$

and it follows that

$$\text{Im} f(s, b=0) = \frac{\sigma_{\text{tot}}}{8\pi B} = \frac{2\sigma_{\text{el}}}{\sigma_{\text{tot}}}. \quad (201)$$

Equation (201) offers a very clear way to see the breakdown of GS and to identify semihard interactions from the growth of the central partial wave.

In general unitarity requires $\text{Im} f(s, b) \leq \frac{1}{2}$, which in turn implies $\sigma_{\text{el}}/\sigma_{\text{tot}} \leq \frac{1}{2}$ [561]. This seems to indicate that the Gaussian form (200) may not longer be applicable at ultra-high energies, but rather it is expected that the proton will approximate a “black disk” of radius b_0 , *i.e.* $f(s, b) = \frac{i}{2}$ for $0 < b \lesssim b_0$ and zero for $b \gtrsim b_0$. Then $\sigma_{\text{el}} \simeq \frac{1}{2}\sigma_{\text{tot}} \simeq \pi b_0^2$. In order to satisfy the unitarity constraints, it is convenient to introduce the eikonal χ defined by

$$f(s, b) = \frac{i}{2} \{1 - \exp[i\chi(s, b)]\}, \quad (202)$$

where $\text{Im} \chi \geq 0$. If we neglect for the moment the shadowing corrections to the PDFs and take $xg \propto x^{-\Delta_{\text{H}}}$ in the small- x limit we obtain, as explained above, power growth of the cross section for SH interactions, $\sigma_{\text{QCD}} \sim s^{\Delta_{\text{H}}}$ and $\text{Im} \chi(s, b=0) \gg 1$ as $s \rightarrow \infty$. Indeed we expect $\text{Im} \chi \gg 1$ (and unitarity to be saturated) for a range of b about $b=0$. Then we have

$$\sigma_{\text{tot}} = 4\pi \int_0^\infty b db \Theta(b_0 - b) \simeq 4\pi \int_0^{b_0(s)} b db = 2\pi b_0^2, \quad (203)$$

with $\chi \simeq \chi_{\text{SH}}$ and where $b_0(s)$ is such that

$$\text{Im} \chi_{\text{SH}}(s, b_0(s)) \simeq 1. \quad (204)$$

Hereafter, we ignore the small real part of the scattering amplitude, which is good approximation at high energies. The unitarized elastic, inelastic, and total cross sections (considering now a real eikonal function) are given by [562–565]

$$\sigma_{\text{el}} = 2\pi \int db b \{1 - \exp[-\chi_{\text{soft}}(s, b) - \chi_{\text{SH}}(s, b)]\}^2, \quad (205a)$$

$$\sigma_{\text{inel}} = 2\pi \int db b \{1 - \exp[-2\chi_{\text{soft}}(s, b) - 2\chi_{\text{SH}}(s, b)]\}, \quad (205b)$$

$$\sigma_{\text{tot}} = 4\pi \int db b \{1 - \exp[-\chi_{\text{soft}}(s, b) - \chi_{\text{SH}}(s, b)]\}, \quad (205c)$$

where the scattering is compounded as a sum of QCD ladders via SH and soft processes through the eikonals χ_{SH} and χ_{soft} .

Now, if the eikonal function, $\chi(s, b) \equiv \chi_{\text{soft}}(s, b) + \chi_{\text{SH}}(s, b) = \lambda/2$, indicates the mean number of partonic interaction pairs at impact parameter b , the probability p_n for having n independent partonic interactions using Poisson statistics reads, $p_n = (\lambda^n/n!) e^{-\lambda}$. Therefore, the factor $1 - e^{-2\chi} = \sum_{n=1}^{\infty} p_n$ in (205b) can be interpreted semi-classically as the probability that at least 1 of the 2 protons is broken up in a collision at impact parameter b . With this in mind, the inelastic cross section is simply the integral over all collision impact parameters of the probability of having at least 1 interaction, yielding a mean minijet multiplicity of $\langle n_{\text{minijet}} \rangle \approx \sigma_{\text{QCD}}/\sigma_{\text{inel}}$ [566]. The leading contenders to approximate the (unknown) cross sections at cosmic ray energies, SIBYLL [567] and QGSJET [568], share the eikonal approximation but differ in their *ansätze* for the eikonals. In both cases, the core of dominant scattering at very high energies is the SH cross section given in (188),

$$\chi_{\text{SH}} = \frac{1}{2} \sigma_{\text{QCD}}(s, p_T^{\text{min}}) A(s, \vec{b}), \quad (206)$$

where the normalized profile function, $2\pi \int_0^{\infty} db b A(s, b) = 1$, indicates the distribution of partons in the plane transverse to the collision axis.

In the QGSJET-like models, the core of the SH eikonal is dressed with a soft-pomeron pre-evolution factor. This amounts to taking a parton distribution which is Gaussian in the transverse coordinate distance b ,

$$A(s, b) = \frac{e^{-b^2/R^2(s)}}{\pi R^2(s)}, \quad (207)$$

with R being a parameter. For a QCD cross section dependence, $\sigma_{\text{QCD}} \sim s^{\Delta_{\text{H}}}$, one gets for a Gaussian profile

$$b_0^2(s) \sim R^2 \Delta_{\text{H}} \ln s \quad (208)$$

and at high energy

$$\sigma_{\text{inel}} = 2\pi \int_0^{b_0(s)} db b \sim \pi R^2 \Delta_{\text{H}} \ln s. \quad (209)$$

If the effective radius R (which controls parton shadowing) is energy-independent, the cross section increases only logarithmically with rising energy. However, the parameter R itself depends on the collision energy through a convolution with the parton momentum fractions, $R^2(s) \sim R_0^2 + 4\alpha'_{\text{eff}} \ln^2 s$, with

$\alpha'_{\text{eff}} \approx 0.11 \text{ GeV}^{-2}$ [569]. Thus, the QGSJET cross section exhibits a faster than $\ln s$ rise,

$$\sigma_{\text{inel}} \sim 4\pi \alpha'_{\text{eff}} \Delta_{\text{H}} \ln^2 s. \quad (210)$$

In SIBYLL-like models, the transverse density distribution is taken as the Fourier transform of the proton electric form factor, resulting in an energy-independent exponential (rather than Gaussian) fall-off of the parton density profile for large b ,

$$A(b) = \frac{\mu^2}{96\pi} (\mu b)^3 K_3(\mu b) \sim e^{-\mu b}, \quad (211)$$

where $K_3(x)$ denotes the modified Bessel function of the third kind and $\mu^2 \approx 0.71 \text{ GeV}^2$ [567]. Thus, (206) becomes

$$\chi_{\text{SH}} \sim e^{-\mu b} s^{\Delta_{\text{H}}}, \quad (212)$$

and (204) is satisfied when

$$b_0(s) = \frac{\Delta_{\text{H}}}{\mu} \ln s. \quad (213)$$

Therefore, for SIBYLL-like models, the growth of the inelastic cross section also saturates the $\ln^2 s$ Froissart bound [570], but with a multiplicative constant which is larger than the one in QGSJET-like models

$$\sigma_{\text{inel}} \sim \pi c \frac{\Delta_{\text{H}}^2}{\mu^2} \ln^2 s, \quad (214)$$

where the coefficient $c \approx 2.5$ is found numerically [569].

The main characteristics of the pp cascade spectrum resulting from these choices are readily predictable: the harder form of the SIBYLL form factor allows a greater retention of energy by the leading particle, and hence less available for the ensuing shower. Consequently, on average SIBYLL-like models predict a smaller multiplicity than QGSJET-like models [39].

In QGSJET-like models, both the soft and hard processes are formulated in terms of Pomeron exchanges. To describe the minijets, the soft Pomeron mutates into a ‘‘semihard Pomeron’’, an ordinary soft Pomeron with the middle piece replaced by a QCD parton ladder, as sketched in the previous paragraph. This is generally referred to as the ‘‘quasi-eikonal’’ model. In contrast, SIBYLL follows a ‘‘two channel’’ eikonal model, where the soft and the semi-hard regimes are demarcated by a sharp cut in the transverse momentum: SIBYLL uses a cutoff parametrization inspired in the double leading logarithmic approximation of the DGLAP equations,

$$p_T^{\text{min}}(\sqrt{s}) = p_T^0 + 0.065 \text{ GeV} \exp[0.9 \sqrt{\ln s}], \quad (215)$$

where $p_T^0 = 1 \text{ GeV}$ [571].

The transition process from asymptotically free partons to colour-neutral hadrons is described in all codes by string fragmentation models [572]. Different choices of fragmentation functions can lead to some differences in the hadron multiplicities. However, the main difference in the predictions of QGSJET-like and SIBYLL-like models arises from different assumptions in extrapolation of the parton distribution function to low energy.

The proton-air collisions of interest for air shower development cause additional headaches for event generators. Both SIBYLL and QGSJET adopt the Glauber formalism [562], which is equivalent to the eikonal approximation in nucleon-nucleon scattering, except that the nucleon density functions of the target nucleus are folded with that of the nucleon. The inelastic and production cross sections read:

$$\sigma_{\text{inel}}^{p\text{-air}} \approx 2\pi \int db b \{1 - \exp[\sigma_{\text{tot}} AT_N(b)]\} , \quad (216)$$

$$\sigma_{\text{prod}}^{p\text{-air}} \approx 2\pi \int db b \{1 - \exp[\sigma_{\text{inel}} AT_N(b)]\} , \quad (217)$$

where $T_N(b)$ is the transverse distribution function of a nucleon inside a nucleus. Here, σ_{inel} and σ_{tot} are given by (205b) and (205c), respectively. The p -air inelastic cross section is the sum of the ‘‘quasi-elastic’’ cross section, which corresponds to cases where the target nucleus breaks up without production of any new particles, and the production cross section, in which at least one new particle is generated. Clearly the development of EASs is mainly sensitive to the production cross section. Overall, the geometrically large size of nitrogen and oxygen nuclei dominates the inclusive proton-target cross section, and as a result the disagreement from model-dependent extrapolation is not more than about 15%. More complex nucleus-nucleus interactions are discussed in [573].

Adding a greater challenge to the determination of the proton air cross section at ultra-high energies is the lack of direct measurements in a controlled laboratory environment. The measured shower attenuation length, Λ_m , is not only sensitive to the interaction length of the protons in the atmosphere, $\lambda_{p\text{-air}}$, with

$$\Lambda_m = k\lambda_{p\text{-air}} = k \frac{14.4 m_p}{\sigma_{\text{prod}}^{p\text{-air}}} , \quad (218)$$

but also depends on the rate at which the energy of the primary proton is dissipated into the electromagnetic (EM) shower energy observed in the experiment. Here, Λ_m and $\lambda_{p\text{-air}}$ are in g cm^{-2} , the proton mass m_p is in g, and the inelastic production cross section $\sigma_{\text{prod}}^{p\text{-air}}$ is in mb. The value of k depends critically on the inclusive particle production cross section and its energy dependence in nucleon and meson interactions on the light nuclear target of the atmosphere. The measured depth X_{max} at which a shower reaches maximum development in the atmosphere has been the basis of cross section measurements from experiments prior to HiRes and Auger. However, X_{max} is a combined measure of the depth of the first interaction (which is determined by the inelastic cross section) and of the subsequent shower development (which has to be corrected for). The model dependent rate of shower development and its fluctuations are the origin of the deviation of k from unity in (218). As can be seen in Table 4, there is a large range of k values (from 1.6 for a very old model where the inclusive cross section exhibited Feynman scaling, to 1.15 for modern models with large scaling violations) that make the published values of $\sigma_{p\text{-air}}$ unreliable.

The HiRes Collaboration developed a quasi-model-free method of measuring $\sigma_{\text{prod}}^{p\text{-air}}$ directly [574]. This is accomplished by folding a randomly generated exponential distribution of first interaction points into the shower development program, and therefore fitting the entire distribution and not just the trailing edge. Interestingly, the measured $k = 1.21_{-0.09}^{+0.14}$ by the HiRes group is in agreement with the one obtained by tuning the data to the theory [575, 576].

A compilation of published proton-air cross section measurements is shown in Fig. 24. In the left panel we show the data without any modification. In the right panel, the published values of $\sigma_{\text{prod}}^{p\text{-air}}$ for Fly’s

Table 4: Different k -values used in cosmic ray experiments.

Experiment	k
Fly's Eye	1.6
Akeno	1.5
Yakutsk-99	1.4
EAS-TOP	1.15

Eye [584], Akeno [580], Yakutsk-99 [582], and EAS-TOP [578] collaborations have been renormalized using the *common* value of $k = 1.264 \pm 0.033(\text{stat}) \pm 0.013(\text{syst})$ [576]. We have parametrized the rise of the cross section using a functional form that saturates the Froissart bound,

$$\sigma_{\text{prod}}^{p\text{-air}} = \mathcal{A} - \mathcal{B} \ln(E/\text{GeV}) + \mathcal{C} \ln^2(E/\text{GeV}) \text{ mb}. \quad (219)$$

The curve with a fast rise, hereafter referred to as case-*i*, corresponds to $\mathcal{A} = 280$, $\mathcal{B} = 5.7$, and $\mathcal{C} = 0.9$. The slow rise of case-*ii* has the following parameters: $\mathcal{A} = 290$, $\mathcal{B} = 6.2$, and $\mathcal{C} = 0.64$.

In summary, high energy hadronic interaction models are still being refined and therefore the disparity between them can vary even from version to version [587]. At the end of the day, however, the relevant parameters boil down to two: the mean free path, $\lambda_{\text{CR-air}} = (\sigma_{\text{prod}}^{\text{CR-air}} n_{\text{atm}})^{-1}$, and the inelasticity, $y_{\text{CR-air}} = 1 - E_{\text{lead}}/E_{\text{proj}}$, where n_{atm} is the number density of atmospheric target nucleons, E_{lead} is the energy of the most energetic hadron with a long lifetime, and E_{proj} is the energy of the projectile particle. The first parameter characterizes the frequency of interactions, whereas the second one quantifies the energy lost per collision. Overall, SIBYLL has a shorter mean free path and a smaller inelasticity than QGSJET. Since a shorter mean free path tends to compensate for a smaller inelasticity, the two codes generate similar predictions for an air shower which has lived through several generations. Both models predict the same multiplicity below about 10^7 GeV, but the predictions diverge above that energy. Such a divergence readily increases with rising energy. While QGSJET predicts a power law-like increase of the number of secondaries up to the highest energy, SIBYLL multiplicity exhibits a logarithmic growth. As it is extremely difficult to observe the first interactions experimentally, it is not straightforward to determine which model is closer to reality.

4.3. Electromagnetic processes

The evolution of an extensive air shower is dominated by EM processes. The interaction of a baryonic cosmic ray with an air nucleus high in the atmosphere leads to a cascade of secondary mesons and baryons. The first few generations of charged pions interact again, producing a hadronic core, which continues to feed the EM and muonic components of the shower. Up to about 50 km above sea level, the density of atmospheric target nucleons is $n_{\text{atm}} \sim 10^{20} \text{ cm}^{-3}$, and so even for relatively low energies, say $E_{\pi^\pm} \approx 1 \text{ TeV}$, the probability of decay before interaction falls below 10%. Ultimately, the EM cascade dissipates around 90% of the primary particle's energy, and hence the total number of EM particles is very nearly proportional to the shower energy [588].

Roughly speaking, at 10^{11} GeV, baryons and charged pions have interaction lengths of the order of 40 g/cm^2 , increasing to about 60 g/cm^2 at 10^7 GeV. Additionally, below 10^{10} GeV, photons, electrons,

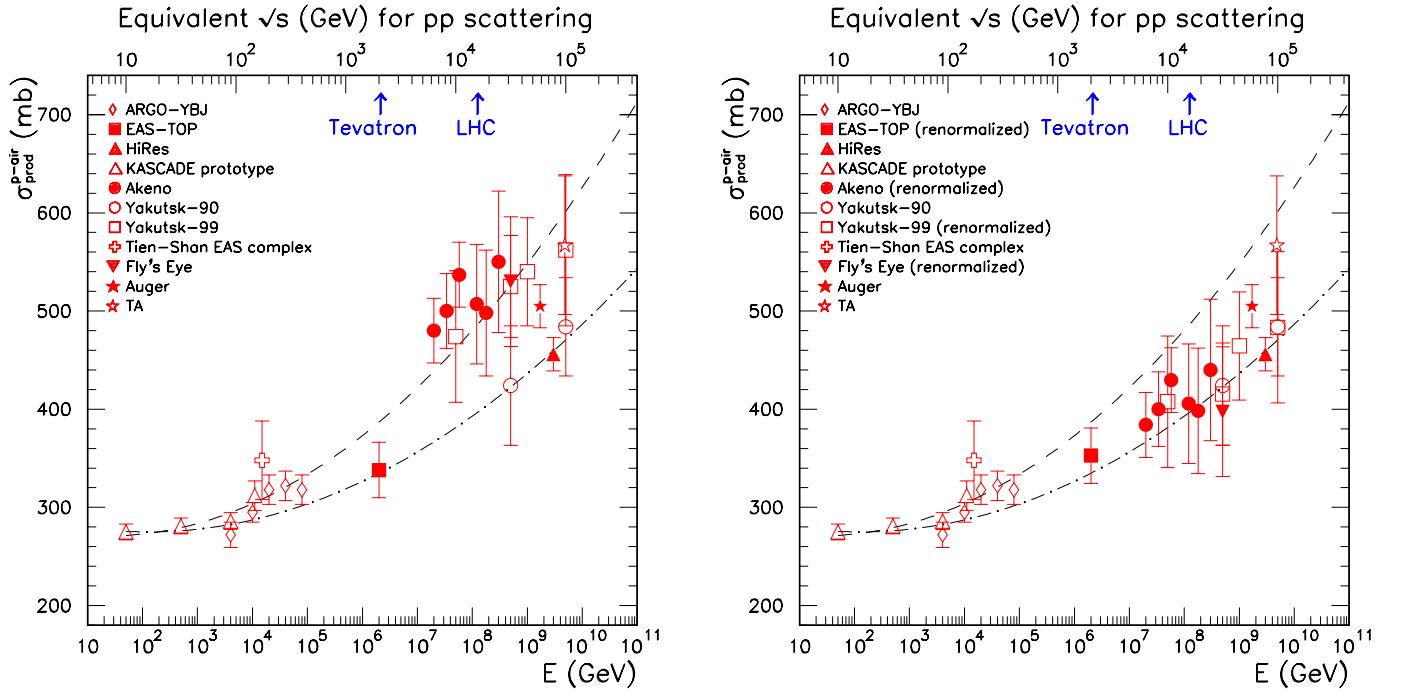


Figure 24: Compilation of proton-air production cross section from cosmic ray measurements (ARGO-YBJ [577], EAS-TOP [578], HiRes [574], KASCADE prototype [579], Akeno [580], Yakutsk-90 [581], Yakutsk-99 [582], Tien-Shan EAS complex [583], Fly’s Eye [584], Auger [585], and TA [586]). The data are compared to the parametrizations discussed in the text; case-*i* corresponds to the dashed line and case-*ii* to the dot-dashed line.

and positrons have mean interaction lengths of 37.6 g/cm^2 . Altogether, the atmosphere acts as a natural calorimeter with variable density, providing a vertical thickness of 26 radiation lengths and about 15 interaction lengths. Amusingly, this is not too different from the number of radiation and interaction lengths at the LHC detectors. For example, the CMS electromagnetic calorimeter is $\gtrsim 25$ radiation lengths deep, and the hadron calorimeter constitutes 11 interaction lengths.

By the time a vertically incident 10^{11} GeV proton shower reaches the ground, there are about 10^{11} secondaries with energy above 90 keV in the annular region extending 8 m to 8 km from the shower core. Of these, 99% are photons, electrons, and positrons, with a typical ratio of γ to e^+e^- of 9 to 1. Their mean energy is around 10 MeV and they transport 85% of the total energy at ground level. Of course, photon-induced showers are even more dominated by the electromagnetic channel, as the only significant muon generation mechanism in this case is the decay of charged pions and kaons produced in γ -air interactions [589].

It is worth mentioning that these figures dramatically change for the case of very inclined showers. For a primary zenith angle, $\theta > 70^\circ$, the electromagnetic component becomes attenuated exponentially with atmospheric depth, being almost completely absorbed at ground level. Note that the vertical atmosphere is approximately $1,000 \text{ g/cm}^2$, and is about 36 times deeper for completely horizontal showers [16]. As a result, most of the energy at ground level from an inclined shower is carried by muons.

In contrast to hadronic collisions, the electromagnetic interactions of shower particles can be calculated very accurately from quantum electrodynamics. Electromagnetic interactions are thus not a major source of systematic errors in shower simulations. The first comprehensive treatment of electromagnetic showers was elaborated by Rossi and Greisen [590]. This treatment was recently cast in a more pedagogical form by

Gaisser [243], which we summarize in the subsequent paragraphs.

The generation of the electromagnetic component is driven by electron bremsstrahlung and pair production [591]. Eventually the average energy per particle drops below a critical energy, ϵ_0 , at which point ionization takes over from bremsstrahlung and pair production as the dominant energy loss mechanism. The e^\pm energy loss rate due to bremsstrahlung radiation is nearly proportional to their energy, whereas the ionization loss rate varies only logarithmically with the e^\pm energy. Though several different definitions of the critical energy appear in the literature [11], throughout we take the critical energy to be that at which the ionization loss per radiation length is equal to the electron energy; this leads to $\epsilon_0 = 710 \text{ MeV}/(Z_{\text{eff}} + 0.92) \sim 86 \text{ MeV}$ [592].²⁰ The changeover from radiation losses to ionization losses depopulates the shower. One can thus categorize the shower development in three phases: the growth phase, in which all the particles have energy $> \epsilon_0$; the shower maximum, X_{max} ; and the shower tail, where the particles only lose energy, get absorbed or decay.

The relevant quantities participating in the development of the electromagnetic cascade are the probability for an electron of energy E to radiate a photon of energy $k = y_{\text{brem}} E$ and the probability for a photon to produce a pair e^+e^- in which one of the particles (hereafter e^-) has energy $E = y_{\text{pair}} k$. These probabilities are determined by the properties of the air and the cross sections of the two processes.

In the energy range of interest, the impact parameter of the electron or photon is larger than an atomic radius, so the nuclear field is screened by its electron cloud. In the case of complete screening, where the momentum transfer is small, the cross section for bremsstrahlung can be approximated by

$$\frac{d\sigma_{e \rightarrow \gamma}}{dk} \approx \frac{A_{\text{eff}}}{X_{\text{EM}} N_A k} \left(\frac{4}{3} - \frac{4}{3} y_{\text{brem}} + y_{\text{brem}}^2 \right), \quad (220)$$

where A_{eff} is the effective mass number of the air, X_{EM} is a constant, and N_A is Avogadro's number [594]. In the infrared limit (*i.e.* $y_{\text{brem}} \ll 1$) this approximation is inaccurate at the level of about 2.5%, which is small compared to typical experimental errors associated with cosmic air shower detectors. Of course, the approximation fails as $y_{\text{brem}} \rightarrow 1$, when nuclear screening becomes incomplete, and as $y_{\text{brem}} \rightarrow 0$, at which point the LPM and dielectric suppression effects become important, as we discuss below.

Using similar approximations, the cross section for pair production can be written as [594]

$$\frac{d\sigma_{\gamma \rightarrow e^+e^-}}{dE} \approx \frac{A_{\text{eff}}}{X_{\text{EM}} N_A} \left(1 - \frac{4}{3} y_{\text{pair}} + \frac{4}{3} y_{\text{pair}}^2 \right). \quad (221)$$

The similarities between this expression and (220) are to be expected, as the Feynman diagrams for pair production and bremsstrahlung are variants of one another.

The probability for an electron to radiate a photon with energy in the range $(k, k + dk)$ in traversing $dt = dX/X_{\text{EM}}$ of atmosphere is

$$\frac{d\sigma_{e \rightarrow \gamma}}{dk} \frac{X_{\text{EM}} N_A}{A_{\text{eff}}} dk dt \approx \left(y_{\text{brem}} + \frac{4}{3} \frac{1 - y_{\text{brem}}}{y_{\text{brem}}} \right) dy_{\text{brem}} dt, \quad (222)$$

²⁰For altitudes up to 90 km above sea level, the air is a mixture of 78.09% of N_2 , 20.95% of O_2 , and 0.96% of other gases [593]. Such a mixture is generally modeled as an homogeneous substance with atomic charge and mass numbers $Z_{\text{eff}} = 7.3$ and $A_{\text{eff}} = 14.6$, respectively.

whereas the corresponding probability density for a photon producing a pair, with electron energy in the range $(E, E + dE)$, is

$$\frac{d\sigma_{\gamma \rightarrow e^+e^-}}{dE} \frac{X_{\text{EM}} N_A}{A_{\text{eff}}} dE dt \approx \left(1 - \frac{4}{3}y_{\text{pair}} + \frac{4}{3}y_{\text{pair}}^2\right) dy_{\text{pair}} dt. \quad (223)$$

The total probability for pair production per unit of X_{EM} follows from integration of (223),

$$\int \frac{d\sigma_{\gamma \rightarrow e^+e^-}}{dE} \frac{X_{\text{EM}} N_A}{A_{\text{eff}}} dE \approx \int_0^1 \left(1 - \frac{4}{3}y_{\text{pair}} + \frac{4}{3}y_{\text{pair}}^2\right) dy_{\text{pair}} = \frac{7}{9}. \quad (224)$$

As can be seen from (222), the total probability for bremsstrahlung radiation is logarithmically divergent. However, this infrared divergence is eliminated by the interference of bremsstrahlung amplitudes from multiple scattering centers. This collective effect of the electric potential of several atoms is known as the LPM effect [44, 45]. Of course, the LPM suppression of the cross section results in an effective increase of the mean free path of electrons and photons. This effectively retards the development of the electromagnetic component of the shower. It is natural to introduce an energy scale, E_{LPM} , at which the inelasticity is low enough that the LPM effect becomes significant [595]. Below E_{LPM} , the energy loss rate due to bremsstrahlung is roughly

$$\frac{dE}{dX} \approx -\frac{1}{X_{\text{EM}}} \int_0^1 y_{\text{brem}} E \left(y_{\text{brem}} + \frac{4}{3} \frac{1 - y_{\text{brem}}}{y_{\text{brem}}}\right) dy_{\text{brem}} = -\frac{E}{X_{\text{EM}}}. \quad (225)$$

With this in mind, we now identify the constant $X_{\text{EM}} \approx 36.7 \text{ g cm}^{-2}$ with the radiation length in air defined as the mean distance over which a high-energy electron loses $1/e$ of its energy, or equivalently $7/9$ of the mean free path for pair production by a high-energy photon [11].

The most evident signatures of the LPM effect on shower development are a shift in the position of the shower maximum X_{max} and larger fluctuations in the shower development. When considering the LPM effect in the development of air showers produced by UHECRs, one has to keep in mind that the suppression in the cross sections is strongly dependent on the atmospheric depth.²¹ Since the upper atmosphere is very thin, the LPM effect becomes noticeable only for photons and electrons with energies $E_{\text{LPM}} \gtrsim 10^{10} \text{ GeV}$. For baryonic primaries, the LPM effect does not become important until the primary energy exceeds 10^{12} GeV . This is because the electromagnetic shower does not commence until after a significant fraction of the primary energy has been dissipated through hadronic interactions. At energies at which the LPM effect is important (viz. $E > E_{\text{LPM}}$), γ -ray showers will have already commenced in the geomagnetic field at almost all latitudes: primary photons with $E > 10^{10} \text{ GeV}$ convert into e^+e^- pairs, which in turn emit synchrotron photons. This reduces the energies of the primaries that reach the atmosphere, and thereby compensates for the tendency of the LPM effect to retard the shower development [597].

The muonic component of an EAS differs from the electromagnetic component for two main reasons [598]. First, muons are generated through the decay of cooled ($E_{\pi^\pm} \lesssim 1 \text{ TeV}$) charged pions, and thus the muon content is sensitive to the initial baryonic content of the primary particle. Furthermore, since there is no ‘‘muonic cascade’’, the number of muons reaching the ground is much smaller than the number of electrons. Specifically, there are about 5×10^8 muons above 10 MeV at ground level for a vertical

²¹The same occurs for dielectric suppression, although the influence is not as important as for the LPM effect [596].

10^{11} GeV proton induced shower. Second, the muon has a much smaller cross section for radiation and pair production than the electron, and so the muonic component of an EAS develops differently than does the electromagnetic component. The smaller multiple scattering suffered by muons leads to earlier arrival times at the ground for muons than for the electromagnetic component.

The ratio of electrons to muons depends strongly on the distance from the core; for example, the e^+e^- to $\mu^+\mu^-$ ratio for a 10^{11} GeV vertical proton shower varies from 17 to 1 at 200 m from the core to 1 at 2000 m. The ratio between the electromagnetic and muonic shower components behaves somewhat differently in the case of inclined showers. For zenith angles greater than 60° , the $e^+e^-/\mu^+\mu^-$ ratio remains roughly constant at a given distance from the core. As the zenith angle grows beyond 60° , this ratio decreases, until at $\theta = 75^\circ$, it is 400 times smaller than for a vertical shower. Another difference between inclined and vertical showers is that the average muon energy at ground level changes dramatically. For horizontal showers, the lower energy muons are filtered out by a combination of energy loss mechanisms and the finite muon lifetime: for vertical showers, the average muon energy is 1 GeV, while for horizontal showers it is about 2 orders of magnitude greater. The muon densities obtained in shower simulations using SIBYLL-like models fall more rapidly with lateral distance to the shower core than those obtained using QGSJET-like models. This can be understood as a manifestation of the enhanced leading particle effect in SIBYLL, which can be traced to the relative hardness of the electromagnetic form factor profile function. The curvature of the distribution ($d^2\rho_\mu/dr^2$) is measurably different in the two cases, and, with sufficient statistics, could possibly serve as a discriminator between hadronic interaction models, provided the primary species can be determined from some independent observable(s) [599].

4.4. Paper-and-pencil air shower modeling

Most of the general features of an electromagnetic cascade can be understood in terms of the toy model due to Heitler [600]. In this model, the shower is imagined to develop exclusively via bremsstrahlung and pair production, each of which results in the conversion of one particle into two. As was previously discussed, these physical processes are characterized by an interaction length $X_{\text{EM}} \approx 37.6 \text{ g/cm}^2$. One can thus imagine the shower as a particle tree with branches that bifurcate every X_{EM} , until they fall below a critical energy, $\epsilon_0 \approx 86 \text{ MeV}$, at which point energy loss processes dominate. Up to ϵ_0 , the number of particles grows geometrically, so that after $n = X/X_{\text{EM}}$ branchings, the total number of particles in the shower is $N \approx 2^n$. At the depth of shower maximum X_{max} , all particles are at the critical energy, ϵ_0 , and the energy of the primary particle, E_0 , is split among all the $N_{\text{max}} = E_0/\epsilon_0$ particles. Putting this together, we get:

$$X_{\text{max}} \approx X_{\text{EM}} \frac{\ln(E_0/\epsilon_0)}{\ln 2} . \quad (226)$$

Changes in the mean mass composition of the CR flux as a function of energy will manifest as changes in the mean values of X_{max} . This change of X_{max} with energy is commonly known as the elongation rate [601]:

$$D_e = \frac{\delta X_{\text{max}}}{\delta \ln E} . \quad (227)$$

For purely electromagnetic showers, $X_{\text{max}}(E) \approx X_{\text{EM}} \ln(E/\epsilon_0)$, and hence $D_e \approx X_{\text{EM}}$. For convenience, the elongation rate is often written in terms of energy decades, $D_{10} = \partial\langle X_{\text{max}} \rangle / \partial \log E$, where $D_{10} = 2.3D_e$. The elongation rate obtain from the Heitler model, $D_{10}^\gamma \approx 84 \text{ g/cm}^2$, is in very good agreement with the results from Monte Carlo simulations. However, the prediction for the particle number at

maximum is overestimated by a factor of about 2 to 3. Moreover, Heitler's model predicts a ratio of electron to photons of 2, whereas simulations and direct cascade measurements in the air show a ratio of the order of 1/6. This difference is due to the fact that multiple photons are emitted during bremsstrahlung and that electrons lose energy much faster than photons do.

As we have seen, baryon-induced showers are also dominated by electromagnetic processes, thus Heitler's toy model is still enlightening for such cases. For proton primaries, the multiplicity rises with energy, and the resulting elongation rate becomes smaller. This can be understood by noting that, on average, the first interaction is determined by the proton mean free path in the atmosphere, $\lambda_{p\text{-air}} = X_0$. In this first interaction the incoming proton splits into $\langle n(E) \rangle$ secondary particles, each carrying an average energy $E/\langle n(E) \rangle$. Assuming that $X_{\text{max}}(E)$ depends dominantly on the first generation of γ subshowers, the depth of maximum is obtained as in (226),

$$X_{\text{max}}(E) \approx X_0 + X_{\text{EM}} \ln[E/\langle n(E) \rangle] . \quad (228)$$

For a proper evaluation of X_{max} , it would be necessary to sum each generation of subshowers carefully from their respective points of origin, accounting for their attenuation near and after the maxima. If we now further assume a multiplicity dependence $\langle n(E) \rangle \approx n_0 E^\Delta$, then the elongation rate becomes,

$$\frac{\delta X_{\text{max}}}{\delta \ln E} = X_{\text{EM}} \left[1 - \frac{\delta \ln \langle n(E) \rangle}{\delta \ln E} \right] + \frac{\delta X_0}{\delta \ln E} \quad (229)$$

which corresponds to the form given by Linsley and Watson [43],

$$D_e = X_{\text{EM}} \left[1 - \frac{\delta \ln \langle n(E) \rangle}{\delta \ln E} + \frac{X_0}{X_{\text{EM}}} \frac{\delta \ln(X_0)}{\delta \ln E} \right] = X_{\text{EM}} (1 - B) , \quad (230)$$

where

$$B \equiv \Delta - \frac{X_0}{X_{\text{EM}}} \frac{\delta \ln X_0}{\delta \ln E} . \quad (231)$$

A precise calculation of a proton shower evolution has been carried out by Matthews [602], using the simplifying assumption that hadronic interactions produce exclusively pions, $2N_\pi$ charged and N_π neutral. π^0 's decay immediately and feed the electromagnetic component of the shower, whereas π^\pm 's soldier on. The hadronic shower continues to grow, feeding the electromagnetic component at each interaction, until charged pions reach a characteristic energy at which decay is more likely than a new interaction. The interaction length and the pion multiplicity ($3N_\pi$) are energy independent in the Heitler-Matthews model. The energy is equally shared by the secondary pions. For pion energy between 1 GeV and 10 TeV, a charged multiplicity of 10 ($N_\pi = 5$) is an appropriate number.

The first interaction diverts 1/3 of the available energy ($E_0/3$) into the EM component while the remaining 2/3 continue as hadrons. The number of hadrons increases through subsequent generation of particles and in each generation about 30% of the energy is transferred to the EM cascade. Therefore the longer it takes for pions to reach the characteristic energy $\xi_c^{\pi^\pm} \sim 20$ GeV (below which they will decay into muons), the larger will be the EM component. Consequently, in long developing showers the energy of the muons from decaying pions will be smaller. In addition, because of the density profile of the atmosphere, $\xi_c^{\pi^\pm}$ is larger high above ground than at sea level and deep showers will produce fewer muons.

This positive correlation introduces a link between the primary cosmic ray interaction cross section on air and the muon content at ground level. According to those principles, primaries with higher cross sections will have a larger muon to electron ratio at ground level.

To obtain the number of muons in the shower, one simply assumes that all charged pions decay into muons when they reach the critical energy: $N_\mu = (2N_\pi)^{n_c}$, where $n_c = \ln(E_0/\xi_c^{\pi^\pm})/\ln(3N_\pi)$ is the number of steps needed for the pions to reach ξ_c^π . Introducing $\beta = \ln(2N_\pi)/\ln(3N_\pi)$ we have

$$N_\mu = (E_0/\xi_c^{\pi^\pm})^\beta. \quad (232)$$

For $N_\pi = 5$, $\beta = 0.85$. Unlike the electron number, the muon multiplicity does not grow linearly with the primary energy, but at a slower rate. The precise value of β depends on the average pion multiplicity used. It also depends on the inelasticity of the hadronic interactions. Assuming that only half of the available energy goes into the pions at each step (rather than all of it, as done above) would lead to $\beta = 0.93$. Detailed simulations give values of β in the range 0.9 to 0.95 [569].

The first interaction yields $N_\gamma = 2N_{\pi^0} = N_{\pi^\pm}$. Each photon initiates an EM shower of energy $E_0/(3N_{\pi^\pm}) = E_0/(6N_\pi)$. Using pp data [11], we parametrized the charged particle production in the first interaction as $N_{\pi^\pm} = 41.2(E_0/1 \text{ PeV})^{1/5}$. Now, from the approximation in (228), based on the sole evolution of the EM cascade initiated by the first interaction, we obtain

$$X_{\text{max}}^p = X_0 + X_{\text{EM}} \ln[E_0/(6N_\pi\epsilon_0)] = (470 + 58 \log_{10}[E_0/1 \text{ PeV}]) \text{ g/cm}^2. \quad (233)$$

This falls short of the full simulation value by about 100 g/cm^2 [602].

A good approximation of the elongation rate can be obtained when introducing the cross section and multiplicity energy dependence. Using a p -air cross section of 550 mb at 10^9 GeV and a rate of change of about 50 mb per decade of energy leads to [603]

$$X_0 \simeq 90 - 9 \log(E_0/\text{EeV}) \text{ g/cm}^2. \quad (234)$$

Now, assuming (as in [602]) that the first interaction initiates $2N_\pi$ EM cascades of energy $E_0/6N_\pi$, with $N_\pi \propto (E_0/\text{PeV})^{1/5}$ for the evolution of the first interaction multiplicity with energy, we can calculate the elongation rate

$$D_{10}^p = \frac{dX_{\text{max}}}{d \log E_0} = \frac{d(X_0 \ln 2 + X_{\text{EM}} \ln[E_0/(6N_\pi\epsilon_0)])}{d \log E_0} = \frac{4}{5} D_{10}^\gamma - 9 \ln 2 \simeq 62 \text{ g/cm}^2. \quad (235)$$

This result is quite robust as it only depends on the cross section and multiplicity evolution with energy. It is in good agreement with Monte Carlo simulation [569].

To extend this discussion to heavy nuclei, we can apply the superposition principle as a reasonable first approximation. In this approximation, we pretend that the nucleus comprises unbound nucleons, such that the point of first interaction of one nucleon is independent of all the others. Specifically, a shower produced by a nucleus with energy E_0 and baryon number A is modeled by a collection of A proton showers, each with A^{-1} of the nucleus energy. Modifying Eq. (226) accordingly one easily obtains $X_{\text{max}} \propto \ln(E_0/A)$. Assuming that B is not changing with energy, one obtains for mixed primary composition [43]

$$D_e = X_0 (1 - B) \left[1 - \frac{\partial \langle \ln A \rangle}{\partial \ln E} \right]. \quad (236)$$

Thus, the elongation rate provides a measurement of the change of the mean logarithmic mass with energy. One caveat of the procedure discussed above is that (230) accounts for the energy dependence of the

cross section and violation of Feynman scaling only for the first interaction. Note that subsequent interactions are assumed to be characterized by Feynman scaling and constant interaction cross sections; see Eq. (231). Above 10^7 GeV, these secondary interactions play a more important role, and thus the predictions of Eq. (236), depending on the hadronic interaction model assumed, may vary by up to 20% [569].

The muon content of an EAS at ground level N_μ , as well as the ratio N_μ/N_e , are sensitive to primary composition (here, N_e is the electron content at ground level). To estimate the ratio of the muon content of nucleus-induced to proton-induced showers, we can resort again to the principle of superposition. Using $\beta = 0.93$ we find that the total number of muons produced by the superposition of A individual proton showers is, $N_\mu^A \propto A(E_A/A)^{0.93}$. Consequently, in a vertical shower, one expects a cosmic ray nucleus to produce about $A^{0.07}$ more muons than a proton. This implies that a shower initiated by an iron nucleus produces about 30% more muons than a proton shower.

Over the past few decades, it has been suspected that the number of registered muons at the surface of the Earth is by some tens of percentage points higher than expected with extrapolations of existing hadronic interaction models [604, 605]. The latest study from the Auger Collaboration has strengthened this suspicion, using a novel technique to mitigate some of the measurement uncertainties of earlier methods [42]. The new analysis of Auger data suggests that the hadronic component of showers (with primary energy $10^{9.8} < E/\text{GeV} < 10^{10.2}$) contains about 30% to 60% more muons than expected. The significance of the discrepancy between data and model prediction is somewhat above 2.1σ . The TA Collaboration also reported a muon signal which is larger in the data than in the air shower Monte Carlo prediction [606]. Many models have been proposed to explain this anomaly [607–610].

While the toys models discussed above are very useful for imparting a first intuition regarding global shower properties, the details of shower evolution are far too complex to be fully described by a simple analytical model. Full Monte Carlo simulation of interaction and transport of each individual particle is required for precise modeling of the shower development. For details on the various Monte Carlo packages and their predictions, see e.g., [611, 612].

5. UHECR as probes of particle physics beyond the electroweak scale

5.1. Testing models of the early universe via top-down production of cosmic rays and neutrinos

In an epic paper, well ahead of its time, Lemaître – a forerunner of the Big Bang hypothesis – introduced the idea that the entire material filling the universe, as well as the universe’s expansion, originated in the super-radioactive disintegration of a “Primeval Atom”, which progressively decayed into atoms of smaller and smaller atomic weight [613]. The CRs were introduced in this picture as the energetic particles emitted in intermediate stages of the decay-chain. Echoing Lemaître, in the so-called “top-down models”, extreme energy ($\gg 10^{11}$ GeV) cosmic rays and neutrinos arise in the decay of topological defects [614–623] and super-heavy elementary X -particles [624–630].

To maintain an appreciable decay rate today, it is necessary to tune the X lifetime to be longer (but not too much longer) than the age of the universe, or else “store” short-lived X particles in topological vestiges of early universe phase transitions (such as magnetic monopoles, cosmic strings, cosmic necklaces, etc.). Discrete gauged symmetries [631–633] or hidden sectors [634, 635] are generally introduced to stabilize the X particles. Higher dimensional operators, wormholes, and instantons are then invoked to break the new

symmetry super-softly to maintain the long lifetime [624, 636] (collisional annihilation has been considered too [637]). Quanta associated with these fields are typically of the order of the symmetry-breaking scale, which in Grand Unified Theories (GUTs) can be $\sim 10^{16} - 10^{19}$ GeV. Arguably, these metastable super-heavy relics may constitute (a fraction of) the dark matter in galactic haloes.

The cascade decay to cosmic ray particles is driven by the ratio of the number density of the X -particle $n_X = \rho_c \Omega_X / M_X$ to its decay time τ_X , where M_X is the mass of the X -particle and $\rho_c \simeq 1.054 \times 10^{-4} h^2 \text{ GeV cm}^{-3}$ is the critical density in terms of the present Hubble parameter $h \equiv H_0 / 100 \text{ km s}^{-1} \text{ Mpc}^{-1}$. This cascade is very model dependent, as neither the cosmic average mass density contributed by the relics Ω_X , nor τ_X is known with any degree of confidence. In addition, the precise decay modes of the X 's and the detailed dynamics of the first generation of secondaries depend on the exact nature of the X particles under consideration. However, one expects the bulk flow of outgoing particles to be almost independent of such details, enabling one to infer from the “known” evolution of quarks and leptons the gross features of the X particle decay: the strongly interacting quarks would fragment into jets of hadrons containing mainly pions together with a 3% admixture of nucleons [638–640]. This implies that the injection spectrum is a rather hard fragmentation-type shape (with an upper limit usually fixed by the GUT scale) and dominated by γ -rays and neutrinos produced via pion decay. Therefore, the ν/p and γ/p ratios can be used as a diagnostic tool in determining the possible contribution of X particle decay to the UHECR spectrum without violating any observational flux measurements or limits at higher or lower energies [641, 642]. In particular, neutrino and γ -ray fluxes depend on the energy released integrated over redshift, and thus on the specific top-down model. Recall that the electromagnetic energy injected into the Universe above the pair production threshold on the CMB is recycled into a generic cascade spectrum below this threshold on a short time scale compared with the Hubble time. Therefore, it can have several potential observable effects, such as modified light element abundances due to ${}^4\text{He}$ photodisintegration, or induce spectral distortions of universal γ -ray and neutrino backgrounds [643, 644]. Additionally, measurements of the diffuse GeV γ -ray flux, to which the generic cascade spectrum would contribute directly, limit significantly the parameter space in which X 's can contribute to the UHECR intensity, especially if there is already a significant contribution to this background from conventional sources such as unresolved γ -ray blazars [645, 646]. EGRET data in the energy interval $10 \text{ MeV} < E_\gamma < 100 \text{ GeV}$, with a spectrum $\propto E_\gamma^{-2.10 \pm 0.03}$ [647], constrain the energy density of the cascade photons $\omega_{\text{cas}} < 5 \times 10^{-6} \text{ eV/cm}^3$ [648]. The first 10 months of *Fermi*-LAT observations have provided a stronger limit on the isotropic diffuse gamma-ray background [649]. For the $200 \text{ MeV} < E_\gamma < 120 \text{ GeV}$, the more steep power-law spectrum $\propto E_\gamma^{-(2.41 \pm 0.05)}$ leads to a lower cascade energy density $\omega_{\text{cas}} = 5.8 \times 10^{-7} \text{ eV/cm}^3$ [650]. A more stringent limit can be extracted from the 50 months observation of *Fermi*-LAT [651]. The limit becomes stronger due to the highest energy bin $580 < E_\gamma / \text{GeV} < 820$, where the *Fermi*-LAT intensity is particularly low. The current upper bound on the energy density of cascade radiation, $\omega_{\text{cas}} < 8.3 \times 10^{-8} \text{ eV/cm}^3$ [652], limits significantly the parameter space in which cosmologically distant X 's can generate on decay UHECRs and UHEC ν s [661].²²

Super-heavy X -particles could behave as cold dark matter and cluster efficiently in all gravitational potential wells. If this were the case, their abundance in our galactic halo would be enhanced above their cosmological abundance by a factor $f_{\text{cos}} \equiv n_X^{\text{halo}} / n_X^{\text{cos}}$. If for simplicity we assume an spherical halo of radius $R_{\text{halo}} \sim 100 \text{ kpc}$ and density $\rho_{\text{halo}} \sim 0.3 \text{ GeV cm}^{-3}$, then $f_{\text{cos}} \sim 3 \times 10^4 h^{-2}$ [628]. The actual

²²The cascade limit on Φ_γ also constrains the photon flux produced by extreme energy neutrinos interacting in the local universe via the Z -burst mechanism [653–655].

density of dark matter in the halo must of course fall off as r^{-2} to account for the flat rotation curve of the disk but we do not consider it necessary herein to investigate realistic mass models. All in all, the universal density of X -particles is smaller than the halo density by about the same numerical factor by which the distance to the horizon ($\sim 3000 h^{-1}$ Mpc) exceeds the halo radius. Therefore, in this scenario ultra-high-energy photons and nucleons from the halo of our Galaxy would provide the dominant contribution to the intensity observed on Earth. This is because photons from the decay of X -particles which are clustered on the Galactic halo are not degraded in energy. The extragalactic component of UHECRs is suppressed by the smaller extragalactic density of X -particles and so the cascade photon limit is relaxed [636]. Currently, the most restrictive constraint on the lifetime τ_X of super-heavy relics clustered on the Galactic halo comes from Auger upper limits on the intensity of ultra-high-energy photons; see Table 2. Auger data place a lower bound $\tau_X \gtrsim 10^{22}$ yr [656]. Next generation of UHECR observatories will be able to effectively study supermassive X 's, with possible lifetime detections or constraints reaching values as high as $\tau_X \sim 10^{24}$ yr [656].

Extreme-energy CR and ν physics provides a framework to search for cosmic strings complementary to those based on the gravitational effects of strings, including structure formation, CMB data, gravitational radiation, and gravitational lensing. For strings with a symmetry breaking energy scale Λ , the strongest bound due to lensing effects is $G\Lambda^2 \lesssim 10^{-7}$ [657], and the bound from millisecond pulsar observations is $G\Lambda^2 \lesssim 4 \times 10^{-9}$, where G is Newton's constant. Next generation gravitational wave detectors are expected to probe $G\Lambda^2 \sim 10^{-12}$ [659, 660]. Remarkably, next generation UHECR detectors will be able to detect extreme energy neutrinos from strings with $G\Lambda^2$ values as small as $\sim 10^{-20}$ [661].

In summary, at the present level of knowledge we can argue that astrophysical sources cannot accelerate CRs to energies $\gtrsim 10^{12}$ GeV, with the maximum neutrino energy an order of magnitude lower. Therefore, detection of neutrinos with $E_\nu > 10^{11}$ GeV would be momentous discovery, and a clean signature that top-down models are at play.

Super-heavy right-handed neutrinos (ν_R 's) are also interesting dark matter candidates, particularly in minimal extensions of the SM, i.e. constructs with the usual gauge group $SU(3)_C \otimes SU(2)_L \otimes U(1)_Y$ and the usual matter fields but including a right-handed neutrino in each generation [662, 663]. If one of the ν_R 's contributes to the dark matter sector, then its non-gravitational couplings do not necessarily have to vanish, but have to be small enough so that the ν_R has a lifetime $\tau_{\nu_R} \gg H_0^{-1} = 9.778 h^{-1}$ Gyr.²³ This opens up the possibility to indirectly observe ν_R through its decay products. For two-body decays, conservation of angular momentum forces the ν_R to decay into a Higgs boson and a light Majorana neutrino, i.e. $\nu_R \rightarrow H\nu_L$. This decay mode is particularly interesting for recent observations of the ANITA experiment.²⁴

The three balloon flights of the ANITA experiment have resulted in the observation of two unusual upgoing showers with energies of $\mathcal{O}(100)$ PeV [667, 668]. In principle, these events could originate in the atmospheric decay of an upgoing τ -lepton produced through a charged current interaction of ν_τ inside the

²³IceCube data set a lower limit on the lifetime of the right-handed neutrino of $\mathcal{O}(10^{29}$ s) [664].

²⁴The Antarctic Impulsive Transient Antenna (ANITA) is an experiment which has completed four long-duration balloon flights above Antarctica. ANITA searches for impulsive radio-Cherenkov emission arising from the Askaryan charge excess which develops in ultra-high energy neutrino-induced particle cascades in the Antarctic ice. The large radio transparency of ice allows for the radio-Cherenkov pulse from these cascades to be recorded by a cluster of balloon-borne antennas, flying at an altitude of 35 to 40 km. The details of the ANITA instrument are given in e.g. [665]. ANITA Collaboration reported the most stringent upper limits to date on the intensity of extreme energy neutrinos, e.g., for $E_\nu \sim 10^{12}$ GeV, the energy-squared-weighted intensity is at the level of 20 WB [666].

Earth. However, the relatively steep arrival angles of these events (about 30° above the horizon) create a tension with the SM neutrino-nucleon interaction cross section. It is compelling that the two ANITA events are similar in energy and were observed at roughly the same angle above the horizon. This fueled speculation that the two events have similar energies because they result from the two-body decay of a new quasi-stable relic, itself gravitationally trapped inside the Earth [669].

A dense population of ν_R is expected at the center of the Earth because as the Earth moves through the halo, the ν_R scatter with Earth matter, lose energy and become gravitationally trapped. An accumulated ν_R then decays into a Higgs and an active neutrino that propagates through the Earth and produces a τ lepton near the Earth's surface. The particular angle of the ANITA events is a combination of the dark matter distribution in the Earth, the neutrino interaction cross section, and the τ survival probability. The non-gravitational couplings have to be chosen to produce a long lifetime and the needed abundance of right-handed neutrinos in the Earth to yield the two ANITA events. To achieve a sizable dark matter density in the Earth self-interactions may be invoked.²⁵

The event rate integrated over the entire Earth at a particular time is

$$\text{Rate} \equiv \frac{dN}{dt} = 4\pi \int_0^{R_\oplus} r^2 dr \frac{n(r, t)}{\tau_{\nu_R}},$$

where $n(r, t)$ is the number density of ν_R at time t and R_\oplus is the Earth's radius [669]. The observable rate today ($t = t_0$), as a function of nadir angle θ_n is given by

$$A_{\text{eff}} \frac{d\text{Rate}}{d|\cos\theta_n|} = 2\pi A_0 \times 2\pi \int_{R_\oplus \sin\theta_n}^{R_\oplus} r^2 dr \frac{n(r, t_0)}{\tau_{\nu_R}} \left(e^{-(l_+/\lambda)} + e^{-(l_-/\lambda)} \right) \mathcal{E}(\theta_n), \quad (237)$$

where the effective area $A_{\text{eff}} = A_0 \mathcal{E}(\theta_n)$ defines the experimental efficiency \mathcal{E} that includes the target area dependence on θ_n but not the $e^{-l/\lambda}$ suppression factor, which is given explicitly in the integrand, and where $\lambda = 1.7 \times 10^7 / (\sigma/\text{pb}) \text{ km w.e.}$ is the mean-free-path, with σ the neutrino-nucleon CC cross section. Here, l_\pm are the roots of $R_\oplus^2 + l^2 - 2R_\oplus l \cos\theta_n = r^2$, i.e., $l_\pm = R_\oplus [\cos\theta_n \pm \sqrt{(r/R_\oplus)^2 - \sin^2\theta_n}]$. The fact that for fixed r , we have two special values for l , i.e. l_\pm , can be easily seen as follows: Draw a circle at constant r less than R_\oplus about the earth's center. Then draw a line through the circle, and intersecting the ANITA detector. This line represents the trajectory of the traveling particle to ANITA, and necessarily crosses the fixed circle at two special points, at trajectory distances which here we have named l_\pm . The quadratic equation for l derives from the cosine theorem. Of course, if r were too small, then the trajectory at fixed θ_n would not intersect the circle at fixed radius r at all; this is the origin of the lower limit in the integration of dr . Note that (237) has a factor of 2π and not the original 4π of (237) because we do not integrate over $d\cos\theta_n$; this angle is fixed by the experimental observation. The second factor of 2π comes from the fact that the decay of the right-handed neutrino is isotropic. For ANITA, $\mathcal{E}(\theta_n)$ vanishes for $\theta_n < 35^\circ$, peaks at about 75° , and vanishes above 85° . The two unusual ANITA events occur at similar angles above the horizon, so we may

²⁵The number of right-handed neutrinos intercepted by the Earth during its lifetime is $\sim t_\oplus \rho_{\text{DM}} v_\oplus \pi R_\oplus^2 / M_{\nu_R} \sim 10^{33.6}$, where $t_\oplus = 4.55 \text{ Gyr}$ is the age of the Earth [670], $\rho_{\text{DM}} \simeq 0.5 \text{ (GeV}/c^2) \text{ cm}^{-3}$ is the dark matter mass density in the Galactic plane [671–674], $v_\oplus \simeq 200 \text{ km/s}$ is the average velocity of the Earth relative to the dark matter particles, and $M_{\nu_R} \sim 5 \text{ PeV}$ [662, 663]. The average number density within the Earth is $\sim 3f_{\text{cap}} t_\oplus \rho_{\text{DM}} v_\oplus / (4R_\oplus M_{\nu_R}) \sim 10^{21.7} f_{\text{cap}} \text{ km}^{-3}$, where f_{cap} is the fraction of ν_R 's captured by the Earth [675]. Thus, for $\tau_{\nu_R} \sim 10^{29} \text{ s}$ [664], a decay rate on the order of 1 per km^3 per yr would require f_{cap} to be $\mathcal{O}(1)$.

set the peak of the distribution at $\sim 30^\circ$ above the horizon, corresponding to a nadir angle of $\theta_n \sim 60^\circ$. So, taking the view that the event distribution is maximized at $\theta_n = 60^\circ$ by a combination of ANITA's efficiency and the dark matter distribution in the Earth, it follows that

$$\left. \frac{d^2 \text{Rate}}{d|\cos \theta_n|^2} \right|_{\cos \theta_n = \frac{1}{2}} = 0. \quad (238)$$

This result becomes a constraint on the model parameters in (237), suggesting an atypical dark matter density distribution in the Earth. Integrating over the duration of the experiment yields the event number as opposed to the event rate.

Data from the fourth ANITA flight is currently being analyzed and may lead to further enlightenment. The second generation of the Extreme Universe Space Observatory (EUSO) instrument, to be flown aboard a super-pressure balloon (SPB) in 2022 will monitor the night sky of the Southern hemisphere for upgoing showers emerging at large angles below the horizon, providing an important test of the unusual ANITA events [676].

5.2. Search for Lorentz invariant breaking effects

At present, there is no reason to anticipate the existence of a universal scale below which our present notion of flat spacetime geometry is not valid. However, Lorentz invariance should not be accepted on faith but rather as a plausible hypothesis subject to experimental test. It is possible to introduce the notion of Lorentz invariance violation either with or without accompanying anomalous kinematics. If no anomalous kinematics is involved [677–679], any search for Lorentz invariant breaking effects will require testing length scales below 10^{-20} cm or less. However, introducing anomalous kinematical constraints allows tiny departures from Lorentz invariance, which would be undetectable at the electroweak scale, to be magnified rapidly with rising energy. For example, if Lorentz invariance is broken in the form of non-standard dispersion relations for free particles,

$$E^2 = \mathbf{p}^2(1 + 2\delta) + m^2 \quad (239)$$

then absorption and energy loss processes for UHECR interactions would be modified [680]. Recall that the GZK interactions (photopion production and nucleus photodisintegration) are characterized by well defined energy thresholds (near the excitation of the $\Delta^+(1232)$ and the GDR, respectively), which can be predicted on the basis of Lorentz invariance. Therefore, the experimental confirmation that UHECR processes occur at the expected energy thresholds can be considered as an indirect piece of evidence supporting Lorentz symmetry under colossal boost transformations [681].

The canonical formalism to explore observable consequences of Lorentz invariant breaking effects was developed by Coleman and Glashow (CG), assuming renormalizable and gauge invariant perturbations to the SM Lagrangian that are rotationally invariant in a preferred frame, but not Lorentz invariant [680]. By shifting both the renormalized mass by the small amount $m \rightarrow m/(1 + 2\delta)$ and the velocity by the amount $c_{\text{mav}} = \sqrt{1 + 2\delta} \simeq 1 + \delta$ in (239) one recovers the standard form of the dispersion relations

$$E^2 = \mathbf{p}^2 c_{\text{mav}}^2 + m^2 c_{\text{mav}}^4, \quad (240)$$

where c_{mav} is identified as the maximum attainable velocity of the free particle in the CMB frame. This implies that in the CG framework different particles may have different maximum attainable velocities,

which in principle can all be different from 1 and also different from one another. In such a case, the possible departure from Lorentz invariance can be phrased in terms of the difference between the particle maximum attainable velocities

$$\delta_{ij} = c_i - c_j, \quad (241)$$

where c_i denotes the maximum attainable velocity of a particle species i . From (239) and (241), a dispersion relation can be constructed for a particle species i ,

$$E^2 = \mathbf{p}^2(1 + 2\delta_i) + m_i^2, \quad (242)$$

where δ_i is the difference between the maximum attainable velocity for particle species i and the speed of light in the low momentum limit where $c = 1$. As long as all limiting velocities are less than or equal to the limiting velocity of the photon, causality is preserved: new “lightcones” appear inside the lightcone. To be generic, it is feasible to add small energy-dependent Lorentz-violating terms in the free particle Lagrangian that are suppressed by powers of some quantum gravity energy scale $\mathcal{O}(M_{\text{Pl}})$ [682–686]. This leads to dispersion relations having a series of smaller and smaller terms proportional to $\mathbf{p}^{n+2}/M_{\text{Pl}}^n \simeq E^{n+2}/M_{\text{Pl}}^n$,

$$\delta_i = \sum_{n=0}^{\infty} \eta_i^{(n)} \left(\frac{E}{M_{\text{Pl}}} \right)^n. \quad (243)$$

In our discussion we will adopt the GC formalism that truncates the series (243) considering only the first $n = 0$ term. For a comprehensive review on astrophysical constraints on Lorentz symmetry, see e.g., [687, 688].

As we have seen in Sec. 3.2.2 if one assumes Lorentz invariant kinematics, the energy threshold of photopion production via interactions of UHECR protons (with initial laboratory energy E) and low energy photons of the CMB (with laboratory energy ε) is determined by the relativistic invariance of the square of the total four-momentum of the proton-photon system, and is given by (4). Now, (4) together with (125b) evaluated at threshold, $s = (m_p + m_\pi)^2$, lead to the threshold condition for head on collisions in the laboratory frame,

$$4\varepsilon E_\pi = \frac{m_\pi^2(2m_p + m_\pi)}{m_p + m_\pi}. \quad (244)$$

If Lorentz invariance is broken because $c_\pi > c_p$, then the threshold energy for photopion production is modified. Namely, using (239), (241) and (244) it is easily seen that the square of the four-momentum is shifted from its Lorentz invariant form and the threshold condition (244) becomes [680]

$$4\varepsilon E_\pi = \frac{m_\pi^2(2m_p + m)}{m_p + m_\pi} + 2\delta_{\pi p} E_\pi^2. \quad (245)$$

If Lorentz symmetry is unbroken, $\delta_{\pi p} = 0$ and (245) leads to the conventional threshold for a head-on collision (244). Otherwise, (245) is a quadratic form in E_π , with real roots if

$$\delta_{\pi p} \leq \frac{2\varepsilon^2(m_p + m_\pi)}{m^2(2m_p + m_\pi)} \simeq \frac{\varepsilon^2}{m_\pi^2} \simeq 3.23 \times 10^{-24} \left(\frac{\varepsilon}{2.35 \times 10^4 \text{ eV}} \right)^2. \quad (246)$$

If one hypothesizes a Lorentz invariance violation with $\delta_{\pi p} > 0$, pion photoproduction would only proceed through interactions with CMB photons that can satisfy (246). As noted above, the dominance of photopion

production –via excitation of $\Delta^+(1232)$ – is near the photopion production threshold. Hence, combining (245) and (246) it is straightforward to see that for $\delta_{\pi p} > 0$ photopion interactions leading to the GZK suppression would occur for “low energy” protons interacting with CMB photons on the Wien tail of the Planck distribution. Note, however, that for “high energy” protons, which would normally interact with “low energy” photons, the photopion production process will be forbidden. Thus, the observed UHECR spectrum may exhibit the characteristics of GZK suppression near the normal GZK energy threshold, but the UHECR spectrum can *recover* at higher energies, because photopion interactions at higher proton energies may be forbidden. The observed spectrum, which is shown in Fig. 2, has no signal of the GZK recovery. Indeed, the best fit to the data considering Lorentz invariant violation effects and uniform distribution of proton sources yields $\delta_{\pi p} = 3.0_{-3.0}^{+1.5} \times 10^{-23}$, consistent with an upper limit of 4.5×10^{-23} [689, 690].

Studies of the CR nuclear composition, which are also shown in Fig. 2, indicate that there is a significant fraction of nuclei at the high-end of the energy spectrum. The dispersion relation for nuclei can be written assuming a superposition model for nuclei, i.e. considering them as the combination of A nucleons of energy E/A [691, 692]. Actually, since we expect nuclear physics to have negligible Lorentz effects it is reasonable to assume $\delta_{A,Z} = \delta/A^2$, where δ regulates deviations from Lorentz symmetry in the nucleon.

Duplicating the procedure established to simultaneously fit the spectrum and nuclear composition [97] the Auger Collaboration performed a search for Lorentz invariant breaking effects [32]. In the Auger analysis the UHECR sources are assumed to be identical and homogeneously distributed in a co-moving volume, and the nuclear composition at the sources is assumed to be a mix of ^1H , ^4He , ^{14}N , and ^{28}Si . The source emission rate per volume is described by

$$\mathcal{Q}_0(E', A') = f(A') \mathcal{Q}_0 \left(\frac{E'}{\text{EeV}} \right)^{-\gamma} f_{\text{cut}}(E', Z', E_p^{\text{max}}), \quad (247)$$

where $f(A')$ is the fraction of isotopes of type A' emitted with $E = 10^9$ GeV. The cutoff of the source spectra is modulated by

$$f_{\text{cut}}(E', Z', E_p^{\text{max}}) = \begin{cases} 1 & E' < Z' E_p^{\text{max}} \\ \exp[1 - E'/(Z' E_p^{\text{max}})] & E' > Z' E_p^{\text{max}} \end{cases} ; \quad (248)$$

note a minor difference with the cutoff function in (163). The free parameters of the fit are the spectral index γ , the cutoff rigidity E_p^{max} , the normalization \mathcal{Q}_0 , and three of the fractions $f(A')$, the fourth being fixed by $\sum_{A'} f(A') = 1$. Since the effect of enhancing δ is to increase the interaction length of the particles, a way to investigate an extreme case is to switch off all the interactions with background photons [693]. The maximal Lorentz invariance violation, δ_{max} , is simulated with a simplified version of the propagation code, where only the adiabatic energy losses due to the expansion of the Universe are taken into account. Both the spectrum and composition are fitted at energies $\log_{10}(E/\text{GeV}) > 9.7$, i.e. above the ankle.

Because the intensity J and the X_{max} distribution are independent measurements, the likelihood function can be written as $\mathcal{L} = \mathcal{L}_J \mathcal{L}_{X_{\text{max}}}$. The goodness-of-fit is assessed with a generalized χ^2 (the deviance, D), defined as the negative log-likelihood ratio of a given model and the saturated model that perfectly describes the data [97]

$$D = D(J) + D(X_{\text{max}}) = -2 \ln(\mathcal{L}/\mathcal{L}^{\text{sat}}) = -2 \ln(\mathcal{L}_J/\mathcal{L}_J^{\text{sat}}) - 2 \ln(\mathcal{L}_{X_{\text{max}}}/\mathcal{L}_{X_{\text{max}}}^{\text{sat}}). \quad (249)$$

The parameter δ characterizing the level of Lorentz invariance violation is taken to be the same for the photopion and photodisintegration process. The simulations are performed for various values of δ and the

Table 5: Best fit parameters. Fractions are defined at fixed energy = 10^9 GeV [32].

δ	γ	$\log_{10}(E_p^{\max}/\text{GeV})$	H (%)	He (%)	N (%)	Si (%)	$D(J)$	$D(X_{\max})$	D
0	0.96	9.68	0.	67.3	28.1	4.6	13.3	161.1	174.4
5×10^{-24}	0.91	9.65	0.	71.8	23.9	4.3	15.1	163.5	178.5
1×10^{-23}	0.91	9.65	0.	71.4	24.3	4.3	14.9	163.6	178.5
1×10^{-22}	0.94	9.65	0.	72.8	22.7	4.6	18.2	163.6	181.8
δ_{\max}	0.95	9.40	62.3	32.2	5.4	0.08	27.3	162.0	189.3

corresponding best-fit parameters are given in Table 5. The best-fit parameters are found to be almost independent of δ : the spectral index is hard and the rigidity cutoff is low, so as to reproduce the low level of A mixture at each energy. For δ_{\max} , a visible difference appears in the proton fraction with respect to other analyzed values of δ . This is because protons must be present already at the source so as to compensate for the absence of interactions. By comparing the values of the deviance at the minimum, δ_{\max} is disfavored at more than 3σ over $\delta = 0$ [32].

5.3. Delve into the electroweak sector in search for new physics at subfermi distances

If new physics interactions occur at LHC energies, then CR collisions with c.m. energies ranging up to 250 TeV would obviously involve new physics as well. The question is, can new physics be detected by CR experiments? At ultra-high energies, the cosmic ray luminosity $\sim 7 \times 10^{-10} (E/\text{PeV})^{-2} \text{ cm}^{-2} \text{ s}^{-1}$ (taking a single nucleon in the atmosphere as a target and integrating over 2π sr) is about 50 orders of magnitude smaller than the LHC luminosity. This renders the hunt for physics beyond the electroweak scale futile in hadronic cosmic ray interactions occurring in the atmosphere.²⁶ However, there is still a possibility of uncovering new physics at sub-fermi distances in cosmic neutrino interactions.

Neutrinos are unique probes of new physics, as their interactions are uncluttered by the strong and electromagnetic forces and, upon arrival at the Earth, they may experience collisions with c.m. energies up to $\sqrt{s} \lesssim 250$ TeV. However, rates for new physics processes are difficult to test since the flux of UHEC ν is virtually unknown. Interestingly, it is possible in principle to disentangle the unknown flux and new physics processes by using multiple observables [695, 696].

For example, possible deviations of the neutrino–nucleon cross section due to new non-perturbative interactions can be uncovered at UHECR facilities by combining information from Earth-skimming and quasi-horizontal showers.²⁷ In particular, if an anomalously large rate is found for deeply developing quasi-horizontal showers, it may be ascribed either to an enhancement of the incoming neutrino flux, or an enhancement in the neutrino-nucleon cross section (assuming non-neutrino final states dominate). However, these possibilities can be distinguished by comparing the rates of Earth-skimming and quasi-horizontal events. For instance, an enhanced flux will increase both quasi-horizontal and Earth-skimming event rates,

²⁶See, however, [694].

²⁷Herein we use this term to describe neutrino interactions in which the final state energy is dominated by the hadronic component. We are *not* considering here new “perturbative” physics *e.g.* (softly broken) supersymmetry at the TeV scale which would have quite different signatures in cosmic neutrino showers.

whereas an enhanced interaction cross section will also increase the former but *suppress* the latter, because the hadronic decay products cannot escape the Earth’s crust. Essentially this approach constitutes a straightforward counting experiment, as the detailed shower properties are not employed to search for the hypothesized new physics. Hence, this constitutes an entirely general approach to searching for non-perturbative interactions without any dependence on what hypothetical mechanism might actually cause the “hadrophilia.”

Consider first a flux of Earth-skimming tau neutrinos with energy E_0 . Given the high energies required for detection, the most relevant energies are $10^9 \lesssim E_0/\text{GeV} \lesssim 10^{10}$ GeV, and we may therefore limit the discussion to this rather narrow band of energy. The neutrinos can convert to τ leptons in the Earth via the CC interaction $\nu_{\tau\pm} N \rightarrow \tau^\pm X$. In the (perturbative) SM, the interaction path length for the neutrino is

$$L_{\text{CC}}^\nu = [N_A \rho_s \sigma_{\text{CC}}]^{-1} , \quad (250)$$

where σ_{CC} is the CC cross section for a neutrino energy $E_\nu = E_0$. The density of the material through which the neutrinos pass, ρ_s , is about 2.65 g/cm^3 for the Earth’s crust. Here we have neglected NC interactions, which at these energies only reduce the neutrino energy by approximately 20%, which is within the systematic uncertainty. For $E_0 \sim 10^{10}$ GeV, $L_{\text{CC}}^\nu \sim \mathcal{O}(100)$ km. Let us assume some hypothetical non-perturbative physics process enhances the νN cross section. Then the interaction path length becomes

$$L_{\text{tot}}^\nu = [N_A \rho_s (\sigma_{\text{CC}} + \sigma_{\text{NP}})]^{-1} , \quad (251)$$

where σ_{NP} is the non-perturbative contribution to the cross section for $E_\nu = E_0$.

Once a τ is produced by a CC interaction, it can be absorbed in the Earth or escape and possibly decay, generating a detectable air shower. For $E_\nu \gtrsim 10^{8.5}$ GeV, the τ propagation length in the Earth is dominated by energy loss rather than the finite τ lifetime. The energy loss can be expressed as

$$\frac{dE_\tau}{dz} = -(\alpha_\tau + \beta_\tau E_\tau) \rho_s , \quad (252)$$

where α_τ characterizes energy loss due to ionization and β_τ characterizes losses through bremsstrahlung, pair production and hadronic interactions. At these energies, energy losses due to ionization turn out to be negligible, while $\beta_\tau \simeq 0.8 \times 10^{-6} \text{ cm}^2/\text{g}$ [697]. From (252), we observe that the maximum path length for a detectable τ can be written

$$L^\tau = \frac{1}{\beta_\tau \rho_s} \ln (E_{\text{max}}/E_{\text{min}}) , \quad (253)$$

where $E_{\text{max}} \approx E_0$ is the energy at which the τ is created, and E_{min} is the minimal energy at which a τ can produce a shower big enough to be detected. For $E_{\text{max}}/E_{\text{min}} = 10$, $L^\tau = 11$ km.

The probability for a neutrino with incident nadir angle θ to emerge as a detectable τ is

$$P(\theta) = \int_0^l \frac{dz}{L_{\text{CC}}^\nu} e^{-z/L_{\text{tot}}^\nu} \Theta [z - (l - L^\tau)] , \quad (254)$$

where $l = 2R_\oplus \cos \theta$ is the chord length of the intersection of the neutrino’s trajectory with the Earth. Note that we have neglected the possibility that non-perturbative processes could lead to a detectable signal, since the hadrons which dominate the final state will be absorbed in the Earth. The step function in (254) reflects the fact that a τ will only escape the Earth if $z + L^\tau > l$ [696].

Assuming an isotropic tau neutrino flux, the number of taus that emerge from the Earth with sufficient energy to be detected is proportional to an “effective solid angle”

$$\Omega_{\text{eff}} \equiv \int P(\theta) \cos \theta d \cos \theta d\phi. \quad (255)$$

Evaluation of the integrals [695] yields the unfortunate expression

$$\Omega_{\text{eff}} = 2\pi \frac{L_{\text{tot}}^\nu}{L_{\text{CC}}^\nu} [e^{L^\tau/L_{\text{tot}}^\nu} - 1] \left[\left(\frac{L_{\text{tot}}^\nu}{2R_\oplus} \right)^2 - \left(\frac{L_{\text{tot}}^\nu}{2R_\oplus} + \left(\frac{L_{\text{tot}}^\nu}{2R_\oplus} \right)^2 \right) e^{-2R_\oplus/L_{\text{tot}}^\nu} \right]. \quad (256)$$

At the relevant energies, however, the neutrino interaction length satisfies $L_{\text{tot}}^\nu \ll R_\oplus$. In addition, if the hypothesized non-perturbative cross section enhancement is less than typical hadronic cross sections, we have $L_{\text{tot}}^\nu \gg L^\tau$. With these approximations, (256) simplifies to [696]

$$\Omega_{\text{eff}} \approx 2\pi \frac{L_{\text{tot}}^{\nu 2} L^\tau}{4R_\oplus^2 L_{\text{CC}}^\nu}. \quad (257)$$

Equation (257) describes the functional dependence of the Earth-skimming event rate on the non-perturbative cross section. This rate is, of course, also proportional to the neutrino flux $\Phi_{\nu_{\text{all}}}$ at E_0 . Thus, the number of Earth-skimming neutrinos is given by

$$N_{\text{ES}} \approx C_{\text{ES}} \frac{\Phi_{\nu_{\text{all}}}}{\Phi_{\nu_{\text{all}}}^{\text{WB}}} \frac{\sigma_{\text{CC}}^{\nu 2}}{(\sigma_{\text{CC}}^\nu + \sigma_{\text{NP}}^\nu)^2}, \quad (258)$$

where C_{ES} is the number of Earth-skimming events expected for some benchmark flux $\Phi_{\nu_{\text{all}}}^{\text{WB}}$ in the absence of new physics. In contrast to (258), the rate for quasi-horizontal showers has the form

$$N_{\text{QH}} = C_{\text{QH}} \frac{\Phi_{\nu_{\text{all}}}}{\Phi_{\nu_{\text{all}}}^{\text{WB}}} \frac{\sigma_{\text{CC}}^\nu + \sigma_{\text{NP}}^\nu}{\sigma_{\text{CC}}^\nu}, \quad (259)$$

where C_{QH} is the number of quasi-horizontal events expected for flux $\Phi_{\nu_{\text{all}}}^{\text{WB}}$.

Given a flux $\Phi_{\nu_{\text{all}}}$ and new non-perturbative physics cross section σ_{NP} , both N_{ES} and N_{QH} are determined. On the other hand, given just a quasi-horizontal event rate N_{QH} , it is impossible to differentiate between an enhancement of the cross section due to non-perturbative physics and an increase of the flux. However, in the region where significant event rates are expected, the contours of N_{QH} and N_{ES} , given by (258) and (259), are more or less orthogonal and provide complementary information. This is illustrated in Fig. 25. With measurements of $N_{\text{QH}}^{\text{obs}}$ and $N_{\text{ES}}^{\text{obs}}$, both σ_{NP} and $\Phi_{\nu_{\text{all}}}$ may be determined independently, and neutrino interactions beyond the (perturbative) SM may be unambiguously identified [696]. Event rate estimates assuming a neutrino flux at the level of the WB bound suggest that existing ground-based experiments [698, 699] and future space-based missions [700] would be within reach of testing possible enhancement of the neutrino-nucleon cross section.

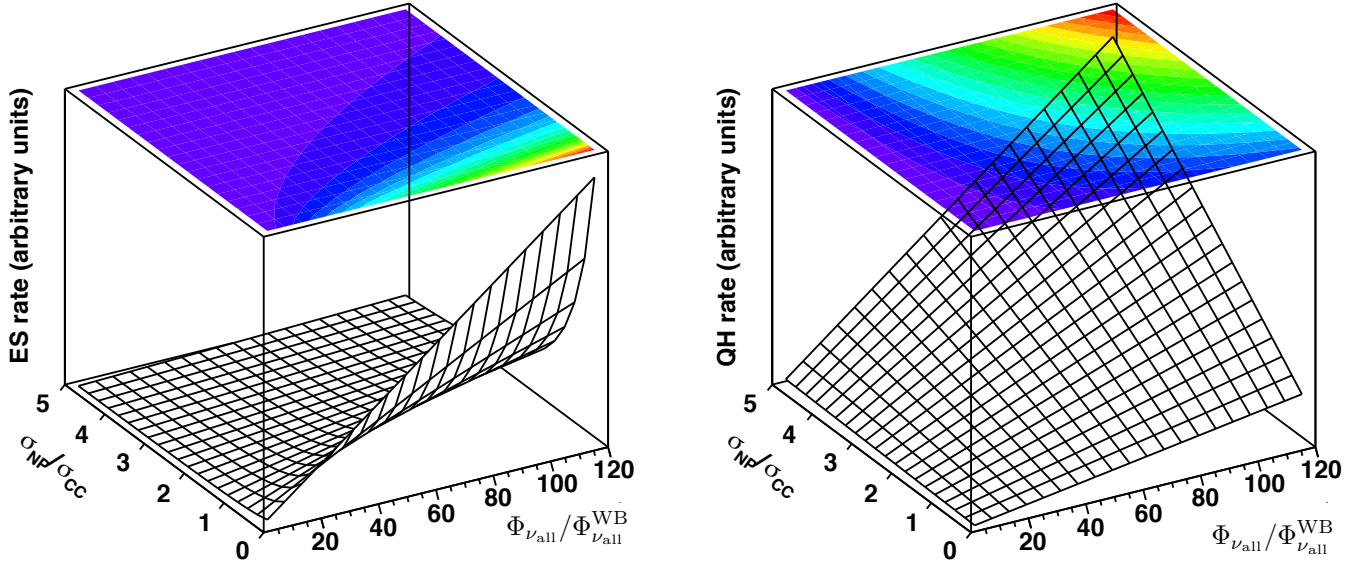


Figure 25: Event rates for Earth-skimming (left) and quasi-horizontal (right) events in the $\Phi_{\nu_{\text{all}}}/\Phi_{\nu_{\text{all}}}^{\text{WB}} - \sigma_{\text{NP}}/\sigma_{\text{CC}}$ plane. Note that the contours are roughly orthogonal, and so the two types of event provide complementary information about flux and cross section. From Ref. [12].

6. Looking ahead

Thanks to a prodigious experimental effort the origin of the highest energy particles in the Universe are beginning to be revealed. Nonetheless, 60 years after their discovery much remains a mystery. Even the reason for the sharp suppression on the region of the expected GZK effect remains uncertain. Resolving the UHECR origin(s) and investigating particle physics above accelerator energies, will require both enhanced experimental techniques implemented at the existing observatories, as well as a significant increase in exposure to catch the exceedingly rare highest energy events. Even before we know the results from the upcoming generation of UHECR observatories it seems clear that still larger aperture observatories with much better energy and X_{max} resolution will be called for, in order to measure the spectra of individual sources. The way forward is clear and practical. The next-generation UHECR observatories will have three primary goals:

- *Increased statistics in both Northern and Southern hemispheres.* A large increase in statistics is obviously important to increase the significance and resolution of all results. In particular, it will improve the chances for anisotropy searches, allow a more sensitive measurement of the spectral suppression, and potentially establish variations in the spectrum in different regions of the sky. Furthermore, increased statistics will aid in reducing systematic uncertainties (of all sorts) for all measurements.
- *Composition-tagging for each individual event.* Probabilistic composition-tagging for all events will address the question of how the baryonic composition evolves with energy, thereby clarifying the nature of the spectral cutoff and the acceleration mechanism(s). It will also aid in source identification by allowing events to be backtracked through the Galactic magnetic field, with reduced ambiguity from their charge assignment, and allow correlation studies to be restricted to proton-like events with smaller deflections.

- *Detailed observations of UHECR showers.* It is essential to have reliable shower-development measurements to be able to understand hadronic interactions in the ultra-high-energy regime and to infer the nuclear composition from the shower properties. UHECRs are also Nature’s highest energy particle beam and thus present an opportunity to explore particle physics beyond collider energies.

Moving beyond existing technologies, it is inspiring to note that some 5 million UHECRs with energies above about 5.5×10^{10} GeV strike the Earth’s atmosphere each year, from which we currently collect only about 50 or so with present observatories. In this sense, there exists some 5 orders of magnitude room for improvement! It may well be that the best hope to make inroads in this area is to take the search for UHECR sources into space.

At present the most advanced project in pursuit of this objective is the Probe Of Extreme Multi-Messenger Astrophysics (POEMMA) satellites, selected by NASA for an in-depth probe mission concept study in preparation for the next decadal survey [701]. POEMMA will boldly go where no UHECR observatory has gone before, combining the well-developed Orbiting Wide-field Light-collectors (OWL) concept [702] with the recently proposed Cherenkov from Astrophysical Neutrinos Telescope (CHANT) concept [703] to form a multi-messenger probe of the most extreme environments in the universe. In addition to its unprecedented physics potential, POEMMA will serve as a pathfinder for future space-based missions, establishing feasibility and cost-effectiveness, uncovering challenges and opportunities, and stimulating development of second-generation technology for more ambitious projects. An optimist might even imagine an eventual constellation of satellites eating their way into the 5 orders of magnitude of thus-far untapped UHECR luminosity.

In summary, pursuing improved ground-based detection techniques and pioneering space-based observation will offer complementary tools to piece together challenging astrophysical puzzles to unmask the UHECR origin(s). Moreover, with the combined power of the space- and ground-based approaches, a few decades from now we may even have harnessed the study of UHECR showers to explore particle physics at energies inaccessible to terrestrial accelerators. As exemplified time and again, the development of novel ways of looking into space invariably results in the discovery of unanticipated phenomena.

Acknowledgments

I would like to thank Rasha Abbasi, Jim Adams, Felix Aharonian, Markus Ahlers, Roberto Aloisio, Rita dos Anjos, Vernon Barger, John Beacom, Marty Block, Mark Christl, Jorge Combi, Rafael Colon, Alessandro De Angelis, Hans Dembinski, Peter Denton, Tere Dova, Loyal Durand, Ralph Engel, Luis Epele, Glenys Farrar, Anatoli Fedynitch, Jonathan Feng, Jorge Fernandez Soriano, Tom Gaisser, Carlos García Canal, Haim Goldberg, Daniel Gómez Dumm, Concha Gonzalez Garcia, Juan Guerra, Phuock Ha, Francis Halzen, Tao Han, Dan Hooper, Albrecht Karle, John Krizmanic, Alex Kusenko, John Learned, Manuela Mallamaci, Danny Marfatia, Tom McCauley, Rob Moncada, Teresa Montaruli, Kohta Murase, Marco Muzio, Andrii Neronov, Matt O’Dowd, Angela Olinto, Tim Paglione, Sandip Pakvasa, Sergio Palomares-Ruiz, Tom Paul, Santiago Perez Bergliaffa, Hallsie Reno, Felix Riehn, Andreas Ringwald, Gustavo Romero, Subir Sarkar, Sergio Sciutto, Dmitri Semikoz, Al Shapere, Todor Stanev, Andy Taylor, Diego Torres, Peter Tinyakov, Michael Unger, Tom Weiler, and Lawrence Wiencke for valuable discussions and permission to reproduce some of the figures. I would also like to thank my colleagues of the Pierre Auger and POEMMA collaborations for valuable discussions, and the TA Collaboration for permission to reproduce Fig. 4. The research of

L.A.A. is supported by the U.S. National Science Foundation (NSF Grant PHY-1620661) and the National Aeronautics and Space Administration (NASA Grant 80NSSC18K0464). Any opinions, findings, and conclusions or recommendations expressed in this material are those of the author and do not necessarily reflect the views of the NSF or NASA.

Appendix A.

In the absence of a well justified model for the CR intensity, one may prefer performing an interpolation to the data. This is not a choice free approach, since one has to decide the functions used to interpolate. In this Appendix a method is described using cubic splines to achieve this task [82].

In the GSF model, the CR intensity is divided into four baryonic groups, which cover roughly equal ranges in logarithmic baryon number $\ln A$, because air-shower measurements are sensitive to changes in $\ln A$ rather than A . Each group has a leading element L that contributes most of the intensity per energy interval. For each particle type, the interpolating intensity is written as a function of the rigidity $J_L(\mathcal{R})$, with $J(\mathcal{R}) = \sum_{L=1}^4 J_L(\mathcal{R})$.²⁸ Note that if two elements have the same abundance in intensity per rigidity interval $J(\mathcal{R}) \propto dN/(d\mathcal{R} dA dt d\Omega)$, the element with the higher charge contributes more to the intensity per energy interval $dN/(dE dA dt d\Omega)$. As a consequence, the leading elements are the heaviest abundant elements in each group; namely proton, helium, oxygen, and iron. The oxygen and iron groups contain many sub-leading elements. In the oxygen group, carbon contributes nearly as much as oxygen. In the GSF model, the flux $J_i(\mathcal{R})$ of a sub-leading element i is kept in a constant ratio f_{iL} to the leading element $L \in \{p, \text{He}, \text{O}, \text{Fe}\}$ of its group, $J_i(\mathcal{R}) = f_{iL} \times J_L(\mathcal{R})$. To remove the major power law contribution to the intensity, it is convenient to consider a function that exhibits a softer dependance on \mathcal{R} than J_L ; namely,

$$f_L(x) \equiv \left(\frac{\mathcal{R}}{\text{GV}} \right)^3 J_L(\mathcal{R}), \quad (\text{A.1})$$

where $x \equiv \ln(\mathcal{R}/\text{GV})$.

Let $\mathcal{D} = \{x_i, y_i\}$ be a set of $N + 1$ experimental points, and $\Omega_k = [x_k, x_{k+1}]$ the intervals between contiguous pairs of points. A degree n spline interpolator for \mathcal{D} is a piecewise function

$$f(x) = f_k(x) \text{ if } x \in \Omega_k, \quad (\text{A.2})$$

exhibiting some smoothness properties at the internal ($k \neq 0, N$) points, where $f_k(x)$ are polynomials of degree at most n . For a fixed set of points, fixed degree n , and fixed smoothness properties at the points, the set of all possible splines forms a vector space. A B-spline is an element of a basis $\{b_k\}$ of the vector space. Then, the spline function f can be written as

$$f(x) = \sum_{k=0}^{N-1} \alpha_k b_k(x). \quad (\text{A.3})$$

²⁸Rigidity, energy divided by charge, is a relevant parameter for CR propagation in a magnetic field. Rigidity is properly measured in units of GV but when only magnetic deflections and not energy losses are of concern, GV and GeV may be used interchangeably since knowing the deflection of a proton of energy E_p in GeV specifies the deflection of any CR with the same value of $E_p = E/Z$.

For cubic splines, the smoothness properties require f to be C^3 at the points. The cubic basis functions are obtained by recurrence from the lower order basis functions. One can write $b_k(x) = B_{k,3}(x)$, where

$$B_{k,0}(x) := \begin{cases} 1 & \text{if } x \in \Omega_k, \\ 0 & \text{otherwise,} \end{cases} \quad (\text{A.4a})$$

$$B_{k,i}(x) := \frac{x - x_k}{x_{k+i} - x_k} B_{k,i-1}(x) + \frac{x_{k+i+1} - x}{x_{k+i+1} - x_{k+1}} B_{k+1,i-1}(x). \quad (\text{A.4b})$$

This would give a set of N polynomials completely determined by the data points and the smoothness conditions at them. There is still a freedom on the spline interpolator, written as a linear combinations of these B-splines. In order to find the coefficients α_k in (A.3), one performs a least squares fit, minimizing

$$U(\alpha_1, \dots, \alpha_{N-1}) = \sum_{j=0}^N w_j \left(y_j - \sum_{k=0}^{N-1} \alpha_k b_k(x_j) \right)^2, \quad (\text{A.5})$$

where w_j is the weight assigned to each point. If the data is accompanied with a series of uncertainties σ_i for each value y_i , one can choose the weight to be $w_i = 1/\sigma_i^2$, which would make $U(\alpha_1, \dots, \alpha_{N-1})$ be the familiar quantity

$$\chi^2 = \sum_{j=0}^N \left(\frac{y_j - f(x_j)}{\sigma_j} \right)^2. \quad (\text{A.6})$$

Note that $J(\mathcal{R})$ parametrizes the differential flux of nuclei per rigidity interval. Air-shower measurements of the CR flux are reported as the differential flux of nuclei per energy interval $J(E)$. The latter is computed from the former as $J(E) = J(\mathcal{R}) d\mathcal{R}/dE$. The relation between total energy E and rigidity \mathcal{R} depends on the number of nucleons A and protons Z and must be computed individually for each element. Note that a primary CR with rigidity \mathcal{R}/GV could be a proton with energy E_p/GeV or a nucleus with energy ZE_p/GeV , with $\mathcal{R}/\text{GV} = E_p/\text{GeV}$. Thereupon, we will specify, all through, the CR rigidity of a nucleus of charge Ze using the proton energy E_p . Air-shower measurements describe the flux of mass groups. In the GSF model a sum of the flux of all elements in each group is carried out when comparing the model to such measurements.

For the GSF model shown in Fig. 2, the $\chi^2 = 385.2$ for 724 degrees of freedom, which indicates a good fit [82]. The good agreement of the fit (when systematic uncertainties are taken into account) in turn implies that the data sets are overall consistent. The fit shown in Fig. 2 has been carried out discarding the proton-helium data of ARGO-YBJ beyond 10^6 GeV and assigning 10% to 20% systematic uncertainty to results where none were reported.²⁹ One can refer to the original paper [82] for a careful assessment of the adjustment of the energy scales within systematic uncertainties.

Appendix B.

This Appendix contains a guide, as complete as possible, to the use of statistical likelihood-based methods in data analysis. For further details, see e.g. [704, 705].

²⁹For ARGO-YBJ, the reported proton+helium intensity drops sharply for $E > 10^6$ GeV, in contradiction to three other data sets.

The probability density function for a random variable, x , conditioned on a set of parameters, $\boldsymbol{\theta} = \{\theta_1, \dots, \theta_m\}$, is denoted $f(x; \boldsymbol{\theta})$. This function identifies the data-generating process that underlies an observed sample of data and, at the same time, provides a mathematical description of the data that the process will produce. The joint density of N independent and identically distributed observations from this process, $\mathbf{x} = \{x_1, \dots, x_N\}$, is the product of the individual densities,

$$f(x_1 \dots x_N; \boldsymbol{\theta}) = \prod_{i=1}^N f(x_i; \boldsymbol{\theta}) = \mathcal{L}(\boldsymbol{\theta}; \mathbf{x}). \quad (\text{B.1})$$

This joint density is the likelihood function, defined as a function of the unknown parameter vector, $\boldsymbol{\theta}$. Note that the joint density is written as a function of the data conditioned on the parameters, whereas when one forms the likelihood function, the function is written in reverse, i.e. as a function of the parameters, conditioned on the data. Though the two functions are the same, it is to be emphasized that the likelihood function is written in this fashion to highlight the interest in the parameters, and the information about them that is contained in the observed data. However, it is understood that the likelihood function is not meant to represent a probability density for the parameters. In this classical estimation framework, the parameters are assumed to be fixed constants that one awaits to learn about from the data.

Extension to a multivariate density, $\mathbf{f} = \{f_1, \dots, f_N\}$, is straightforward. Note that in general the experimental data do not need to be of the same kind, but rather each point in the data-sample may follow a different statistical model f_i . Strictly speaking, for a given set of m parameters $\boldsymbol{\theta}$, a function f_i assigns the probability density of a random variable x to take the a value x_i , and so $f_i(x_i; \boldsymbol{\theta})$ gives *the probability of the data point x_i given the individual model $\{f_i, \boldsymbol{\theta}\}$* , i.e. $f_i(x_i; \boldsymbol{\theta}) \equiv \mathcal{P}(x_i | \text{model}_i)$. The likelihood function,

$$\mathcal{L}(\boldsymbol{\theta}; \mathbf{x}) = \prod_{i=1}^N f_i(x_i; \boldsymbol{\theta}), \quad (\text{B.2})$$

is *the probability of all the data, \mathbf{x} , given the complete model $\{\mathbf{f}, \boldsymbol{\theta}\}$* , i.e. $\mathcal{P}(\mathbf{x} | \text{model})$.

The estimated values $\boldsymbol{\theta} = \hat{\boldsymbol{\theta}}$ of the parameters are obtained by finding the global maximum of the likelihood function,

$$\left. \frac{\partial \mathcal{L}(\boldsymbol{\theta}; \mathbf{x})}{\partial \theta_i} \right|_{\boldsymbol{\theta}=\hat{\boldsymbol{\theta}}} = 0, \quad \text{with } 1 \leq i \leq m. \quad (\text{B.3})$$

In practice, it is often more convenient to work with the logarithm of the likelihood function, called the log-likelihood and to search for the minimum of the negative log-likelihood function:

$$-\ln \mathcal{L}(\boldsymbol{\theta}, \mathbf{x}) = -\sum_{i=1}^N \ln f(x_i, \boldsymbol{\theta}). \quad (\text{B.4})$$

Unless the minimum occurs at the boundary of the allowed range of values for $\boldsymbol{\theta}$, a necessary condition for the minimum is that the negative log-likelihood satisfies the following m equations:

$$-\left. \frac{\partial \ln \mathcal{L}(\boldsymbol{\theta}; \mathbf{x})}{\partial \theta_i} \right|_{\boldsymbol{\theta}=\hat{\boldsymbol{\theta}}} = 0. \quad (\text{B.5})$$

The likelihood function must be constructed using normalized probability density functions: $\int f(x; \boldsymbol{\theta}) dx = 1$, so that $\int \mathcal{L}(\boldsymbol{\theta}; \mathbf{x}) dx_1 \cdots dx_N = 1$. In other words it is essential that the integral of the likelihood function does not depend on the parameters $\boldsymbol{\theta}$.

Likelihood maximization methods can be used to find the parameters $\hat{\boldsymbol{\theta}}$ maximizing the likelihood, as well as to find the confidence region(s) of certain parameter(s) in $\boldsymbol{\theta}$ around $\hat{\boldsymbol{\theta}}$. Consider a set of parameters $\boldsymbol{\mu} \subseteq \boldsymbol{\theta}$ whose study is of interest, and a set of nuisance parameters collectively denoted by $\boldsymbol{\nu} = \boldsymbol{\theta} \setminus \boldsymbol{\mu}$. To make the splitting of $\boldsymbol{\theta}$ explicit, the likelihood is written hereafter as $\mathcal{L}(\boldsymbol{\mu}, \boldsymbol{\nu}; \mathbf{x})$. For the evaluation of the confidence regions, it is practical to use the profile likelihood ratio,

$$\lambda(\boldsymbol{\mu}) \equiv \frac{\mathcal{L}(\boldsymbol{\mu}, \hat{\boldsymbol{\nu}}(\boldsymbol{\mu}); \mathbf{x})}{\mathcal{L}(\hat{\boldsymbol{\mu}}, \hat{\boldsymbol{\nu}}; \mathbf{x})}, \quad (\text{B.6})$$

where in the numerator there is a profile likelihood function in which $\hat{\boldsymbol{\nu}}$ is the value of $\boldsymbol{\nu}$ maximizing \mathcal{L} for the assumed $\boldsymbol{\mu}$, namely

$$\left. \frac{\partial \mathcal{L}(\boldsymbol{\mu}, \boldsymbol{\nu}; \mathbf{x})}{\partial \nu_i} \right|_{\boldsymbol{\nu}=\hat{\boldsymbol{\nu}}(\boldsymbol{\mu})} = 0, \quad \text{with } 1 \leq i \leq \dim \boldsymbol{\nu}; \quad (\text{B.7})$$

i.e. the likelihood is maximised only in the parameters $\hat{\boldsymbol{\nu}}$ for each $\boldsymbol{\mu}$. Note that $\hat{\boldsymbol{\nu}}$ is the conditional maximum likelihood estimator of $\boldsymbol{\nu}$ and consequently is a function of $\boldsymbol{\mu}$ itself. The denominator, instead, is maximized in an unconstrained way, thus $\hat{\boldsymbol{\mu}}$ and $\hat{\boldsymbol{\nu}}$ are the true maximum likelihood estimators. By definition then the profile likelihood ratio is comprised between $0 \leq \lambda(\boldsymbol{\mu}) \leq 1$. The upper limit is picked up when the hypothesized $\boldsymbol{\nu}$ coincides with $\hat{\boldsymbol{\nu}}$, showing therefore great compatibility between the data and the hypothesis. The lower limits is instead picked up when the assumed $\boldsymbol{\nu}$ is at odd with $\hat{\boldsymbol{\nu}}$, denoting in this way a high degree of incompatibility between the data and the hypothesis.

In the large-sample limit, where the likelihood approaches a Gaussian, $-2 \ln \lambda(\boldsymbol{\mu})$ follows a χ^2 distribution with $d = \dim \boldsymbol{\mu}$ degrees of freedom. This condition is usually referred to as the Wilks theorem [706]. One can then use the quantiles $\chi_c^2(d, \alpha)$ of the χ^2 distribution to evaluate α -confidence regions,

$$\alpha = \int_0^{\chi_c^2(d, \alpha)} f_{\chi^2}(z; d) dz, \quad (\text{B.8})$$

where

$$f_{\chi^2}(z; d) = \frac{z^{d/2-1} e^{-z/2}}{2^{d/2} \Gamma(\frac{d}{2})} \quad (\text{B.9})$$

is the probability density for a random variable z following a χ^2 distribution of d degrees of freedom. These quantiles define the rise in $-2 \ln \lambda(\boldsymbol{\mu})$ corresponding to the points of $\boldsymbol{\mu}$ on the border of the confidence region,

$$-2 \ln \lambda(\boldsymbol{\mu}) \leq \chi_c^2(d, \alpha). \quad (\text{B.10})$$

With this construction, the region $[0, \chi_c^2(d, \alpha)]$ contains the values of $-2 \ln \lambda(\boldsymbol{\mu})$ that allows one to phrase the statement: *$\boldsymbol{\mu}$ is in the region defined by (B.10) with a confidence level α .*

If a statistical hypothesis to be tested can be expressed in terms of the parameters $\boldsymbol{\theta}$ in the likelihood, one can use the function defined in (B.6) to build a TS and asses the confidence an experiment gives to say

that the hypothesis is true or false. In general, the hypothesis to be tested, referred as *null hypothesis*, may be expressed in terms only of a subset ($\boldsymbol{\mu}$) of all the involved parameters. Let $H_0 : \boldsymbol{\mu} = \boldsymbol{\mu}_0$ define the null hypothesis, to be confronted with its negation, the *alternative hypothesis* $H_1 : \boldsymbol{\mu} \neq \boldsymbol{\mu}_0$. According to the method developed above, the condition

$$-2 \ln \lambda(\boldsymbol{\mu}_0) \equiv -2 \ln \lambda_0 = \chi_0^2(d, \alpha), \quad (\text{B.11})$$

gives the α -confidence in the exclusion of the null hypothesis, with

$$\alpha = \int_0^{-2 \ln \lambda_0} f_{\chi^2}(z; d) dz. \quad (\text{B.12})$$

One can measure the significance associated with the previous α -confidence using the standard method to relate significance and p -values, with a unit normal distribution. For a confidence level α , the significance S is given by

$$\alpha = \int_{\mu - S\sigma}^{\mu + S\sigma} f_{\mathcal{N}}(z; \mu, \sigma) dz = \text{erf} \left(\frac{S}{\sqrt{2}} \right). \quad (\text{B.13})$$

Comparing (B.12) with (B.13) the significance is found to be

$$S_d = \sqrt{2} \text{erf}^{-1} \left(\int_0^{-2 \ln \lambda_0} f_{\chi^2}(z; d) dz \right). \quad (\text{B.14})$$

For one and two degrees of freedom, which are particularly relevant cases in this review, (B.14) becomes

$$S_1 = \sqrt{2} \text{erf}^{-1} \left[\text{erf} \left(\sqrt{\frac{-2 \ln \lambda_0}{2}} \right) \right] = \sqrt{-2 \ln \lambda_0}, \quad (\text{B.15a})$$

$$S_2 = \sqrt{2} \text{erf}^{-1} \left[1 - e^{-\frac{-2 \ln \lambda_0}{2}} \right] = \sqrt{2} \text{erf}^{-1}(1 - \lambda_0). \quad (\text{B.15b})$$

The significance for one and two degrees of freedom as a function of λ_0 is display in Fig. B.26.

A useful application of the statistical methods described above is the rejection of *background only hypothesis* against a *background and source hypothesis*. Consider an experiment (possibly combined with simulations) that provides a number of observed events N_{on} in a certain region (or sample) where the hypotheses will be analyzed, and a number of events N_{off} in another region (or in a Monte Carlo sample) where the null hypothesis is understood to be true. A comparison of the sizes of those two regions (or samples) is necessary to infer the background in the region of interest from the background in the auxiliary region, assuming that its nature in both regions is the same. To this end it is useful to introduce the parameter $\eta = N/N_{\text{sim}}$, where N is the total number of observed events in the data-sample and N_{sim} is the number of events in the Monte Carlo sample. Then, in the notation introduced above:

- $\mathbf{x} = \{N_{\text{on}}, N_{\text{off}}\}$,
- $\boldsymbol{\theta} = \{\langle N_S \rangle, \langle N_B \rangle\}$,
 - $\boldsymbol{\mu} = \{\langle N_S \rangle\}$,
 - $\boldsymbol{\nu} = \{\langle N_B \rangle\}$,
- $\mathbf{f} = \{p(\cdot, \langle N_S \rangle + \langle N_B \rangle), p(\cdot, \langle N_S \rangle / \eta)\}$,

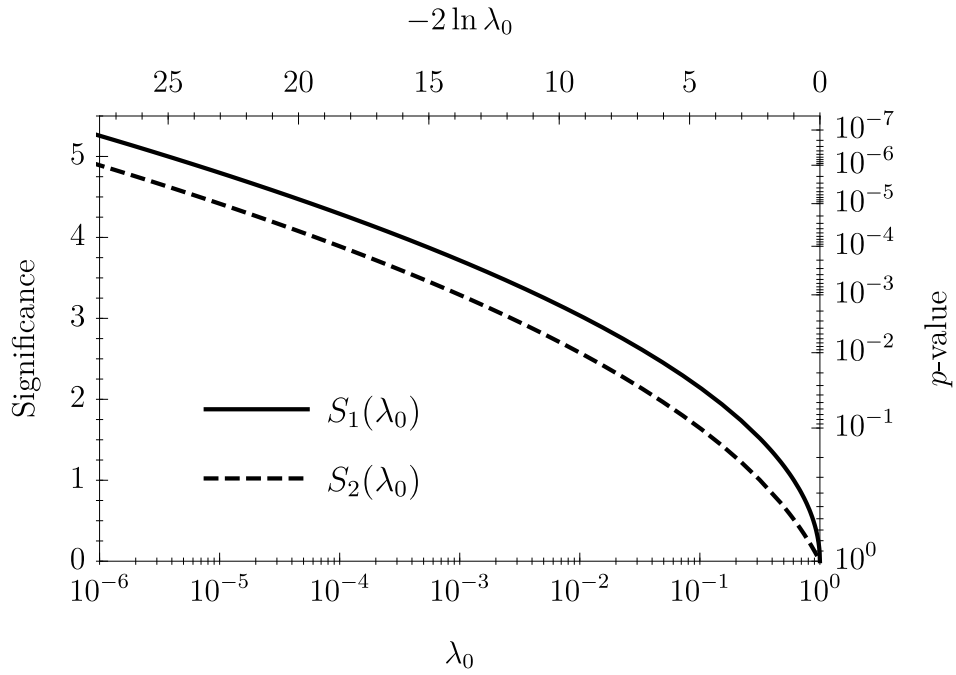


Figure B.26: Relation between the significance and λ_0 for $d = 1$ and $d = 2$.

where $\langle N_S \rangle$ and $\langle N_B \rangle$ are the expected number of source and background events in the *on* region, respectively. The functions $p(\cdot, N)$ are Poisson distribution functions with mean N , given by

$$p(x, N) = \frac{e^{-N} N^x}{x!}. \quad (\text{B.16})$$

The likelihood is given by

$$\mathcal{L}(\langle N_S \rangle, \langle N_B \rangle; \mathbf{x}) = p(N_{\text{on}}, \langle N_S \rangle + \langle N_B \rangle) p(N_{\text{off}}, \langle N_B \rangle / \eta). \quad (\text{B.17})$$

The maximum likelihood conditions (B.3) yield

$$\langle \hat{N}_S \rangle = N_{\text{on}} - \eta N_{\text{off}} \quad (\text{B.18a})$$

and

$$\langle \hat{N}_B \rangle = \eta N_{\text{off}}. \quad (\text{B.18b})$$

The condition (B.7) gives

$$\langle \hat{N}_B \rangle(\langle N_S \rangle) = \frac{N_{\text{on}} + N_{\text{off}} - \langle N_S \rangle \varkappa \pm \sqrt{[N_{\text{on}} + N_{\text{off}} - \langle N_S \rangle \varkappa]^2 + 4 \langle N_S \rangle \varkappa N_{\text{off}}}}{2\varkappa}, \quad (\text{B.19})$$

where $\varkappa = 1 + 1/\eta$. For the null hypothesis, $\langle N_S \rangle = 0$, and so

$$\langle \hat{N}_B \rangle_0 \equiv \langle \hat{N}_B \rangle(0) = \frac{N_{\text{on}} + N_{\text{off}}}{1 + 1/\eta}. \quad (\text{B.20})$$

Then,

$$\begin{aligned}\lambda_0 &= \frac{\mathcal{L}(0, \langle \hat{N}_B \rangle_0; \mathbf{x})}{\mathcal{L}(\langle \hat{N}_S \rangle, \langle \hat{N}_B \rangle; \mathbf{x})} = \frac{p(N_{\text{on}}, (N_{\text{on}} + N_{\text{off}})/(1 + 1/\eta)) p(N_{\text{off}}, (N_{\text{on}} + N_{\text{off}})/(\eta + 1))}{p(N_{\text{on}}, N_{\text{on}}) p(N_{\text{off}}, N_{\text{off}})} \\ &= \left[\frac{\eta(N_{\text{on}} + N_{\text{off}})}{(\eta + 1)N_{\text{on}}} \right]^{N_{\text{on}}} \left[\frac{N_{\text{on}} + N_{\text{off}}}{(\eta + 1)N_{\text{off}}} \right]^{N_{\text{off}}},\end{aligned}\quad (\text{B.21})$$

and for $d = 1$, the statistical Li-Ma significance is given by (16) [103].

Appendix C.

This Appendix provides an overview of some generalities of the Rayleigh distribution. The statistical properties of the estimators $\{\hat{a}_m, \hat{b}_m\}$ in (21) derive from the Poissonian nature of the sampling of N points over the circle, matching the underlying angular distribution. Namely, the first and second moments of $\delta\hat{J}(\alpha)$ in (17) averaged over a large realization of events are

$$\langle \delta\hat{J}(\alpha) \rangle_{\text{P}} = \delta J(\alpha), \quad (\text{C.1a})$$

and

$$\langle \delta\hat{J}(\alpha) \delta\hat{J}(\alpha') \rangle_{\text{P}} = \delta J(\alpha) \delta J(\alpha') + \delta J(\alpha) \delta(\alpha, \alpha'), \quad (\text{C.1b})$$

respectively. The mean and root-mean-square of \hat{a}_m and \hat{b}_m can be calculated propagating these properties into (20) while taking \hat{a}_0 constant (the latter is a very precise approximation in most practical cases). All in all, it is easily seen that the estimators are unbiased, $\langle \hat{a}_m \rangle_{\text{P}} = a_m$ and $\langle \hat{b}_m \rangle_{\text{P}} = b_m$, and obey the covariance matrix coefficients given by [707]

$$\text{cov}(\hat{a}_i, \hat{a}_j) = \frac{J_0 \omega_0}{2\pi^3 a_0^2} \int \frac{d\alpha}{1 + \delta\omega(\alpha)} \delta J(\alpha) \cos(i\alpha) \cos(j\alpha), \quad (\text{C.2a})$$

$$\text{cov}(\hat{b}_i, \hat{b}_j) = \frac{J_0 \omega_0}{2\pi^3 a_0^2} \int \frac{d\alpha}{1 + \delta\omega(\alpha)} \delta J(\alpha) \sin(i\alpha) \sin(j\alpha). \quad (\text{C.2b})$$

For small anisotropies, $|a_m| \ll 1$ and $|b_n| \ll 1$, and so the uncertainties of the estimators are given by

$$\sigma(\hat{a}_m) = \left[\frac{2}{\pi \mathcal{N}_\alpha} \int \frac{d\alpha}{1 + \delta\omega(\alpha)} \cos^2(m\alpha) \right]^{1/2}, \quad (\text{C.3a})$$

$$\sigma(\hat{b}_m) = \left[\frac{2}{\pi \mathcal{N}_\alpha} \int \frac{d\alpha}{1 + \delta\omega(\alpha)} \sin^2(m\alpha) \right]^{1/2}. \quad (\text{C.3b})$$

Since $\delta\omega(\alpha)$ is in practice always small and smooth, the integrals in (C.3) approximate very well near π , yielding $\sigma(\hat{a}_m) = \sigma(\hat{b}_m) = \sqrt{2/\mathcal{N}_\alpha}$. The coefficients \hat{a}_m and \hat{b}_m are endowed with Gaussian probability density functions, p_{A_m} and p_{B_m} , which derive from the central limit theorem and are fully determined by the following parameter pairs: $\{\langle \hat{a}_m \rangle_{\text{P}}, \sigma^2\}$ and $\{\langle \hat{b}_m \rangle_{\text{P}}, \sigma^2\}$, with $\sigma^2 = 2/\mathcal{N}_\alpha$.

For any given data-sample containing N events, \hat{a}_m and \hat{b}_m are random variables. Therefore, in the limit of large statistics the joint probability distribution function p_{A_m, B_m} can be factorized as a product of p_{A_m}

and p_{B_m} . For any harmonic m , the joint probability distribution function of the estimated \hat{r}_m and $\hat{\varphi}_m$ can be derived using the pertinent Jacobian transformation [110]

$$p_{R_m, \Phi_m}(\hat{r}_m \hat{\varphi}_m; r_m \varphi_m) = \frac{\hat{r}_m}{2\pi\sigma^2} \exp\{-[\hat{r}_m^2 + r_m^2 - 2\hat{r}_m r_m \cos(\hat{\varphi}_m - \varphi_m)]/2\sigma^2\}. \quad (\text{C.4})$$

The probability distribution function of the amplitude, p_{R_m} , is obtained by marginalizing (C.4) over the phase

$$p_{R_m}(\hat{r}_m; r) = \frac{\hat{r}_m}{\sigma^2} \exp\left(-\frac{\hat{r}_m^2 + r_m^2}{2\sigma^2}\right) I_0\left(\frac{\hat{r}_m r_m}{\sigma^2}\right), \quad (\text{C.5})$$

with $I_0(x)$ the modified Bessel function of first kind with order zero. Likewise, the probability distribution function of the phase, p_{Φ_m} , is obtained by marginalizing (C.4) over the amplitude

$$\begin{aligned} p_{\Phi_m}(\hat{\varphi}_m; r_m, \varphi_m) &= \frac{1}{2\pi} \exp\left(-\frac{r_m^2}{2\sigma^2}\right) \left\{ 1 + \sqrt{\frac{\pi}{2}} \frac{r_m}{\sigma} \cos(\psi_m) \exp\left(\frac{r_m^2 \cos^2 \psi_m}{2\sigma^2}\right) \right. \\ &\times \left. \left[1 + \xi_m \operatorname{erf}\left(\frac{\xi_m r_m \cos(\psi_m)}{\sqrt{2} \sigma}\right) \right] \right\}, \end{aligned} \quad (\text{C.6})$$

where $\psi_m = \hat{\varphi}_m - \varphi_m$, and $\xi = 1$ if $|\psi_m| \leq \pi/2$ and -1 otherwise.

Note that if the underlying distribution is isotropic the p_{Φ_m} is uniform, whereas p_{R_m} reduces to the Rayleigh distribution. This lets out a genuine estimation of the probability that an observed amplitude \hat{r}_m arises from pure statistical fluctuations as

$$p(\geq \hat{r}_m) = \int_0^\infty dr'_m p_{R_m}(\hat{r}'_m; r_m = 0) = \exp\left(-\frac{\mathcal{N}_\alpha \hat{r}_m^2}{4}\right) \quad (\text{C.7})$$

For a non-zero amplitude r_m , depending on the signal-to-noise ratio parameter r_m/σ , both p_{R_m} and p_{Φ_m} smoothly evolve from the Rayleigh and uniform distributions to bell curves well-defined about the values of r_m and φ_m . For $r_m/\sigma \rightarrow \infty$, the bell curves are identical to Gaussian ones.

Bibliography

References

- [1] B. P. Abbott *et al.* [LIGO Scientific and Virgo and Fermi GBM and INTEGRAL and IceCube and IPN and Insight-Hxmt and ANTARES and Swift and Dark Energy Camera GW-EM and Dark Energy Survey and DLT40 and GRAWITA and Fermi-LAT and ATCA and ASKAP and OzGrav and DWF (Deeper Wider Faster Program) and AST3 and CAASTRO and VINROUGE and MASTER and J-GEM and GROWTH and JAGWAR and CaltechNRAO and TTU-NRAO and NuSTAR and Pan-STARRS and KU and Nordic Optical Telescope and ePESSTO and GROND and Texas Tech University and TOROS and BOOTES and MWA and CALET and IKI-GW Follow-up and H.E.S.S. and LOFAR and LWA and HAWC and Pierre Auger and ALMA and Pi of Sky and DFN and ATLAS Telescopes and High Time Resolution Universe Survey and RIMAS and RATIR and SKA South Africa/MeerKAT Collaborations and AstroSat Cadmium Zinc Telluride Imager Team and AGILE Team and 1M2H Team and Las Cumbres Observatory Group and MAXI Team and TZAC Consortium and SALT Group and Euro VLBI

- Team and Chandra Team at McGill University], **Multi-messenger observations of a binary neutron star merger**, *Astrophys. J.* **848**, no. 2, L12 (2017) doi:10.3847/2041-8213/aa91c9 [arXiv:1710.05833 [astro-ph.HE]].
- [2] M. G. Aartsen *et al.* [IceCube and Fermi-LAT and MAGIC and AGILE and ASAS-SN and HAWC and H.E.S.S. and INTEGRAL and Kanata and Kiso and Kapteyn and Liverpool Telescope and Subaru and Swift NuSTAR and VERITAS and VLA/17B-403 Collaborations], **Multimessenger observations of a flaring blazar coincident with high-energy neutrino IceCube-170922A**, *Science* **361**, no. 6398, eaat1378 (2018) doi:10.1126/science.aat1378 [arXiv:1807.08816 [astro-ph.HE]].
- [3] A. Aab *et al.* [Pierre Auger Collaboration], **Indication of anisotropy in arrival directions of ultra-high-energy cosmic rays through comparison to the flux pattern of extragalactic gamma-ray sources**, *Astrophys. J. Lett.* doi:10.3847/2041-8213/aaa66d [arXiv:1801.06160 [astro-ph.HE]].
- [4] L. A. Anchordoqui, G. E. Romero and J. A. Combi, **Heavy nuclei at the end of the cosmic ray spectrum?**, *Phys. Rev. D* **60**, 103001 (1999) doi:10.1103/PhysRevD.60.103001 [astro-ph/9903145].
- [5] R. U. Abbasi *et al.* [HiRes Collaboration], **First observation of the Greisen-Zatsepin-Kuzmin suppression**, *Phys. Rev. Lett.* **100**, 101101 (2008) doi:10.1103/PhysRevLett.100.101101 [astro-ph/0703099].
- [6] J. Abraham *et al.* [Pierre Auger Collaboration], **Observation of the suppression of the flux of cosmic rays above 4×10^{19} eV**, *Phys. Rev. Lett.* **101**, 061101 (2008) doi:10.1103/PhysRevLett.101.061101 [arXiv:0806.4302 [astro-ph]].
- [7] J. Abraham *et al.* [Pierre Auger Collaboration], **Measurement of the energy spectrum of cosmic rays above 10^{18} eV using the Pierre Auger Observatory**, *Phys. Lett. B* **685**, 239 (2010) doi:10.1016/j.physletb.2010.02.013 [arXiv:1002.1975 [astro-ph.HE]].
- [8] K. Greisen, **End to the cosmic ray spectrum?**, *Phys. Rev. Lett.* **16**, 748 (1966) doi:10.1103/PhysRevLett.16.748.
- [9] G. T. Zatsepin and V. A. Kuzmin, **Upper limit of the spectrum of cosmic rays**, *JETP Lett.* **4**, 78 (1966) [*Pisma Zh. Eksp. Teor. Fiz.* **4**, 114 (1966)].
- [10] P. A. R. Ade *et al.* [Planck Collaboration], **Planck 2015 results. XIII. Cosmological parameters**, *Astron. Astrophys.* **594**, A13 (2016) doi:10.1051/0004-6361/201525830 [arXiv:1502.01589 [astro-ph.CO]].
- [11] M. Tanabashi *et al.* [Particle Data Group], **Review of Particle Physics**, *Phys. Rev. D* **98**, 030001 (2018).
- [12] L. A. Anchordoqui, **Ultra-high-energy cosmic rays: facts, myths, and legends**, doi:10.5170/CERN-2013-003.303 arXiv:1104.0509 [hep-ph].
- [13] L. A. Anchordoqui *et al.*, **Roadmap for ultra-high energy cosmic ray physics and astronomy (whitepaper for Snowmass 2013)**, arXiv:1307.5312 [astro-ph.HE].
- [14] L. Anchordoqui, T. C. Paul, S. Reucroft and J. Swain, **Ultrahigh-energy cosmic rays: The state of the art before the Auger Observatory**, *Int. J. Mod. Phys. A* **18**, 2229 (2003) doi:10.1142/S0217751X03013879 [hep-ph/0206072].

- [15] D. F. Torres and L. A. Anchordoqui, *Astrophysical origins of ultrahigh energy cosmic rays*, Rept. Prog. Phys. **67**, 1663 (2004) doi:10.1088/0034-4885/67/9/R03 [astro-ph/0402371].
- [16] L. Anchordoqui, M. T. Dova, A. G. Mariazzi, T. McCauley, T. C. Paul, S. Reucroft and J. Swain, *High energy physics in the atmosphere: Phenomenology of cosmic ray air showers*, Annals Phys. **314**, 145 (2004) doi:10.1016/j.aop.2004.07.003 [hep-ph/0407020].
- [17] V. F. Hess, *Über Beobachtungen der durchdringenden Strahlung bei sieben Freiballonfahrten [Observation of penetrating radiation in seven free balloon flights]*, Phys. Z. **13**, 1084 (1912).
- [18] P. Auger, R. Maze and T. Grivet-Mayer, *Grandes gerbes cosmiques atmosphériques contenant des corpuscules ultrapénétrants [Extensive cosmic showers in the atmosphere containing ultra-penetrating particles]*, Compt. Rend. Hebd. Seances Acad. Sci. **206**, 1721 (1938).
- [19] P. Auger, P. Ehrenfest, R. Maze, J. Daudin and R. A. Fréon, *Extensive cosmic ray showers*, Rev. Mod. Phys. **11**, 288 (1939). doi:10.1103/RevModPhys.11.288
- [20] G. W. Clark, J. Earl, W. L. Kraushaar, J. Linsley, B. B. Rossi, F. Scherb and D. W. Scott, *Cosmic-ray air showers at sea level*, Phys. Rev. **122**, 637 (1961). doi:10.1103/PhysRev.122.637
- [21] J. Linsley, *Evidence for a primary cosmic-ray particle with energy 10^{20} eV* Phys. Rev. Lett. **10**, 146 (1963). doi:10.1103/PhysRevLett.10.146
- [22] A. A. Penzias and R. W. Wilson, *A measurement of excess antenna temperature at 4080-Mc/s*, Astrophys. J. **142**, 419 (1965). doi:10.1086/148307
- [23] F. W. Stecker, *Photodisintegration of ultrahigh-energy cosmic rays by the universal radiation field*, Phys. Rev. **180**, 1264 (1969). doi:10.1103/PhysRev.180.1264
- [24] J. L. Puget, F. W. Stecker and J. H. Bredekamp, *Photonuclear interactions of ultrahigh-energy cosmic rays and their astrophysical consequences*, Astrophys. J. **205**, 638 (1976). doi:10.1086/154321
- [25] M. Nagano and A. A. Watson, *Observations and implications of the ultrahigh-energy cosmic rays*, Rev. Mod. Phys. **72**, 689 (2000).
- [26] K. H. Kampert and A. A. Watson, *Extensive air showers and ultra-high-energy cosmic rays: a historical review*, Eur. Phys. J. H **37**, 359 (2012) doi:10.1140/epjh/e2012-30013-x [arXiv:1207.4827 [physics.hist-ph]].
- [27] R. M. Baltrusaitis *et al.*, *The Utah Fly's Eye detector*, Nucl. Instrum. Meth. A **240**, 410 (1985).
- [28] T. Abu-Zayyad *et al.*, *The prototype high-resolution Fly's Eye cosmic ray detector*, Nucl. Instrum. Meth. A **450**, 253 (2000).
- [29] T. Abu-Zayyad *et al.* [Telescope Array Collaboration], *The surface detector array of the Telescope Array experiment*, Nucl. Instrum. Meth. A **689**, 87 (2013) doi:10.1016/j.nima.2012.05.079 [arXiv:1201.4964 [astro-ph.IM]].

- [30] H. Tokuno *et al.*, [New air fluorescence detectors employed in the Telescope Array experiment](#), Nucl. Instrum. Meth. A **676**, 54 (2012) doi:10.1016/j.nima.2012.02.044 [arXiv:1201.0002 [astro-ph.IM]].
- [31] J. Abraham *et al.* [Pierre Auger Collaboration], [Properties and performance of the prototype instrument for the Pierre Auger Observatory](#), Nucl. Instrum. Meth. A **523**, 50 (2004).
- [32] A. Aab *et al.* [Pierre Auger Collaboration], [The Pierre Auger Observatory: Contributions to the 35th International Cosmic Ray Conference \(ICRC 2017\)](#), arXiv:1708.06592 [astro-ph.HE].
- [33] J. Abraham *et al.* [Pierre Auger Collaboration], [Trigger and aperture of the surface detector array of the Pierre Auger Observatory](#), Nucl. Instrum. Meth. A **613**, 29 (2010).
- [34] J. A. Abraham *et al.* [Pierre Auger Collaboration], [The fluorescence detector of the Pierre Auger Observatory](#), Nucl. Instrum. Meth. A **620**, 227 (2010) [arXiv:0907.4282].
- [35] P. Abreu *et al.* [Pierre Auger Collaboration], [The exposure of the hybrid detector of the Pierre Auger Observatory](#), Astropart. Phys. **34**, 368 (2011) [arXiv:1010.6162 [astro-ph.HE]].
- [36] G. B. Rybicki and A. P. Lightman, [Radiative Processes in Astrophysics](#), (John Wiley & Sons, Massachusetts, 1979) ISBN 978-0-471-82759-7.
- [37] M. Kachelriess, [Lecture notes on high energy cosmic rays](#), arXiv:0801.4376 [astro-ph].
- [38] D. Maurin, F. Melot and R. Taillet, [A database of charged cosmic rays](#), Astron. Astrophys. **569**, A32 (2014) doi:10.1051/0004-6361/201321344 [arXiv:1302.5525 [astro-ph.HE]].
- [39] L. A. Anchordoqui, M. T. Dova, L. N. Epele and S. J. Sciutto, [Hadronic interactions models beyond collider energies](#), Phys. Rev. D **59**, 094003 (1999) doi:10.1103/PhysRevD.59.094003 [hep-ph/9810384].
- [40] C. A. Garcia Canal, S. J. Sciutto and T. Tarutina, [Testing hadronic interaction packages at cosmic ray energies](#), Phys. Rev. D **79**, 054006 (2009) doi:10.1103/PhysRevD.79.054006 [arXiv:0903.2409 [astro-ph.HE]].
- [41] P. Gondolo, G. Ingelman and M. Thunman, [Charm production and high-energy atmospheric muon and neutrino fluxes](#), Astropart. Phys. **5**, 309 (1996) doi:10.1016/0927-6505(96)00033-3 [hep-ph/9505417].
- [42] A. Aab *et al.* [Pierre Auger Collaboration], [Testing hadronic interactions at ultrahigh energies with air showers measured by the Pierre Auger Observatory](#), Phys. Rev. Lett. **117**, 192001 (2016) doi:10.1103/PhysRevLett.117.192001 [arXiv:1610.08509 [hep-ex]].
- [43] J. Linsley and A. A. Watson, [Validity of scaling to \$10^{20}\$ eV and high-energy cosmic ray composition](#), Phys. Rev. Lett. **46**, 459 (1981). doi:10.1103/PhysRevLett.46.459
- [44] L. D. Landau and I. Pomeranchuk, [Limits of applicability of the theory of Bremsstrahlung electrons and pair production at high-energies](#), Dokl. Akad. Nauk Ser. Fiz. **92**, 535 (1953).
- [45] A. B. Migdal, [Bremsstrahlung and pair production in condensed media at high-energies](#), Phys. Rev. **103**, 1811 (1956). doi:10.1103/PhysRev.103.1811

- [46] A. Aab *et al.* [Pierre Auger Collaboration], [Search for photons with energies above \$10^{18}\$ eV using the hybrid detector of the Pierre Auger Observatory](#), JCAP **1704** (2017) no.04, 009 doi:10.1088/1475-7516/2017/04/009 [arXiv:1612.01517 [astro-ph.HE]].
- [47] J. Abraham *et al.* [Pierre Auger Collaboration], [An upper limit to the photon fraction in cosmic rays above \$10^{19}\$ -eV from the Pierre Auger Observatory](#), Astropart. Phys. **27**, 155 (2007) doi:10.1016/j.astropartphys.2006.10.004 [astro-ph/0606619].
- [48] J. Abraham *et al.* [Pierre Auger Collaboration], [Upper limit on the cosmic-ray photon flux above \$10^{19}\$ eV using the surface detector of the Pierre Auger Observatory](#), Astropart. Phys. **29**, 243 (2008) doi:10.1016/j.astropartphys.2008.01.003 [arXiv:0712.1147 [astro-ph]].
- [49] J. Abraham *et al.* [Pierre Auger Collaboration], [Upper limit on the cosmic-ray photon fraction at EeV energies from the Pierre Auger Observatory](#), Astropart. Phys. **31**, 399 (2009) doi:10.1016/j.astropartphys.2009.04.003 [arXiv:0903.1127 [astro-ph.HE]].
- [50] J. Abraham *et al.* [Pierre Auger Collaboration], [Measurement of the depth of maximum of extensive air showers above \$10^{18}\$ eV](#), Phys. Rev. Lett. **104**, 091101 (2010) doi:10.1103/PhysRevLett.104.091101 [arXiv:1002.0699 [astro-ph.HE]].
- [51] A. Aab *et al.* [Pierre Auger Collaboration], [Depth of maximum of air-shower profiles at the Pierre Auger Observatory I: Measurements at energies above \$10^{17.8}\$ eV](#), Phys. Rev. D **90**, no. 12, 122005 (2014) doi:10.1103/PhysRevD.90.122005 [arXiv:1409.4809 [astro-ph.HE]].
- [52] M. Unger [Pierre Auger Collaboration], [Highlights from the Pierre Auger Observatory](#), PoS ICRC **2017**, 1102 (2017) [arXiv:1710.09478 [astro-ph.HE]].
- [53] R. U. Abbasi *et al.*, [Study of ultrahigh energy cosmic ray composition using Telescope Arrays Middle Drum detector and surface array in hybrid mode](#), Astropart. Phys. **64**, 49 (2014) doi:10.1016/j.astropartphys.2014.11.004 [arXiv:1408.1726 [astro-ph.HE]].
- [54] R. Abbasi *et al.* [Pierre Auger and Telescope Array Collaborations], [Report of the working group on the composition of ultrahigh energy cosmic rays](#), JPS Conf. Proc. **9**, 010016 (2016) doi:10.7566/JPSCP.9.010016 [arXiv:1503.07540 [astro-ph.HE]].
- [55] R. U. Abbasi *et al.* [Telescope Array Collaboration], [Depth of ultra-high energy cosmic ray induced air shower maxima measured by the Telescope Array Black Rock and Long Ridge FADC fluorescence detectors and surface array in hybrid mode](#), arXiv:1801.09784 [astro-ph.HE].
- [56] W. Hanlon *et al.*, [Report of the working group on the mass composition of ultrahigh energy cosmic rays](#), JPS Conf. Proc. **19**, 011013 (2018). doi:10.7566/JPSCP.19.011013
- [57] A. Aab *et al.* [Pierre Auger Collaboration], [Evidence for a mixed mass composition at the “ankle” in the cosmic-ray spectrum](#), Phys. Lett. B **762**, 288 (2016) doi:10.1016/j.physletb.2016.09.039 [arXiv:1609.08567 [astro-ph.HE]].

- [58] A. Aab *et al.* [Pierre Auger Collaboration], [Inferences on mass composition and tests of hadronic interactions from 0.3 to 100 EeV using the water-Cherenkov detectors of the Pierre Auger Observatory](#), Phys. Rev. D **96**, no. 12, 122003 (2017) doi:10.1103/PhysRevD.96.122003 [arXiv:1710.07249 [astro-ph.HE]].
- [59] D. Ivanov, [TA spectrum summary](#), PoS ICRC **2015**, 349 (2016).
- [60] J. J. Engelmann, P. Ferrando, A. Soutoul, P. Goret and E. Juliusson, [Charge composition and energy spectra of cosmic-ray for elements from Be to Ni: Results from HEAO-3-C2](#), Astron. Astrophys. **233** (1990) 96.
- [61] E. Juliusson, [Charge composition and energy spectra of cosmic-ray nuclei at energies above 20 GeV per nucleon](#) Astrophys. J. **191**, 331 (1974) doi:10.1086/152972.
- [62] O. Adriani *et al.* [PAMELA Collaboration], [PAMELA measurements of cosmic-ray proton and helium spectra](#), Science **332**, 69 (2011) doi:10.1126/science.1199172 [arXiv:1103.4055 [astro-ph.HE]].
- [63] O. Adriani *et al.*, [Time dependence of the proton flux measured by PAMELA during the July 2006 - December 2009 solar minimum](#), Astrophys. J. **765**, 91 (2013) doi:10.1088/0004-637X/765/2/91 [arXiv:1301.4108 [astro-ph.HE]].
- [64] M. Aguilar *et al.* [AMS Collaboration], [Precision measurement of the proton flux in primary cosmic rays from rigidity 1 GV to 1.8 TV with the Alpha Magnetic Spectrometer on the International Space Station](#), Phys. Rev. Lett. **114**, 171103 (2015). doi:10.1103/PhysRevLett.114.171103
- [65] M. Aguilar *et al.* [AMS Collaboration], [Precision measurement of the helium flux in primary cosmic rays of rigidities 1.9 GV to 3 TV with the Alpha Magnetic Spectrometer on the International Space Station](#), Phys. Rev. Lett. **115**, no. 21, 211101 (2015). doi:10.1103/PhysRevLett.115.211101
- [66] M. Aguilar *et al.* [AMS Collaboration], Phys. Rev. Lett. **119**, no. 25, 251101 (2017). doi:10.1103/PhysRevLett.119.251101
- [67] H. S. Ahn *et al.*, [Energy spectra of cosmic-ray nuclei at high energies](#), Astrophys. J. **707**, 593 (2009) doi:10.1088/0004-637X/707/1/593 [arXiv:0911.1889 [astro-ph.HE]].
- [68] Y. S. Yoon *et al.*, [Cosmic-ray proton and helium spectra from the first CREAM flight](#), Astrophys. J. **728**, 122 (2011) doi:10.1088/0004-637X/728/2/122 [arXiv:1102.2575 [astro-ph.HE]].
- [69] P. Maestro *et al.*, [Measurements of cosmic-ray energy spectra with the 2nd CREAM flight](#), Nucl. Phys. Proc. Suppl. **196**, 239 (2009) doi:10.1016/j.nuclphysbps.2009.09.045 [arXiv:1003.5757 [astro-ph.HE]].
- [70] Y. S. Yoon *et al.*, [Proton and helium spectra from the CREAM-III flight](#), Astrophys. J. **839**, no. 1, 5 (2017) doi:10.3847/1538-4357/aa68e4 [arXiv:1704.02512 [astro-ph.HE]].
- [71] G. A. de Nolfo *et al.*, [Observations of the Li, Be, and B isotopes and constraints on cosmic-ray propagation](#), Adv. Space Res. **38**, 1558 (2006) doi:10.1016/j.asr.2006.09.008 [astro-ph/0611301].

- [72] K. A. Lave *et al.*, **Galactic cosmic-ray energy spectra and composition during the 2009-2010 solar minimum period**, *Astrophys. J.* **770**, 117 (2013) doi:10.1088//0004-637X/770/2/117.
- [73] S. P. Swordy, D. Mueller, P. Meyer, J. L'Heureux, J. M. Grunsfeld, **Relative abundances of secondary and primary cosmic rays at high energies** *Astrophys. J.* **349**, 625 (1990) doi:10.1086/168349.
- [74] D. Mueller, S. P. Swordy, P. Meyer, J. L'Heureux, J. M. Grunsfeld, **Energy spectra and composition of primary cosmic rays** *Astrophys. J.* **374**, 356 (1991) doi:10.1086/170125.
- [75] F. Aharonian *et al.* [H.E.S.S. Collaboration], **First ground based measurement of atmospheric Cherenkov light from cosmic rays**, *Phys. Rev. D* **75**, 042004 (2007) doi:10.1103/PhysRevD.75.042004 [astro-ph/0701766 [ASTRO-PH]].
- [76] P. Montini *et al.* [ARGO-YBJ Collaboration], **The bending of the proton plus helium flux in primary cosmic rays measured by the ARGO-YBJ experiment in the energy range from 20 TeV to 5 PeV**, arXiv:1608.01389 [hep-ex].
- [77] V. V. Prosin *et al.*, **Tunka-133: Results of 3 year operation**, *Nucl. Instrum. Meth. A* **756**, 94 (2014). doi:10.1016/j.nima.2013.09.018
- [78] E. E. Korosteleva, V. V. Prosin, L. A. Kuzmichev and G. Navarra, **Measurement of cosmic ray primary energy with the atmospheric Cherenkov light technique in extensive air showers**, *Nucl. Phys. Proc. Suppl.* **165**, 74 (2007). doi:10.1016/j.nuclphysbps.2006.11.012
- [79] M. G. Aartsen *et al.* [IceCube Collaboration], **The IceCube neutrino observatory contributions to ICRC 2015 Part III: cosmic rays**, arXiv:1510.05225 [astro-ph.HE].
- [80] W. D. Apel *et al.* [KASCADE-Grande Collaboration], **The spectrum of high-energy cosmic rays measured with KASCADE-Grande**, arXiv:1206.3834 [astro-ph.HE].
- [81] S. Schoo *et al.* [KASCADE-Grande Collaboration], **The energy spectrum of cosmic rays in the range from 10^{14} to 10^{18} eV**, *PoS ICRC 2015*, 263 (2016).
- [82] H. P. Dembinski, R. Engel, A. Fedynitch, T. Gaisser, F. Riehn and T. Stanev, **Data-driven model of the cosmic-ray flux and mass composition from 10 GeV to 10^{11} GeV**, *PoS ICRC 2017*, 533 (2017) [arXiv:1711.11432 [astro-ph.HE]].
- [83] L. J. Gleeson and W. I. Axford, **Solar modulation of Galactic cosmic rays**, *Astrophys. J.* **154**, 1011 (1968). doi:10.1086/149822
- [84] I. G. Usoskin, G. A. Bazilevskaya, and G. A. Kovaltsov, **Solar modulation parameter for cosmic rays since 1936 reconstructed from ground-based neutron monitors and ionization chambers**, *J. Geophys. Res. Space Phys.* **116**, A02104 (2011) doi:10.1029/2010JA016105.
- [85] R. U. Abbasi *et al.*, **Evidence for declination dependence of ultra-high-energy cosmic ray spectrum in the Northern hemisphere**, arXiv:1801.07820 [astro-ph.HE].
- [86] R. U. Abbasi *et al.* [Telescope Array Collaboration], **Search for anisotropy in the ultra-high-energy cosmic ray spectrum using the Telescope Array surface detector**, [arXiv:1707.04967 [astro-ph.HE]].

- [87] A. Aab *et al.* [Pierre Auger Collaboration], [Depth of maximum of air-shower profiles at the Pierre Auger Observatory II: Composition implications](#), Phys. Rev. D **90**, no. 12, 122006 (2014) doi:10.1103/PhysRevD.90.122006 [arXiv:1409.5083 [astro-ph.HE]].
- [88] A. Aab *et al.* [Pierre Auger Collaboration], [The Pierre Auger Observatory contributions to the 34th International Cosmic Ray Conference \(ICRC 2015\)](#), arXiv:1509.03732 [astro-ph.HE].
- [89] B. Peters, [Primary cosmic radiation and extensive air showers](#), Nuovo Cim. **22**, 800 (1961) doi:10.1007/BF02783106
- [90] R. U. Abbasi *et al.*, [The cosmic-ray energy spectrum between 2 PeV and 2 EeV observed with the TALE detector in monocular mode](#), arXiv:1803.01288 [astro-ph.HE].
- [91] M. Hillas, [The energy spectrum of cosmic rays in an evolving universe](#), Phys. Lett. A **24**, 677 (1967) doi:10.1016/0375-9601(67)91023-7.
- [92] V. Berezhinsky, A. Z. Gazizov and S. I. Grigorieva, [On astrophysical solution to ultrahigh-energy cosmic rays](#), Phys. Rev. D **74**, 043005 (2006) doi:10.1103/PhysRevD.74.043005 [hep-ph/0204357].
- [93] R. Aloisio, V. Berezhinsky and P. Blasi, [Ultrahigh energy cosmic rays: implications of Auger data for source spectra and chemical composition](#), JCAP **1410**, no. 10, 020 (2014) doi:10.1088/1475-7516/2014/10/020 [arXiv:1312.7459 [astro-ph.HE]].
- [94] M. Unger, G. R. Farrar and L. A. Anchordoqui, [Origin of the ankle in the ultrahigh energy cosmic ray spectrum, and of the extragalactic protons below it](#), Phys. Rev. D **92**, no. 12, 123001 (2015) doi:10.1103/PhysRevD.92.123001 [arXiv:1505.02153 [astro-ph.HE]].
- [95] L. A. Anchordoqui, [Neutron \$\beta\$ -decay as the origin of IceCubes PeV \(anti\)neutrinos](#), Phys. Rev. D **91**, 027301 (2015) doi:10.1103/PhysRevD.91.027301 [arXiv:1411.6457 [astro-ph.HE]].
- [96] G. R. Farrar, M. Unger and L. Anchordoqui, [The origin of the ankle in the UHECR spectrum, and of the extragalactic protons below it](#), PoS ICRC **2015**, 513 (2016) doi:10.22323/1.236.0513 [arXiv:1512.00484 [astro-ph.HE]].
- [97] A. Aab *et al.* [Pierre Auger Collaboration], [Combined fit of spectrum and composition data as measured by the Pierre Auger Observatory](#), JCAP **1704**, 038 (2017) Erratum: [JCAP **1803**, E02 (2018)] doi:10.1088/1475-7516/2018/03/E02, 10.1088/1475-7516/2017/04/038 [arXiv:1612.07155 [astro-ph.HE]].
- [98] P. Sommers, [Cosmic ray anisotropy analysis with a full-sky observatory](#), Astropart. Phys. **14**, 271 (2001) doi:10.1016/S0927-6505(00)00130-4 [astro-ph/0004016].
- [99] A. di Matteo *et al.*, [Arrival directions of cosmic rays at ultra-high energies](#), JPS Conf. Proc. **19**, 011020 (2018). doi:10.7566/JPSCP.19.011020
- [100] R. U. Abbasi *et al.* [Telescope Array Collaboration], [Indications of intermediate-scale anisotropy of cosmic rays with energy greater than 57 EeV in the Northern sky measured with the surface detector of the Telescope Array Experiment](#), Astrophys. J. **790**, L21 (2014) doi:10.1088/2041-8205/790/2/L21 [arXiv:1404.5890 [astro-ph.HE]].

- [101] J. Abraham *et al.* [Pierre Auger Collaboration], **Correlation of the highest energy cosmic rays with nearby extragalactic objects**, *Science* **318**, 938 (2007) doi:10.1126/science.1151124 [arXiv:0711.2256 [astro-ph]].
- [102] A. Aab *et al.* [Pierre Auger Collaboration], **Searches for anisotropies in the arrival directions of the highest energy cosmic rays detected by the Pierre Auger Observatory**, *Astrophys. J.* **804**, no. 1, 15 (2015) doi:10.1088/0004-637X/804/1/15 [arXiv:1411.6111 [astro-ph.HE]].
- [103] T.-P. Li and Y.-Q. Ma, **Analysis methods for results in gamma-ray astronomy**, *Astrophys. J.* **272**, 317 (1983). doi:10.1086/161295
- [104] J. N. Matthews, **Highlights from the Telescope Array**, *PoS ICRC 2017*, 1096 (2017).
- [105] R. U. Abbasi *et al.*, **Evidence of intermediate-scale energy spectrum anisotropy of cosmic rays $E \geq 10^{19.2}$ eV with the Telescope Array surface detector**, arXiv:1802.05003 [astro-ph.HE].
- [106] L. A. Anchordoqui, C. Hojvat, T. P. McCauley, T. C. Paul, S. Reucroft, J. D. Swain and A. Widom, **Full-sky search for ultra-high-energy cosmic ray anisotropies**, *Phys. Rev. D* **68**, 083004 (2003) doi:10.1103/PhysRevD.68.083004 [astro-ph/0305158].
- [107] P. B. Denton and T. J. Weiler, **The fortuitous latitude of the Pierre Auger Observatory and Telescope Array for reconstructing the quadrupole moment**, *Astrophys. J.* **802**, no. 1, 25 (2015) doi:10.1088/0004-637X/802/1/25 [arXiv:1409.0883 [astro-ph.HE]].
- [108] A. Aab *et al.* [Telescope Array and Pierre Auger Collaborations], **Searches for large-scale anisotropy in the arrival directions of cosmic rays detected above energy of 10^{19} eV at the Pierre Auger Observatory and the Telescope Array**, *Astrophys. J.* **794**, no. 2, 172 (2014) doi:10.1088/0004-637X/794/2/172 [arXiv:1409.3128 [astro-ph.HE]].
- [109] P. B. Denton and T. J. Weiler, **Sensitivity of full-sky experiments to large scale cosmic ray anisotropies**, *JHEAp* **8**, 1 (2015) doi:10.1016/j.jheap.2015.06.002 [arXiv:1505.03922 [astro-ph.HE]].
- [110] J. Linsley, **Fluctuation effects on directional data**, *Phys. Rev. Lett.* **34**, 1530 (1975). doi:10.1103/PhysRevLett.34.1530
- [111] D. Wittkowski and K. H. Kampert, **On the anisotropy in the arrival directions of ultra-high-energy cosmic rays**, *Astrophys. J.* **854**, no. 1, L3 (2018) doi:10.3847/2041-8213/aaa2f9 [arXiv:1710.05617 [astro-ph.HE]].
- [112] J. Aublin and E. Parizot, **Generalized 3D-reconstruction method of a dipole anisotropy in cosmic-ray distributions**, *Astron. Astrophys.* **441**, 407 (2005) doi:10.1051/0004-6361:20052833 [astro-ph/0504575].
- [113] P. Abreu *et al.* [Pierre Auger Collaboration], **Search for first harmonic modulation in the right ascension distribution of cosmic rays detected at the Pierre Auger Observatory**, *Astropart. Phys.* **34**, 627 (2011) doi:10.1016/j.astropartphys.2010.12.007 [arXiv:1103.2721 [astro-ph.HE]].

- [114] A. Aab *et al.* [Pierre Auger Collaboration], **Large scale distribution of ultra high energy cosmic rays detected at the Pierre Auger Observatory with zenith angles up to 80°** , *Astrophys. J.* **802**, no. 2, 111 (2015) doi:10.1088/0004-637X/802/2/111 [arXiv:1411.6953 [astro-ph.HE]].
- [115] A. Aab *et al.* [Pierre Auger Collaboration], **Observation of a large-scale anisotropy in the arrival directions of cosmic rays above 8×10^{18} eV**, *Science* **357**, no. 6537, 1266 (2017) doi:10.1126/science.aan4338 [arXiv:1709.07321 [astro-ph.HE]].
- [116] R. Jansson and G. R. Farrar, **A new model of the Galactic magnetic field**, *Astrophys. J.* **757**, 14 (2012) doi:10.1088/0004-637X/757/1/14 [arXiv:1204.3662 [astro-ph.GA]].
- [117] R. Jansson and G. R. Farrar, **The Galactic magnetic field** *Astrophys. J.* **761**, L11 (2012) doi:10.1088/2041-8205/761/1/L11 [arXiv:1210.7820 [astro-ph.GA]].
- [118] M. Unger and G. R. Farrar, **Uncertainties in the magnetic field of the Milky Way**, *PoS ICRC 2017*, 558 (2017) [arXiv:1707.02339 [astro-ph.GA]].
- [119] A. Aab *et al.* [Pierre Auger Collaboration], **Large-scale cosmic-ray anisotropies above 4 EeV measured by the Pierre Auger Observatory**, *Astrophys. J.* **868** (2018) no.1, 4 doi:10.3847/1538-4357/aae689 [arXiv:1808.03579 [astro-ph.HE]].
- [120] G. Lemaitre and M. S. Vallarta, **On Compton's latitude effect of cosmic radiation**, *Phys. Rev.* **43**, 87 (1933). doi:10.1103/PhysRev.43.87
- [121] W. F. G. Swann, **Application of Liouville's theorem to electron orbits in the Earth's magnetic field**, *Phys. Rev.* **44**, 224 (1933). doi:10.1103/PhysRev.44.224
- [122] A. H. Compton and I. A. Getting, **An apparent effect of Galactic rotation on the intensity of cosmic rays**, *Phys. Rev.* **47**, 817 (1935). doi:10.1103/PhysRev.47.817
- [123] A. Kogut *et al.*, **Dipole anisotropy in the COBE DMR first year sky maps**, *Astrophys. J.* **419**, 1 (1993) doi:10.1086/173453 [astro-ph/9312056].
- [124] G. Hinshaw *et al.* [WMAP Collaboration], **Five-year Wilkinson Microwave Anisotropy Probe (WMAP) observations: Data processing, sky maps, and basic results**, *Astrophys. J. Suppl.* **180**, 225 (2009) doi:10.1088/0067-0049/180/2/225 [arXiv:0803.0732 [astro-ph]].
- [125] R. Adam *et al.* [Planck Collaboration], **Planck 2015 results I: Overview of products and scientific results**, *Astron. Astrophys.* **594**, A1 (2016) doi:10.1051/0004-6361/201527101 [arXiv:1502.01582 [astro-ph.CO]].
- [126] M. Kachelriess and P. D. Serpico, **The Compton-Getting effect on ultra-high energy cosmic rays of cosmological origin**, *Phys. Lett. B* **640**, 225 (2006) doi:10.1016/j.physletb.2006.08.006 [astro-ph/0605462].
- [127] N. Globus and T. Piran, **The extragalactic ultra-high energy cosmic-ray dipole**, *Astrophys. J.* **850**, no. 2, L25 (2017) doi:10.3847/2041-8213/aa991b [arXiv:1709.10110 [astro-ph.HE]].

- [128] N. Globus, D. Allard and E. Parizot, [Propagation of high-energy cosmic rays in extragalactic turbulent magnetic fields: resulting energy spectrum and composition](#), *Astron. Astrophys.* **479**, 97 (2008) doi:10.1051/0004-6361:20078653 [arXiv:0709.1541 [astro-ph]].
- [129] P. P. Kronberg, [Extragalactic magnetic fields](#), *Rept. Prog. Phys.* **57**, 325 (1994). doi:10.1088/0034-4885/57/4/001
- [130] P. Blasi, S. Burles and A. V. Olinto, [Cosmological magnetic fields limits in an inhomogeneous universe](#), *Astrophys. J.* **514**, L79 (1999) doi:10.1086/311958 [astro-ph/9812487].
- [131] M. S. Pshirkov, P. G. Tinyakov and F. R. Urban, [New limits on extragalactic magnetic fields from rotation measures](#), *Phys. Rev. Lett.* **116**, no. 19, 191302 (2016) doi:10.1103/PhysRevLett.116.191302 [arXiv:1504.06546 [astro-ph.CO]].
- [132] E. Parizot, [GZK horizon and magnetic fields](#), *Nucl. Phys. Proc. Suppl.* **136**, 169 (2004) doi:10.1016/j.nuclphysbps.2004.10.034 [astro-ph/0409191].
- [133] J. P. Huchra *et al.*, [The 2MASS redshift survey: Description and data release](#), *Astrophys. J. Suppl.* **199**, 26 (2012) doi:10.1088/0067-0049/199/2/26 [arXiv:1108.0669 [astro-ph.CO]].
- [134] P. Erdogdu *et al.*, [The dipole anisotropy of the 2 Micron All-Sky Redshift Survey](#), *Mon. Not. Roy. Astron. Soc.* **368**, 1515 (2006) doi:10.1111/j.1365-2966.2006.10243.x [astro-ph/0507166].
- [135] D. Harari, S. Mollerach and E. Roulet, [Anisotropies of ultrahigh energy cosmic ray nuclei diffusing from extragalactic sources](#), *Phys. Rev. D* **92**, no. 6, 063014 (2015) doi:10.1103/PhysRevD.92.063014 [arXiv:1507.06585 [astro-ph.HE]].
- [136] R. W. Clay [Pierre Auger Collaboration], [The anisotropy search program for the Pierre Auger Observatory](#), astro-ph/0308494.
- [137] M. Ackermann *et al.* [Fermi-LAT Collaboration], [2FHL: The second catalog of hard Fermi-LAT sources](#), *Astrophys. J. Suppl.* **222**, no. 1, 5 (2016) doi:10.3847/0067-0049/222/1/5 [arXiv:1508.04449 [astro-ph.HE]].
- [138] M. Ackermann *et al.* [Fermi-LAT Collaboration], [GeV observations of star-forming galaxies with Fermi-LAT](#), *Astrophys. J.* **755**, 164 (2012) doi:10.1088/0004-637X/755/2/164 [arXiv:1206.1346 [astro-ph.HE]].
- [139] Q. W. Tang, X. Y. Wang and P. H. Thomas Tam, [Discovery of GeV emission from the direction of the luminous infrared galaxy NGC 2146](#), *Astrophys. J.* **794**, no. 1, 26 (2014) doi:10.1088/0004-637X/794/1/26 [arXiv:1407.3391 [astro-ph.HE]].
- [140] F. K. Peng, X. Y. Wang, R. Y. Liu, Q. W. Tang and J. F. Wang, [First detection of GeV emission from an ultraluminous infrared galaxy: Arp 220 as seen with the Fermi Large Area Telescope](#), *Astrophys. J.* **821**, no. 2, L20 (2016) doi:10.3847/2041-8205/821/2/L20 [arXiv:1603.06355 [astro-ph.HE]].
- [141] M. Hayashida *et al.*, [Discovery of GeV emission from the Circinus galaxy with the Fermi Large Area Telescope](#), *Astrophys. J.* **779**, 131 (2013) doi:10.1088/0004-637X/779/2/131 [arXiv:1310.1913 [astro-ph.HE]].

- [142] V. A. Acciari *et al.*, [A connection between star formation activity and cosmic rays in the starburst galaxy M82](#), *Nature* **462**, 770 (2009) doi:10.1038/nature08557 [arXiv:0911.0873 [astro-ph.CO]].
- [143] H. Abdalla *et al.* [H.E.S.S. Collaboration], [The starburst galaxy NGC 253 revisited by H.E.S.S. and Fermi-LAT](#), [arXiv:1806.03866 [astro-ph.HE]].
- [144] R. A. Fisher, [Dispersion on a sphere](#) *Proc. Roy. Soc. London Ser. A.* **217** 295 (1953).
- [145] P. Abreu *et al.* [Pierre Auger Collaboration], [Update on the correlation of the highest energy cosmic rays with nearby extragalactic matter](#), *Astropart. Phys.* **34**, 314 (2010) doi:10.1016/j.astropartphys.2010.08.010 [arXiv:1009.1855 [astro-ph.HE]].
- [146] D. Harari, S. Mollerach and E. Roulet, [Kolmogorov-Smirnov test as a tool to study the distribution of ultra-high energy cosmic ray sources](#), *Mon. Not. Roy. Astron. Soc.* **394**, 916 (2009) doi:10.1111/j.1365-2966.2008.14327.x [arXiv:0811.0008 [astro-ph]].
- [147] J. K. Becker, P. L. Biermann, J. Dreyer and T. M. Kneiske, [Cosmic Rays VI: Starburst galaxies at multiwavelengths](#), arXiv:0901.1775 [astro-ph.HE].
- [148] F. Acero *et al.* [Fermi-LAT Collaboration], [Fermi Large Area Telescope third source catalog](#), *Astrophys. J. Suppl.* **218**, no. 2, 23 (2015) doi:10.1088/0067-0049/218/2/23 [arXiv:1501.02003 [astro-ph.HE]].
- [149] L. A. Anchordoqui, T. C. Paul, L. H. M. da Silva, D. F. Torres and B. J. Vlcek, [What IceCube data tell us about neutrino emission from star-forming galaxies \(so far\)](#), *Phys. Rev. D* **89**, no. 12, 127304 (2014) doi:10.1103/PhysRevD.89.127304 [arXiv:1405.7648 [astro-ph.HE]].
- [150] K. Fang, T. Fujii, T. Linden and A. V. Olinto, [Is the ultra-high energy cosmic-ray excess observed by the Telescope Array correlated with IceCube neutrinos?](#), *Astrophys. J.* **794**, no. 2, 126 (2014) doi:10.1088/0004-637X/794/2/126 [arXiv:1404.6237 [astro-ph.HE]].
- [151] H. N. He, A. Kusenko, S. Nagataki, B. B. Zhang, R. Z. Yang and Y. Z. Fan, [Monte Carlo Bayesian search for the plausible source of the Telescope Array hot spot](#), *Phys. Rev. D* **93**, 043011 (2016) doi:10.1103/PhysRevD.93.043011 [arXiv:1411.5273 [astro-ph.HE]].
- [152] D. N. Pfeffer, E. D. Kovetz and M. Kamionkowski, [Ultrahigh-energy cosmic ray hotspots from tidal disruption events](#), *Mon. Not. Roy. Astron. Soc.* **466**, no. 3, 2922 (2017) doi:10.1093/mnras/stw3337 [arXiv:1512.04959 [astro-ph.HE]].
- [153] R. Attallah and D. Bouchachi, [Ultra-high-energy cosmic rays from nearby starburst galaxies](#), *Mon. Not. Roy. Astron. Soc.* **478**, no. 1, 800 (2018) doi:10.1093/mnras/sty986 [arXiv:1804.06603 [astro-ph.HE]].
- [154] L. A. Anchordoqui, V. Barger and T. J. Weiler, [Cosmic mass spectrometer](#), *JHEAp* **17**, 38 (2018) doi:10.1016/j.jheap.2017.12.001 [arXiv:1707.05408 [astro-ph.HE]].
- [155] N. Globus, D. Allard, E. Parizot, C. Lachaud and T. Piran, [Can we reconcile the TA excess and hotspot with Auger observations?](#), *Astrophys. J.* **836**, no. 2, 163 (2017) doi:10.3847/1538-4357/836/2/163 [arXiv:1610.05319 [astro-ph.HE]].

- [156] L. A. Anchordoqui, H. Goldberg and D. F. Torres, *Anisotropy at the end of the cosmic ray spectrum?*, Phys. Rev. D **67**, 123006 (2003) doi:10.1103/PhysRevD.67.123006 [astro-ph/0209546].
- [157] A. Letessier-Selvon and T. Stanev, *Ultrahigh energy cosmic rays*, Rev. Mod. Phys. **83**, 907 (2011) doi:10.1103/RevModPhys.83.907 [arXiv:1103.0031 [astro-ph.HE]].
- [158] D. S. Gorbunov, P. G. Tinyakov, I. I. Tkachev and S. V. Troitsky, *On the interpretation of the cosmic-ray anisotropy at ultra-high energies*, arXiv:0804.1088 [astro-ph].
- [159] J. H. Matthews, A. R. Bell, K. M. Blundell and A. T. Araudo, *Fornax A, Centaurus A and other radio galaxies as sources of ultra-high energy cosmic rays*, doi:10.1093/mnrasl/sly099 arXiv:1805.01902 [astro-ph.HE].
- [160] R. Smida and R. Engel, *The ultra-high-energy cosmic rays image of Virgo A*, PoS ICRC **2015**, 470 (2016) doi:10.22323/1.236.0470 [arXiv:1509.09033 [astro-ph.HE]].
- [161] R. C. d. Anjos, J. F. Soriano, L. A. Anchordoqui, T. C. Paul, D. F. Torres, J. F. Krizmanic, T. A. D. Paglione, R. J. Moncada, F. Sarazin, L. Wiencke, and A. V. Olinto, *Ultrahigh-energy cosmic ray composition from the distribution of arrival directions*, Phys. Rev. D **98**, 123018 (2018) doi:10.1103/PhysRevD.98.123018 [arXiv:1810.04251 [astro-ph.HE]].
- [162] J. Biteau *et al.* [Telescope Array and Pierre Auger Collaborations], *Covering the sphere at ultra-high energies: full-sky cosmic-ray maps beyond the ankle and the flux suppression*, To be published in Proceedings of Ultra High Energy Cosmic Rays 2018, 8 - 12 October 2018, Paris.
- [163] R. U. Abbasi *et al.* [Telescope Array Collaboration], *Testing a reported correlation between arrival directions of ultra-high-energy cosmic rays and a flux pattern from nearby starburst galaxies using Telescope Array data*, Astrophys. J. **867**, no. 2, L27 (2018) doi:10.3847/2041-8213/aabf9 [arXiv:1809.01573 [astro-ph.HE]].
- [164] T. Abu-Zayyad *et al.* [Telescope Array Collaboration], *The cosmic ray energy spectrum observed with the surface detector of the Telescope Array experiment*, Astrophys. J. **768**, L1 (2013) doi:10.1088/2041-8205/768/1/L1 [arXiv:1205.5067 [astro-ph.HE]].
- [165] M. Lemoine and E. Waxman, *Anisotropy vs chemical composition at ultra-high energies*, JCAP **0911**, 009 (2009) doi:10.1088/1475-7516/2009/11/009 [arXiv:0907.1354 [astro-ph.HE]].
- [166] R. Y. Liu, A. M. Taylor, M. Lemoine, X. Y. Wang and E. Waxman, *Constraints on the source of ultra-high-energy cosmic rays using anisotropy versus chemical composition*, Astrophys. J. **776**, 88 (2013) doi:10.1088/0004-637X/776/2/88 [arXiv:1308.5699 [astro-ph.HE]].
- [167] A. Aab *et al.* [Pierre Auger Collaboration], *The Pierre Auger Observatory upgrade: Preliminary design report*, arXiv:1604.03637 [astro-ph.IM].
- [168] A. Aab *et al.* [Pierre Auger Collaboration], *Measurement of the radiation energy in the radio signal of extensive air showers as a universal estimator of cosmic-ray energy*, Phys. Rev. Lett. **116**, no. 24, 241101 (2016) doi:10.1103/PhysRevLett.116.241101 [arXiv:1605.02564 [astro-ph.HE]].

- [169] A. Aab *et al.* [Pierre Auger Collaboration], **Observation of inclined EeV air showers with the radio detector of the Pierre Auger Observatory**, arXiv:1806.05386 [astro-ph.IM].
- [170] E. Kido [for the TA Collaboration], **The TA×4 experiment**, PoS ICRC **2017**, 386 (2017).
- [171] A. M. Hillas, **The origin of ultrahigh-energy cosmic rays**, Ann. Rev. Astron. Astrophys. **22**, 425 (1984). doi:10.1146/annurev.aa.22.090184.002233
- [172] W. F. G. Swann, **A mechanism of acquirement of cosmic ray energies by electrons**, Phys. Rev. **43**, 217 (1933). doi:10.1103/PhysRev.43.217
- [173] O. C. de Jager, **Evidence for particle acceleration in a magnetized white dwarf from radio and gamma-ray observations** Astrophys. J. Suppl. **90**, 775 (1994) doi:10.1086/191902
- [174] N. R. Ikhsanov and P. L. Biermann, **High-energy emission of fast rotating white dwarfs**, Astron. Astrophys. **445**, 305 (2006) doi:10.1051/0004-6361:20053179 [astro-ph/0509070].
- [175] J. E. Gunn and J. P. Ostriker, **Acceleration of high-energy cosmic rays by pulsars**, Phys. Rev. Lett. **22**, 728 (1969). doi:10.1103/PhysRevLett.22.728
- [176] P. Blasi, R. I. Epstein and A. V. Olinto, **Ultrahigh-energy cosmic rays from young neutron star winds**, Astrophys. J. **533**, L123 (2000) doi:10.1086/312626 [astro-ph/9912240].
- [177] J. Arons, **Magnetars in the metagalaxy: an origin for ultrahigh-energy cosmic rays in the nearby universe**, Astrophys. J. **589**, 871 (2003) doi:10.1086/374776 [astro-ph/0208444].
- [178] K. Fang, K. Kotera and A. V. Olinto, **Newly-born pulsars as sources of ultrahigh energy cosmic rays**, Astrophys. J. **750**, 118 (2012) doi:10.1088/0004-637X/750/2/118 [arXiv:1201.5197 [astro-ph.HE]].
- [179] K. Fang, K. Kotera and A. V. Olinto, **Ultrahigh energy cosmic ray nuclei from extragalactic pulsars and the effect of their Galactic counterparts**, JCAP **1303**, 010 (2013) doi:10.1088/1475-7516/2013/03/010 [arXiv:1302.4482 [astro-ph.HE]].
- [180] R. D. Blandford and R. L. Znajek, **Electromagnetic extractions of energy from Kerr black holes**, Mon. Not. Roy. Astron. Soc. **179**, 433 (1977).
- [181] R. L. Znajek **The electric and magnetic conductivity of a Kerr hole**, Mon. Not. Roy. Astron. Soc. **185**, 833 (1978).
- [182] R. V. E. Lovelace, **Dynamo model of double radio sources** Nature **262**, 649 (1976).
- [183] E. Fermi, **On the origin of the cosmic radiation**, Phys. Rev. **75**, 1169 (1949). doi:10.1103/PhysRev.75.1169
- [184] E. Fermi, **Galactic magnetic fields and the origin of cosmic radiation**, Astrophys. J. **119**, 1 (1954). doi:10.1086/145789
- [185] J. R. Jokipii, **Propagation of cosmic rays in the solar wind**, Rev. Geophys. **9**, 27 (1971) doi:10.1029/RG009i001p00027

- [186] K. P. Wenzel, **Charged particle acceleration processes in the interplanetary medium**, *Adv. Space Res.* **9**, 179 (1989) doi:10.1016/0273-1177(89)90112-9
- [187] J. S. Scott and R. A. Chevalier, **Cosmic-ray production in the Cassiopeia A supernova remnant**, *Astrophys. J.* **197** L5 (1975) doi:10.1086/181763
- [188] R. A. Chevalier, J. W. Robertson, and J. S. Scott **Cosmic ray acceleration and the radio evolution of Cassiopeia A** *Astrophys. J.* **207**, 450 (1979) doi:10.1086/154514
- [189] R. A. Chevalier, W. R. Oegerle and J. S. Scott, **Further studies of particle acceleration in Cassiopeia A**, *Astrophys. J.* **222**, 527 (1978). doi:10.1086/156165
- [190] R. Cowsik and S. Sarkar, **The evolution of supernova remnants as radio sources**, *Mon. Not. Roy. Astron. Soc.* **207**, 745 (1984) Erratum: [*Mon. Not. Roy. Astron. Soc.* **209**, 719 (1984)]. doi:10.1093/mnras/209.4.719, 10.1093/mnras/207.4.745
- [191] D. F. Torres, G. E. Romero, T. M. Dame, J. A. Combi and Y. M. Butt, **Supernova remnants and gamma-ray sources**, *Phys. Rept.* **382**, 303 (2003) doi:10.1016/S0370-1573(03)00201-1 [astro-ph/0209565].
- [192] P. Blasi, **Cosmic ray acceleration in supernova remnants**, doi:10.1142/9789814329033_0061 arXiv:1012.5005 [astro-ph.HE].
- [193] J. R. Jokipii and G. Morfill, **On the origin of high-energy cosmic rays** *Astrophys. J.* **290**, L1 (1985) doi:10.1086/184430
- [194] J. R. Jokipii and G. Morfill, **Ultra-high-energy cosmic rays in a Galactic wind and its termination shock**, *Astrophys. J.* **312**, 170 (1987) doi:10.1086/164857
- [195] C. Bustard, E. G. Zweibel and C. Cotter, **Cosmic ray acceleration by a versatile family of galactic wind termination shocks**, *Astrophys. J.* **835**, no. 1, 72 (2017) doi:10.3847/1538-4357/835/1/72 [arXiv:1610.06565 [astro-ph.HE]].
- [196] L. Merten, C. Bustard, E. G. Zweibel and J. Becker Tjus, **The propagation of cosmic rays from the Galactic wind termination shock: Back to the Galaxy?**, *Astrophys. J.* **859**, no. 1, 63 (2018) doi:10.3847/1538-4357/aabfdd [arXiv:1803.08376 [astro-ph.HE]].
- [197] R. J. Protheroe and D. Kazanas, **On the origin of relativistic particles and gamma-rays in quasars**, *Astrophys. J.* **265**, 620 (1983) doi:10.1086/160707
- [198] D. Kazanas and D. C. Ellison, **The central engine of quasars and AGNs: hadronic interactions of shock accelerated relativistic protons**, *Astrophys. J.* **304**, 178 (1986) doi:10.1086/164152
- [199] R. J. Protheroe and A. P. Szabo, **High-energy cosmic rays from active galactic nuclei**, *Phys. Rev. Lett.* **69**, 2885 (1992). doi:10.1103/PhysRevLett.69.2885
- [200] P. L. Biermann and P. A. Strittmatter, **Synchrotron emission from shock waves in active galactic nuclei**, *Astrophys. J.* **322**, 643 (1987). doi:10.1086/165759

- [201] J. P. Rachen and P. L. Biermann, **Extragalactic ultrahigh-energy cosmic rays I: Contribution from hot spots in FR-II radio galaxies**, *Astron. Astrophys.* **272**, 161 (1993) [astro-ph/9301010].
- [202] G. E. Romero, J. A. Combi, L. A. Anchordoqui and S. E. Perez Bergliaffa, **A possible source of extragalactic cosmic rays with arrival energies beyond the GZK cutoff**, *Astropart. Phys.* **5**, 279 (1996) doi:10.1016/0927-6505(96)00029-1 [gr-qc/9511031].
- [203] R. D. Blandford and A. Konigl, **Relativistic jets as compact radio sources**, *Astrophys. J.* **232**, 34 (1979). doi:10.1086/157262
- [204] K. Mannheim, **The proton blazar**, *Astron. Astrophys.* **269**, 67 (1993) [astro-ph/9302006].
- [205] C. D. Dermer, S. Razzaque, J. D. Finke and A. Atoyan, **Ultrahigh energy cosmic rays from black hole jets of radio galaxies**, *New J. Phys.* **11**, 065016 (2009) doi:10.1088/1367-2630/11/6/065016 [arXiv:0811.1160 [astro-ph]].
- [206] D. Caprioli, **"Espresso" acceleration of ultra-high-energy cosmic rays**, *Astrophys. J.* **811**, no. 2, L38 (2015) doi:10.1088/2041-8205/811/2/L38 [arXiv:1505.06739 [astro-ph.HE]].
- [207] E. Waxman, **Cosmological gamma-ray bursts and the highest energy cosmic rays**, *Phys. Rev. Lett.* **75**, 386 (1995) doi:10.1103/PhysRevLett.75.386 [astro-ph/9505082].
- [208] M. Vietri, **On the acceleration of ultrahigh-energy cosmic rays in gamma-ray bursts**, *Astrophys. J.* **453**, 883 (1995) doi:10.1086/176448 [astro-ph/9506081].
- [209] L. A. Anchordoqui, **Acceleration of ultrahigh-energy cosmic rays in starburst superwinds**, *Phys. Rev. D* **97**, no. 6, 063010 (2018) doi:10.1103/PhysRevD.97.063010 [arXiv:1801.07170 [astro-ph.HE]].
- [210] A. Levinson and E. Waxman, **Probing microquasars with TeV neutrinos**, *Phys. Rev. Lett.* **87**, 171101 (2001) doi:10.1103/PhysRevLett.87.171101 [hep-ph/0106102].
- [211] F. A. Aharonian, L. A. Anchordoqui, D. Khangulyan and T. Montaruli, **Microquasar LS 5039: a TeV gamma-ray emitter and a potential TeV neutrino source**, *J. Phys. Conf. Ser.* **39**, 408 (2006) doi:10.1088/1742-6596/39/1/106 [astro-ph/0508658].
- [212] C. A. Norman, D. B. Melrose, and A. Achterberg, **The origin of cosmic rays above $10^{18.5}$ eV** *Astrophys. J.* **454**, 60 (1995). doi:10.1086/176465
- [213] H. Kang, J. P. Rachen and P. L. Biermann, **Contributions to the cosmic ray flux above the ankle: clusters of galaxies**, *Mon. Not. Roy. Astron. Soc.* **286**, 257 (1997) doi:10.1093/mnras/286.2.257 [astro-ph/9608071].
- [214] D. Ryu, H. Kang, E. Hallman and T. W. Jones, **Cosmological shock waves and their role in the large scale structure of the universe**, *Astrophys. J.* **593**, 599 (2003) doi:10.1086/376723 [astro-ph/0305164].
- [215] M. Ahlers, L. A. Anchordoqui, J. K. Becker, T. K. Gaisser, F. Halzen, D. Hooper, S. R. Klein, P. Mészáros, S. Razzaque, and S. Sarkar, **Neutrinos on the rocks: The IceCube yellow book**, FERMI-LAB-FN-0847-A, YITP-SB-10-01.

- [216] K. V. Ptitsyna and S. V. Troitsky, **Physical conditions in potential sources of ultra-high-energy cosmic rays I: Updated Hillas plot and radiation-loss constraints**, *Phys. Usp.* **53**, 691 (2010) doi:10.3367/UFNe.0180.201007c.0723 [arXiv:0808.0367 [astro-ph]].
- [217] N. Chamel and P. Haensel, **Physics of neutron star crusts**, *Living Rev. Rel.* **11**, 10 (2008) doi:10.12942/lrr-2008-10 [arXiv:0812.3955 [astro-ph]].
- [218] M. A. Ruderman and P. G. Sutherland, **Theory of pulsars: Polar caps, sparks, and coherent microwave radiation**, *Astrophys. J.* **196**, 51 (1975). doi:10.1086/153393
- [219] D. Viganó, **Magnetic fields in neutron stars**, arXiv:1310.1243 [astro-ph.HE].
- [220] P. Goldreich and W. H. Julian, **Pulsar electrodynamics**, *Astrophys. J.* **157**, 869 (1969). doi:10.1086/150119
- [221] V. S. Berezhinsky, **Acceleration to ultra high energies in magnetospheres of young pulsars**, in *Proceedings of the 18th International Cosmic Ray Conference* **2**, 275 (1983).
- [222] C. A. Faucher-Giguere and V. M. Kaspi, **Birth and evolution of isolated radio pulsars**, *Astrophys. J.* **643**, 332 (2006) doi:10.1086/501516 [astro-ph/0512585].
- [223] P. Haensel, J. P. Lasota and J. L. Zdunik, **On the minimum period of uniformly rotating neutron stars**, *Astron. Astrophys.* **344**, 151 (1999) [astro-ph/9901118].
- [224] Y. P. Ochelkov and V. V. Usov, **Curvature radiation of relativistic particles in the magnetosphere of pulsars** *Astrophys. Space Sci.* **69**, 439 (1980) doi:10.1007/BF00661929.
- [225] K. Kotera, E. Amato and P. Blasi, **The fate of ultrahigh energy nuclei in the immediate environment of young fast-rotating pulsars**, *JCAP* **1508**, no. 08, 026 (2015) doi:10.1088/1475-7516/2015/08/026 [arXiv:1503.07907 [astro-ph.HE]].
- [226] A. Spitkovsky, **Time-dependent force-free pulsar magnetospheres: axisymmetric and oblique rotators**, *Astrophys. J.* **648**, L51 (2006) doi:10.1086/507518 [astro-ph/0603147].
- [227] E. Boldt and P. Ghosh, **Cosmic rays from remnants of quasars?**, *Mon. Not. Roy. Astron. Soc.* **307**, 491 (1999) doi:10.1046/j.1365-8711.1999.02600.x [astro-ph/9902342].
- [228] E. Boldt and M. Loewenstein, **Cosmic ray generation by quasar remnants: Constraints and implications**, *Mon. Not. Roy. Astron. Soc.* **316**, L29 (2000) doi:10.1046/j.1365-8711.2000.03768.x [astro-ph/0006221].
- [229] A. Y. Neronov, D. V. Semikoz and I. I. Tkachev, **Ultra-high energy cosmic ray production in the polar cap regions of black hole magnetospheres**, *New J. Phys.* **11**, 065015 (2009) doi:10.1088/1367-2630/11/6/065015 [arXiv:0712.1737 [astro-ph]].
- [230] R. J. Moncada, R. A. Colon, J. J. Guerra, M. J. O'Dowd and L. A. Anchordoqui, **Ultra-high energy cosmic ray nuclei from remnants of dead quasars**, *JHEAp* **13-14**, 32 (2017) doi:10.1016/j.jheap.2017.04.001 [arXiv:1702.00053 [astro-ph.HE]].

- [231] L. O. Drury, [Acceleration of cosmic rays](#), *Contemp. Phys.* **35**, 231 (1994). doi:10.1080/00107519408222090
- [232] G. F. Krymskii, [A regular mechanism for the acceleration of charged particles on the front of a shock wave](#), *Akademiia Nauk SSSR Doklady* **234**, 1306 (1977).
- [233] W. I. Axford, E. Leer, and G. Skadron [The acceleration of cosmic rays by shock waves](#), in *Proceedings of the 15th International Cosmic Ray Conference* **11**, 132 (1977).
- [234] A. R. Bell, [The acceleration of cosmic rays in shock fronts I](#), *Mon. Not. Roy. Astron. Soc.* **182**, 147 (1978).
- [235] A. R. Bell, [The acceleration of cosmic rays in shock fronts II](#), *Mon. Not. Roy. Astron. Soc.* **182**, 443 (1978).
- [236] R. D. Blandford and J. P. Ostriker, [Particle acceleration by astrophysical shocks](#), *Astrophys. J.* **221**, L29 (1978). doi:10.1086/182658
- [237] P. O. Lagage and C. J. Cesarsky, [The maximum energy of cosmic rays accelerated by supernova shocks](#), *Astron. Astrophys.* **125**, 249 (1983).
- [238] L. O. Drury, [An introduction to the theory of diffusive shock acceleration of energetic particles in tenuous plasmas](#), *Rept. Prog. Phys.* **46**, 973 (1983). doi:10.1088/0034-4885/46/8/002
- [239] R. Blandford and D. Eichler, [Particle acceleration at astrophysical shocks: A theory of cosmic ray origin](#), *Phys. Rept.* **154**, 1 (1987). doi:10.1016/0370-1573(87)90134-7
- [240] R. J. Protheroe, [Acceleration and interaction of ultrahigh-energy cosmic rays](#), astro-ph/9812055.
- [241] A. R. Bell, [Cosmic ray acceleration](#), *Astropart. Phys.* **43**, 56 (2013). doi:10.1016/j.astropartphys.2012.05.022
- [242] P. Baerwald, M. Bustamante and W. Winter, [UHECR escape mechanisms for protons and neutrons from GRBs, and the cosmic ray-neutrino connection](#), *Astrophys. J.* **768**, 186 (2013) doi:10.1088/0004-637X/768/2/186 [arXiv:1301.6163 [astro-ph.HE]].
- [243] T. K. Gaisser, [Cosmic rays and particle physics](#), (Cambridge University Press, UK, 1990)
- [244] G. E. Romero, A. L. Mller and M. Roth, [Particle acceleration in the superwinds of starburst galaxies](#), arXiv:1801.06483 [astro-ph.HE].
- [245] J. R. Jokipii, [Rate of energy gain and maximum energy in diffusive shock acceleration](#) *Astrophys. J.* **313**, 842 (1987). doi:10.1086/165022
- [246] G. Ferrand, R. J. Danos, A. Shalchi, S. Safi-Harb, P. Edmon and P. Mendygral, [Cosmic ray acceleration at perpendicular shocks in supernova remnants](#), *Astrophys. J.* **792**, no. 2, 133 (2014) doi:10.1088/0004-637X/792/2/133 [arXiv:1407.6728 [astro-ph.HE]].
- [247] E. Waxman, [Extra-galactic sources of high energy neutrinos](#), *Phys. Scripta T* **121**, 147 (2005) doi:10.1088/0031-8949/2005/T121/022 [astro-ph/0502159].

- [248] T. Piran, [A new limit on the distances of nuclei UHECRs sources](#), arXiv:1005.3311 [astro-ph.HE].
- [249] H. C. Spruit, [Essential magnetohydrodynamics for astrophysics](#), arXiv:1301.5572 [astro-ph.IM].
- [250] L. A. Anchordoqui, D. Hooper, S. Sarkar and A. M. Taylor, [High-energy neutrinos from astrophysical accelerators of cosmic ray nuclei](#), *Astropart. Phys.* **29**, 1 (2008) doi:10.1016/j.astropartphys.2007.10.006 [astro-ph/0703001].
- [251] X. Y. Wang, S. Razzaque and P. Mészáros, [On the origin and survival of UHE cosmic-ray nuclei in GRBs and hypernovae](#), *Astrophys. J.* **677**, 432 (2008) doi:10.1086/529018 [arXiv:0711.2065 [astro-ph]].
- [252] K. Murase, K. Ioka, S. Nagataki and T. Nakamura, [High-energy cosmic-ray nuclei from high- and low-luminosity gamma-ray bursts and implications for multi-messenger astronomy](#), *Phys. Rev. D* **78**, 023005 (2008) doi:10.1103/PhysRevD.78.023005 [arXiv:0801.2861 [astro-ph]].
- [253] N. Globus, D. Allard, R. Mochkovitch and E. Parizot, [UHECR acceleration at GRB internal shocks](#), *Mon. Not. Roy. Astron. Soc.* **451**, no. 1, 751 (2015) doi:10.1093/mnras/stv893 [arXiv:1409.1271 [astro-ph.HE]].
- [254] D. Biehl, D. Boncioli, A. Fedynitch and W. Winter, [Cosmic-ray and neutrino emission from gamma-ray bursts with a nuclear cascade](#), *Astron. Astrophys.* **611**, A101 (2018) doi:10.1051/0004-6361/201731337 [arXiv:1705.08909 [astro-ph.HE]].
- [255] B. T. Zhang, K. Murase, S. S. Kimura, S. Horiuchi and P. Mészáros, [Low-luminosity gamma-ray bursts as the sources of ultrahigh-energy cosmic ray nuclei](#), *Phys. Rev. D* **97**, no. 8, 083010 (2018) doi:10.1103/PhysRevD.97.083010 [arXiv:1712.09984 [astro-ph.HE]].
- [256] R. D. Blandford, [Acceleration of ultrahigh-energy cosmic rays](#), *Phys. Scripta T* **85**, 191 (2000) doi:10.1238/Physica.Topical.085a00191 [astro-ph/9906026].
- [257] C. D. Dermer and S. Razzaque, [Acceleration of ultra-high energy cosmic rays in the colliding shells of blazars and GRBs: Constraints from the Fermi Gamma ray Space Telescope](#), *Astrophys. J.* **724**, 1366 (2010) doi:10.1088/0004-637X/724/2/1366 [arXiv:1004.4249 [astro-ph.HE]].
- [258] M. Cannoni, [Lorentz invariant relative velocity and relativistic binary collisions](#), *Int. J. Mod. Phys. A* **32**, no. 02n03, 1730002 (2017) doi:10.1142/S0217751X17300022 [arXiv:1605.00569 [hep-ph]].
- [259] F. W. Stecker, [Effect of photomeson production by the universal radiation field on high-energy cosmic rays](#), *Phys. Rev. Lett.* **21**, 1016 (1968). doi:10.1103/PhysRevLett.21.1016
- [260] V. S. Berezhinsky and S. I. Grigoreva, [The hump in the ultrahigh-energy cosmic ray spectrum](#), *Sov. Phys. JETP* **66**, 457 (1987) [*Zh. Eksp. Teor. Fiz.* **93**, 812 (1987)].
- [261] V. S. Berezhinsky and S. I. Grigor'eva, [A bump In the ultrahigh-energy cosmic ray spectrum](#), *Astron. Astrophys.* **199**, 1 (1988).
- [262] D. J. Fixsen, [The temperature of the cosmic microwave background](#), *Astrophys. J.* **707**, 916 (2009) doi:10.1088/0004-637X/707/2/916 [arXiv:0911.1955 [astro-ph.CO]].

- [263] G. R. Blumenthal, **Energy loss of high-energy cosmic rays in pair-producing collisions with ambient photons**, Phys. Rev. D **1**, 1596 (1970). doi:10.1103/PhysRevD.1.1596
- [264] F. A. Aharonian and J. W. Cronin, **Influence of the universal microwave background radiation on the extragalactic cosmic ray spectrum**, Phys. Rev. D **50**, 1892 (1994). doi:10.1103/PhysRevD.50.1892
- [265] T. A. Armstrong *et al.*, **Total hadronic cross-section of gamma rays in hydrogen in the energy range 0.265 GeV to 4.215 GeV**, Phys. Rev. D **5**, 1640 (1972). doi:10.1103/PhysRevD.5.1640
- [266] L. Montanet *et al.* [Particle Data Group], **Review of particle properties** Phys. Rev. D **50**, 1173 (1994). See p. 1335. doi:10.1103/PhysRevD.50.1173
- [267] I. Golyak, **A connection of inelasticity with multiplicity distribution at high-energies**, Mod. Phys. Lett. A **7**, 2401 (1992). doi:10.1142/S0217732392003839
- [268] L. A. Anchordoqui, M. T. Dova, L. N. Epele and J. D. Swain, **Opacity of the microwave background radiation to ultra-high-energy cosmic rays**, Nucl. Phys. Proc. Suppl. **52B**, 249 (1997). doi:10.1016/S0920-5632(96)00898-5
- [269] L. A. Anchordoqui, M. T. Dova, L. N. Epele and J. D. Swain, **Effect of the 3-K background radiation on ultrahigh-energy cosmic rays**, Phys. Rev. D **55**, 7356 (1997) doi:10.1103/PhysRevD.55.7356 [hep-ph/9704387].
- [270] M. Abramowitz, I. A. Stegun, **Handbook of Mathematical Functions**, (Dover, New York, 1970).
- [271] L. A. Anchordoqui, **From 3K to 10^{20} eV**, PhD Thesis, UNLP 1998 [astro-ph/9812445].
- [272] M. J. Chodorowski, A. A. Zdziarski, and M. Sikora, **Reaction rate and energy-loss rate for photopair production by relativistic nuclei**, Astrophys. J. **400**, 181 (1992) doi:10.1086/171984
- [273] S. Michalowski, D. Andrews, J. Eickmeyer, T. Gentile, N. B. Mistry, R. Talman and K. Ueno, **Experimental study of nuclear shadowing in photoproduction**, Phys. Rev. Lett. **39**, 737 (1977). doi:10.1103/PhysRevLett.39.737
- [274] E. Hayward, **Photodisintegration of light nuclei**, Rev. Mod. Phys. **35**, 324 (1963). doi:10.1103/RevModPhys.35.324
- [275] M. Danos and E. G. Fuller, **Photonuclear reactions**, Ann. Rev. Nucl. Part. Sci. **15**, 29 (1965). doi:10.1146/annurev.ns.15.120165.000333
- [276] F. W. Stecker and M. H. Salamon, **Photodisintegration of ultrahigh-energy cosmic rays: A New determination**, Astrophys. J. **512**, 521 (1999) doi:10.1086/306816 [astro-ph/9808110].
- [277] E. Khan, S. Goriely, D. Allard, E. Parizot, T. Suomijarvi, A. J. Koning, S. Hilaire and M. C. Duijvestijn, **Photodisintegration of ultra-high-energy cosmic rays revisited**, Astropart. Phys. **23**, 191 (2005) doi:10.1016/j.astropartphys.2004.12.007 [astro-ph/0412109].
- [278] D. Boncioli, A. Fedynitch and W. Winter, **Nuclear physics meets the sources of the ultra-high-energy cosmic rays**, Sci. Rep. **7**, no. 1, 4882 (2017) doi:10.1038/s41598-017-05120-7 [arXiv:1607.07989 [astro-ph.HE]].

- [279] S. Karakula and W. Tkaczyk, [The formation of the cosmic ray energy spectrum by a photon field](#), *Astropart. Phys.* **1**, 229 (1993). doi:10.1016/0927-6505(93)90023-7
- [280] L. A. Anchordoqui, J. F. Beacom, H. Goldberg, S. Palomares-Ruiz and T. J. Weiler, [TeV \$\gamma^-\$ rays and neutrinos from photo-disintegration of nuclei in Cygnus OB2](#), *Phys. Rev. D* **75**, 063001 (2007) doi:10.1103/PhysRevD.75.063001 [astro-ph/0611581].
- [281] J. F. Soriano, L. A. Anchordoqui and D. F. Torres, [Photodisintegration of \$^4\text{He}\$ on the cosmic microwave background is less severe than earlier thought](#), *Phys. Rev. D*, in press [arXiv:1805.00409 [astro-ph.HE]].
- [282] L. A. Anchordoqui, J. F. Beacom, H. Goldberg, S. Palomares-Ruiz and T. J. Weiler, [TeV gamma-rays from photo-disintegration/de-excitation of cosmic-ray nuclei](#), *Phys. Rev. Lett.* **98**, 121101 (2007) doi:10.1103/PhysRevLett.98.121101 [astro-ph/0611580].
- [283] R. Alves Batista, D. Boncioli, A. di Matteo, A. van Vliet and D. Walz, [Effects of uncertainties in simulations of extragalactic UHECR propagation, using CRPropa and SimProp](#), *JCAP* **1510**, no. 10, 063 (2015) doi:10.1088/1475-7516/2015/10/063 [arXiv:1508.01824 [astro-ph.HE]].
- [284] R. C. Gilmore, R. S. Somerville, J. R. Primack and A. Dominguez, [Semi-analytic modeling of the EBL and consequences for extragalactic gamma-ray spectra](#), *Mon. Not. Roy. Astron. Soc.* **422**, 3189 (2012) doi:10.1111/j.1365-2966.2012.20841.x [arXiv:1104.0671 [astro-ph.CO]].
- [285] L. N. Epele and E. Roulet, [On the propagation of the highest energy cosmic ray nuclei](#), *JHEP* **9810**, 009 (1998) doi:10.1088/1126-6708/1998/10/009 [astro-ph/9808104].
- [286] C. T. Hill and D. N. Schramm, [The ultrahigh-energy cosmic ray spectrum](#), *Phys. Rev. D* **31**, 564 (1985). doi:10.1103/PhysRevD.31.564
- [287] F. W. Stecker, [Extragalactic radiation and the ultrahigh-energy cosmic ray spectrum](#), *Nature* **342**, 401 (1989). doi:10.1038/342401a0
- [288] L. A. Anchordoqui, M. T. Dova, L. N. Epele and J. D. Swain, [A depression before the bump in the highest energy cosmic ray spectrum](#), *Phys. Rev. D* **57**, 7103 (1998) doi:10.1103/PhysRevD.57.7103 [astro-ph/9708082].
- [289] D. Allard, N. G. Busca, G. Decerprit, A. V. Olinto and E. Parizot, [Implications of the cosmic ray spectrum for the mass composition at the highest energies](#), *JCAP* **0810**, 033 (2008) doi:10.1088/1475-7516/2008/10/033 [arXiv:0805.4779 [astro-ph]].
- [290] D. Allard, [Extragalactic propagation of ultrahigh energy cosmic-rays](#), *Astropart. Phys.* **39-40**, 33 (2012) doi:10.1016/j.astropartphys.2011.10.011 [arXiv:1111.3290 [astro-ph.HE]].
- [291] K. Kotera and A. V. Olinto, [The astrophysics of ultrahigh energy cosmic rays](#), *Ann. Rev. Astron. Astrophys.* **49**, 119 (2011) doi:10.1146/annurev-astro-081710-102620 [arXiv:1101.4256 [astro-ph.HE]].
- [292] E. Waxman and J. Miralda-Escude, [Images of bursting sources of high-energy cosmic rays I: Effects of magnetic fields](#), *Astrophys. J.* **472**, L89 (1996) doi:10.1086/310367 [astro-ph/9607059].

- [293] G. R. Farrar, R. Jansson, I. J. Feain and B. M. Gaensler, [Galactic magnetic deflections and Centaurus A as a UHECR source](#), *JCAP* **1301**, 023 (2013) doi:10.1088/1475-7516/2013/01/023 [arXiv:1211.7086 [astro-ph.HE]].
- [294] G. R. Farrar and M. S. Sutherland, [Deflections of UHECRs in the Galactic magnetic field](#), arXiv:1711.02730 [astro-ph.HE].
- [295] B. L. Fannaroff and J. M. Riley, [The morphology of extragalactic radio sources of high and low luminosity](#), *Mon. Not. Roy. Astron. Soc.* **167**, 31 (1974).
- [296] R. D. Blandford and M. J. Rees, [A 'twin-exhaust' model for double radio sources](#), *Mon. Not. Roy. Astron. Soc.* **169**, 395 (1974).
- [297] A. Rosen, P. A. Hughes, G. C. Duncan and P. E. Hardee, [A comparison of the morphology and stability of relativistic and nonrelativistic jets](#), *Astrophys. J.* **516**, 729 (1999) doi:10.1086/307143 [astro-ph/9901046].
- [298] M. C. Begelman, R. D. Blandford and M. J. Rees, [Theory of extragalactic radio sources](#), *Rev. Mod. Phys.* **56**, 255 (1984). doi:10.1103/RevModPhys.56.255
- [299] A. N. Kolmogorov, [The local structure of turbulence in incompressible viscous fluid for very large Reynolds numbers](#), *Compt. Rend. Acad. Sci. U.R.S.S.* **30**, 201 (1941).
- [300] L. A. Anchordoqui, H. Goldberg and T. J. Weiler, [An Auger test of the Cen A model of highest energy cosmic rays](#), *Phys. Rev. Lett.* **87**, 081101 (2001) doi:10.1103/PhysRevLett.87.081101 [astro-ph/0103043].
- [301] L. A. Anchordoqui, H. Goldberg and T. J. Weiler, [Update on tests of the Cen A neutron-emission model of highest energy cosmic rays](#), *Phys. Rev. D* **84**, 067301 (2011) doi:10.1103/PhysRevD.84.067301 [arXiv:1103.0536 [astro-ph.HE]].
- [302] L. A. Anchordoqui and H. Goldberg, [A lower bound on the local extragalactic magnetic field](#), *Phys. Rev. D* **65**, 021302 (2002) doi:10.1103/PhysRevD.65.021302 [hep-ph/0106217].
- [303] F. P. Israel, [Centaurus A \(NGC 5128\)](#), *Astron. Astrophys. Rev.* **8**, 237 (1998) doi:10.1007/s001590050011 [astro-ph/9811051].
- [304] M. J. Hardcastle, D. M. Worrall, R. P. Kraft, W. R. Forman, C. Jones and S. S. Murray, [Radio and X-ray observations of the jet in Centaurus A](#), *Astrophys. J.* **593**, 169 (2003) doi:10.1086/376519 [astro-ph/0304443].
- [305] J. O. Burns, E. D. Feigelson, and E. J. Schreier, [The inner radio structure of Centaurus A: clues to the origin of the jet X-ray emission](#), *Astrophys. J.* **273**, 128 (1983) doi:10.1086/161353
- [306] P. Sreekumar, D. L. Bertsch, R. C. Hartman, P. L. Nolan and D. J. Thompson, [GeV emission from the nearby radio galaxy Centaurus A](#), *Astropart. Phys.* **11**, 221 (1999) doi:10.1016/S0927-6505(99)00054-7 [astro-ph/9901277].

- [307] J. E. Grindlay, H. F. Helmken, R. H. Brown, J. Davis, and L. R. Allen, **Evidence for the detection of gamma rays from Centaurus A at $E_\gamma \geq 3 \times 10^{11}$ eV**, *Astrophys. J.* **197**, L9 (1975) doi:10.1086/181764
- [308] A. A. Abdo *et al.* [Fermi-LAT Collaboration], **Fermi Large Area Telescope bright gamma-ray source list**, *Astrophys. J. Suppl.* **183**, 46 (2009) doi:10.1088/0067-0049/183/1/46 [arXiv:0902.1340 [astro-ph.HE]].
- [309] A. A. Abdo *et al.* [Fermi-LAT Collaboration], **Bright AGN source list from the first three months of the Fermi Large Area Telescope all-sky survey**, *Astrophys. J.* **700**, 597 (2009) doi:10.1088/0004-637X/700/1/597 [arXiv:0902.1559 [astro-ph.HE]].
- [310] F. Aharonian *et al.* [H.E.S.S. Collaboration], **Discovery of very high energy gamma-ray emission from Centaurus A with H.E.S.S.**, *Astrophys. J.* **695**, L40 (2009) doi:10.1088/0004-637X/695/1/L40 [arXiv:0903.1582 [astro-ph.CO]].
- [311] A. A. Abdo *et al.* [Fermi Collaboration], **Fermi Large Area Telescope view of the core of the radio galaxy Centaurus A**, *Astrophys. J.* **719**, 1433 (2010) doi:10.1088/0004-637X/719/2/1433 [arXiv:1006.5463 [astro-ph.HE]].
- [312] A. A. Abdo *et al.* [Fermi-LAT Collaboration], **Fermi gamma-ray imaging of a radio galaxy**, *Science* **328**, 725 (2010) doi:10.1126/science.1184656 [arXiv:1006.3986 [astro-ph.HE]].
- [313] H. Abdalla *et al.* [H. E. S. S. and Fermi-LAT Collaborations], **The γ -ray spectrum of the core of Centaurus A as observed with H.E.S.S. and Fermi-LAT**, arXiv:1807.07375 [astro-ph.HE].
- [314] M. Honda, **Ultra-high energy cosmic-ray acceleration in the jet of Centaurus A**, *Astrophys. J.* **706**, 1517 (2009) doi:10.1088/0004-637X/706/2/1517 [arXiv:0911.0921 [astro-ph.HE]].
- [315] N. Junkes, R. F. Haynes, J. I. Harnett, and D. L. Jauncey, **Radio polarization surveys of Centaurus A (NGC 5128) I: The complete radio source at 6.3 cm**, *Astron. Astrophys.* **269**, 29 (1993) [Erratum, *ibid* **274**, 1009 (1993)].
- [316] F. M. Rieger and P. Duffy, **Shear acceleration in relativistic astrophysical jets**, *Astrophys. J.* **617**, 155 (2004) doi:10.1086/425167 [astro-ph/0410269].
- [317] F. M. Rieger and F. A. Aharonian, **Cen A as TeV gamma-ray and possible UHE cosmic-ray source**, *Astron. Astrophys.* **506**, L41 (2009) doi:10.1051/0004-6361/200912562 [arXiv:0910.2327 [astro-ph.HE]].
- [318] S. Wykes *et al.*, **Mass entrainment and turbulence-driven acceleration of ultra-high energy cosmic rays in Centaurus A**, *Astron. Astrophys.* **558**, A19 (2013) doi:10.1051/0004-6361/201321622 [arXiv:1305.2761 [astro-ph.HE]].
- [319] J. A. Eilek, **The dynamic age of Centaurus A**, *New J. Phys.* **16**, 045001 (2014) doi:10.1088/1367-2630/16/4/045001 [arXiv:1402.4166 [astro-ph.GA]].
- [320] G. R. Farrar and A. Gruzinov, **Giant AGN flares and cosmic ray bursts**, *Astrophys. J.* **693**, 329 (2009) doi:10.1088/0004-637X/693/1/329 [arXiv:0802.1074 [astro-ph]].

- [321] G. R. Farrar and T. Piran, [Tidal disruption jets as the source of ultra-high energy cosmic rays](#), arXiv:1411.0704 [astro-ph.HE].
- [322] R. Alves Batista and J. Silk, [Ultrahigh-energy cosmic rays from tidally-ignited white dwarfs](#), Phys. Rev. D **96**, no. 10, 103003 (2017) doi:10.1103/PhysRevD.96.103003 [arXiv:1702.06978 [astro-ph.HE]].
- [323] B. T. Zhang, K. Murase, F. Oikonomou and Z. Li, [High-energy cosmic ray nuclei from tidal disruption events: origin, survival, and implications](#), Phys. Rev. D **96**, no. 6, 063007 (2017) Addendum: [Phys. Rev. D **96**, no. 6, 069902 (2017)] doi:10.1103/PhysRevD.96.063007, 10.1103/PhysRevD.96.069902 [arXiv:1706.00391 [astro-ph.HE]].
- [324] D. Biehl, D. Boncioli, C. Lunardini and W. Winter, [Tidally disrupted stars as a possible origin of both cosmic rays and neutrinos at the highest energies](#), Sci. Rep. **8**, no. 1, 10828 (2018) doi:10.1038/s41598-018-29022-4 [arXiv:1711.03555 [astro-ph.HE]].
- [325] T. M. Heckman and T. A. Thompson, [A brief review of galactic winds](#) arXiv:1701.09062.
- [326] S. Veilleux, G. Cecil and J. Bland-Hawthorn, [Galactic winds](#), Ann. Rev. Astron. Astrophys. **43**, 769 (2005) doi:10.1146/annurev.astro.43.072103.150610 [astro-ph/0504435].
- [327] K. S. Long, K. D. Kuntz, W. P. Blair, L. Godfrey, P. P. Plucinsky, R. Soria, C. Stockdale and P. F. Winkler, [A deep Chandra ACIS survey of M83](#), Astrophys. J. Suppl. **212**, 21 (2014) doi:10.1088/0067-0049/212/2/21 [arXiv:1404.3218 [astro-ph.GA]].
- [328] A. MacFadyen and S. E. Woosley, [Collapsars: Gamma-ray bursts and explosions in “failed supernovae”](#), Astrophys. J. **524**, 262 (1999) doi:10.1086/307790 [astro-ph/9810274].
- [329] J. Dreyer, J. K. Becker and W. Rhode, [The starburst-GRB connection](#), arXiv:0909.0158 [astro-ph.HE].
- [330] P. L. Biermann *et al.*, [The nature and origin of ultrahigh-energy cosmic ray particles](#), arXiv:1610.00944 [astro-ph.HE].
- [331] R. Chary, E. E. Becklin and L. Armus, [Are starburst galaxies the hosts of gamma-ray bursts ?](#), Astrophys. J. **566**, 229 (2002) doi:10.1086/337964 [astro-ph/0110010].
- [332] K. Z. Stanek *et al.*, [Protecting life in the milky way: metals keep the GRBs away](#), Acta Astron. **56**, 333 (2006) [astro-ph/0604113].
- [333] M. Modjaz, L. Kewley, R. P. Kirshner, K. Z. Stanek, P. Challis, P. M. Garnavich, J. E. Greene and J. L. Prieto, [Measured metallicities at the sites of nearby broad-lined type Ic supernovae and implications for the SN-GRB connection](#), Astron. J. **135**, 1136 (2008) doi:10.1088/0004-6256/135/4/1136 [astro-ph/0701246].
- [334] R. Jimenez and T. Piran, [Reconciling the gamma-ray burst rate and star formation histories](#), Astrophys. J. **773**, 126 (2013) doi:10.1088/0004-637X/773/2/126 [arXiv:1303.4809 [astro-ph.HE]].

- [335] X. Y. Wang, S. Razzaque, P. Meszaros and Z. G. Dai, **High-energy cosmic rays and neutrinos from semi-relativistic hypernovae**, Phys. Rev. D **76**, 083009 (2007) doi:10.1103/PhysRevD.76.083009 [arXiv:0705.0027 [astro-ph]].
- [336] V. S. Ptuskin, V. N. Zirakashvili and E. S. Seo, **Spectrum of Galactic cosmic rays accelerated in supernova remnants**, Astrophys. J. **718**, 31 (2010) doi:10.1088/0004-637X/718/1/31 [arXiv:1006.0034 [astro-ph.CO]].
- [337] R. A. Chevalier and A. W. Clegg, **Wind from a starburst galaxy nucleus**, Nature **317**, 44 (1985). doi:10.1038/317044a0
- [338] B. C. Lacki, **The Fermi Bubbles as starburst wind termination shocks**, Mon. Not. Roy. Astron. Soc. **444**, L39 (2014) doi:10.1093/mnrasl/slu107 [arXiv:1304.6137 [astro-ph.HE]].
- [339] P. Kroupa, **The Initial mass function of stars: Evidence for uniformity in variable systems**, Science **295**, 82 (2002) doi:10.1126/science.1067524 [astro-ph/0201098].
- [340] D. K. Strickland and T. M. Heckman, **Supernova feedback efficiency and mass loading in the starburst and galactic superwind exemplar M82**, Astrophys. J. **697**, 2030 (2009) doi:10.1088/0004-637X/697/2/2030 [arXiv:0903.4175 [astro-ph.CO]].
- [341] T. M. Heckman, M. D. Lehnert, D. K. Strickland and L. Armus, **Absorption-line probes of gas and dust in galactic superwinds**, Astrophys. J. Suppl. **129**, 493 (2000) doi:10.1086/313421 [astro-ph/0002526].
- [342] C. G. Hoopes *et al.*, **The diverse properties of the most ultraviolet luminous galaxies discovered by the Galaxy Evolution Explorer**, Astrophys. J. Suppl. **173**, 441 (2007) doi:10.1086/516644 [astro-ph/0609415].
- [343] P. Beirão *et al.*, **Spatially resolved Spitzer-IRS spectral maps of the superwind in M82**, Mon. Not. Roy. Astron. Soc. **451**, 2640 (2015). doi:10.1093/mnras/stv1101
- [344] A. Contursi *et al.*, **Spectroscopic FIR mapping of the disk and galactic wind of M82 with Herschel-PACS**, Astron. Astrophys. **549**, A118 (2013) doi:10.1051/0004-6361/201219214 [arXiv:1210.3496 [astro-ph.GA]].
- [345] T. M. Heckman, L. Armus and G. K. Miley, **On the nature and implications of starburst-driven galactic superwinds**, Astrophys. J. Suppl. **74**, 833 (1990). doi:10.1086/191522
- [346] S. Veilleux, D. S. N. Rupke and R. Swaters, **Warm molecular hydrogen in the galactic wind of M82**, Astrophys. J. **700**, L149 (2009) doi:10.1088/0004-637X/700/2/L149 [arXiv:0907.1422 [astro-ph.CO]].
- [347] A. Leroy *et al.*, **The multi-phase cold fountain in M82 revealed by a wide, sensitive map of the molecular interstellar medium**, Astrophys. J. **814**, 83 (2015) doi:10.1088/0004-637X/814/2/83.
- [348] A. D. Bolatto *et al.*, **The starburst-driven molecular wind in NGC 253 and the suppression of star formation**, Nature **499**, 450 (2013) doi:10.1038/nature12351 [arXiv:1307.6259 [astro-ph.CO]].

- [349] B. C. Lacki, *From 10K to 10 TK: Insights on the interaction between cosmic rays and gas in starbursts*, *Astrophys. Space Sci. Proc.* **34**, 411 (2013) doi:10.1007/978-3-642-35410-6_29 [arXiv:1308.5241 [astro-ph.HE]].
- [350] A. Shukurov, G. R. Sarson, A. Nordlund, B. Gudiksen and A. Brandenburg, *The effects of spiral arms on the multi-phase ISM*, *Astrophys. Space Sci.* **289**, 319 (2004) doi:10.1023/B:ASTR.0000014960.35780.2e [astro-ph/0212260].
- [351] B. Adebahr, M. Krause, U. Klein, M. Wezgowiec, D. J. Bomans and R.-J. Dettmar, *M82 - A radio continuum and polarisation study I: Data reduction and cosmic ray propagation*, *Astron. Astrophys.* **555**, A23 (2013) doi:10.1051/0004-6361/201220226 [arXiv:1209.5552 [astro-ph.GA]].
- [352] R. Beck, C. L. Carilli, M. A. Holdaway, and U. Klein, *Multifrequency observations of the radio continuum emission from NGC 253 I: Magnetic fields and rotation measures in the bar and halo*, *Astron. Astrophys.* **292**, 409 (1994).
- [353] V. Heesen, R. Beck, M. Krause and R.-J. Dettmar, *Cosmic rays and the magnetic field in the nearby starburst galaxy NGC 253 I: The distribution and transport of cosmic rays*, *Astron. Astrophys.* **494**, 563 (2009) doi:10.1051/0004-6361:200810543 [arXiv:0812.0346 [astro-ph]].
- [354] V. Heesen, M. Krause, R. Beck and R. J. Dettmar, *Cosmic rays and the magnetic field in the nearby starburst galaxy NGC 253 II: The magnetic field structure*, *Astron. Astrophys.* **506**, 1123 (2009) doi:10.1051/0004-6361/200911698 [arXiv:0908.2985 [astro-ph.CO]].
- [355] V. Heesen, R. Beck, M. Krause and R. J. Dettmar, *Cosmic rays and the magnetic field in the nearby starburst galaxy NGC 253 III: Helical magnetic fields in the nuclear outflow*, *Astron. Astrophys.* **535**, A79 (2011) doi:10.1051/0004-6361/201117618 [arXiv:1109.0255 [astro-ph.CO]].
- [356] M. Krause, *Magnetic fields and halos in spiral galaxies*, arXiv:1401.1317 [astro-ph.GA].
- [357] T. A. Thompson, E. Quataert, E. Waxman, N. Murray and C. L. Martin, *Magnetic fields in starburst galaxies and the origin of the fir-radio correlation*, *Astrophys. J.* **645**, 186 (2006) [astro-ph/0601626].
- [358] T. A. D. Paglione and R. D. Abrahams, *Properties of nearby starburst galaxies based on their diffuse gamma-ray emission*, *Astrophys. J.* **755**, 106 (2012) doi:10.1088/0004-637X/755/2/106 [arXiv:1206.3530 [astro-ph.HE]].
- [359] B. C. Lacki and R. Beck, *The equipartition magnetic field formula in starburst galaxies: Accounting for pionic secondaries and strong energy losses*, *Mon. Not. Roy. Astron. Soc.* **430**, 3171 (2013) doi:10.1093/mnras/stt122 [arXiv:1301.5391 [astro-ph.CO]].
- [360] E. Domingo-Santamaria and D. F. Torres, *High energy gamma-ray emission from the starburst nucleus of NGC 253*, *Astron. Astrophys.* **444**, 403 (2005) doi:10.1051/0004-6361:20053613 [astro-ph/0506240].
- [361] E. de Cea del Pozo, D. F. Torres and A. Y. R. Marrero, *Multi-messenger model for the starburst galaxy M82*, *Astrophys. J.* **698**, 1054 (2009) doi:10.1088/0004-637X/698/2/1054 [arXiv:0901.2688 [astro-ph.GA]].

- [362] B. C. Lacki, *Sturm und drang: Supernova-driven turbulence, magnetic fields, and cosmic rays in the chaotic starburst interstellar medium*, arXiv:1308.5232 [astro-ph.CO].
- [363] M. D. Thornley, N. M. Forster Schreiber, D. Lutz, R. Genzel, H. W. W. Spoon, D. Kunze and A. Sternberg, *Massive star formation and evolution in starburst galaxies: mid-infrared spectroscopy with ISO-SWS*, *Astrophys. J.* **539**, 641 (2000) doi:10.1086/309261 [astro-ph/0003334].
- [364] D. F. Torres, *Theoretical modelling of the diffuse emission of gamma-rays from extreme regions of star formation: The Case of Arp 220*, *Astrophys. J.* **617**, 966 (2004) doi:10.1086/425415 [astro-ph/0407240].
- [365] D. F. Torres, A. Cillis, B. Lacki and Y. Rephaeli, *Building up the spectrum of cosmic-rays in star-forming regions*, *Mon. Not. Roy. Astron. Soc.* **423**, 822 (2012) doi:10.1111/j.1365-2966.2012.20920.x [arXiv:1203.2798 [astro-ph.HE]].
- [366] G. R. Meurer, *Star clusters and the duration of starbursts*, *ASP Conf. Ser.* **211**, 81 (2000) [astro-ph/0003161].
- [367] K. B. W. McQuinn, E. D. Skillman, J. M. Cannon, J. J. Dalcanton, A. Dolphin, D. Stark and D. Weisz, *The true durations of starbursts: HST observations of three nearby dwarf starburst galaxies*, *Astrophys. J.* **695**, 561 (2009) doi:10.1088/0004-637X/695/1/561 [arXiv:0901.2361 [astro-ph.GA]].
- [368] K. B. W. McQuinn *et al.*, *The nature of starbursts II: The duration of starbursts in dwarf galaxies*, *Astrophys. J.* **724**, 49 (2010) doi:10.1088/0004-637X/724/1/49 [arXiv:1009.2940 [astro-ph.CO]].
- [369] R. de Grijs, *Star formation time-scales in the nearby, prototype starburst galaxy M82*, *Astron. Geophys.* **42**, 14 (2001) [astro-ph/0106564].
- [370] R. de Grijs, N. Bastian and H. J. G. L. M. Lamers, *Star cluster formation and disruption time-scales II: Evolution of the star cluster system in M82's fossil starburst*, *Mon. Not. Roy. Astron. Soc.* **340**, 197 (2003) doi:10.1046/j.1365-8711.2003.06283.x [astro-ph/0211420].
- [371] T. J. Davidge, *Shaken, not stirred: The disrupted disk of the starburst galaxy NGC 253*, *Astrophys. J.* **725**, 1342 (2010) doi:10.1088/0004-637X/725/1/1342 [arXiv:1011.3006 [astro-ph.CO]].
- [372] T. J. Davidge *The compact star-forming complex at the heart of NGC 253*, *Astrophys. J.* **818**, 142 (2016) doi:10.3847/0004-637X/818/2/142 [arXiv:1602.01400 [astro-ph.GA]].
- [373] G. H. Rieke, M. J. Lebofsky, R. I. Thompson, F. J. Low and A. T. Tokunaga, *The nature of the nuclear sources in M82 and NGC 253*, *Astrophys. J.* **238**, 24 (1980). doi:10.1086/157954
- [374] J. Vink and J. M. Laming, *On the magnetic fields and particle acceleration in Cas A*, *Astrophys. J.* **584**, 758 (2003) doi:10.1086/345832 [astro-ph/0210669].
- [375] R. Yamazaki, T. Yoshida, T. Terasawa, A. Bamba and K. Koyama, *Constraints on the diffusive shock acceleration from the nonthermal X-ray thin shells in SN1006 NE rim*, *Astron. Astrophys.* **416**, 595 (2004) doi:10.1051/0004-6361:20034212 [astro-ph/0311345].

- [376] H. J. Volk, E. G. Berezhko and L. T. Ksenofontov, **Magnetic field amplification in Tycho and other shell-type supernova remnants**, *Astron. Astrophys.* **433**, 229 (2005) doi:10.1051/0004-6361:20042015 [astro-ph/0409453].
- [377] S. G. Lucek and A. R. Bell, **Non-linear amplification of a magnetic field driven by cosmic ray streaming**, *Mon. Not. Roy. Astron. Soc.* **314**, 65 (2000). doi:10.1046/j.1365-8711.2000.03363.x
- [378] A. R. Bell, **Turbulent amplification of magnetic field and diffusive shock acceleration of cosmic rays**, *Mon. Not. Roy. Astron. Soc.* **353**, 550 (2004) doi:10.1111/j.1365-2966.2004.08097.x
- [379] A. R. Bell, **The interaction of cosmic rays and magnetized plasma**, *Mon. Not. Roy. Astron. Soc.* **358**, 181 (2005) doi:10.1111/j.1365-2966.2005.08774.x
- [380] J. H. Matthews, A. R. Bell, K. M. Blundell and A. T. Araudo, **Amplification of perpendicular and parallel magnetic fields by cosmic ray currents**, *Mon. Not. Roy. Astron. Soc.* **469**, no. 2, 1849 (2017) doi:10.1093/mnras/stx905 [arXiv:1704.02985 [astro-ph.HE]].
- [381] S. Lípari, Z. Tsvetanov, and F. Macchetto **Luminous infrared galaxies II – NGC 4945: A nearby obscured starburst/sefvert nucleus**, *Astrophys. J. Suppl.* **111**, 369 (1997).
- [382] A. Marconi, E. Oliva, P. P. van der Werf, R. Maiolino, E. J. Schreier, F. Macchetto and A. F. M. Moorwood, **The elusive active nucleus of NGC 4945**, *Astron. Astrophys.* **357**, 24 (2000) [astro-ph/0002244].
- [383] N. A. Levenson, J. H. Krolik, P. T. Zycki, T. M. Heckman, K. A. Weaver, H. Awaki and Y. Terashima, **Extreme X-ray iron lines in active galactic nuclei**, *Astrophys. J.* **573**, L81 (2002) doi:10.1086/342092 [astro-ph/0206071].
- [384] D. K. Strickland, T. M. Heckman, E. J. M. Colbert, C. G. Hoopes and K. A. Weaver, **A high spatial resolution X-ray and H-alpha study of hot gas in the halos of star-forming disk galaxies I: Spatial and spectral properties of the diffuse X-ray emission**, *Astrophys. J. Suppl.* **151**, 193 (2004) doi:10.1086/382214 [astro-ph/0306592].
- [385] N. A. Levenson, K. A. Weaver and T. M. Heckman, **The sefvert-starburst connection in X-rays I: the data**, *Astrophys. J. Suppl.* **133**, 269 (2001) doi:10.1086/320355 [astro-ph/0012035].
- [386] N. A. Levenson, K. A. Weaver and T. M. Heckman, **The sefvert-starburst connection in X-rays 2: Results and implications**, *Astrophys. J.* **550**, 230 (2001) doi:10.1086/319726 [astro-ph/0012036].
- [387] N. A. Levenson, K. A. Weaver, T. M. Heckman, H. Awaki and Y. Terashima, **Accretion and outflow in the AGN and starburst of NGC 5135**, *Astrophys. J.* **602**, 135 (2004) doi:10.1086/380836 [astro-ph/0310669].
- [388] D. K. Strickland, **Winds from nuclear starbursts: Old truths and recent progress on superwinds**, *IAU Symp.* **222**, 249 (2004) doi:10.1017/S1743921304002194 [astro-ph/0404316].
- [389] E. J. M. Colbert, S. A. Baum, J. F. Gallimore, C. P. O’Dea, M. D. Lehnert, Z. I. Tsvetanov, J. S. Mulchaey and S. Caganoff, **Large scale outflows in edge-on sefvert galaxies I: optical emission-line imaging and optical spectroscopy**, *Astrophys. J. Suppl.* **105**, 75 (1996) doi:10.1086/192307 [astro-ph/9512169].

- [390] E. J. M. Colbert, S. A. Baum, C. P. O’Dea and S. Veilleux, [Large scale outflows in edge-on seyfert galaxies III: Kiloparsec-scale soft X-ray emission](#), *Astrophys. J.* **496**, 786 (1998) doi:10.1086/305417 [astro-ph/9711137].
- [391] J. H. Krolik and M. C. Begelman, [An X-ray heated wind in NGC 1068](#), *Astrophys. J.* **308**, L55 (1986).
- [392] R. Soria and K. Wu, [X-ray sources in the starburst spiral galaxy M83: nuclear region and discrete source population](#), *Astron. Astrophys.* **384**, no. 1, 99 (2002) doi:10.1051/0004-6361:20020026 [astro-ph/0201059].
- [393] A. Vogler, S. C. Madden, R. Beck, A. A. Lundgren, M. Sauvage, L. Vigroux and M. Ehle, [Dissecting the spiral galaxy M83: Mid-infrared emission and comparison with other tracers of star formation](#), *Astron. Astrophys.* **441**, 491 (2005) doi:10.1051/0004-6361:20042342 [astro-ph/0508027].
- [394] S. Veilleux and J. Bland-Hawthorn, [Artillery shells over Circinus](#), *Astrophys. J.* **479**, L105 (1997) doi:10.1086/310588 [astro-ph/9703040].
- [395] M. Elmouttie, B. Koribalski, S. Gordon, K. Taylor, S. Houghton, T. Lavezzi, R. Haynes, and K. Jones, [The kinematics of the ionized gas in the Circinus galaxy](#), *Mon. Not. Roy. Astron. Soc.* **297**, 49 (1998).
- [396] G. A. Luppino and J. L. Tonry [Infrared surface brightness fluctuations: \$K'\$ -band observations of M32, M32, and Maffei 1](#), *Astrophys. J.* **410**, 81 (1993).
- [397] M. Krismer, R. B. Tully, and I. Gioia, [IC 342/Maffei group of galaxies and distances for two of its members](#), *Astron. J.* **110**, 1584 (1995).
- [398] R. J. Buta and M. L. McCall, [The IC 342/Maffei group revealed](#) *Astrophys. J. Suppl.* **124**, 33 (1999).
- [399] N. A. Tikhonov and O. A. Galazutdinova, [Distance to the galaxy IC 342](#), *Astron. Lett.* **36**, 167 (2010) doi:10.1134/S1063773710030023 [arXiv:1003.0321 [astro-ph.CO]].
- [400] E. Schinnerer, T. Boeker, D. S. Meier and D. Calzetti, [Self-regulated fueling of galaxy centers: Evidence for star-formation feedback in IC342’s nucleus](#), *Astrophys. J.* **684**, L21 (2008) doi:10.1086/592109 [arXiv:0808.0793 [astro-ph]].
- [401] J. N. Bregman, C. V. Cox, and K. Tomisaka, [X-ray emission from the starburst galaxy IC 342](#), *Astrophys. J.* **415**, L79 (1993).
- [402] A. M. Taylor, M. Ahlers and F. A. Aharonian, [The need for a local source of UHE CR nuclei](#), *Phys. Rev. D* **84**, 105007 (2011) doi:10.1103/PhysRevD.84.105007 [arXiv:1107.2055 [astro-ph.HE]].
- [403] M. Ahlers, L. A. Anchordoqui and A. M. Taylor, [Ensemble fluctuations of the flux and nuclear composition of ultrahigh energy cosmic ray nuclei](#), *Phys. Rev. D* **87**, no. 2, 023004 (2013) doi:10.1103/PhysRevD.87.023004 [arXiv:1209.5427 [astro-ph.HE]].
- [404] L. A. Anchordoqui, M. Ahlers, A. V. Olinto, T. C. Paul and A. M. Taylor, [Sensitivity of JEM-EUSO to ensemble fluctuations in the ultra-high energy cosmic ray flux](#), arXiv:1306.0910 [astro-ph.CO].

- [405] B. E. Robertson, R. S. Ellis, S. R. Furlanetto and J. S. Dunlop, [Cosmic reionization and early star-forming galaxies: a joint analysis of new constraints from Planck and the Hubble Space Telescope](#), *Astrophys. J.* **802**, no. 2, L19 (2015) doi:10.1088/2041-8205/802/2/L19 [arXiv:1502.02024 [astro-ph.CO]].
- [406] K. H. Kampert, J. Kulbartz, L. Maccione, N. Nierstenhoefer, P. Schiffer, G. Sigl and A. R. van Vliet, [CRPropa 2.0: a public framework for propagating high energy nuclei, secondary gamma rays and neutrinos](#), *Astropart. Phys.* **42**, 41 (2013) doi:10.1016/j.astropartphys.2012.12.001 [arXiv:1206.3132 [astro-ph.IM]].
- [407] R. Alves Batista *et al.*, [CRPropa 3.0: a public framework for propagating UHE cosmic rays through Galactic and extragalactic space](#), arXiv:1307.2643 [astro-ph.IM].
- [408] D. Hooper, S. Sarkar and A. M. Taylor, [The intergalactic propagation of ultra-high energy cosmic ray nuclei: an analytic approach](#), *Phys. Rev. D* **77**, 103007 (2008) doi:10.1103/PhysRevD.77.103007 [arXiv:0802.1538 [astro-ph]].
- [409] M. Ahlers and A. M. Taylor, [Analytic solutions of ultra-high energy cosmic ray nuclei revisited](#), *Phys. Rev. D* **82**, 123005 (2010) doi:10.1103/PhysRevD.82.123005 [arXiv:1010.3019 [astro-ph.HE]].
- [410] A. P. Szabo and R. J. Protheroe, [Implications of particle acceleration in active galactic nuclei for cosmic rays and high-energy neutrino astronomy](#), *Astropart. Phys.* **2**, 375 (1994) doi:10.1016/0927-6505(94)90027-2 [astro-ph/9405020].
- [411] R. J. Protheroe and T. Stanev, [Cut-offs and pile-ups in shock acceleration spectra](#), *Astropart. Phys.* **10**, 185 (1999) doi:10.1016/S0927-6505(98)00055-3 [astro-ph/9808129].
- [412] A. Aab *et al.* [Pierre Auger Collaboration], [The Pierre Auger Observatory: Contributions to the 33rd International Cosmic Ray Conference \(ICRC 2013\)](#), arXiv:1307.5059 [astro-ph.HE].
- [413] P. Abreu *et al.* [Pierre Auger Collaboration], [Interpretation of the Depths of Maximum of Extensive Air Showers Measured by the Pierre Auger Observatory](#), *JCAP* **1302**, 026 (2013) doi:10.1088/1475-7516/2013/02/026 [arXiv:1301.6637 [astro-ph.HE]].
- [414] T. Pierog, I. Karpenko, J. M. Katzy, E. Yatsenko and K. Werner, [EPOS LHC: Test of collective hadronization with data measured at the CERN Large Hadron Collider](#), *Phys. Rev. C* **92**, no. 3, 034906 (2015) doi:10.1103/PhysRevC.92.034906 [arXiv:1306.0121 [hep-ph]].
- [415] N. Globus, D. Allard and E. Parizot, [A complete model of the cosmic ray spectrum and composition across the Galactic to extragalactic transition](#), *Phys. Rev. D* **92**, no. 2, 021302 (2015) doi:10.1103/PhysRevD.92.021302 [arXiv:1505.01377 [astro-ph.HE]].
- [416] L. A. Anchordoqui, [Unmasking the ultra-high-energy cosmic ray origin](#), *PoS EPS -HEP2017*, 001 (2017) doi:10.22323/1.314.0001 [arXiv:1707.09338 [astro-ph.HE]].
- [417] A. D. Supanitsky, A. Cobos and A. Etchegoyen, [Origin of the light cosmic ray component below the ankle](#), *Phys. Rev. D* **98**, no. 10, 103016 (2018) doi:10.1103/PhysRevD.98.103016 [arXiv:1810.12367 [astro-ph.HE]].

- [418] G. Hasinger, T. Miyaji and M. Schmidt, **Luminosity-dependent evolution of soft X-ray selected AGN: New Chandra and XMM-Newton surveys**, *Astron. Astrophys.* **441**, 417 (2005) doi:10.1051/0004-6361:20042134 [astro-ph/0506118].
- [419] T. Stanev, **Ultra high energy cosmic rays and neutrinos after Auger**, arXiv:0808.1045 [astro-ph].
- [420] A. M. Taylor, M. Ahlers and D. Hooper, **Indications of negative evolution for the sources of the highest energy cosmic rays**, *Phys. Rev. D* **92**, no. 6, 063011 (2015) doi:10.1103/PhysRevD.92.063011 [arXiv:1505.06090 [astro-ph.HE]].
- [421] M. Ajello *et al.*, **The cosmic evolution of Fermi BL Lacertae objects**, *Astrophys. J.* **780**, 73 (2014) doi:10.1088/0004-637X/780/1/73 [arXiv:1310.0006 [astro-ph.CO]].
- [422] E. Waxman and J. N. Bahcall, **High-energy neutrinos from astrophysical sources: an upper bound**, *Phys. Rev. D* **59**, 023002 (1999) doi:10.1103/PhysRevD.59.023002 [hep-ph/9807282].
- [423] M. Ahlers, L. A. Anchordoqui, H. Goldberg, F. Halzen, A. Ringwald and T. J. Weiler, **Neutrinos as a diagnostic of cosmic ray galactic/extra-galactic transition**, *Phys. Rev. D* **72**, 023001 (2005) doi:10.1103/PhysRevD.72.023001 [astro-ph/0503229].
- [424] T. K. Gaisser, **Neutrino astronomy: Physics goals, detector parameters**, astro-ph/9707283.
- [425] E. Waxman, **Cosmological origin for cosmic rays above 10^{19} eV**, *Astrophys. J.* **452**, L1 (1995) doi:10.1086/309715 [astro-ph/9508037].
- [426] M. Ahlers and F. Halzen, **Opening a new window onto the universe with IceCube**, *Prog. Part. Nucl. Phys.* **102**, 73 (2018) doi:10.1016/j.pnpnp.2018.05.001 [arXiv:1805.11112 [astro-ph.HE]].
- [427] L. A. Anchordoqui, H. Goldberg, F. Halzen and T. J. Weiler, **Galactic point sources of TeV antineutrinos**, *Phys. Lett. B* **593**, 42 (2004) doi:10.1016/j.physletb.2004.04.054 [astro-ph/0311002].
- [428] G. M. Frichter, T. K. Gaisser and T. Stanev, **Inelasticity in p -nucleus collisions and its application to high-energy cosmic ray cascades**, *Phys. Rev. D* **56**, 3135 (1997) doi:10.1103/PhysRevD.56.3135 [astro-ph/9704061].
- [429] J. G. Learned and S. Pakvasa, **Detecting tau-neutrino oscillations at PeV energies**, *Astropart. Phys.* **3**, 267 (1995) doi:10.1016/0927-6505(94)00043-3 [hep-ph/9405296, hep-ph/9408296].
- [430] V. S. Berezinsky and G. T. Zatsepin, **Cosmic rays at ultrahigh-energies (neutrino?)**, *Phys. Lett.* **28B**, 423 (1969). doi:10.1016/0370-2693(69)90341-4
- [431] F. W. Stecker, **Diffuse fluxes of cosmic high-energy neutrinos**, *Astrophys. J.* **228**, 919 (1979). doi:10.1086/156919
- [432] C. T. Hill and D. N. Schramm, **Ultra-high-energy cosmic ray neutrinos**, *Phys. Lett. B* **131**, 247 (1983) [*Phys. Lett.* **131B**, 247 (1983)]. doi:10.1016/0370-2693(83)91130-9
- [433] R. Engel, D. Seckel and T. Stanev, **Neutrinos from propagation of ultrahigh-energy protons**, *Phys. Rev. D* **64**, 093010 (2001) doi:10.1103/PhysRevD.64.093010 [astro-ph/0101216].

- [434] Z. Fodor, S. D. Katz, A. Ringwald and H. Tu, **Bounds on the cosmogenic neutrino flux**, JCAP **0311**, 015 (2003) doi:10.1088/1475-7516/2003/11/015 [hep-ph/0309171].
- [435] D. Hooper, A. Taylor and S. Sarkar, **The Impact of heavy nuclei on the cosmogenic neutrino flux**, Astropart. Phys. **23**, 11 (2005) doi:10.1016/j.astropartphys.2004.11.002 [astro-ph/0407618].
- [436] M. Ave, N. Busca, A. V. Olinto, A. A. Watson and T. Yamamoto, **Cosmogenic neutrinos from ultra-high energy nuclei**, Astropart. Phys. **23**, 19 (2005) doi:10.1016/j.astropartphys.2004.11.001 [astro-ph/0409316].
- [437] L. A. Anchordoqui, H. Goldberg, D. Hooper, S. Sarkar and A. M. Taylor, **Predictions for the cosmogenic neutrino flux in light of new data from the Pierre Auger Observatory**, Phys. Rev. D **76**, 123008 (2007) doi:10.1103/PhysRevD.76.123008 [arXiv:0709.0734 [astro-ph]].
- [438] K. Kotera, D. Allard and A. V. Olinto, **Cosmogenic neutrinos: parameter space and detectability from PeV to ZeV**, JCAP **1010**, 013 (2010) doi:10.1088/1475-7516/2010/10/013 [arXiv:1009.1382 [astro-ph.HE]].
- [439] M. Ahlers and F. Halzen, **Minimal cosmogenic neutrinos**, Phys. Rev. D **86**, 083010 (2012) doi:10.1103/PhysRevD.86.083010 [arXiv:1208.4181 [astro-ph.HE]].
- [440] R. Alves Batista, R. M. de Almeida, B. Lago and K. Kotera, **Cosmogenic photon and neutrino fluxes in the Auger era**, arXiv:1806.10879 [astro-ph.HE].
- [441] M. Ahlers, L. A. Anchordoqui, M. C. Gonzalez-Garcia, F. Halzen and S. Sarkar, **GZK neutrinos after the Fermi-LAT diffuse photon flux measurement**, Astropart. Phys. **34**, 106 (2010) doi:10.1016/j.astropartphys.2010.06.003 [arXiv:1005.2620 [astro-ph.HE]].
- [442] T. K. Gaisser, F. Halzen and T. Stanev, **Particle astrophysics with high-energy neutrinos**, Phys. Rept. **258**, 173 (1995) Erratum: [Phys. Rept. **271**, 355 (1996)] doi:10.1016/0370-1573(95)00003-Y [hep-ph/9410384].
- [443] J. G. Learned and K. Mannheim, **High-energy neutrino astrophysics**, Ann. Rev. Nucl. Part. Sci. **50**, 679 (2000). doi:10.1146/annurev.nucl.50.1.679
- [444] F. Halzen and D. Hooper, **High-energy neutrino astronomy: The Cosmic ray connection**, Rept. Prog. Phys. **65**, 1025 (2002) doi:10.1088/0034-4885/65/7/201 [astro-ph/0204527].
- [445] L. A. Anchordoqui and T. Montaruli, **In search for extraterrestrial high energy neutrinos**, Ann. Rev. Nucl. Part. Sci. **60**, 129 (2010) doi:10.1146/annurev.nucl.012809.104551 [arXiv:0912.1035 [astro-ph.HE]].
- [446] F. Halzen, **Neutrino astrophysics experiments beneath the sea and ice**, Science **315**, 66 (2007). doi:10.1126/science.1136504
- [447] K. S. Capelle, J. W. Cronin, G. Parente and E. Zas, **On the detection of ultrahigh-energy neutrinos with the Auger Observatory**, Astropart. Phys. **8**, 321 (1998) doi:10.1016/S0927-6505(97)00059-5 [astro-ph/9801313].

- [448] G. Domokos and S. Kovesi-Domokos, **Observation of UHE interactions neutrinos from outer space**, AIP Conf. Proc. **433**, no. 1, 390 (1998) doi:10.1063/1.56127 [hep-ph/9801362].
- [449] G. Domokos and S. Kovesi-Domokos, **Observation of ultrahigh-energy neutrino interactions by orbiting detectors**, hep-ph/9805221.
- [450] X. Bertou, P. Billoir, O. Deligny, C. Lachaud and A. Letessier-Selvon, **Tau neutrinos in the Auger Observatory: a new window to UHECR sources**, Astropart. Phys. **17**, 183 (2002) doi:10.1016/S0927-6505(01)00147-5 [astro-ph/0104452].
- [451] J. L. Feng, P. Fisher, F. Wilczek and T. M. Yu, **Observability of earth skimming ultrahigh-energy neutrinos**, Phys. Rev. Lett. **88**, 161102 (2002) doi:10.1103/PhysRevLett.88.161102 [hep-ph/0105067].
- [452] D. Fargion, **Discovering ultra high energy neutrinos by horizontal and upward tau air-showers: evidences in terrestrial gamma flashes?**, Astrophys. J. **570**, 909 (2002) doi:10.1086/339772 [astro-ph/0002453].
- [453] J. Abraham *et al.* [Pierre Auger Collaboration], **Upper limit on the diffuse flux of UHE tau neutrinos from the Pierre Auger Observatory**, Phys. Rev. Lett. **100**, 211101 (2008) doi:10.1103/PhysRevLett.100.211101 [arXiv:0712.1909 [astro-ph]].
- [454] J. Abraham *et al.* [Pierre Auger Collaboration], **Limit on the diffuse flux of ultra-high energy tau neutrinos with the surface detector of the Pierre Auger Observatory**, Phys. Rev. D **79**, 102001 (2009) doi:10.1103/PhysRevD.79.102001 [arXiv:0903.3385 [astro-ph.HE]].
- [455] P. Abreu *et al.* [Pierre Auger Collaboration], **A search for ultra-high-energy neutrinos in highly inclined events at the Pierre Auger Observatory**, Phys. Rev. D **84**, 122005 (2011) Erratum: [Phys. Rev. D **84**, 029902 (2011)] doi:10.1103/PhysRevD.85.029902, 10.1103/PhysRevD.84.122005 [arXiv:1202.1493 [astro-ph.HE]].
- [456] P. Abreu *et al.* [Pierre Auger Collaboration], **Search for point-like sources of ultra-high energy neutrinos at the Pierre Auger Observatory and improved limit on the diffuse flux of tau neutrinos**, Astrophys. J. **755**, L4 (2012) doi:10.1088/2041-8205/755/1/L4 [arXiv:1210.3143 [astro-ph.HE]].
- [457] P. Abreu *et al.* [Pierre Auger Collaboration], **Ultra-high-energy neutrinos at the Pierre Auger Observatory**, Adv. High Energy Phys. **2013**, 708680 (2013) doi:10.1155/2013/708680 [arXiv:1304.1630 [astro-ph.HE]].
- [458] A. Aab *et al.* [Pierre Auger Collaboration], **Improved limit to the diffuse flux of ultra-high-energy neutrinos from the Pierre Auger Observatory**, Phys. Rev. D **91**, no. 9, 092008 (2015) doi:10.1103/PhysRevD.91.092008 [arXiv:1504.05397 [astro-ph.HE]].
- [459] L. A. Anchordoqui, J. L. Feng, H. Goldberg and A. D. Shapere, **Neutrino bounds on astrophysical sources and new physics**, Phys. Rev. D **66**, 103002 (2002) doi:10.1103/PhysRevD.66.103002 [hep-ph/0207139].
- [460] G. J. Feldman and R. D. Cousins, **A unified approach to the classical statistical analysis of small signals**, Phys. Rev. D **57**, 3873 (1998) doi:10.1103/PhysRevD.57.3873 [physics/9711021 [physics.data-an]].

- [461] R. Gandhi, C. Quigg, M. H. Reno and I. Sarcevic, **Neutrino interactions at ultrahigh-energies**, Phys. Rev. D **58**, 093009 (1998) doi:10.1103/PhysRevD.58.093009 [hep-ph/9807264].
- [462] M. G. Aartsen *et al.* [IceCube Collaboration], **Differential limit on the extremely-high-energy cosmic neutrino flux in the presence of astrophysical background from nine years of IceCube data**, arXiv:1807.01820 [astro-ph.HE].
- [463] M. Ahlers, L. A. Anchordoqui and S. Sarkar, **Neutrino diagnostics of ultra-high energy cosmic ray protons**, Phys. Rev. D **79**, 083009 (2009) doi:10.1103/PhysRevD.79.083009 [arXiv:0902.3993 [astro-ph.HE]].
- [464] R. Aloisio, D. Boncioli, A. di Matteo, A. F. Grillo, S. Petrera and F. Salamida, **Cosmogenic neutrinos and ultra-high energy cosmic ray models**, JCAP **1510**, no. 10, 006 (2015) doi:10.1088/1475-7516/2015/10/006 [arXiv:1505.04020 [astro-ph.HE]].
- [465] J. Heinze, D. Boncioli, M. Bustamante and W. Winter, **Cosmogenic neutrinos challenge the cosmic ray proton dip model**, Astrophys. J. **825**, no. 2, 122 (2016) doi:10.3847/0004-637X/825/2/122 [arXiv:1512.05988 [astro-ph.HE]].
- [466] A. D. Supanitsky, **Implications of gamma-ray observations on proton models of ultra-high-energy cosmic rays**, Phys. Rev. D **94**, no. 6, 063002 (2016) doi:10.1103/PhysRevD.94.063002 [arXiv:1607.00290 [astro-ph.HE]].
- [467] M. G. Aartsen *et al.* [IceCube Collaboration], **Constraints on ultra-high-energy cosmic-ray sources from a search for neutrinos above 10 PeV with IceCube**, Phys. Rev. Lett. **117**, no. 24, 241101 (2016) Erratum: [Phys. Rev. Lett. **119**, no. 25, 259902 (2017)] doi:10.1103/PhysRevLett.117.241101, 10.1103/PhysRevLett.119.259902, 10.1103/PhysRevLett.117.241101, 10.1103/PhysRevLett.119.259902 [arXiv:1607.05886 [astro-ph.HE]].
- [468] K. Fang, K. Kotera, K. Murase and A. V. Olinto, **Testing the newborn pulsar origin of ultrahigh-energy cosmic rays with EeV neutrinos**, Phys. Rev. D **90**, no. 10, 103005 (2014) [Phys. Rev. D **90**, 103005 (2014)] Erratum: [Phys. Rev. D **92**, no. 12, 129901 (2015)] doi:10.1103/PhysRevD.90.103005, 10.1103/PhysRevD.92.129901 [arXiv:1311.2044 [astro-ph.HE]].
- [469] K. Fang, K. Kotera, K. Murase and A. V. Olinto, **IceCube constraints on fast-spinning pulsars as high-energy neutrino sources**, JCAP **1604**, no. 04, 010 (2016) doi:10.1088/1475-7516/2016/04/010 [arXiv:1511.08518 [astro-ph.HE]].
- [470] A. Loeb and E. Waxman, **The cumulative background of high energy neutrinos from starburst galaxies**, JCAP **0605**, 003 (2006) doi:10.1088/1475-7516/2006/05/003 [astro-ph/0601695].
- [471] M. G. Aartsen *et al.* [IceCube Collaboration], **IceCube-Gen2: A vision for the future of neutrino astronomy in Antarctica**, arXiv:1412.5106 [astro-ph.HE].
- [472] M. T. Ressell and M. S. Turner, **The grand unified photon spectrum: a coherent view of the diffuse extragalactic background radiation**, Comments Astrophys. **14**, 323 (1990) [Bull. Am. Astron. Soc. **22**, 753 (1990)].

- [473] A. De Angelis and M. Mallamaci, [Gamma-ray astrophysics](#), arXiv:1805.05642 [astro-ph.HE].
- [474] A. I. Nikishov, [Absorption of high-energy photons in the Universe](#) Sov. Phys. JETP **14**, 393 (1962) [ZhETF **41** 549 (1962)].
- [475] R. Gould and G. Schreder, [Opacity of the Universe to high-energy photons](#), Phys. Rev. Lett. **16**, no. 6, 252 (1966). doi:10.1103/PhysRevLett.16.252
- [476] R. J. Gould and G. P. Schreder, [Opacity of the Universe to high-energy photons](#), Phys. Rev. **155**, 1408 (1967). doi:10.1103/PhysRev.155.1408
- [477] F. W. Stecker, [The cosmic gamma-ray spectrum from secondary-particle production in the meta-galaxy](#), Astrophys. J. **157**, 507 (1969). doi:10.1086/150091
- [478] G. G. Fazio and F. W. Stecker, [Predicted high energy break in the isotropic gamma-ray spectrum: A test of cosmological origin](#), Nature **226**, 135 (1970). doi:10.1038/226135a0
- [479] M. G. Aartsen *et al.* [IceCube Collaboration], [First observation of PeV-energy neutrinos with IceCube](#), Phys. Rev. Lett. **111**, 021103 (2013) doi:10.1103/PhysRevLett.111.021103 [arXiv:1304.5356 [astro-ph.HE]].
- [480] S. Schonert, T. K. Gaisser, E. Resconi and O. Schulz, [Vetoing atmospheric neutrinos in a high energy neutrino telescope](#), Phys. Rev. D **79**, 043009 (2009) doi:10.1103/PhysRevD.79.043009 [arXiv:0812.4308 [astro-ph]];
- [481] T. K. Gaisser, K. Jero, A. Karle and J. van Santen, [Generalized self-veto probability for atmospheric neutrinos](#), Phys. Rev. D **90**, no. 2, 023009 (2014) doi:10.1103/PhysRevD.90.023009 [arXiv:1405.0525 [astro-ph.HE]].
- [482] M. G. Aartsen *et al.* [IceCube Collaboration], [Evidence for high-energy extraterrestrial neutrinos at the IceCube detector](#), Science **342**, 1242856 (2013) doi:10.1126/science.1242856 [arXiv:1311.5238 [astro-ph.HE]].
- [483] M. G. Aartsen *et al.* [IceCube Collaboration], [Observation of high-energy astrophysical neutrinos in three years of IceCube data](#), Phys. Rev. Lett. **113**, 101101 (2014) doi:10.1103/PhysRevLett.113.101101 [arXiv:1405.5303 [astro-ph.HE]].
- [484] M. G. Aartsen *et al.* [IceCube Collaboration], [Atmospheric and astrophysical neutrinos above 1 TeV interacting in IceCube](#), Phys. Rev. D **91**, no. 2, 022001 (2015) doi:10.1103/PhysRevD.91.022001 [arXiv:1410.1749 [astro-ph.HE]].
- [485] M. G. Aartsen *et al.* [IceCube Collaboration], [The IceCube neutrino observatory contributions to ICRC 2017 Part II: Properties of the atmospheric and astrophysical neutrino flux](#), arXiv:1710.01191 [astro-ph.HE].
- [486] M. G. Aartsen *et al.* [IceCube Collaboration], [A combined maximum-likelihood analysis of the high-energy astrophysical neutrino flux measured with IceCube](#), Astrophys. J. **809**, no. 1, 98 (2015) doi:10.1088/0004-637X/809/1/98 [arXiv:1507.03991 [astro-ph.HE]].

- [487] M. G. Aartsen *et al.* [IceCube Collaboration], **Evidence for astrophysical muon neutrinos from the Northern sky with IceCube**, Phys. Rev. Lett. **115**, no. 8, 081102 (2015) doi:10.1103/PhysRevLett.115.081102 [arXiv:1507.04005 [astro-ph.HE]].
- [488] M. G. Aartsen *et al.* [IceCube Collaboration], **Observation and characterization of a cosmic muon neutrino flux from the Northern hemisphere using six years of IceCube data**, Astrophys. J. **833**, no. 1, 3 (2016) doi:10.3847/0004-637X/833/1/3 [arXiv:1607.08006 [astro-ph.HE]].
- [489] L. A. Anchordoqui *et al.*, **Cosmic neutrino pevatrons: A brand new pathway to astronomy, astrophysics, and particle physics**, JHEAp **1-2**, 1 (2014) doi:10.1016/j.jheap.2014.01.001 [arXiv:1312.6587 [astro-ph.HE]].
- [490] M. Ahlers and F. Halzen, **High-energy cosmic neutrino puzzle: a review**, Rept. Prog. Phys. **78**, no. 12, 126901 (2015). doi:10.1088/0034-4885/78/12/126901
- [491] P. Meszaros, **Astrophysical sources of high energy neutrinos in the IceCube era**, Ann. Rev. Nucl. Part. Sci. **67**, 45 (2017) doi:10.1146/annurev-nucl-101916-123304 [arXiv:1708.03577 [astro-ph.HE]].
- [492] M. G. Aartsen *et al.* [IceCube Collaboration], **Constraints on Galactic neutrino emission with seven years of IceCube data**, Astrophys. J. **849**, no. 1, 67 (2017) doi:10.3847/1538-4357/aa8dfb [arXiv:1707.03416 [astro-ph.HE]].
- [493] L. A. Anchordoqui, H. Goldberg, M. H. Lynch, A. V. Olinto, T. C. Paul and T. J. Weiler, **Pinning down the cosmic ray source mechanism with new IceCube data**, Phys. Rev. D **89**, no. 8, 083003 (2014) doi:10.1103/PhysRevD.89.083003 [arXiv:1306.5021 [astro-ph.HE]].
- [494] A. Neronov, D. V. Semikoz and C. Tchernin, **PeV neutrinos from interactions of cosmic rays with the interstellar medium in the Galaxy**, Phys. Rev. D **89**, no. 10, 103002 (2014) doi:10.1103/PhysRevD.89.103002 [arXiv:1307.2158 [astro-ph.HE]].
- [495] L. A. Anchordoqui, H. Goldberg, T. C. Paul, L. H. M. da Silva and B. J. Vlcek, **Estimating the contribution of Galactic sources to the diffuse neutrino flux**, Phys. Rev. D **90**, no. 12, 123010 (2014) doi:10.1103/PhysRevD.90.123010 [arXiv:1410.0348 [astro-ph.HE]].
- [496] A. Neronov and D. V. Semikoz, **Evidence the Galactic contribution to the IceCube astrophysical neutrino flux**, Astropart. Phys. **75**, 60 (2016) doi:10.1016/j.astropartphys.2015.11.002 [arXiv:1509.03522 [astro-ph.HE]].
- [497] A. Neronov and D. Semikoz, **Galactic and extragalactic contributions to the astrophysical muon neutrino signal**, Phys. Rev. D **93**, no. 12, 123002 (2016) doi:10.1103/PhysRevD.93.123002 [arXiv:1603.06733 [astro-ph.HE]].
- [498] A. Neronov, M. Kachelrie and D. V. Semikoz, **Multi-messenger gamma-ray counterpart of the IceCube neutrino signal**, Phys. Rev. D **98**, no. 2, 023004 (2018) doi:10.1103/PhysRevD.98.023004 [arXiv:1802.09983 [astro-ph.HE]].

- [499] M. G. Aartsen *et al.* [IceCube and Pierre Auger and Telescope Array Collaborations], [Search for correlations between the arrival directions of IceCube neutrino events and ultrahigh-energy cosmic rays detected by the Pierre Auger Observatory and the Telescope Array](#), *JCAP* **1601**, no. 01, 037 (2016) doi:10.1088/1475-7516/2016/01/037 [arXiv:1511.09408 [astro-ph.HE]].
- [500] M. Ahlers and F. Halzen, [IceCube: Neutrinos and multi-messenger astronomy](#), *PTEP* **2017**, no. 12, 12A105 (2017). doi:10.1093/ptep/ptx021
- [501] M. G. Aartsen *et al.* [IceCube Collaboration], [Neutrino emission from the direction of the blazar TXS 0506+056 prior to the IceCube-170922A alert](#), *Science* **361**, no. 6398, 147 (2018). doi:10.1126/science.aat2890 [arXiv:1807.08794 [astro-ph.HE]].
- [502] M. Ackermann *et al.* [Fermi-LAT Collaboration], [The second catalog of active galactic nuclei detected by the Fermi Large Area Telescope](#), *Astrophys. J.* **743**, 171 (2011) doi:10.1088/0004-637X/743/2/171 [arXiv:1108.1420 [astro-ph.HE]].
- [503] M. G. Aartsen *et al.* [IceCube Collaboration], [The contribution of Fermi-2LAC blazars to the diffuse TeV-PeV neutrino flux](#), *Astrophys. J.* **835**, no. 1, 45 (2017) doi:10.3847/1538-4357/835/1/45 [arXiv:1611.03874 [astro-ph.HE]].
- [504] O. Mena, S. Palomares-Ruiz and A. C. Vincent, [Flavor composition of the high-energy neutrino events in IceCube](#), *Phys. Rev. Lett.* **113**, 091103 (2014) doi:10.1103/PhysRevLett.113.091103 [arXiv:1404.0017 [astro-ph.HE]].
- [505] C. Y. Chen, P. S. Bhupal Dev and A. Soni, [Two-component flux explanation for the high energy neutrino events at IceCube](#), *Phys. Rev. D* **92**, no. 7, 073001 (2015) doi:10.1103/PhysRevD.92.073001 [arXiv:1411.5658 [hep-ph]].
- [506] M. G. Aartsen *et al.* [IceCube Collaboration], [Flavor ratio of astrophysical neutrinos above 35 TeV in IceCube](#), *Phys. Rev. Lett.* **114**, no. 17, 171102 (2015) doi:10.1103/PhysRevLett.114.171102 [arXiv:1502.03376 [astro-ph.HE]].
- [507] S. Palomares-Ruiz, A. C. Vincent and O. Mena, [Spectral analysis of the high-energy IceCube neutrinos](#), *Phys. Rev. D* **91**, no. 10, 103008 (2015) doi:10.1103/PhysRevD.91.103008 [arXiv:1502.02649 [astro-ph.HE]].
- [508] A. C. Vincent, S. Palomares-Ruiz and O. Mena, [Analysis of the 4-year IceCube high-energy starting events](#), *Phys. Rev. D* **94**, no. 2, 023009 (2016) doi:10.1103/PhysRevD.94.023009 [arXiv:1605.01556 [astro-ph.HE]].
- [509] L. A. Anchordoqui, M. M. Block, L. Durand, P. Ha, J. F. Soriano and T. J. Weiler, [Evidence for a break in the spectrum of astrophysical neutrinos](#), *Phys. Rev. D* **95**, no. 8, 083009 (2017) doi:10.1103/PhysRevD.95.083009 [arXiv:1611.07905 [astro-ph.HE]].
- [510] M. Muzio, G. R. Farrar, and M. Unger, [Detailed simulations of Fermi-LAT constraints on UHECR production scenarios](#) *PoS ICRC 2017*, 557 (2017).

- [511] M. Kachelriess, O. Kalashev, S. Ostapchenko and D. V. Semikoz, [Minimal model for extragalactic cosmic rays and neutrinos](#), Phys. Rev. D **96**, no. 8, 083006 (2017) doi:10.1103/PhysRevD.96.083006 [arXiv:1704.06893 [astro-ph.HE]].
- [512] B. P. Abbott *et al.* [LIGO Scientific and Virgo Collaborations], [Observation of gravitational waves from a binary black hole merger](#), Phys. Rev. Lett. **116**, no. 6, 061102 (2016) doi:10.1103/PhysRevLett.116.061102 [arXiv:1602.03837 [gr-qc]].
- [513] B. P. Abbott *et al.* [LIGO Scientific and Virgo Collaborations], [Properties of the binary black hole merger GW150914](#), Phys. Rev. Lett. **116**, no. 24, 241102 (2016) doi:10.1103/PhysRevLett.116.241102 [arXiv:1602.03840 [gr-qc]].
- [514] B. P. Abbott *et al.* [LIGO Scientific and Virgo Collaborations], [GW151226: observation of gravitational waves from a 22-solar-mass binary black hole coalescence](#), Phys. Rev. Lett. **116**, no. 24, 241103 (2016) doi:10.1103/PhysRevLett.116.241103 [arXiv:1606.04855 [gr-qc]].
- [515] B. P. Abbott *et al.* [LIGO Scientific and Virgo Collaborations], [Binary black hole mergers in the first Advanced LIGO observing run](#), Phys. Rev. X **6**, no. 4, 041015 (2016) doi:10.1103/PhysRevX.6.041015 [arXiv:1606.04856 [gr-qc]].
- [516] K. Murase, K. Kashiyama, P. Mszros, I. Shoemaker and N. Senno, [Ultrafast outflows from black hole mergers with a minidisk](#), Astrophys. J. **822**, no. 1, L9 (2016) doi:10.3847/2041-8205/822/1/L9 [arXiv:1602.06938 [astro-ph.HE]].
- [517] K. Kotera and J. Silk, [Ultra-high energy cosmic rays and black hole mergers](#), Astrophys. J. **823**, no. 2, L29 (2016) doi:10.3847/2041-8205/823/2/L29 [arXiv:1602.06961 [astro-ph.HE]].
- [518] L. A. Anchordoqui, [Neutrino lighthouse powered by Sagittarius A* disk dynamo](#), Phys. Rev. D **94**, 023010 (2016) doi:10.1103/PhysRevD.94.023010 [arXiv:1606.01816 [astro-ph.HE]].
- [519] A. Aab *et al.* [Pierre Auger Collaboration], [Ultra-high-energy neutrino follow-up of gravitational wave events GW150914 and GW151226 with the Pierre Auger Observatory](#), Phys. Rev. D **94**, no. 12, 122007 (2016) doi:10.1103/PhysRevD.94.122007 [arXiv:1608.07378 [astro-ph.HE]].
- [520] B. P. Abbott *et al.* [LIGO Scientific and Virgo Collaborations], [GW170817: Observation of gravitational waves from a binary neutron star inspiral](#), Phys. Rev. Lett. **119**, no. 16, 161101 (2017) doi:10.1103/PhysRevLett.119.161101 [arXiv:1710.05832 [gr-qc]].
- [521] B. P. Abbott *et al.* [LIGO Scientific and Virgo and Fermi-GBM and INTEGRAL Collaborations], [Gravitational waves and gamma-rays from a binary neutron star merger: GW170817 and GRB 170817A](#), Astrophys. J. **848**, no. 2, L13 (2017) doi:10.3847/2041-8213/aa920c [arXiv:1710.05834 [astro-ph.HE]].
- [522] D. A. Coulter *et al.*, [Swope supernova survey 2017a \(SSS17a\), the optical counterpart to a gravitational wave source](#), Science [Science **358**, 1556 (2017)] doi:10.1126/science.aap9811 [arXiv:1710.05452 [astro-ph.HE]].

- [523] M. Soares-Santos *et al.* [DES and Dark Energy Camera GW-EM Collaborations], **The electromagnetic counterpart of the binary neutron star merger LIGO/Virgo GW170817 I: Discovery of the optical counterpart using the Dark Energy Camera**, *Astrophys. J.* **848**, no. 2, L16 (2017) doi:10.3847/2041-8213/aa9059 [arXiv:1710.05459 [astro-ph.HE]].
- [524] S. Valenti *et al.*, **The discovery of the electromagnetic counterpart of GW170817: kilonova AT 2017gfo/DLT17ck**, *Astrophys. J.* **848**, no. 2, L24 (2017) doi:10.3847/2041-8213/aa8edf [arXiv:1710.05854 [astro-ph.HE]].
- [525] I. Arcavi *et al.*, **Optical emission from a kilonova following a gravitational-wave-detected neutron-star merger**, *Nature* **551**, 64 (2017) doi:10.1038/nature24291 [arXiv:1710.05843 [astro-ph.HE]].
- [526] V. M. Lipunov *et al.*, **MASTER optical detection of the first LIGO/Virgo neutron star binary merger GW170817**, *Astrophys. J.* **850**, no. 1, L1 (2017) doi:10.3847/2041-8213/aa92c0 [arXiv:1710.05461 [astro-ph.HE]].
- [527] N. R. Tanvir *et al.*, **The emergence of a Lanthanide-Rich kilonova following the merger of two neutron stars**, *Astrophys. J.* **848**, no. 2, L27 (2017) doi:10.3847/2041-8213/aa90b6 [arXiv:1710.05455 [astro-ph.HE]].
- [528] E. Pian *et al.*, **Spectroscopic identification of r-process nucleosynthesis in a double neutron star merger**, *Nature* **551**, 67 (2017) doi:10.1038/nature24298 [arXiv:1710.05858 [astro-ph.HE]].
- [529] E. Troja *et al.*, **The X-ray counterpart to the gravitational wave event GW 170817**, *Nature* **551**, 71 (2017) [Nature **551**, 71 (2017)] doi:10.1038/nature24290 [arXiv:1710.05433 [astro-ph.HE]].
- [530] D. Haggard, M. Nynka, J. J. Ruan, V. Kalogera, S. Bradley Cenko, P. Evans and J. A. Kennea, **A deep Chandra X-ray study of neutron star coalescence GW170817**, *Astrophys. J.* **848**, no. 2, L25 (2017) doi:10.3847/2041-8213/aa8ede [arXiv:1710.05852 [astro-ph.HE]].
- [531] G. Hallinan *et al.*, **A radio counterpart to a neutron star merger**, *Science* **358**, 1579 (2017) doi:10.1126/science.aap9855 [arXiv:1710.05435 [astro-ph.HE]].
- [532] M. M. Kasliwal *et al.*, **Illuminating gravitational waves: A concordant picture of photons from a neutron star merger**, *Science* **358**, 1559 (2017) doi:10.1126/science.aap9455 [arXiv:1710.05436 [astro-ph.HE]].
- [533] L. X. Li and B. Paczynski, **Transient events from neutron star mergers**, *Astrophys. J.* **507**, L59 (1998) doi:10.1086/311680 [astro-ph/9807272].
- [534] B. D. Metzger *et al.*, **Electromagnetic counterparts of compact object mergers powered by the radioactive decay of r-process nuclei**, *Mon. Not. Roy. Astron. Soc.* **406**, 2650 (2010) doi:10.1111/j.1365-2966.2010.16864.x [arXiv:1001.5029 [astro-ph.HE]].
- [535] A. Albert *et al.* [ANTARES and IceCube and Pierre Auger and LIGO Scientific and Virgo Collaborations], **Search for high-energy neutrinos from binary neutron star merger GW170817 with ANTARES, IceCube, and the Pierre Auger Observatory**, *Astrophys. J.* **850**, no. 2, L35 (2017) doi:10.3847/2041-8213/aa9aed [arXiv:1710.05839 [astro-ph.HE]].

- [536] D. Biehl, J. Heinze and W. Winter, [Expected neutrino fluence from short gamma-ray burst 170817A and off-axis angle constraints](#), *Mon. Not. Roy. Astron. Soc.* **476**, no. 1, 1191 (2018) doi:10.1093/mnras/sty285 [arXiv:1712.00449 [astro-ph.HE]].
- [537] X. Rodrigues, D. Biehl, D. Boncioli and A. M. Taylor, [Binary neutron star merger remnants as sources of cosmic rays below the "ankle"](#), arXiv:1806.01624 [astro-ph.HE].
- [538] A. Capella, U. Sukhatme, C. I. Tan and J. Tran Thanh Van, [Dual parton model](#), *Phys. Rept.* **236**, 225 (1994).
- [539] E. Predazzi, [Diffraction: past, present and future](#), arXiv:hep-ph/9809454.
- [540] D. Cline, F. Halzen and J. Luthe, [High transverse momentum secondaries and rising total cross-sections in cosmic ray interactions](#), *Phys. Rev. Lett.* **31**, 491 (1973).
- [541] S. D. Ellis and M. B. Kislinger, [Implications of parton model concepts for large transverse momentum production of hadrons](#), *Phys. Rev. D* **9**, 2027 (1974).
- [542] F. Halzen, [High transverse momentum secondaries In cosmic ray interactions up to 10, 000, 000 GeV](#), *Nucl. Phys. B* **92**, 404 (1975).
- [543] G. Pancheri and C. Rubbia, [Events of very high-energy density at the CERN \$Spp\bar{S}\$ Collider](#), *Nucl. Phys. A* **418**, 117C (1984).
- [544] T. K. Gaisser and F. Halzen, [Soft hard scattering in the TeV range](#), *Phys. Rev. Lett.* **54**, 1754 (1985).
- [545] J. Dias de Deus, [Semihard physics at the SPS \$p\bar{p}\$ Colliders?](#), *Nucl. Phys. B* **252**, 369 (1985).
- [546] G. Pancheri and Y. Srivastava, [Jets in minimum bias physics](#), *Phys. Lett. B* **159**, 69 (1985).
- [547] G. Pancheri and Y. N. Srivastava, [Low \$p_T\$ jets and the rise with energy of the inelastic cross-section](#), *Phys. Lett. B* **182**, 199 (1986).
- [548] C. Albajar *et al.* [UA1 Collaboration], [Production of low transverse energy clusters in \$p\bar{p}\$ collisions at \$\sqrt{s} = 0.2\$ TeV to 0.9 TeV and their interpretation in terms of QCD jets](#), *Nucl. Phys. B* **309**, 405 (1988).
- [549] V. N. Gribov and L. N. Lipatov, [\$e^+e^-\$ pair annihilation and deep inelastic \$ep\$ scattering in perturbation theory](#), *Yad. Fiz.* **15**, 1218 (1972) [*Sov. J. Nucl. Phys.* **15**, 675 (1972)].
- [550] V. N. Gribov and L. N. Lipatov, [Deep inelastic \$ep\$ scattering in perturbation theory](#), *Yad. Fiz.* **15**, 781 (1972) [*Sov. J. Nucl. Phys.* **15**, 438 (1972)].
- [551] Y. L. Dokshitzer, [Calculation of the structure functions for deep inelastic scattering and \$e^+e^-\$ annihilation by perturbation theory in quantum chromodynamics](#), *Sov. Phys. JETP* **46**, 641 (1977) [*Zh. Eksp. Teor. Fiz.* **73**, 1216 (1977)].
- [552] G. Altarelli and G. Parisi, [Asymptotic freedom in parton language](#), *Nucl. Phys. B* **126**, 298 (1977).
- [553] M. Dittmar *et al.*, [Parton distributions](#), arXiv:0901.2504 [hep-ph].

- [554] R. Engel, *Models of primary interactions*, Nucl. Phys. Proc. Suppl. **122**, 40 (2003).
- [555] L. Anchordoqui and F. Halzen, *Lessons in particle physics*, arXiv:0906.1271.
- [556] J. Kwiecinski and A. D. Martin, *Semihard QCD expectations for $p\bar{p}$ scattering at CERN, Tevatron and SSC colliders*, Phys. Rev. D **43**, 1560 (1991).
- [557] J. Dias de Deus and J. Kwiecinski, *Semihard QCD: minijets and elastic scattering*, Phys. Lett. B **196**, 537 (1987).
- [558] J. Dias De Deus, *Geometric scaling, multiplicity distributions and cross-sections*, Nucl. Phys. B **59**, 231 (1973).
- [559] U. Amaldi and K. R. Schubert, *Impact parameter interpretation of proton proton scattering from a critical review of all ISR data*, Nucl. Phys. B **166**, 301 (1980).
- [560] R. Castaldi and G. Sanguinetti, *Elastic scattering and total cross-section at very high-energies*, Ann. Rev. Nucl. Part. Sci. **35**, 351 (1983).
- [561] M. M. Block and R. N. Cahn, *High-energy $p\bar{p}$ and pp forward elastic scattering and total cross-sections*, Rev. Mod. Phys. **57**, 563 (1985).
- [562] R. J. Glauber and G. Matthiae, *High-energy scattering of protons by nuclei*, Nucl. Phys. B **21**, 135 (1970).
- [563] P. L'Heureux, B. Margolis and P. Valin, *Quark-gluon model for diffraction at high-energies*, Phys. Rev. D **32**, 1681 (1985).
- [564] L. Durand and H. Pi, *QCD and rising cross sections*, Phys. Rev. Lett. **58**, 303 (1987).
- [565] L. Durand and H. Pi, *High-energy nucleon nucleus scattering and cosmic ray cross-sections*, Phys. Rev. D **38**, 78 (1988).
- [566] T. K. Gaisser and T. Stanev, *Minijets in minimum bias events*, Phys. Lett. B **219**, 375 (1989).
- [567] R. S. Fletcher, T. K. Gaisser, P. Lipari and T. Stanev, *SIBYLL: An Event generator for simulation of high-energy cosmic ray cascades*, Phys. Rev. D **50**, 5710 (1994).
- [568] N. N. Kalmykov, S. S. Ostapchenko and A. I. Pavlov, *Quark-gluon string model and EAS simulation problems at ultra-high energies*, Nucl. Phys. Proc. Suppl. **52B**, 17 (1997).
- [569] J. Alvarez-Muniz, R. Engel, T. K. Gaisser, J. A. Ortiz and T. Stanev, *Hybrid simulations of extensive air showers*, Phys. Rev. D **66**, 033011 (2002) [arXiv:astro-ph/0205302].
- [570] M. Froissart, *Asymptotic behavior and subtractions in the Mandelstam representation*, Phys. Rev. **123**, 1053 (1961).
- [571] E. J. Ahn, R. Engel, T. K. Gaisser, P. Lipari and T. Stanev, *Cosmic ray interaction event generator SIBYLL 2.1*, Phys. Rev. D **80**, 094003 (2009) doi:10.1103/PhysRevD.80.094003 [arXiv:0906.4113 [hep-ph]].

- [572] T. Sjostrand, **Status of fragmentation models**, Int. J. Mod. Phys. A **3**, 751 (1988).
- [573] J. Engel, T. K. Gaisser, T. Stanev and P. Lipari, **Nucleus-nucleus collisions and interpretation of cosmic ray cascades**, Phys. Rev. D **46**, 5013 (1992).
- [574] K. Belov [HiRes Collaboration], **p -air cross-section measurement at $10^{18.5}$ eV**, Nucl. Phys. Proc. Suppl. **151**, 197 (2006).
- [575] M. M. Block, F. Halzen and T. Stanev, **Predicting proton air cross sections at $\sqrt{s} \approx 30$ TeV, using accelerator and cosmic ray data**, Phys. Rev. Lett. **83**, 4926 (1999) [arXiv:hep-ph/9908222].
- [576] M. M. Block, **Ultra-high energy predictions of proton-air cross sections from accelerator data**, Phys. Rev. D **76**, 111503 (2007) [arXiv:0705.3037 [hep-ph]].
- [577] G. Aielli *et al.* [ARGO-YBJ Collaboration], **Proton-air cross section measurement with the ARGO-YBJ cosmic ray experiment**, Phys. Rev. D **80**, 092004 (2009) [arXiv:0904.4198 [hep-ex]].
- [578] M. Aglietta *et al.*, **Measurement of the proton-air Inelastic cross section at $\sqrt{s} \approx 2$ TeV from the EAS-TOP experiment**, Phys. Rev. D **79**, 032004 (2009).
- [579] H. H. Mielke, M. Foeller, J. Engler and J. Knapp, **Cosmic ray hadron flux at sea level up to 15 TeV**, J. Phys. G **20**, 637 (1994).
- [580] M. Honda *et al.*, **Inelastic cross-section for p -air collisions from air shower experiment and total cross-section for pp collisions at SSC energy**, Phys. Rev. Lett. **70**, 525 (1993).
- [581] M. N. Dyakonov *et al.*, **Parameters of hadron interactions at $E_0 > 10^{17}$ eV on EAS development fluctuation data**, in Proceedings of 21st International Cosmic Ray Conference (Adelaide, Australia) **9**, 252 (1990).
- [582] S. P. Knurenko, V. R. Sleptsova, I. E. Sleptsov, N. N. Kalmykov and S. S. Ostapchenko, **Longitudinal EAS development at $E_0 = 10^{18}$ eV to 3×10^{19} eV and the QGSJET model**, in Proceedings of 26th International Cosmic Ray Conference (Salt Lake City, Utah) **1**, 372 (1999).
- [583] R. A. Nam, S. I. Nikolsky, V. P. Pavlyuchenko, A. P. Chubenko and V. I. Yakovlev, **Investigation of nucleon-nuclei of air cross-section at energy greater than 10 TeV**, in Proceedings of 14th International Cosmic Ray Conference (Munich, Germany) **7**, 2258 (1975).
- [584] R. M. Baltrusaitis *et al.*, **Total proton proton cross-section at $\sqrt{s} = 30$ TeV**, Phys. Rev. Lett. **52**, 1380 (1984).
- [585] P. Abreu *et al.* [Pierre Auger Collaboration], **Measurement of the proton-air cross-section at $\sqrt{s} = 57$ TeV with the Pierre Auger Observatory**, Phys. Rev. Lett. **109**, 062002 (2012) doi:10.1103/PhysRevLett.109.062002 [arXiv:1208.1520 [hep-ex]].
- [586] R. U. Abbasi *et al.* [Telescope Array Collaboration], **Measurement of the proton-air cross section with Telescope Arrays Middle Drum detector and surface array in hybrid mode**, Phys. Rev. D **92**, no. 3, 032007 (2015) doi:10.1103/PhysRevD.92.032007 [arXiv:1505.01860 [astro-ph.HE]].

- [587] D. d'Enterria, R. Engel, T. Pierog, S. Ostapchenko and K. Werner, **Constraints from the first LHC data on hadronic event generators for ultra-high energy cosmic-ray physics**, *Astropart. Phys.* **35**, 98 (2011) doi:10.1016/j.astropartphys.2011.05.002 [arXiv:1101.5596 [astro-ph.HE]].
- [588] H. M. J. Barbosa, F. Catalani, J. A. Chinellato and C. Dobrigkeit, **Determination of the calorimetric energy in extensive air showers**, *Astropart. Phys.* **22**, 159 (2004) doi:10.1016/j.astropartphys.2004.06.007 [astro-ph/0310234].
- [589] T. J. L. McComb, R. J. Protheroe and K. E. Turver, **Photoproduction in Large cosmic ray showers**, *J. Phys. G* **5**, 1613 (1979).
- [590] B. Rossi and K. Greisen, **Cosmic-ray theory**, *Rev. Mod. Phys.* **13**, 240 (1941). doi:10.1103/RevModPhys.13.240
- [591] H. Bethe and W. Heitler, **On the stopping of fast particles and on the creation of positive electrons**, *Proc. Roy. Soc. Lond. A* **146**, 83 (1934).
- [592] B. Rossi, **High Energy Particles** (Prentice-Hall, Inc., Englewood Cliffs, NY, 1952).
- [593] R. C. Weast, **CRC Handbook of Chemistry and Physics**, (CRC Press, Boca Raton, FL, USA, 1981).
- [594] Y. S. Tsai, **Pair production and bremsstrahlung of charged leptons**, *Rev. Mod. Phys.* **46**, 815 (1974) [Erratum *Rev. Mod. Phys.* **49**, 421 (1977)].
- [595] T. Stanev, C. Vankov, R. E. Streitmatter, R. W. Ellsworth and T. Bowen, **Development of ultra-high-energy electromagnetic cascades in water and lead including the Landau-Pomeranchuk-Migdal effect**, *Phys. Rev. D* **25**, 1291 (1982).
- [596] A. N. Cillis, H. Fanchiotti, C. A. Garcia Canal and S. J. Sciutto, **Influence of the LPM effect and dielectric suppression on particle air showers**, *Phys. Rev. D* **59**, 113012 (1999) [arXiv:astro-ph/9809334].
- [597] H. P. Vankov, N. Inoue and K. Shinozaki, **Ultra-high energy gamma rays in geomagnetic field and atmosphere**, *Phys. Rev. D* **67**, 043002 (2003) [arXiv:astro-ph/0211051].
- [598] A. N. Cillis and S. J. Sciutto, **Extended air showers and muon interactions**, *Phys. Rev. D* **64**, 013010 (2001) [arXiv:astro-ph/0010488].
- [599] L. Anchordoqui and H. Goldberg, **Footprints of superGZK cosmic rays in the Pilliga State Forest**, *Phys. Lett. B* **583**, 213 (2004) doi:10.1016/j.physletb.2003.12.072 [hep-ph/0310054].
- [600] W. Heitler. **The Quantum Theory of Radiation**, 2nd. Edition, (Oxford University Press, London, 1944).
- [601] J. Linsley, **Structure of large air showers at depth 834 g/cm²: Applications**, in Proceedings of 15th International Cosmic Ray Conference (Plovdiv, Bulgaria) **12**, 89 (1977).
- [602] J. Matthews, **A Heitler model of extensive air showers**, *Astropart. Phys.* **22**, 387 (2005).
- [603] R. Ulrich, J. Blumer, R. Engel, F. Schussler and M. Unger, **On the measurement of the proton-air cross section using air shower data**, *New J. Phys.* **11**, 065018 (2009) [arXiv:0903.0404 [astro-ph.HE]].

- [604] T. Abu-Zayyad *et al.* [HiRes and MIA Collaborations], [Evidence for changing of cosmic ray composition between \$10^{17}\$ eV and \$10^{18}\$ eV from multicomponent measurements](#), Phys. Rev. Lett. **84**, 4276 (2000) doi:10.1103/PhysRevLett.84.4276 [astro-ph/9911144].
- [605] A. Aab *et al.* [Pierre Auger Collaboration], [Muons in air showers at the Pierre Auger Observatory: Mean number in highly inclined events](#), Phys. Rev. D **91**, no. 3, 032003 (2015) Erratum: [Phys. Rev. D **91**, no. 5, 059901 (2015)] doi:10.1103/PhysRevD.91.059901, 10.1103/PhysRevD.91.032003 [arXiv:1408.1421 [astro-ph.HE]].
- [606] R. U. Abbasi *et al.* [Telescope Array Collaboration], [Study of muons from ultrahigh energy cosmic ray air showers measured with the Telescope Array experiment](#), Phys. Rev. D **98**, no. 2, 022002 (2018) doi:10.1103/PhysRevD.98.022002 [arXiv:1804.03877 [astro-ph.HE]].
- [607] G. R. Farrar and J. D. Allen, [A new physical phenomenon in ultrahigh energy collisions](#), EPJ Web Conf. **53**, 07007 (2013) doi:10.1051/epjconf/20135307007 [arXiv:1307.2322 [hep-ph]].
- [608] L. A. Anchordoqui, H. Goldberg and T. J. Weiler, [Strange fireball as an explanation of the muon excess in Auger data](#), Phys. Rev. D **95**, no. 6, 063005 (2017) doi:10.1103/PhysRevD.95.063005 [arXiv:1612.07328 [hep-ph]].
- [609] G. Tomar, [Lorentz invariance violation as an explanation of the muon excess in Auger data](#), Phys. Rev. D **95**, no. 9, 095035 (2017) doi:10.1103/PhysRevD.95.095035 [arXiv:1701.05890 [hep-ph]].
- [610] J. F. Soriano, L. A. Anchordoqui, T. C. Paul and T. J. Weiler, [Probing QCD approach to thermal equilibrium with ultrahigh energy cosmic rays](#), PoS ICRC **2017**, 342 (2018) doi:10.22323/1.301.0342 [arXiv:1811.07728 [hep-ph]].
- [611] J. Knapp, D. Heck, S. J. Sciutto, M. T. Dova and M. Risse, [Extensive air shower simulations at the highest energies](#), Astropart. Phys. **19**, 77 (2003) [arXiv:astro-ph/0206414].
- [612] R. Ulrich, R. Engel and M. Unger, [Hadronic multiparticle production at ultra-high energies and extensive air showers](#), Phys. Rev. D **83**, 054026 (2011) doi:10.1103/PhysRevD.83.054026 [arXiv:1010.4310 [hep-ph]].
- [613] G. Lemaitre, [Republication of: The beginning of the world from the point of view of quantum theory](#), Nature **127**, 706 (1931) [Gen. Rel. Grav. **43**, 2929 (2011)]. doi:10.1007/s10714-011-1214-6, 10.1038/127706b0
- [614] C. T. Hill, [Monopolonium](#), Nucl. Phys. B **224**, 469 (1983).
- [615] E. M. Chudnovsky, G. B. Field, D. N. Spergel and A. Vilenkin, [Superconducting cosmic strings](#), Phys. Rev. D **34**, 944 (1986). doi:10.1103/PhysRevD.34.944
- [616] C. T. Hill, D. N. Schramm and T. P. Walker, [Ultra-high-energy cosmic rays from superconducting cosmic strings](#), Phys. Rev. D **36**, 1007 (1987).
- [617] P. Bhattacharjee, [Cosmic strings and ultra-high-energy cosmic rays](#), Phys. Rev. D **40**, 3968 (1989). doi:10.1103/PhysRevD.40.3968

- [618] P. Bhattacharjee and N. C. Rana, **Ultra-high-energy particle flux from cosmic strings**, Phys. Lett. B **246**, 365 (1990). doi:10.1016/0370-2693(90)90615-D
- [619] P. Bhattacharjee, C. T. Hill and D. N. Schramm, **Grand unified theories, topological defects and ultra-high-energy cosmic rays**, Phys. Rev. Lett. **69**, 567 (1992).
- [620] P. Bhattacharjee and G. Sigl, **Monopole annihilation and highest energy cosmic rays**, Phys. Rev. D **51**, 4079 (1995) doi:10.1103/PhysRevD.51.4079 [astro-ph/9412053].
- [621] V. Berezhinsky, X. Martin and A. Vilenkin, **High energy particles from monopoles connected by strings**, Phys. Rev. D **56**, 2024 (1997) [arXiv:astro-ph/9703077].
- [622] V. Berezhinsky and A. Vilenkin, **Cosmic necklaces and ultrahigh energy cosmic rays**, Phys. Rev. Lett. **79**, 5202 (1997) [arXiv:astro-ph/9704257].
- [623] P. Bhattacharjee and G. Sigl, **Origin and propagation of extremely high-energy cosmic rays**, Phys. Rept. **327**, 109 (2000) doi:10.1016/S0370-1573(99)00101-5 [astro-ph/9811011].
- [624] V. A. Kuzmin and V. A. Rubakov, **Ultra-high-energy cosmic rays: A window on postinflationary reheating epoch of the universe?**, Phys. Atom. Nucl. **61**, 1028 (1998) [Yad. Fiz. **61**, 1122 (1998)] [arXiv:astro-ph/9709187].
- [625] V. Kuzmin and I. Tkachev, **Ultrahigh-energy cosmic rays, superheavy long living particles, and matter creation after inflation**, JETP Lett. **68**, 271 (1998) [Pisma Zh. Eksp. Teor. Fiz. **68**, 255 (1998)] doi:10.1134/1.567858 [hep-ph/9802304].
- [626] S. L. Dubovsky and P. G. Tinyakov, **Galactic anisotropy as signature of CDM related ultrahigh-energy cosmic rays**, JETP Lett. **68**, 107 (1998) doi:10.1134/1.567830 [hep-ph/9802382].
- [627] V. Berezhinsky and M. Kachelriess, **Limiting SUSY QCD spectrum and its application for decays of superheavy particles**, Phys. Lett. B **434**, 61 (1998) doi:10.1016/S0370-2693(98)00728-X [hep-ph/9803500].
- [628] M. Birkel and S. Sarkar, **Extremely high-energy cosmic rays from relic particle decays**, Astropart. Phys. **9**, 297 (1998) doi:10.1016/S0927-6505(98)00028-0 [hep-ph/9804285].
- [629] S. Sarkar and R. Toldra, **The high-energy cosmic ray spectrum from relic particle decay**, Nucl. Phys. B **621**, 495 (2002) doi:10.1016/S0550-3213(01)00565-X [hep-ph/0108098].
- [630] V. A. Kuzmin and I. I. Tkachev, **Ultrahigh-energy cosmic rays and inflation relics**, Phys. Rept. **320**, 199 (1999) doi:10.1016/S0370-1573(99)00064-2 [hep-ph/9903542].
- [631] K. Hamaguchi, Y. Nomura and T. Yanagida, **Superheavy dark matter with discrete gauge symmetries**, Phys. Rev. D **58**, 103503 (1998) [arXiv:hep-ph/9805346].
- [632] K. Hamaguchi, Y. Nomura and T. Yanagida, **Long lived superheavy dark matter with discrete gauge symmetries**, Phys. Rev. D **59**, 063507 (1999) [arXiv:hep-ph/9809426].

- [633] K. Hamaguchi, K. I. Izawa, Y. Nomura and T. Yanagida, **Long-lived superheavy particles in dynamical supersymmetry-breaking models in supergravity**, Phys. Rev. D **60**, 125009 (1999) [arXiv:hep-ph/9903207].
- [634] J. R. Ellis, J. L. Lopez and D. V. Nanopoulos, **Confinement of fractional charges yields integer charged relics in string models**, Phys. Lett. B **247**, 257 (1990).
- [635] K. Benakli, J. R. Ellis and D. V. Nanopoulos, **Natural candidates for superheavy dark matter in string and M theory**, Phys. Rev. D **59**, 047301 (1999) [arXiv:hep-ph/9803333].
- [636] V. Berezhinsky, M. Kachelriess and A. Vilenkin, **Ultra-high-energy cosmic rays without GZK cutoff**, Phys. Rev. Lett. **79**, 4302 (1997) [arXiv:astro-ph/9708217].
- [637] P. Blasi, R. Dick and E. W. Kolb, **Ultrahigh-energy cosmic rays from annihilation of superheavy dark matter**, Astropart. Phys. **18**, 57 (2002) doi:10.1016/S0927-6505(02)00113-5 [astro-ph/0105232].
- [638] C. Coriano and A. E. Faraggi, **SUSY QCD and high energy cosmic rays I: Fragmentation functions of SUSY QCD**, Phys. Rev. D **65**, 075001 (2002) [arXiv:hep-ph/0106326].
- [639] C. Barbot and M. Drees, **Detailed analysis of the decay spectrum of a super-heavy X particle**, Astropart. Phys. **20**, 5 (2003) [arXiv:hep-ph/0211406].
- [640] C. Barbot, **Decay of super-heavy particles: User guide of the SHdecay program**, Comput. Phys. Commun. **157**, 63 (2004) [arXiv:hep-ph/0306303].
- [641] F. A. Aharonian, P. Bhattacharjee and D. N. Schramm, **Photon/proton ratio as a diagnostic tool for topological defects as the sources of extremely high-energy cosmic rays**, Phys. Rev. D **46**, 4188 (1992).
- [642] G. Sigl, S. Lee, P. Bhattacharjee and S. Yoshida, **Probing grand unified theories with cosmic ray, gamma-ray and neutrino astrophysics**, Phys. Rev. D **59**, 043504 (1999) [arXiv:hep-ph/9809242].
- [643] G. Sigl, K. Jedamzik, D. N. Schramm and V. S. Berezhinsky, **Helium photodisintegration and nucleosynthesis: Implications for topological defects, high-energy cosmic rays, and massive black holes**, Phys. Rev. D **52**, 6682 (1995) [arXiv:astro-ph/9503094].
- [644] G. Sigl, S. Lee, D. N. Schramm and P. Coppi, **Cosmological neutrino signatures for grand unification scale physics**, Phys. Lett. B **392**, 129 (1997) [arXiv:astro-ph/9610221].
- [645] R. J. Protheroe and T. Stanev, **Limits on models of the ultrahigh energy cosmic rays based on topological defects**, Phys. Rev. Lett. **77**, 3708 (1996) [Erratum-ibid. **78**, 3420 (1997)] [arXiv:astro-ph/9605036].
- [646] R. J. Protheroe and P. A. Johnson, **Are topological defects responsible for the 300-EeV cosmic rays?**, Nucl. Phys. Proc. Suppl. **48**, 485 (1996) [arXiv:astro-ph/9605006].
- [647] P. Sreekumar *et al.* [EGRET Collaboration], **EGRET observations of the extragalactic gamma-ray emission**, Astrophys. J. **494**, 523 (1998) doi:10.1086/305222 [astro-ph/9709257].

- [648] V. Berezhinsky, P. Blasi and A. Vilenkin, [Ultra-high-energy gamma-rays as signature of topological defects](#), Phys. Rev. D **58**, 103515 (1998) doi:10.1103/PhysRevD.58.103515 [astro-ph/9803271].
- [649] A. A. Abdo *et al.* [Fermi-LAT Collaboration], [The spectrum of the isotropic diffuse gamma-ray emission derived from first-year Fermi Large Area Telescope data](#), Phys. Rev. Lett. **104**, 101101 (2010) doi:10.1103/PhysRevLett.104.101101 [arXiv:1002.3603 [astro-ph.HE]].
- [650] V. Berezhinsky, A. Gazizov, M. Kachelriess and S. Ostapchenko, [Restricting UHECRs and cosmogenic neutrinos with Fermi-LAT](#), Phys. Lett. B **695**, 13 (2011) doi:10.1016/j.physletb.2010.11.019 [arXiv:1003.1496 [astro-ph.HE]].
- [651] M. Ackermann *et al.* [Fermi-LAT Collaboration], [The spectrum of isotropic diffuse gamma-ray emission between 100 MeV and 820 GeV](#), Astrophys. J. **799**, 86 (2015) doi:10.1088/0004-637X/799/1/86 [arXiv:1410.3696 [astro-ph.HE]].
- [652] V. Berezhinsky and O. Kalashev, [High energy electromagnetic cascades in extragalactic space: physics and features](#), Phys. Rev. D **94**, no. 2, 023007 (2016) doi:10.1103/PhysRevD.94.023007 [arXiv:1603.03989 [astro-ph.HE]].
- [653] T. J. Weiler, [Resonant absorption of cosmic ray neutrinos by the relic neutrino background](#), Phys. Rev. Lett. **49**, 234 (1982). doi:10.1103/PhysRevLett.49.234
- [654] T. J. Weiler, [Cosmic ray neutrino annihilation on relic neutrinos revisited: A Mechanism for generating air showers above the Greisen-Zatsepin-Kuzmin cutoff](#), Astropart. Phys. **11**, 303 (1999) doi:10.1016/S0927-6505(98)00068-1 [hep-ph/9710431].
- [655] D. Fargion, B. Mele and A. Salis, [Ultra-high-energy neutrino scattering onto relic light neutrinos in galactic halo as a possible source of highest energy extragalactic cosmic rays](#), Astrophys. J. **517**, 725 (1999) doi:10.1086/307203 [astro-ph/9710029].
- [656] R. Aloisio, S. Matarrese and A. V. Olinto, [Super heavy dark matter in light of BICEP2, Planck and ultra high energy cosmic ray observations](#), JCAP **1508**, no. 08, 024 (2015) doi:10.1088/1475-7516/2015/08/024 [arXiv:1504.01319 [astro-ph.HE]].
- [657] J. L. Christiansen, E. Albin, T. Fletcher, J. Goldman, I. P. W. Teng, M. Foley and G. F. Smoot, [Search for cosmic strings in the COSMOS survey](#), Phys. Rev. D **83**, 122004 (2011) doi:10.1103/PhysRevD.83.122004 [arXiv:1008.0426 [astro-ph.CO]].
- [658] R. van Haasteren *et al.*, [Placing limits on the stochastic gravitational-wave background using European Pulsar Timing Array data](#), Mon. Not. Roy. Astron. Soc. **414**, no. 4, 3117 (2011) Erratum: [Mon. Not. Roy. Astron. Soc. **425**, no. 2, 1597 (2012)] doi:10.1111/j.1365-2966.2011.18613.x, 10.1111/j.1365-2966.2012.20916.x [arXiv:1103.0576 [astro-ph.CO]].
- [659] T. Damour and A. Vilenkin, [Gravitational radiation from cosmic \(super\)strings: Bursts, stochastic background, and observational windows](#), Phys. Rev. D **71**, 063510 (2005) doi:10.1103/PhysRevD.71.063510 [hep-th/0410222].

- [660] S. Olmez, V. Mandic and X. Siemens, [Gravitational-wave stochastic background from kinks and cusps on cosmic strings](#), Phys. Rev. D **81**, 104028 (2010) doi:10.1103/PhysRevD.81.104028 [arXiv:1004.0890 [astro-ph.CO]].
- [661] V. Berezhinsky, E. Sabancilar and A. Vilenkin, [Extremely high energy neutrinos from cosmic strings](#), Phys. Rev. D **84**, 085006 (2011) doi:10.1103/PhysRevD.84.085006 [arXiv:1108.2509 [astro-ph.CO]].
- [662] L. Boyle, K. Finn and N. Turok, [CPT symmetric universe](#), arXiv:1803.08928 [hep-ph].
- [663] L. Boyle, K. Finn and N. Turok, [The Big Bang, CPT, and neutrino dark matter](#), arXiv:1803.08930 [hep-ph].
- [664] M. G. Aartsen *et al.* [IceCube Collaboration], [Search for neutrinos from decaying dark matter with IceCube](#), arXiv:1804.03848 [astro-ph.HE].
- [665] P. W. Gorham *et al.* [ANITA Collaboration], [The Antarctic Impulsive Transient Antenna ultra-high energy neutrino detector design, performance, and sensitivity for 2006-2007 balloon flight](#), Astropart. Phys. **32**, 10 (2009) doi:10.1016/j.astropartphys.2009.05.003 [arXiv:0812.1920 [astro-ph]].
- [666] P. W. Gorham *et al.* [ANITA Collaboration], [Constraints on the diffuse high-energy neutrino flux from the third flight of ANITA](#), Phys. Rev. D **98**, no. 2, 022001 (2018) doi:10.1103/PhysRevD.98.022001 [arXiv:1803.02719 [astro-ph.HE]].
- [667] P. W. Gorham *et al.*, [Characteristics of four upward-pointing cosmic-ray-like events observed with ANITA](#), Phys. Rev. Lett. **117**, no. 7, 071101 (2016) doi:10.1103/PhysRevLett.117.071101 [arXiv:1603.05218 [astro-ph.HE]].
- [668] P. W. Gorham *et al.* [ANITA Collaboration], [Observation of an unusual upward-going cosmic-ray-like event in the third flight of ANITA](#), arXiv:1803.05088 [astro-ph.HE].
- [669] L. A. Anchordoqui, V. Barger, J. G. Learned, D. Marfatia and T. J. Weiler, [Upgoing ANITA events as evidence of the CPT symmetric universe](#), LHEP **1**, no. 1, 13 (2018) doi:10.31526/LHEP.1.2018.03 [arXiv:1803.11554 [hep-ph]].
- [670] C. Patterson, G. Tilton, and M. Inghram, [Age of the Earth](#), Science **121**, 69 (1955) doi:10.1126/science.121.3134.69
- [671] O. Bienaym *et al.*, [Weighing the local dark matter with RAVE red clump stars](#), Astron. Astrophys. **571**, A92 (2014) doi:10.1051/0004-6361/201424478 [arXiv:1406.6896 [astro-ph.GA]].
- [672] T. Piffl *et al.*, [Constraining the Galaxy's dark halo with RAVE stars](#), Mon. Not. Roy. Astron. Soc. **445**, no. 3, 3133 (2014) doi:10.1093/mnras/stu1948 [arXiv:1406.4130 [astro-ph.GA]].
- [673] C. F. McKee, A. Parravano and D. J. Hollenbach, [Stars, gas, and dark matter in the solar neighborhood](#), Astrophys. J. **814**, no. 1, 13 (2015) doi:10.1088/0004-637X/814/1/13 [arXiv:1509.05334 [astro-ph.GA]].

- [674] S. Sivertsson, H. Silverwood, J. I. Read, G. Bertone and P. Steger, [The local dark matter density from SDSS-SEGUE G-dwarfs](#), *Mon. Not. Roy. Astron. Soc.* doi:10.1093/mnras/sty977 [arXiv:1708.07836 [astro-ph.GA]].
- [675] D. A. Neufeld, G. R. Farrar and C. F. McKee, [Dark matter that interacts with baryons: density distribution within the Earth and new constraints on the interaction cross-section](#), arXiv:1805.08794 [astro-ph.CO].
- [676] J. H. Adams *et al.*, [White paper on EUSO-SPB2](#), arXiv:1703.04513 [astro-ph.HE].
- [677] L. B. Rédei, [Possible experimental test of the existence of a universal length](#), *Phys. Rev.* **145**, 999 (1966) doi:10.1103/PhysRev.145.999
- [678] L. B. Rédei, [Validity of Special Relativity at small distances and the velocity dependence of the muon lifetime](#), *Phys. Rev.* **162**, 1299 (1967). doi:10.1103/PhysRev.162.1299
- [679] L. Anchordoqui, M. T. Dova, D. Gomez Dumm and P. LaCentre, [Possible test of local Lorentz invariance from tau decays](#), *Z. Phys. C* **73**, 465 (1997) doi:10.1007/s002880050336 [gr-qc/9512015].
- [680] S. R. Coleman and S. L. Glashow, [High-energy tests of Lorentz invariance](#), *Phys. Rev. D* **59**, 116008 (1999) doi:10.1103/PhysRevD.59.116008 [hep-ph/9812418].
- [681] S. R. Coleman and S. L. Glashow, [Evading the GZK cosmic ray cutoff](#), hep-ph/9808446.
- [682] R. Aloisio, P. Blasi, P. L. Ghia and A. F. Grillo, [Probing the structure of space-time with cosmic rays](#), *Phys. Rev. D* **62**, 053010 (2000) doi:10.1103/PhysRevD.62.053010 [astro-ph/0001258].
- [683] M. Jankiewicz, R. V. Buniy, T. W. Kephart and T. J. Weiler, [Space-time foam and cosmic ray interactions](#), *Astropart. Phys.* **21**, 651 (2004) doi:10.1016/j.astropartphys.2004.04.008 [hep-ph/0312221].
- [684] M. Galaverni and G. Sigl, [Lorentz violation in the photon sector and ultrahigh-energy cosmic rays](#), *Phys. Rev. Lett.* **100**, 021102 (2008) doi:10.1103/PhysRevLett.100.021102 [arXiv:0708.1737 [astro-ph]].
- [685] M. Galaverni and G. Sigl, [Lorentz violation and ultrahigh-energy photons](#), *Phys. Rev. D* **78**, 063003 (2008) doi:10.1103/PhysRevD.78.063003 [arXiv:0807.1210 [astro-ph]].
- [686] D. M. Mattingly, L. Maccione, M. Galaverni, S. Liberati and G. Sigl, [Possible cosmogenic neutrino constraints on Planck-scale Lorentz violation](#), *JCAP* **1002**, 007 (2010) doi:10.1088/1475-7516/2010/02/007 [arXiv:0911.0521 [hep-ph]].
- [687] W. Bietenholz, [Cosmic rays and the search for a Lorentz invariance violation](#), *Phys. Rept.* **505**, 145 (2011) doi:10.1016/j.physrep.2011.04.002 [arXiv:0806.3713 [hep-ph]].
- [688] F. W. Stecker, [Testing Lorentz symmetry using high energy astrophysics observations](#), *Symmetry* **9**, no. 10, 201 (2017) doi:10.3390/sym9100201 [arXiv:1708.05672 [astro-ph.HE]].
- [689] S. T. Scully and F. W. Stecker, [Lorentz invariance violation and the observed spectrum of ultrahigh energy cosmic rays](#), *Astropart. Phys.* **31**, 220 (2009) doi:10.1016/j.astropartphys.2009.01.002 [arXiv:0811.2230 [astro-ph]].

- [690] F. W. Stecker and S. T. Scully, [Searching for new physics with ultra-high energy cosmic rays](#), *New J. Phys.* **11**, 085003 (2009) doi:10.1088/1367-2630/11/8/085003 [arXiv:0906.1735 [astro-ph.HE]].
- [691] A. Saveliev, L. Maccione and G. Sigl, [Lorentz invariance violation and chemical composition of ultra-high-energy cosmic rays](#) *JCAP* **1103**, 046 (2011) doi:10.1088/1475-7516/2011/03/046 [arXiv:1101.2903 [astro-ph.HE]].
- [692] L. A. Anchordoqui and J. F. Soriano, [New test of Lorentz symmetry using ultra-high-energy cosmic rays](#), *Phys. Rev. D* **97**, no. 4, 043010 (2018) doi:10.1103/PhysRevD.97.043010 [arXiv:1710.00750 [hep-ph]].
- [693] D. Boncioli *et al.*, [Future prospects of testing Lorentz invariance with UHECRs](#), *PoS ICRC 2015*, 521 (2016) doi:10.22323/1.236.0521 [arXiv:1509.01046 [astro-ph.HE]].
- [694] V. Pavlidou and T. Tomaras, [What do the highest-energy cosmic-ray data suggest about possible new physics around 50 TeV?](#), arXiv:1802.04806 [astro-ph.HE].
- [695] A. Kusenko and T. J. Weiler, [Neutrino cross-sections at high-energies and the future observations of ultrahigh-energy cosmic rays](#), *Phys. Rev. Lett.* **88**, 161101 (2002) doi:10.1103/PhysRevLett.88.161101 [hep-ph/0106071].
- [696] L. A. Anchordoqui, J. L. Feng, H. Goldberg and A. D. Shapere, [Black holes from cosmic rays: Probes of extra dimensions and new limits on TeV scale gravity](#), *Phys. Rev. D* **65**, 124027 (2002) doi:10.1103/PhysRevD.65.124027 [hep-ph/0112247].
- [697] L. Anchordoqui and F. Halzen, [IceHEP high energy physics at the south pole](#), *Annals Phys.* **321**, 2660 (2006) doi:10.1016/j.aop.2005.11.015 [hep-ph/0510389].
- [698] L. Anchordoqui, T. Han, D. Hooper and S. Sarkar, [Exotic neutrino interactions at the Pierre Auger Observatory](#), *Astropart. Phys.* **25**, 14 (2006) doi:10.1016/j.astropartphys.2005.10.006 [hep-ph/0508312].
- [699] L. A. Anchordoqui, H. Goldberg, D. Gora, T. Paul, M. Roth, S. Sarkar and L. L. Winders, [Using cosmic neutrinos to search for non-perturbative physics at the Pierre Auger Observatory](#), *Phys. Rev. D* **82**, 043001 (2010) doi:10.1103/PhysRevD.82.043001 [arXiv:1004.3190 [hep-ph]].
- [700] S. Palomares-Ruiz, A. Irimia and T. J. Weiler, [Acceptances for space-based and ground-based fluorescence detectors, and inference of the neutrino-nucleon cross-section above \$10^{19}\$ eV](#), *Phys. Rev. D* **73**, 083003 (2006) doi:10.1103/PhysRevD.73.083003 [astro-ph/0512231].
- [701] A. V. Olinto *et al.*, [POEMMA: Probe Of Extreme Multi-Messenger Astrophysics](#), *PoS ICRC 2017*, 542 (2017) [arXiv:1708.07599 [astro-ph.IM]].
- [702] F. W. Stecker, J. F. Krizmanic, L. M. Barbier, E. Loh, J. W. Mitchell, P. Sokolsky and R. E. Streitmatter, [Observing the ultra-high-energy universe with OWL eyes](#), *Nucl. Phys. Proc. Suppl.* **136C**, 433 (2004) doi:10.1016/j.nuclphysbps.2004.10.027 [astro-ph/0408162].
- [703] A. Neronov, D. V. Semikoz, L. A. Anchordoqui, J. Adams and A. V. Olinto, [Sensitivity of a proposed space-based Cherenkov astrophysical-neutrino telescope](#), *Phys. Rev. D* **95**, no. 2, 023004 (2017) doi:10.1103/PhysRevD.95.023004 [arXiv:1606.03629 [astro-ph.IM]].

- [704] G. Cowan, K. Cranmer, E. Gross and O. Vitells, *Asymptotic formulae for likelihood-based tests of new physics*, Eur. Phys. J. C **71**, 1554 (2011) Erratum: [Eur. Phys. J. C **73**, 2501 (2013)] doi:10.1140/epjc/s10052-011-1554-0, 10.1140/epjc/s10052-013-2501-z [arXiv:1007.1727 [physics.data-an]].
- [705] R. D. Cousins, *Lectures on statistics in theory: Prelude to statistics in practice*, arXiv:1807.05996 [physics.data-an].
- [706] S. S. Wilks, *The large-sample distribution of the likelihood ratio for testing composite hypotheses*, Annals Math. Statist. **9**, 60 (1938). doi:10.1214/aoms/1177732360
- [707] O. Deligny, *Measurements and implications of cosmic ray anisotropies from TeV to trans-EeV energies*, Astropart. Phys. **104**, 13 (2019) doi:10.1016/j.astropartphys.2018.08.005 [arXiv:1808.03940 [astro-ph.HE]].